Together ahead. RUAG

PROJECT

GRAS Radio Occultation Performance Study

TITLE

Final Report

Issued by
Magnus Bonnedal
Function
Study Manager

Approved by
Magnus Bonnedal
Function
Study Manager
Date
2012-06-19

RUAG Space AB

Postal address
SE-405 15 Göteborg
Sweden
Telephone
+46 (0)31 735 00 00
Telefax
+46 (0)31 735 40 00
Registered number
556134-2204
VAT number
SE556134220401

Prepared by	Affiliation
Magnus Bonnedal	RUAG Space
Jacob Christensen	RUAG Space
Anders Carlström	RUAG Space
Thomas Lindgren	RUAG Space
Christian Marquardt	EUMETSAT
Axel von Engeln	EUMETSAT
Yago Andres	EUMETSAT
Georg Bergeton Larsen	DMI
Kend Bækgaard Lauritsen	DMI
Stig Syndergaard	DMI
Hans-Henrik Benzon	DMI
Martin Bjært Sørensen	DMI
Mikael Gorbunov	IAP Moscow
Gottfried Kirchengast	WEGC/UoG
Barbara Pirscher	WEGC/UoG
Susanne Schweitzer	WEGC/UoG
Johannes Fritzer	WEGC/UoG
Oliver Montenbruck	DLR
Florian Zus	GFZ
Georg Beyerle	GFZ

DOCUMENT CHANGE RECORD

Changes between issues are marked with an outside-bar.

Issue	Date	Paragraphs affected	Change information
1 (Draft)	2011-01-11	All	New document, Draft version was sent to ESA 2010-12-22
2	2012-03-13	All	General update, ESA comments included, missing sections completed. Since this is the first complete version, no change bars are shown.
3	See header		Comments from ESA included

TABLE OF CONTENTS PAGE

1 INTRODUCTION

1.1 Scope

This document summarises the result from the GRAS Radio Occultation Performance Study [Contr].

The purpose of the study is to analyse in particular open loop data in order find improvements of the instrument measurements and the data processing for the present and future instruments. The main study objectives are:

- to evaluate a selected set of GRAS live data, identify existing and potential tracking problems and to propose solutions for GRAS as well as for future RO instruments
- to validate the reconstruction of open loop data
- to generate ECMWF atmospheric profiles matching the selected data set to be used as reference for retrieved profiles
- to define and evaluate optimum retrieval methods for the open loop data
- to simulate atmospheric propagation using wave optics methods in atmospheres containing inversion layers and at multiple frequency bands. These simulations are to be evaluated in terms of advantages of tracking at several frequencies
- to evaluate phase residuals, from antenna and S/C centre of gravity, with the aim to improve POD processing
- to compare C/No values for GRAS with figures claimed for other receivers

The study team has been composed of members from the user community, operator providing the measurement data and instrument manufacturer. The members and their main tasks are:

- RUAG Space, instrument provider, study manager, instrument aspects
- DMI, operating GRAS SAF, data processing
- EUMETSAT, S/C operator, data processing (not financed by the study)
- Wegener Center, UoG, data processing and wave propagation simulations
- DLR, scientific, handling POD aspects
- GFZ, scientific (participating as observer and consultant – not financed by the study)

In parallel with the study, EUMETSAT funded a joint study with UCAR, contract no. EUM/CO/4600000677/AVE, to perform independent data reconstruction and retrieval processing on the selected GAS data.

1.2 GRAS on the Metop Mission

The GRAS (GNSS (Global Navigation Satellite System) Receiver for Atmospheric Sounding) radio occultation (RO) instrument was launched on board of the Metop-A satellite on 19. October 2006. Metop-A is the first in a series of three satellites forming the EUMETSAT Polar System (EPS), [Klaes], and constitutes Europe's first polar orbiting satellite for operational weather and climate observations. EPS is intended to provide meteorological data for at least 14 years into 2020, with individual satellites having an expected life–time of 5 years. Each satellite flies in a polar, sun-synchronous orbit at an altitude of about 820 km, with a local solar equator crossing time of 9:30 in descending mode.

Since its activation on October 27 2006, the GRAS instrument has been continuously profiling the atmosphere, typically providing more than 650 vertical profiles per day. Data is down-linked for each orbit over the Svalbard Archipelago (78°N), and processed towards level 1a (GPS amplitude and carrier phase) and level 1b (vertical profiles of bending angle) data in the EPS Core Ground Segment at EUMETSAT's Central Application Facility (CAF) in Darmstadt, Germany. Products are disseminated to users within 2 hours and 15 minutes. Further processing towards level 2 data (vertical profiles of atmospheric refractivity, temperature and tropospheric humidity) takes place at the GRAS Satellite Application Facility (SAF), with operational products disseminated to users just a few minutes after the level 1a data. SAFs are specialized development and processing centers in EUMETSAT's member states. The GRAS SAF consortium consists of the British Met Office, ECMWF (European Centre for Medium-Range Weather Forecasting), and IEEC (Institut D'Estudis Espacials de Catalunya, Spain) and is lead by DMI (Danish Meteorological Institute, Denmark), which also hosts the GRAS level 2 product processing. Operational GRAS data products have become available in May 2008, [vonEngeln], and are now used operationally by NWP (Numerical Weather Prediction) centres worldwide.

1.3 Document Structure

The present document is composed from all results in the study, as reported in documents from the individual study members. The disposition within the document is structured as follows:

§1 This section, introduction and document structure

§2 References and abbreviations

§3 A background is provided for the principle of radio occultation and tracking principles of the GRAS instrument

§4 The data set that has been selected for the study, the collection of external navigation data, and generation of the reference profiles are presented. Data reconstruction validation is demonstrated. Also a set of quality measures are discussed and a set of twelve study cases of particular interest from retrieval and instrument point of view are defined.

§5 Instrument behaviour derived from the study cases and other occultation data is analysed, and a set of potential instrument improvements is presented.

§6 Wave optics simulations of a set of occultations where strong multipath has been identified are presented and the impact on the instrument is assessed.

§7 In these section the retrieval processing using spectral methods performed at DMI, UoG, GFZ, UCAR and EUMETSAT are presented. A comparison and evaluation of the different methods is presented together with the plan for implementation of an operational processing.

§8 Zenith measurement data used for POD is investigated in order to find the reason for identified antenna phase residuals and an offset between the estimated centre of gravity and the zenith antenna phase centre. Also in the context of zenith measurement, the difference in reported C/No and codeless tracking loss between different receivers is investigated.

§9 Summary and conclusions from the study

1.4 Acknowledgments

The authors would like to thank the European Space Agency ESA for funding this work under the GRAS Radio Occultation Performance Study contract, no. 21995/08/NL/EL. M. Gorbunov and A. Jensen were supported by GRAS SAF and EUMETSAT Visiting Scientist Programmes, respectively. UCAR retrievals from GRAS data were obtained as part of the “Study on Assessment of the Structural Uncertainty of GRAS Product Retrievals in View of Climate Applications” (contract no. EUM/CO/4600000677/AVE). GFZ Potsdam, UCAR and JPL kindly provided data from their respective navigation bit grabber networks for the study period.

2 DOCUMENTS

2.1 Applicable Documents

[Contr] ESTEC Contract No. 21995/08/NL/EL with RUAG Aerospace Sweden AB, GRAS Radio Occultation Performance Study.

2.2 Reference Documents

The sections covering retrieval processing contain their own references compiled at the end of each section.

[AGGA] AGGA-2 (ATMEL T7905E) Rad Tolerant GPS/GLONASS ASIC User's Manual, Rev. A – 24 Aug-01.

[APSRD] MO-RS-AAE-GR-0001, Algorithm Processing Software Requirement Document

[CIRA86] Kirchengast G., et. al. "The CIRAS86aQ_UoG model: An extension of the CIRA-86 monthly tables including humidity tables and a Fortran95 global moist air climatology model", (1999)

[Dass] Dass T., Freed G., Petzinger J., Rajan J., Lynch T.J., Vaccaro J., (2002) "GPS clocks in space: Current performance and plans for the future", in 34th Annual Precise Time and Time Interval (PTTI) Meeting, Reston, VA, December 03-05, (2002) (www.pttimeeting.org)

[EUM1] Data set from EUMETSAT 2009-09-25, email from C Marquardt, 2009-09-25 12:51

[MDICD] MO-IC-SES-GR-0008, Measurement Data Interface Control Document

[MDID] MO-RS-SES-GR-0036, Measurement Data and Interpretation and Description

[GPSsol] M. Bonnedal, J. Christensen, A. Carlström, A. Berg, Metop-GRAS in-orbit instrument performance, GPS Solutions, Vol 14, p109-120, (2010)

[Marq] C. Marquardt, et.al., "First Results from the Processing of GRAS Raw Sampling Data", Cosmic Workshop, Boulder USA, Oct 2009

[RD1] GRAS Performance Study, Final Presentation by DLR, held at Estec 14 Sep 2007

[RD2] Tracking and orbit determination performance of the GRAS instrument on MetOp-A, Oliver Montenbruck et. All, GPS Solutions, Volume 12, Number 4 / September, 2008

[RD3] Metop-2 Characteristics studied during GRAS RO performance study affecting GRAS POD, EUMETSAT, 12/05/2009

[RD4] MO-TR-DOR-PM-0509, iss 4, METOP PLM, FM2 Aliqnment Test Report

Astrium GmbH, (including AMSU-A1 & AMSU-A2 Measurements

at Baikonur), dated on 10-July-2006

[RD5] Metop-2 Characteristics studied during GRAS RO performance study affecting

GRAS POD, EUMETSAT, 12/05/2009

[AN2] GRAS GZA Phase Centre Evaluation, P-GRDS-NOT-00001-RSE

[GPDF] EUM/OPS/TEN/09/2483, Issue v3A, GRAS Prototype Data Format Description

[Tatarskii] Wave Propagation in Random Media (Scintillations), V.I. Tatarskii, SPIE, ISBN 0-8194-1062-4

[Klaes] Klaes, K. D., M. Cohen, Y. Buhler, P. Schlüssel, R. Munro, J.-P. Luntama, A. V. Engeln, E. O. Clérigh, H. Bonekamp, J. Ackermann, and J. Schmetz (2007). An Introduction to the EUMETSAT Polar system. Bulletin of the American Meteorological Society 88 (7), 1085.

[vonEngeln] von Engeln, A., S. Healy, C. Marquardt, Y. Andres, and F. Sancho (2010). Validation of operational GRAS Radio Occultation Data. Geophysical Research Letters 36.

[Kursinski] Kursinski, E. R., Ph. D. Thesis title: “The GPS Radio Occultation Concept: Theoretical Performance and Initial Results”. Ph D Thesis, California Institute of Technology, Pasadena, CA, 1997

2.3 Abbreviations

Abbreviation	Meaning
AGGA	Advanced GPS GLONASS (signal processing) ASIC
Am	Amplitude Modulation
APC	Antenna Phase Centre
ARF	Antenna Reference Frame
BA	Bending Angle
C/No	Carrier to Noise density
CAF	Central Application Facility
CL	Closed Loop
CODE	Centre for Orbit Determination in Europe
CoM	Centre of Mass
CT	Canonical Transform
DF	Dual Frequency
DLR	Deutches Zentrum für Luft- und Raumfahrt
DMI	Danmarks Meteorologiske Institut
ECMWF	European Centre for Medium range Weather Forecasts
EGOPS	End-to-end GNSS Occultation Performance Simulator
EPC	Electrical Phase Center
EPS	EUMETSAT Polar System
EUM	EUMETSAT
FIR	Finite Impulse Response
FOI	Fourier Integral Operator
FR	Final Review
FSI	Full Spectral Inversion
GFZ	Deutsches GeoForschungsZentrum
GNSS	Global Navigation Satellite System
GO	Geometrical Optics
GPS	Global Position System
GPST	GPS Time
GRAS	GNSS Receiver for Atmospheric Sounding
GRIB	GRIdded Binary (format)
GTD	Geometrical Theory of Diffraction
ICDB	Instrument Characterisation DataBase
I/Q	In phase/Quadrature phase
IEEC	Institute d’Estudis Espacials de Catalunya
IMT	Instrument Measurement Time
IOV	On-Orbit Verification

Abbreviation	Meaning
JPL	Jet Propulsion Laboratory
NAV	Navigation (data or modulation)
NB	Navigation Bit(s)
NCO	Numerically Controlled Oscillator
NetCDF	Network Common Data Form
NH	Navigation Data Health
No	Noise power density
NPD	Noise Power Density
NWP	Numerical Weather Prediction
NRIPA	Nominal Ray Impact Altitude
OBT	On Board Time
OL	Open Loop synonym with RS
OPAC	Occultation for Probing Atmosphere and Climate
OR	Ocean Reflection
PLM	Pay-Load Module
PM	Phase Modulation
POD	Precise Orbit Determination
RAFS	Rubidium Atomic Frequency Standard
RFQ	Request For Quotation
RO	Radio Occultation
ROPP	Radio Occultation Processing Package
RS	Raw Sampling synonym with OL
RSE	RUAG Space AB
S/W	Software
SAF	Software Application Facility
SF	Single Frequency
SH	Signal Health
SLTA	Straight Line Tangent Altitude
SNR	Signal to Noise Ratio
std	standard deviation
SV	Space Vehicle
SVF	Space Vehicle Frame
SVM	Space Vehicle Module
TEC	Total Electron Content
TS	Tracking State
UCAR	University Cooperation for Atmospheric Research
UoG	University of Graz
USO	Ultra Stable Oscillator
WOP	Wave Optics Propagation

3 BACKGROUND

3.1 Radio Occultation Principle, Definition of Terms

The atmospheric profiling technique provides measurements of the Doppler shift of the probing GNSS signals that have passed through the limb of the atmosphere, [Kursinski]. The magnitude of the shift is related to the atmosphere's refractivity gradients along the path of the signal. These in turn are related to the neutral atmosphere's temperature, pressure and humidity fields.

Provided that the signal has sufficiently high quality (i.e. signal-to-noise ratio) and that other variables of the experiment (e.g. the positions of the transmitter and receiver, and the effects of the ionosphere) are known to sufficient accuracy, information on the temperature and humidity fields can be retrieved. More specifically, from series of measurements obtained during the occultation event, the profiles of temperature and humidity close to the tangent point of the signal path can be estimated.

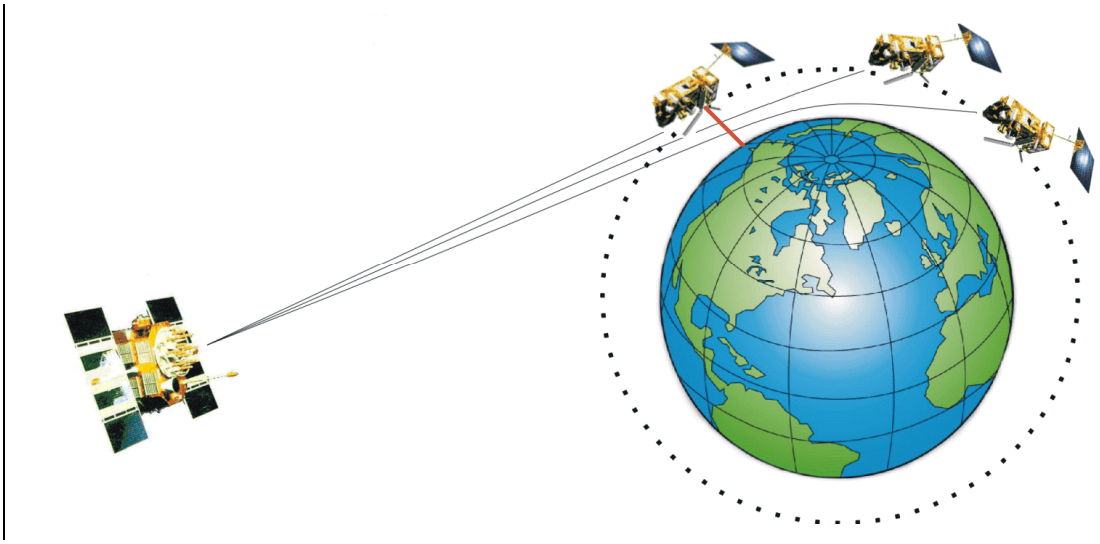

Figure 1 Illustration of the GPS radio occultation technique for a GRAS measurement.

The occultation technique is defined by the geometry, where the transmitter and the receiver are positioned relative to the Earth in such an arrangement, that the radio wave signal traverses the atmosphere from the ionosphere to the limb of the Earth and back again towards the LEO satellite. The propagation path of the GNSS electromagnetic wave through the atmosphere will be influenced by the dispersive characteristics of the medium, due to ionized and neutral part of the gas of the atmosphere. Ray bending and changes in the phase and amplitude of the transmitted signals, caused by the conditions in the ionosphere and troposphere/stratosphere, are the results.

The dispersion relation for the electromagnetic wave probing the atmosphere can be defined as the real part of the refractive index μ, when discarding the absorption of the wave in the media. The relation expressing the total atmosphere refraction becomes,

$$N = k_1 \frac{P_d}{T} + k_2 \frac{P_w}{T^2} + k_3 \frac{P_w}{T} \quad (1)$$

where $N = (\mu - 1) \cdot 10^6$, P_d the partial pressure of the dry air mass (in hPa), T the absolute temperature of the atmosphere (in Kelvin), and P_w the partial pressure of the water vapour content (in hPa). The constants for each of the terms in (1) are evaluated to have the magnitudes, k_1 = 77.60 K/hPa; k_2 = 37.39·10^4 K^2/hPa; k_3 = 70.40 K/hPa.

The first term on the right-hand-side of the above equation is due to the dry part of the atmosphere, and is caused by the wave polarization of the molecules in the lower neutral atmosphere (troposphere and stratosphere). The second and third term relate to the moist atmosphere relation from the permanent dipole moment of water molecules. All these terms are independent of frequency. It is assumed that the ionosphere contribution can be estimated and removed, so that N only carries the neutral atmosphere contributions.

The moist terms have only a substantial impact on the magnitude of N in altitudes below 5 kilometre. Above altitudes of 7-10 kilometres the contribution to N from the water vapour terms is less than 2%. In the tropics the influence of water vapour has to be considered in the retrieval of the lowest part of the troposphere temperature profile. Thus, observations of refractivity itself is a measure of the combined effect of temperature and water vapour, and may ultimately be applied to weather and climate models as a consistent physical parameter describing the state of the atmosphere.

Taking account of the above considerations, N can be reduced to a function of only the dry term in the equation of refractivity. Combining this with the equation of state,

$$P = \frac{\rho R T}{m} \tag{2}$$

where

R is the gas constant

m is the relative molecular weight

results in a directly proportional relation between the air mass density ρ and N. In other words, ρ(r) , where r is the radius from the Earth local centre of curvature, can be obtained from the values of the refractive index. Applying hydrostatic equilibrium,

$$dP = -g\rho \, dr \tag{3}$$

where g represents the acceleration of gravity, establishes a relation between the pressure P(r) at a certain height and the air mass density ρ(r). The temperature T(r) can now be obtained from P(r) and ρ(r). So in summary, vertical profiles of ρ, P, and T can be derived directly from the observed refractive index profile μ(r).

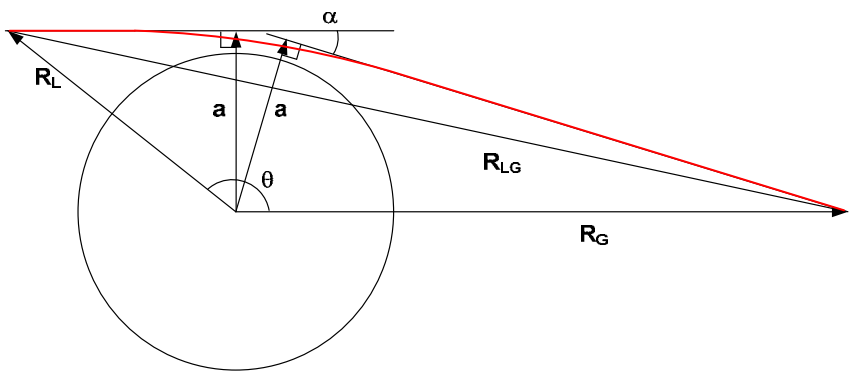

Figure 2 Occultation geometry showing satellite radii, impact parameter a, and bending angle α.

The basic parts of this retrieval procedure can be summarised in the below parameter and equation flow (φ is the excess phase range):

Observables: $\varphi = \int_{ray\,path} \mu ds - R_{LG}$ — φ_1 and φ_2

↓

Ionosphere correction: $\varphi_C = \frac{f_1^2 \varphi_1 - f_2^2 \varphi_2}{f_1^2 - f_2^2}$ — φ_C

↓

Doppler shift: $\frac{d\varphi_C}{dt}$ — $\dot{\varphi}_C$

↓

Impact height: $F(a) = \dot{\varphi}_C + \dot{R}_{LG} - (\dot{R}_L \cos\phi(a) - \dot{R}_G \cos\chi(a)) = 0$ — a

↓ ↑

Bending angle: $\alpha = \theta - \arccos(\frac{a}{R_L}) - \arccos(\frac{a}{R_G})$ — $\alpha(a)$

↓

Abel transform: $\ln(\mu) = \frac{1}{\pi} \int_a^\infty \frac{\alpha(\xi) d\xi}{\sqrt{\xi^2 - a^2}}, \quad r = \frac{a}{\mu}$ — $\mu(r)$

↓

Neutral density: $\rho = \frac{1}{k_1 R}(N - \frac{k_2 P_w + k_3 T P_w}{T^2}), \quad N = (\mu - 1) \cdot 10^6$ — $\rho(r)$

↓

Hydrostatic equation: $P = \int_{R_E+z}^\infty \rho(r) g(r)\, dr$ — $P(z)$

↓

Equation of state: $T = \frac{mP}{R\rho}$ — $T(z)$

The thermal noise and the ionosphere correction at altitudes above 30 km limit the refractivity measurements for the neutral atmosphere, whereas horizontal variations in the atmosphere and especially sharp gradients in the refractivity causing atmospheric multipath propagation limit the accuracy of the measurements for altitudes less than 25 km. The mean error in the refractivity profile can be achieved to be less than 0.4% for altitudes between 5 km and 30 km. This corresponds to accuracy of about 1K on the retrieved temperature profile.

The term Signal to Noise Ratio (SNR) provided in the unit V/V is referred to an equivalent bandwidth of 1Hz. It is related to the signal to noise power density C/No in dBHz as; C/No = 20 log10(SNR).

3.2 Instrument Tracking Behaviour

The GRAS output signal generation is governed by the tracking state parameter as shown in Table 1 below. The table is valid for both rising and setting occultations. Tracking states not mentioned here are internal in the S/W.

Single frequency carrier package refers to data from Closed Loop (CL) tracking of the L1 C/A signal. Dual frequency carrier package refers to data from CL tracking of the L1 C/A and P signals and the L2 P signal.

When the received signal is highly dynamic or has a low signal to noise ratio, the carrier cannot be tracked. In the case only code tracking is achieved, the carrier loop is controlled by a Doppler model, and measurement data is provided in carrier Open Loop (OL), but in code closed loop, tracking. This is in GRAS nomenclature referred to as Raw Sampling (RS). The receiver tracking states and the corresponding generation of measurement data are compiled in Table 1.

Tracking state	Status and description of tracking state	C/A-Code Phase	C/A-, P1-, P2-Code Phase	Open Loop data for Occultation	Single Frequency Carrier Packet	Dual Frequency Carrier Packet
0	**Acquisition and tracking ended.** This is the lowest tracking state					
1	**C/A-code acquisition.** In this state the C/A-code is acquired and the carrier is predicted					
2	**C/A-code lock check.** The initial error in L1 carrier frequency is reduced and the lock check for the acquired C/A-code is performed.	X		X		
3	**L1 carrier lock check.** The bandwidth for the Costas loop is reduced and lock check for the L1 carrier is performed.	X		X		
8	**Single carrier frequency tracking at 1 ms.** The early-Punctual-Late correlator spacing is reduced and the integration time is changed from 1 ms to 10 ms.	X		X	X	
9	**Single carrier frequency tracking at 10 ms.** The bandwidth of the filters are modified as a result of the change of integration time. At the end of this state, a decision is taken to determine weather coded or codeless P-code acquisition shall be started.	X			X	
13	**P-code acquisition.** The P(Y)-code generator is initialised and the two-dimensional P(Y)-code on L1 and L2 code phase uncertainty range is searched to find the P(Y)-code phase.	X			X	
14	**P-code tracking.** The lock check for the P(Y)-code on L2 is performed.	X			X	
15	**P-code and L2 carrier tracking.** All signal components are tracked. This is the highest tracking state		X			X

Table 1 Tracking States (TS) description and data generation.

In summary, measurement data are generated in the following tracking states:

- OL data is generated in TS 2-8
- C/A CL data is generated in TS 8-15
- L2 acquisition starts in TS9, at the same time OL is abandoned.
- C/A, P1 and P2 data including code phase are generated in TS 15

In this document, Open Loop (OL). in GRAS nomenclature named Raw Sampling (RS), mode is used for the TS tracking states where OL data is provided, and Closed Loop (CL) mode refers to the TS where CL data is provided.

This can be illustrated with EUMETSAT data from 30-Sep-2008, 00:20:39, Figure 3, where we see multiple reacquisitions of the C/A carrier loop. Note the C/A CL measurement data is only generated in TS 8 and higher. The TS is provided in the measurement data as the events in time and TS when TS is changed. In the ground processing this data is up-sampled to the OL and CL rates.

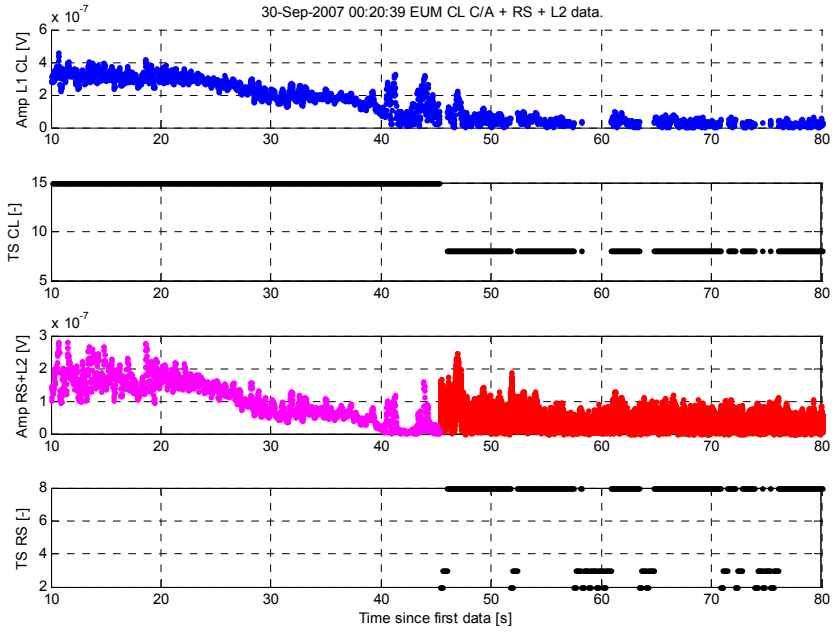

Figure 3 L1 CL, L2, and OL data are shown together with the CL and OL tracking states.

Data generation is closely correlated with corresponding TS. We see no degradation of data quality correlated with TS and hence no possibility to reject data based on TS information.

The instrument uses a number of parameters, given in Straight Line Tangent Altitude SLTA, controlling the instrument tracking states. Of these the following are settable by command:

SLTA_V	Altitude where rising acquisitions starts
SLTA_L2	Altitude where the instrument abandons OL if CL tracking is achieved and starts L2 acquisition. The default value is set to -35 km
SLTA_A	Additional altitude range during which stable CL tracking shall be achieved in order to start L2 acquisition. Presently 0 km
SLTA_AV	Altitude where setting tracking is aborted

The full set of SLTA parameters for rising and setting occultations is shown in Figure 5, [MDID]. Settable parameters are marked with an asterisk.

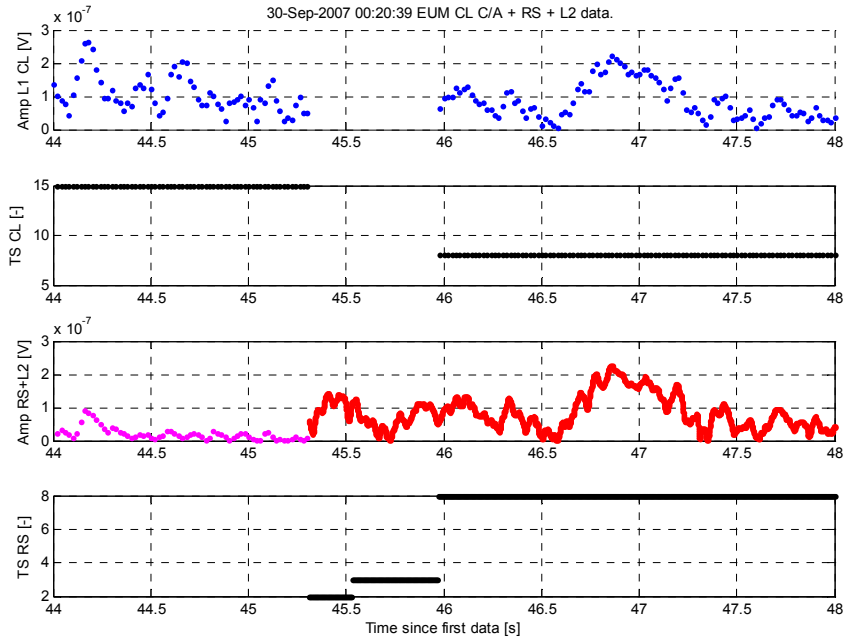

Figure 4 L1 CL, L2, and OL data are shown together with the CL and OL tracking states, blow-up from Figure 3.

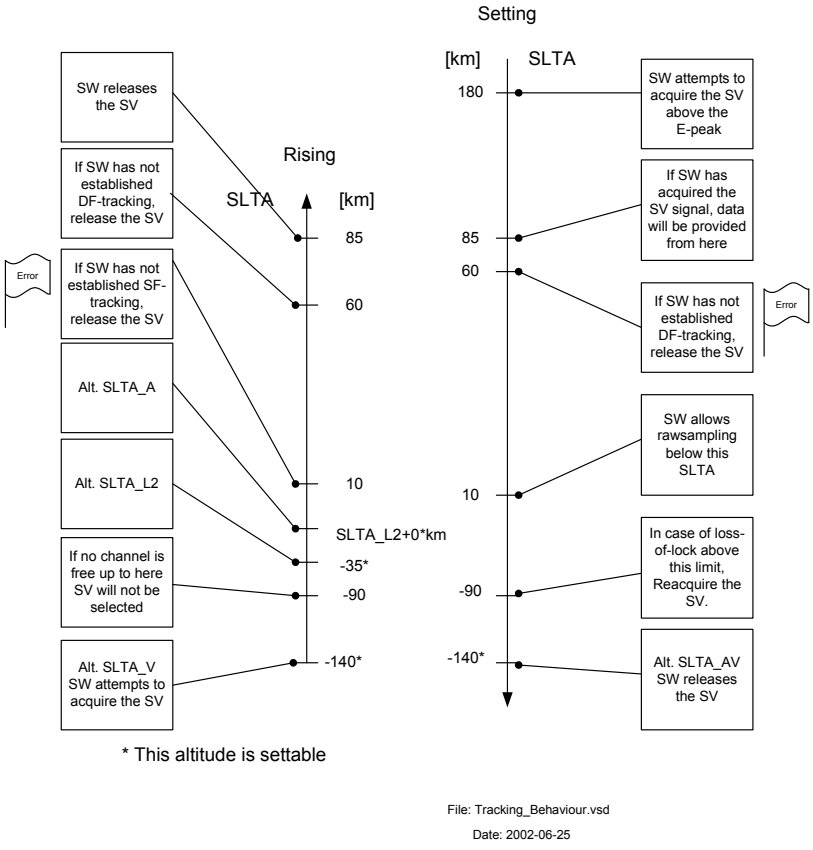

Figure 5 SLTA limits for the occultation channels (default values) [MDID].

4 DATA SET SELECTION AND VALIDATION

4.1 Data Set

The study is based on GRAS observations taken between September 30 and October 31, 2007. EUMETSAT provided a level 1a data set (i.e., amplitude, SNR and carrier phase data reconstructed from level 0 GRAS measurements) along with precise MetOp-A orbits derived from GRAS zenith antenna measurements. For the GPS constellation, final GPS orbits and clocks from the IGS processing performed by CODE (Center for Orbit Determination in Europe) were used. Raw observations of the navigation bit data transmitted by the satellites of the GPS constellation were kindly provided by UCAR, GFZ Potsdam and JPL, and were applied for the demodulation of the navigation bits from the GRAS raw sampling data during the level 1a processing.

The level 1a data set consists of 22105 globally distributed occultations, equally split between rising and setting events. We note that the (successful) validation of the data reconstruction as implemented by EUMETSAT was also undertaken as part of the study, but is not further discussed here. While the same level 1a data was used by all study participants, level 1b (bending angle profile) processing was performed by individual groups using their choice of advanced retrieval algorithms (see more details in section 7). Thus, possible differences in retrieval results highlight structural uncertainties in the level 1b processing applied by the various centres.

4.2 Generation of ECMWF Reference Cases.

The reference profiles produced in the work package has been calculated on the basis of analysis data from the European Centre for Medium-Range Weather Forecasts (ECMWF).

The ECMWF data has been selected as reference since ECMWF provides a global field from which a reference profile can be generated at any location. This data type from a numerical weather model is commonly used as reference when evaluating the quality of radio occultation measurements. The analysis data from ECMWF are based on satellite, ground, and airplane data combined with a physical model, and it is considered the best reference for the atmosphere. Other sources, as e.g. radio sondes, could be used as reference, but for the relatively short period of time where this study evaluates data, only a limited number of collocated measurements can be expected and this will degrade the possibilities of statistical comparisons.

ECMWF provides an analysis every 6 hour. The data from ECMWF is in GRIB (Gridded binary) format and has a 1.0° x 1.0° degree resolution.

The data is on ECMWF model (half) levels and the data consist of a set of coefficients and variables which enables the computation of temperature, humidity and pressure at 91 levels.

4.2.1 Extraction Scheme

Date, time and location of the occultations is defined by EUMETSAT in the file varalpha_20070930-20071027.nc

The analysis most close in time to the occultation time, is selected and the data for the background profile is calculated from the surrounding grid points using bilinear interpolation.

The reference profiles provides information on geopotential height and pressure at the surface, the land/sea mask for the position of the requested reference profile and pressure, temperature and humidity at 91 levels.

4.2.2 Generation of Reference Profiles

Reference profiles are generated using the ECMWF background profile as input for the calculation of refractivity. This is done using a tool developed by the GRAS-SAF as part of the Radio Occultation Processing Package (ROPP).

4.3 Data Reconstruction Validation

4.3.1 General

Six hours of occultation data was provided by EUMETSAT, [EUM1]. The data was dedicated for the validation in that no antenna corrections were applied. Clock corrections are available for subtraction from the measurement times. The data format is described in [GPDF]. A number of occultations have been investigated, and two of these were selected at random for detailed analysis; one rising occultation with file name :

"*gras_occ_20070930001354Z_20070930001459Z_20090925093113Z.nc*"
Start of data: 30-Sep-2007 00:13:54
SVID: 5 (Space Vehicle Identifier)
CH: 9

and one setting occultation with file name:

"gras_occ_20070930002039Z_20070930002203Z_20090925093222Z.nc"
Start of data: 30-Sep-2007 00:20:39
SVID: 19
CH: 10

CH refers to the AGGA processing channel number. 0-7 refer to the navigation or zenith chain, 8-9 refer to the rising occultation chain, and 10-11 refer to the setting occultation chain.

The set of data delivered for the validation is produced with clock corrections and Instrument Characterisation DataBase (ICDB) corrections switched off. However, measurement time including clock correction and the separate clock correction are both provided and measurement times named cl_dtime, rs_dtime are here used after the clock corrections have been removed.

The data files were chosen among the data set provided 2009-09-25 containing 6 h of occultation data.

Detailed results are presented for the rising occultation. Only in cases where the validation results differ, results for the setting occultation are given.

The data is provided in NetCDF files, with data in double precision, i.e. 2^{-53}, or 10^{-16}, corresponding well with the Matlab nominal precision of $2 \cdot 10^{-16}$.

The validation was made in a Matlab environment. The RUAG Space AB (booth RUAG and RSE are used in the following) reconstructed data was available in an internal format named Level IV, with the properties:

- data is sorted into the data components defined in the [MDICD]. Each occultation measurement data track is available in separate files. Data is represented with integer resolution corresponding to the bit-fields defined in [MDICD].

- data is converted into engineering units according to the measurement scaling and processing defined in [MDID].
- data comprise also the GPS Ephemeris data, Navigation solution, and external NAV bits (when available). Further additional parameters and quality measures are added to aid the data analysis.

4.3.2 Summary

The agreement between the EUMETSAT and the RUAG Space AB (RSE) data reconstruction is found to be very good. The phase and time vectors agree to the numerical accuracy. The amplitudes agree to an accuracy of a few hundreds of a dB. The parameters presented in Table 2 have been analysed, where also a summary of the findings in the following sections is given.

Parameter	**Observation on EUM data**
IMT: cl_dtime rs_dtime	- relative time OK
CL CA I/Q Amplitudes cl_i_ca_uncorr, cl_q_ca_uncorr, cl_amplitude_ca	Amplitudes OK, mean 0.01 dB, std 0.02 dB difference in scale factor Phase OK to numerical accuracy
CL P2 I/Q Amplitudes cl_i_p2_uncorr, cl_q_p2_uncorr, cl_amplitude_p2	Amplitudes OK, mean 0.00 dB, std 0.03 dB difference in scale factor Phase OK to numerical accuracy
CL NCO phase_l1_nco	- relative phase OK std. 0.01 mm - differ in starting value (due to different selection of reference time) - differ in sign (EUM use range, RSE phase)
cl_snr_p1 cl_snr_p2	OK, differ a few hundreds of a dB
RS CA I/Q Amplitudes rs_i_ca_uncorr, rs_q_ca_uncorr, rs_amplitude_ca	Amplitudes OK, mean 0.00 dB, std 0.03 dB difference in scale factor Phase OK – very small difference due to numerical accuracy
RS NCO rs_phase_l1_nco	OK, agree to the numerical accuracy - differ in starting value (due to different selection of reference time) - differ in sign (EUM uses range, RSE uses phase)
CL to RS continuity rs_phase_l1_nco rs_i_ca, rs_q_ca cl_phase_l1_nco cl_i_ca, cl_q_ca	OK, bias and std decrease as expected with increased filtering

Table 2 Summary of evaluated parameters and observations.

4.3.3 Time Vectors

Parameter	Observation on EUM data
IMT: cl_dtime rs_dtime	- relative time OK

Available data:

Continuous data for the setting occultation are available for the times given below. Time is counted from the first sample.

Parameter	Time for continuous data
OL CA	10.0 s – 28.6 s
CL CA	13.6 s – 64.6 s
CL P2	35.5 s – 64.6 s

The time vectors are evaluated after clock corrections (clk_rec) have been removed as (in script language):

```
cl_dtime = cl_dtime + cl_clk_rec;
rs_dtime = rs_dtime + rs_clk_rec;
```

The time vectors EUM cl_dtime and the RUAG IMT (Instrument Measurement Time) are identical to the numerical accuracy (2e-16 in Matlab, taking into account that the start time is stripped off) and no drift can be identified.

Starting points for cl_dtime and rs_dtime is the time of the first sample, normally rs_dtime(1) in rising and cl_dtime(1) in setting occultations. The RUAG IMT is in the present validation normalised in the same way.

It should be noted that the in the validation process, the time vectors and measurement data are evaluated separately as the reconstructed data from EUM and RUAG refer to the same measurements.

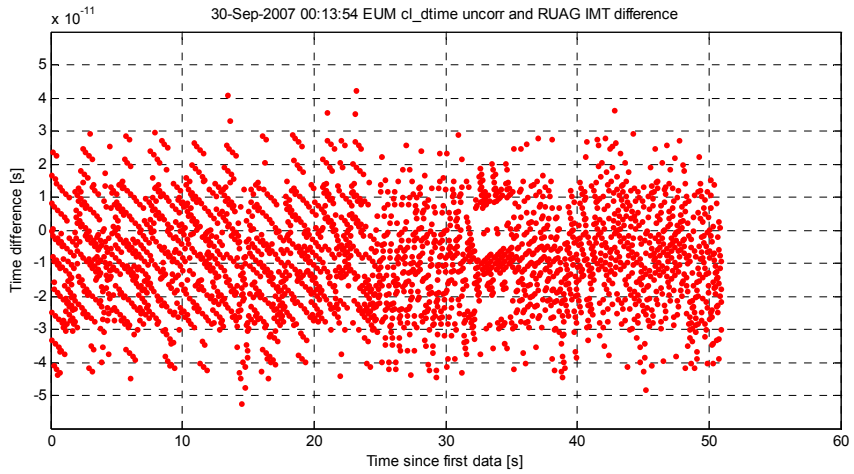

Figure 6 Difference between EUM cl_dtime and RUAG IMT vectors with constant off-set removed

4.3.4 Closed Loop Data

4.3.4.1 CL I/Q Data

Parameter	Observation on EUM data
CL CA I/Q Amplitudes cl_i_ca_uncorr, cl_q_ca_uncorr, cl_amplitude_ca	Amplitudes OK, mean 0.01 dB, std. dev. 0.02 dB difference in scale factor Phase OK to numerical accuracy
CL P2 I/Q Amplitudes cl_i_p2_uncorr, cl_q_p2_uncorr, cl_amplitude_p2	Amplitudes OK, mean 0.00 dB, std. dev. 0.03 dB difference in scale factor Phase OK to numerical accuracy

The normalised amplitude and I/Q data are presented in the same plots in Figure 7, where also the complex ratio of EUM to RUAG complex I+j*Q voltage is shown. We note a minor difference in amplitude, mean and std of the amplitude ratio are 0.01 dB and 0.02 dB respectively. The phases are identical to the numerical accuracy.

I/Q data for the EUM data set: rs_i/q_ca_uncorr with navigation data modulation.

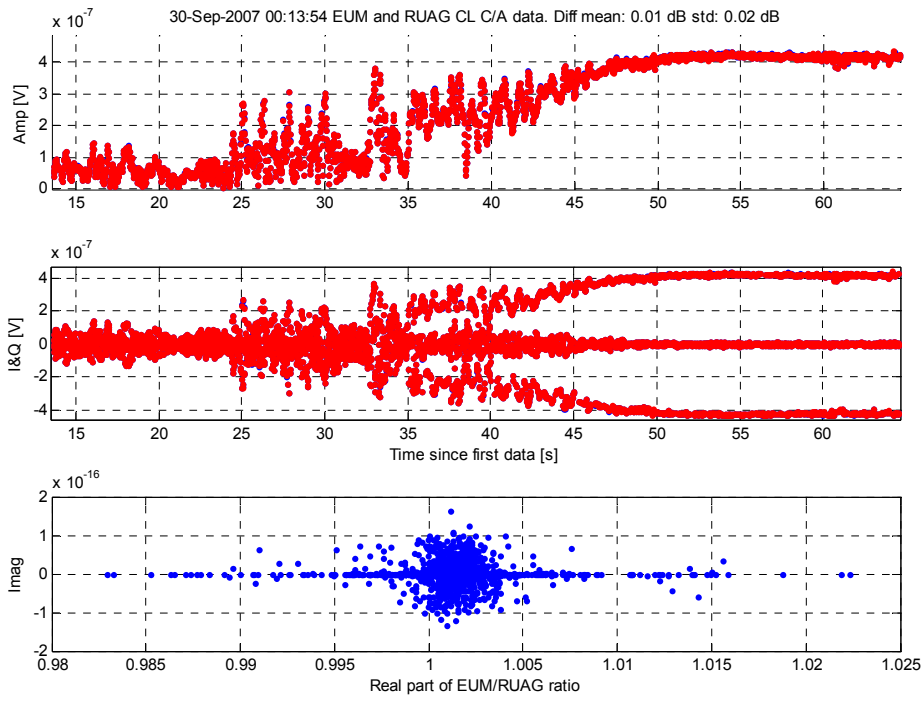

Figure 7 CL C/A data. Top down: Amplitude, I/Q samples EUM (blue) and RUAG (red) data vs. time, and imaginary vs. real part of ratio V_EUM/V_RSE. In the presented resolution, the EUM and RUAG data cannot be discriminated.

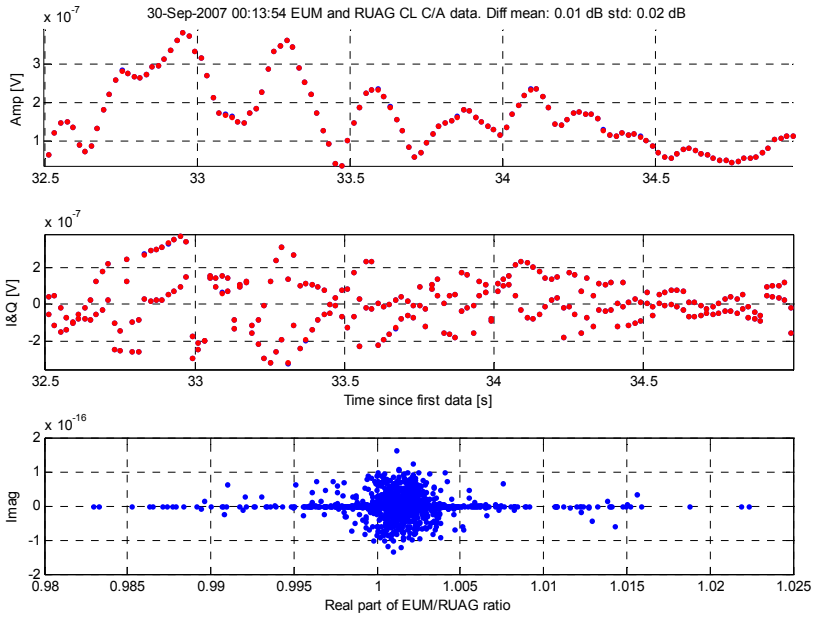

Figure 8 **Blow-up of EUM (blue) and RUAG (red) CL C/A I/Q data vs. time. In the presented resolution, the EUM and RUAG data cannot be discriminated.**

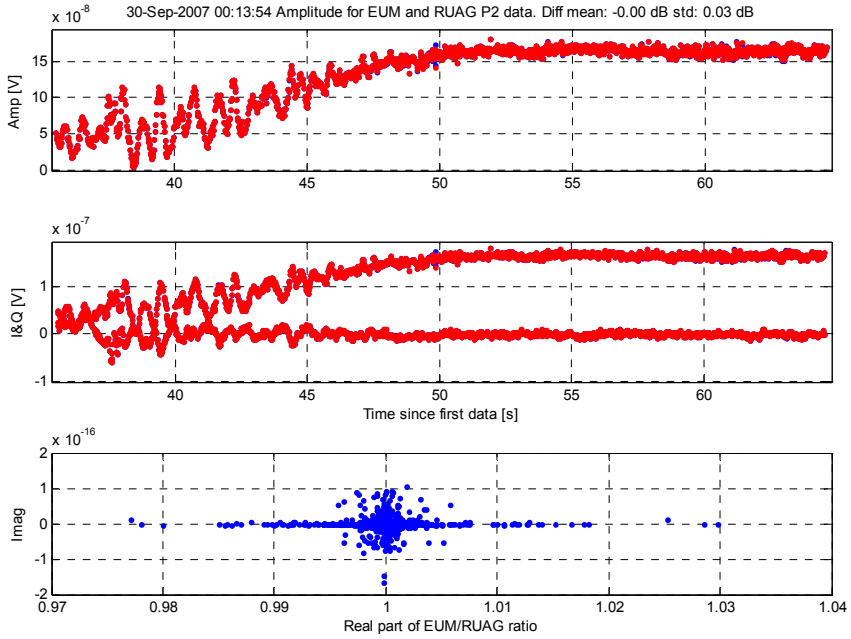

Figure 9 **CL P2 data. Top down: Amplitude, I/Q samples EUM (blue) and RUAG (red) data vs. time, and imaginary vs. real part of ratio V_EUM/V_RSE. In the presented resolution, the EUM and RUAG data cannot be discriminated.**

4.3.4.2 CL NCO Data

Parameter	Observation on EUM data
CL NCO phase_l1_nco	- relative phase OK std 0.01 mm - differ in starting value (due to different selection of reference time) - differ in sign (EUM use range, RUAG phase)

The EUM NCO data is presented using a minus sign, so that the phase is decreasing with the decreasing range. This is the opposite to the sign definition in [MDID]. The starting values also differ. This is due to the reconstruction of the NCO phase from the header frequency multiplied with a reference time. This reference time can be selected arbitrarily, but shall be identical for all NCO phases in one occultation. The reference time has been selected differently in the EUM and RUAG data reconstructions.

Taking this sign and zero phase differences into account, the difference in NCO phase between EUM and RUAG data has a std. dev. of 0.01 mm, Figure 10. The time offset is removed by subtraction the mean phases.

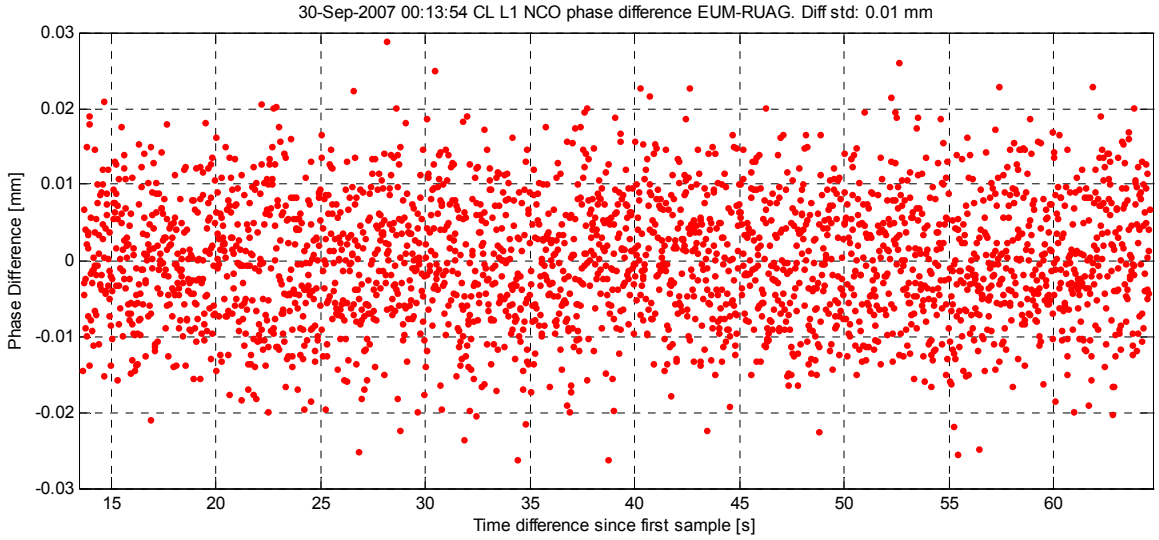

Figure 10 CL L1 NCO phase difference between EUM and RUAG data.

4.3.4.3 CL Combined Complex Voltage

The combined complex voltages are formed as (I+jQ)*exp(jNCO) for RUAG data, and with a negative exponent for the EUM data. The agreement is to the numerical accuracy in phase and to 0.02 dB in amplitude. This consistency is merely a confirmation of the separate I/Q and NCO agreements.

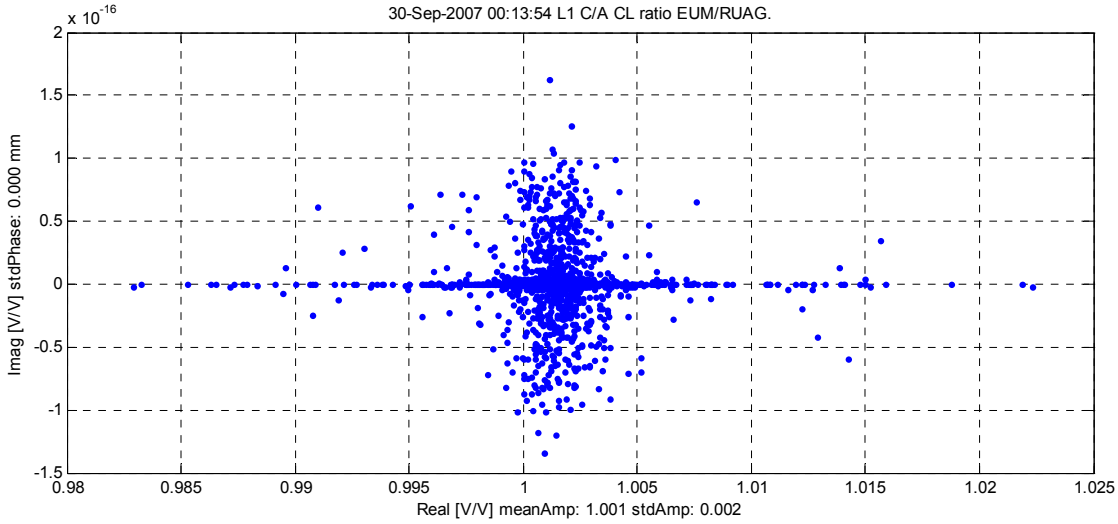

Figure 11 CL L1 ratio of the EUM to RUAG complex voltage data.

4.3.4.4 Noise and C/No Products

Parameter	Observation on EUM data
cl_snr_p1 cl_snr_p2	OK, differ a few hundreds of a dB

In Figure 12 we see the C/No quantity for C/A, which differ some 0.01 dB, the same order of magnitude as the amplitudes. The L2P C/No differ some 0.03 dB, Figure 13. In Figure 14 and Figure 15 we show the noise power densities No for the L1 and L2 bands, given in dBW/Hz. The apparent difference between the EUM and RUAG noise is mainly due to the different presented sampling rates, interpolated up to 50 Hz for EUM and the raw data 10 Hz for RUAG.

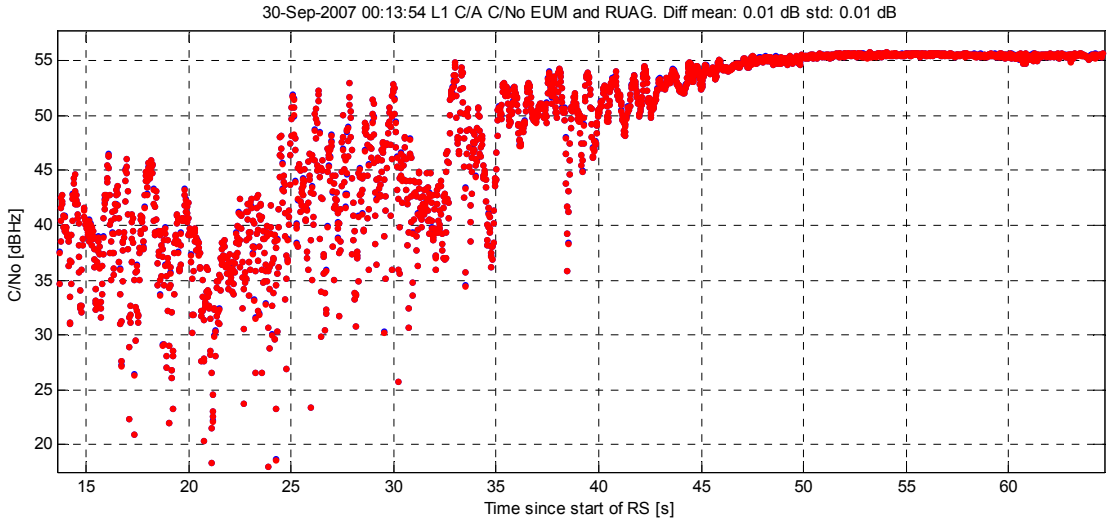

Figure 12 CL L1 C/A C/No for the EUM (blue) and RUAG (red) data. In the presented resolution, the EUM and RUAG data cannot be discriminated.

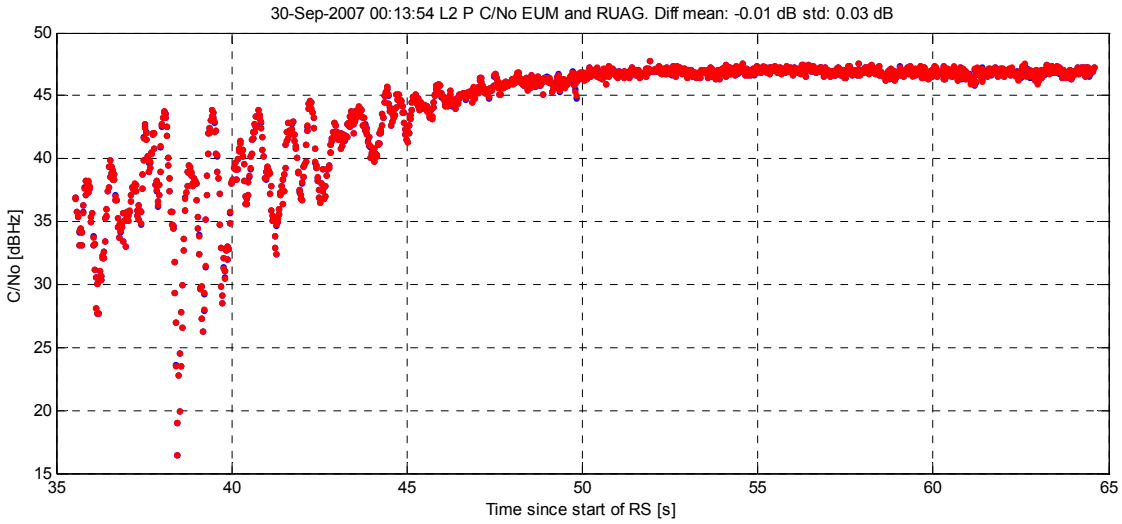

Figure 13 L2 P C/No for the EUM (blue) and RUAG (red) data. In the presented resolution, the EUM and RUAG data cannot be discriminated.

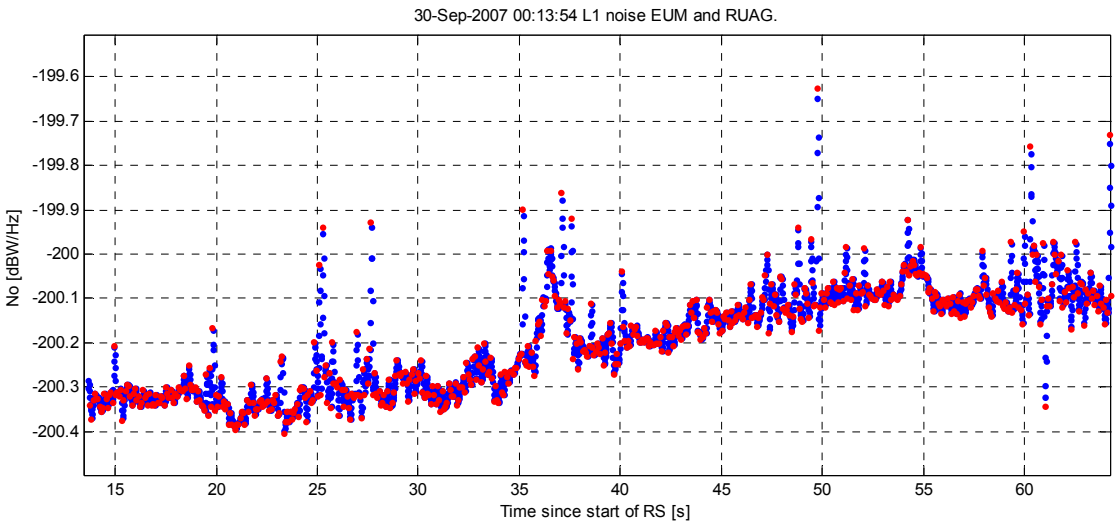

Figure 14 L1 No for the EUM (blue) and RUAG (red) data.

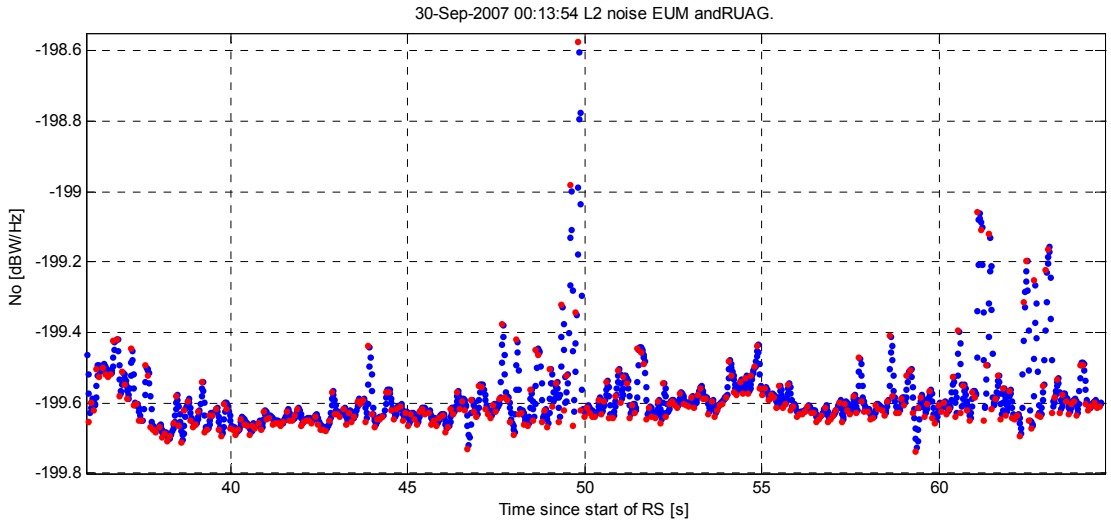

Figure 15 L2 No for the EUM (blue) and RUAG (red) data.

4.3.5 Raw Sampling Data in Open Loop

4.3.5.1 OL I/Q Data

Parameter	Observation on EUM data
RS CA I/Q Amplitudes rs_i_ca_uncorr, rs_q_ca_uncorr, rs_amplitude_ca	Amplitudes OK, mean 0.00 dB, std dev. 0.03 dB difference in scale factor Phase OK to numerical accuracy

The same good agreement in I/Q amplitude as seen for CL data is seen also for OL data. The mean and std. dev. in the difference are both of the order of hundreds of dB. The agreement in I/Q phase is to the numerical precision, see Figure 16, where a 1 s of data is shown.

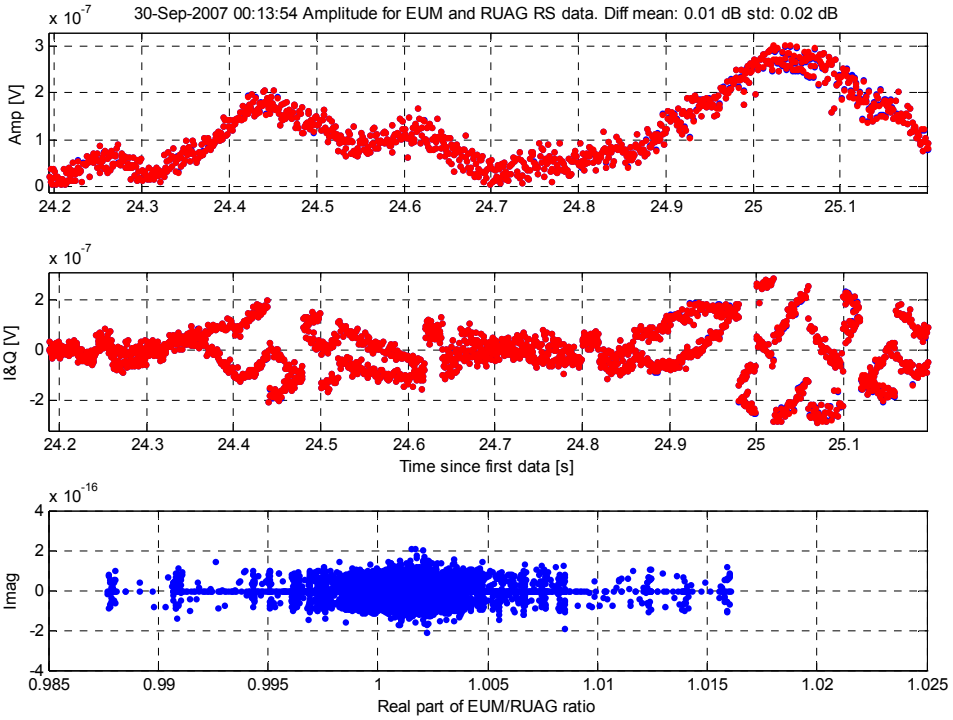

Figure 16 Top down: Amplitude, I/Q samples, EUM (blue) and RUAG (red) data vs. time and imaginary vs. real part of ratio V_EUM/V_RSE.

4.3.5.2 OL NCO Data

Parameter	Observation on EUM data
RS NCO rs_phase_l1_nco	OK, agree to the numerical accuracy - differ in starting value (due to different selection of reference time) - differ in sign (EUM use carrier range, RUAG phase)

The RS NCO data has the same difference in sign convention and in starting value as observed for the CL data. In Figure 17 we plot the difference between EUM and RUAG NCO phase for the start of the continuous RS segment. Considering the phase magnitudes, the agreement of a few hundreds of mm is of the order of the numerical accuracy.

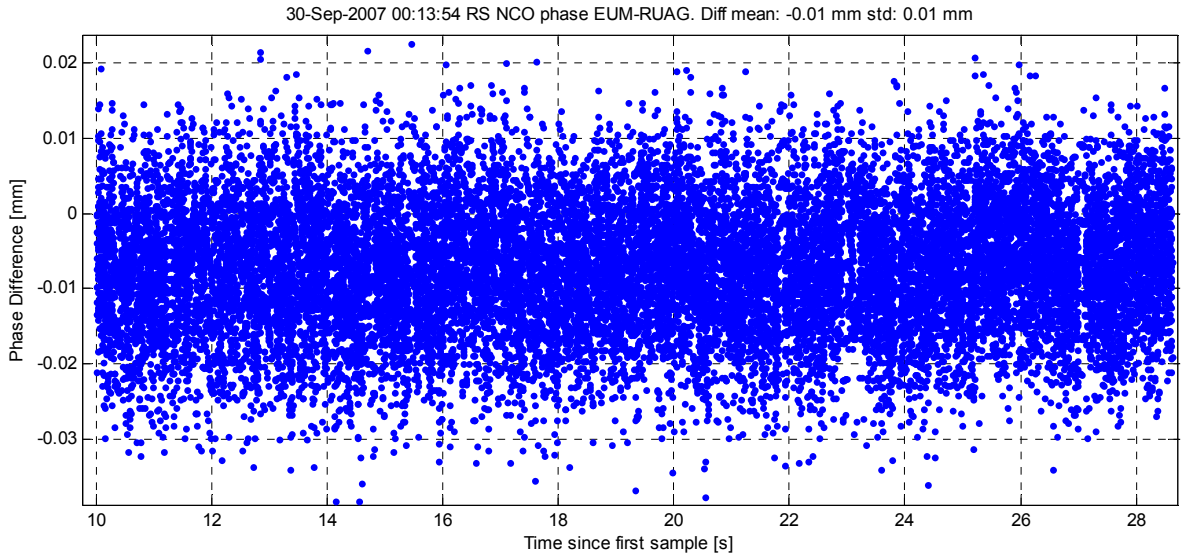

Figure 17 OL NCO phase difference between EUM and RUAG data, for the continuous OL data.

In order to investigate the OL NCO behaviour, we subtract a linear trend from the two NCO data sets and obtain around the time 15 s the behaviour as in Figure 18. It also shows systematic linear deviations in the RUAG data.

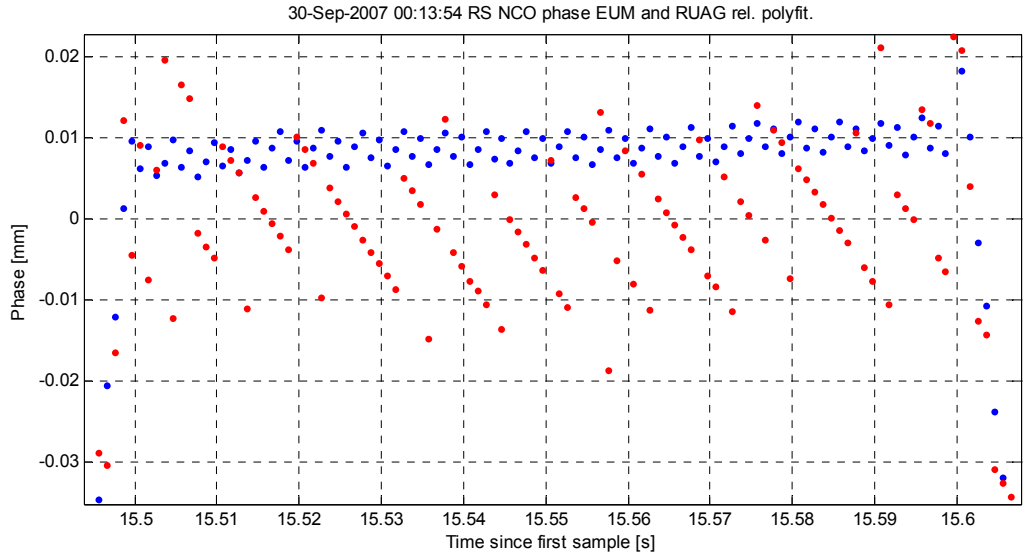

Figure 18 OL NCO phase relative to local linear fit for EUM (blue) and RUAG (red) data, from setting occultation starting 2007-08-30 11:20:30.

Looking at the fine structure of individually calculated NCO Doppler, we see in a blow-up in Figure 19 a minor disagreement between the data sets. The EUM Doppler is essentially constant and changes every 0.1 s as expected from the OL NCO update rate, while the RUAG Doppler is jittering between up to four discrete levels. The levels correspond to the numerical accuracy of the OL header phase and are likely to be due to loss of numerical accuracy of the header frequency in the RUAG reconstruction. The conclusion is that the EUM reconstruction is correct.

The increased Doppler values in between the constant segments are due to the implementation of the Doppler model as piecewise linear segments. These discontinuities are entirely compensated by the residual phase provided by the I/Q data.

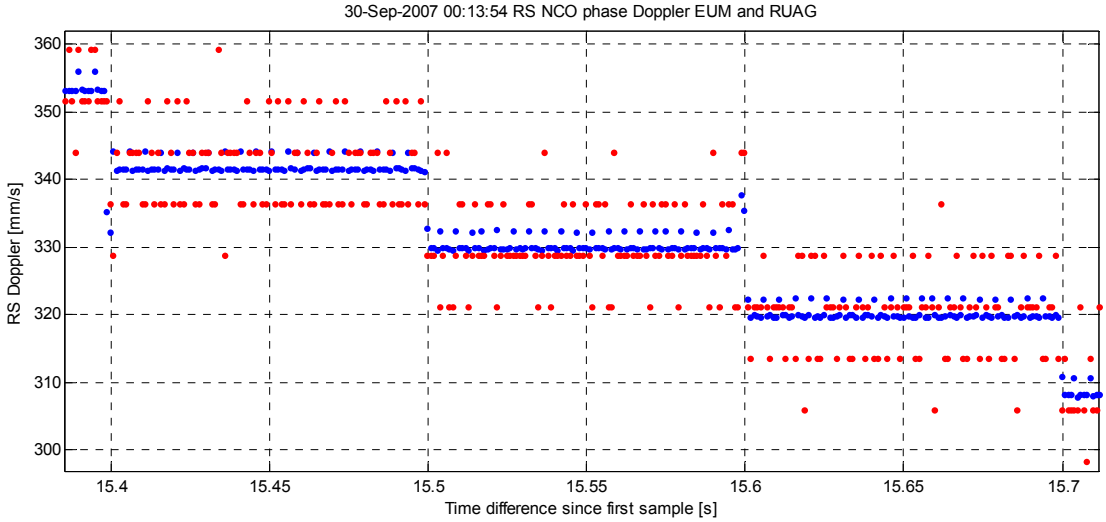

Figure 19 OL NCO Doppler for EUM (blue) and RUAG (red) data.

4.3.5.3 OL to CL Continuity

Parameter	Observation on EUM data
CL to RS continuity rs_phase_l1_nco rs_i_ca, rs_q_ca cl_phase_l1_nco cl_i_ca, cl_q_ca	OK, bias and std decrease as expected with increased filtering

The CL and OL combined complex voltages, (I+jQ)*exp(-jNCO), are compared in the region where they overlap, for the case under study this is 13.6 s to 28.6 s. The NAV bit demodulated data is used in order to be able to filter the data. Since the NCO and I/Q data have been validated separately the purpose of this comparison is to verify that there is no phase bias between the CL and OL data.

The complex signal vectors are formed by combining I/Q and NCO data for OL and CL separately. In order to obtain CL and OL data at the same instant, 20 OL 1 ms data have been summed up to match each CL data. The ratio of the two vectors is formed, the amplitude should be unity and the phase should be zero. The phase and amplitude of this ratio are shown in Figure 21. Some noise remains on phase and amplitude. This can be numerical and decreases as expected with additional filtering.

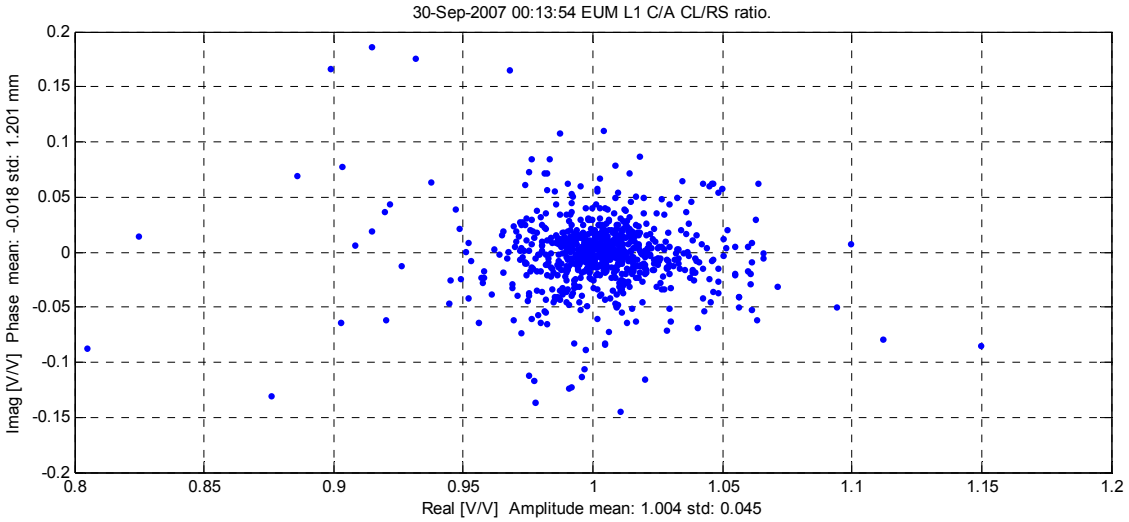

Figure 20 Complex CL to OL voltage ratio for EUM data.

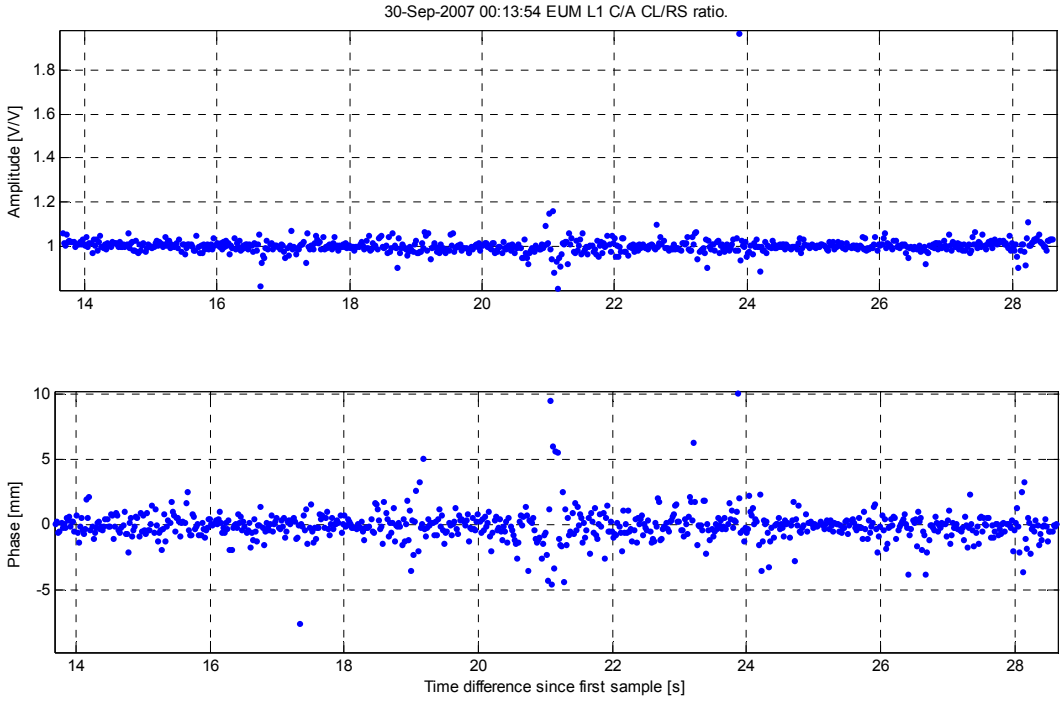

Figure 21 CL to OL voltage ratio for EUM data. Amplitude (top) and Phase (bottom).

4.4 Data Quality Measures

A set of data quality measures have been defined which treat different aspects of signal quality.

One set of the quality measures involve local parameters connected to each measurement sample such as:

1. Carrier to Noise Power Density.
   - o DataQuality.CN0_RS
   - o DataQuality.CN0_CL
2. Data continuity
   - o DataQuality.contRS: continuity of RS data
   - o DataQuality.contL1CL: continuity of CL data
   - o DataQuality.contSF: combined continuity of RS and CL data
   - o DataQuality.contDF: continuity of DF data
3. Doppler accuracy
   - o DataQuality.df_CL difference between the CL carrier frequency and the on board Doppler model
   - o DataQuality.df_RS difference between the RS carrier frequency and the on board Doppler model
4. Scintillation index S4
   - o DataQuality.S4

Other quality measure parameters describe global characteristic, frequently given as Straight Line Tangent Altitude (SLTA) limits, for an entire occultation such as:

5. Max tracking state
    - DataQuality.maxTrkState
6. Raw sampling amplitude saturation
    - DataQuality.minSLTA_RSSat, maxSLTA_RSSat
7. Navigation data health and signal health
    - DataQuality.NH
    - DataQuality.SH
8. Range of single and dual frequency tracking etc.
    - DataQuality.minSLTA_SF, maxSLTA_SF
    - DataQuality.minSLTA_L1CL, maxSLTA_L1CL
    - DataQuality.minSLTA_DF, maxSLTA_DF

In the listing above the data types are named corresponding to the RUAG Level IV data.

The listed data quality measures are evaluated in the following sub-sections. The evaluation is in some cases rather exhaustive in order to illuminate the quality indices, and to support the selection of study cases.

4.4.1 Carrier to Noise Power Density

The Carrier to Noise power density, C/No, is a bandwidth or sample rate independent representation of the signal quality or SNR. It can serve to identify low signal quality due to: false acquisition of a wrong GPS Space Vehicle, false acquisition of the code phase, or simply where little of the signal remains due to the atmosphere attenuation.

The AGGA histogram method, used in the GRAS instrument, has been selected in order to estimate C/N_0 for raw sampling data. The amplitude is computed using coherent summation within subintervals of K samples, and signal power C_n in each subinterval is defined by the following equations:

$$\overline{V}_{I,n}^{IN} = \frac{1}{K}\sum_{k=0}^{K-1} V_{I,k,n}^{IN}$$

$$\overline{V}_{Q,n}^{IN} = \frac{1}{K}\sum_{k=0}^{K-1} V_{Q,k,n}^{IN}$$

$$C_n = \frac{\left|\overline{V}_{I,n}^{IN} + j\overline{V}_{Q,n}^{IN}\right|^2}{50}$$

Note that voltages need to have navigation data removed.

The noise power over a subinterval is estimated with a linear interpolation of the histogram data delivered by the AGGA ASIC, [MDID] §5.9.

Different values of K (number of samples per subset) were tested, between 1 and 1000, and K = 10 was found to be adequate.

The method is very robust, and suitable for low signal amplitudes. It should be noted though, that the AGGA histogram contains the total noise power within the 20 MHz bandwidth and assumes white noise to properly reflect the signal quality. Noise contribution localised in the band edges does not degrade the SNR considerably, but will contribute to the calculated C/No. On the other hand, narrow band noise, like C/A co-channel interference, will not contribute considerably to the AGGA noise, but will degrade the SNR.

4.4.1.1 C/No Distribution

The distribution of C/No for OL, L1-CL and L2-CL are illustrated as percentile limits in Figure 22 through Figure 24. It is noted that the lower 90 % limit for the L2-CL data deviates from the expected behaviour for Straight Line Tangent Altitude (SLTA) > 0 km. These occultations do not reach C/No higher than 27 dBHz, as compared to the expected 40 to 50 dBHz.

Further details of the C/No_{L2} distribution are shown in Figure 25, where the cumulative distribution for C/No_{L2} based on mean C/No for the highest altitudes is plotted. We have used the first 15 s of the setting occultations and the last 15 s of the rising occultations. In total about 5.5% of the occultations have low C/No for L2. The majority of these occultations are rising occultations (~4% of all Dual Frequency occultations).

The cause for the low C/No_{L2} is most likely false acquisitions of the L2 loop. This is further assessed in section 5.4.4.

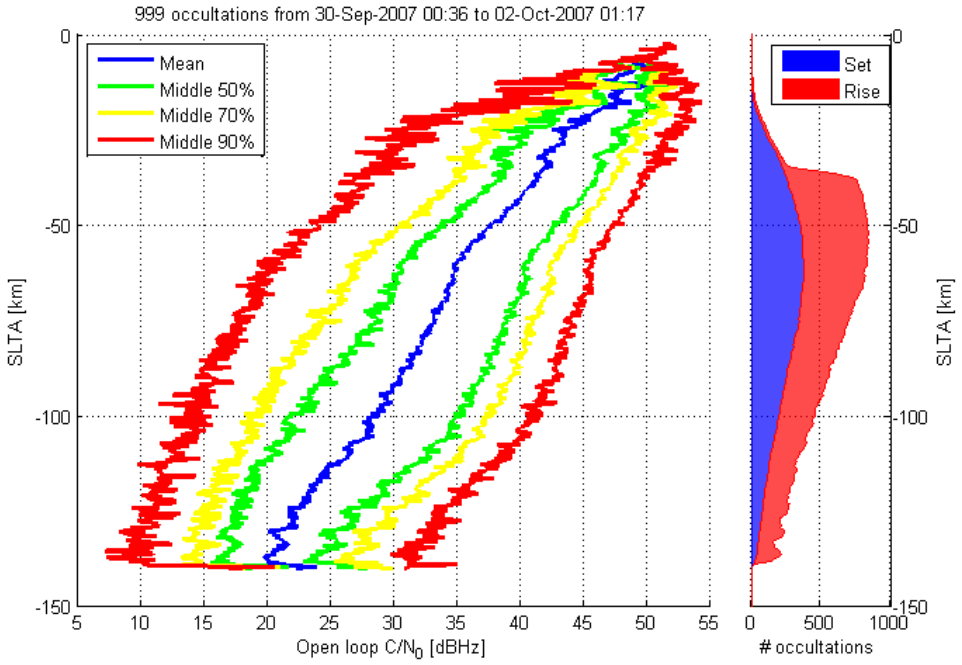

Figure 22. C/N_0 for OL data. As an example, the yellow lines represent the 15th and 85th percentiles at a certain altitude, and thus enclose the middle 70% of data. (qdata_eval_notcum.m)

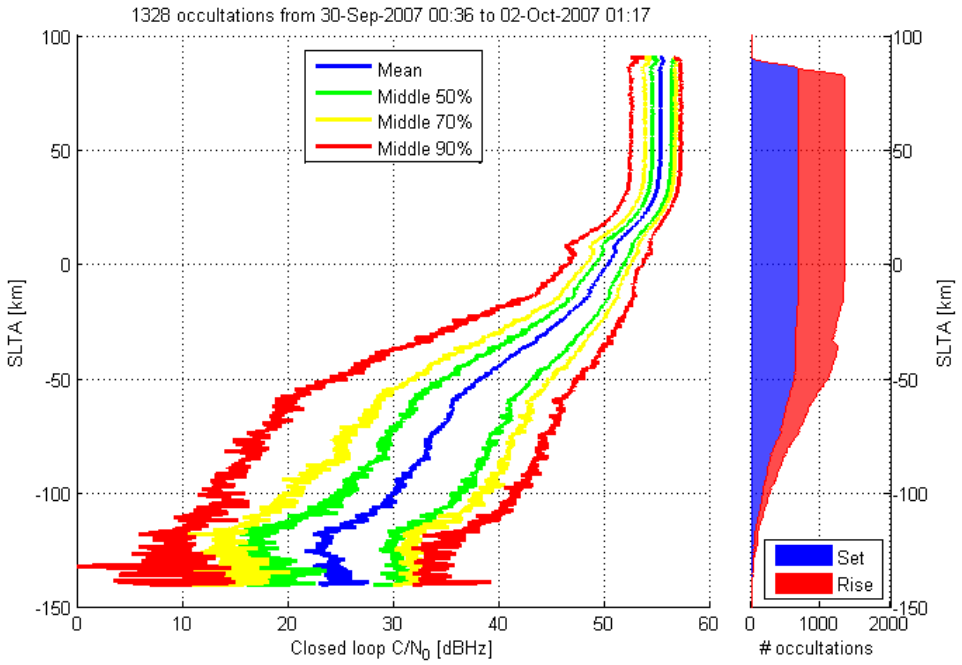

Figure 23. C/N_0 for closed loop L1 C/A. (qdata_eval_notcum.m)

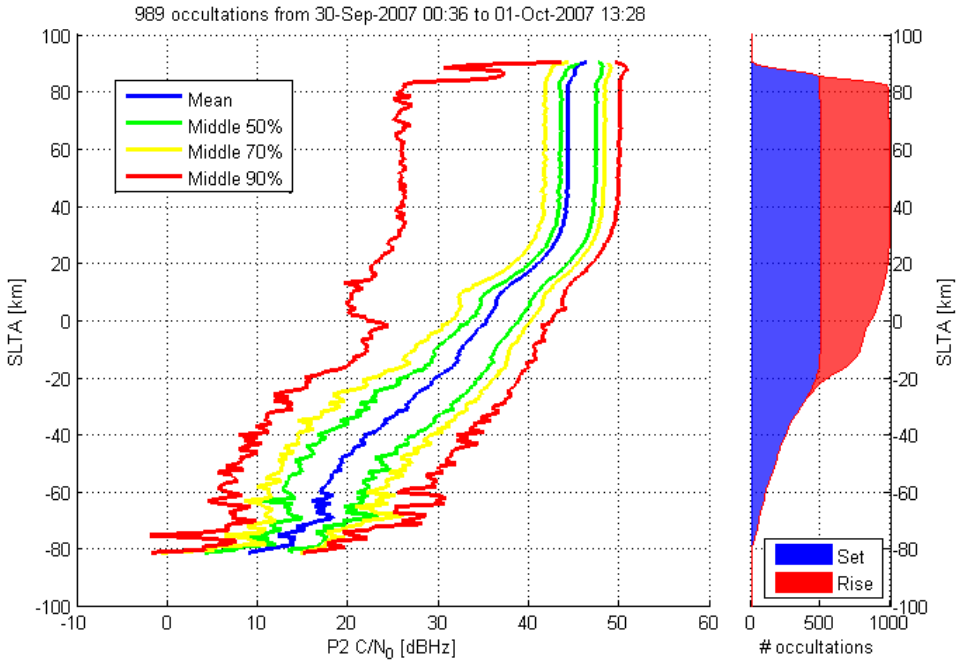

Figure 24. C/N_0 for closed loop P2. (qdata_eval_notcum.m)

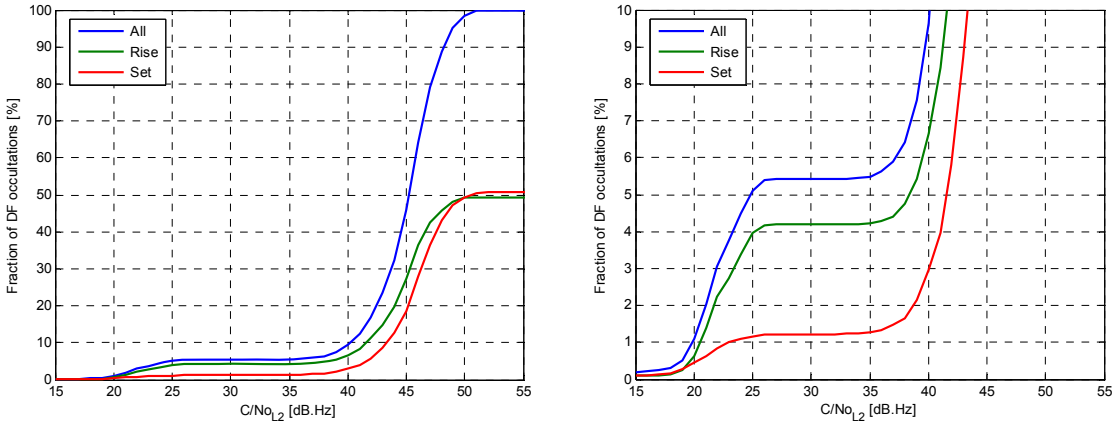

Figure 25 Cumulative distribution for C/No$_{L2}$ based on mean C/No for the highest 15 s of the occultation. Right panel: expanded vertical axis.

4.4.1.2 C/No Latitude Dependence

The latitude dependence of C/No versus SLTA for L1 raw sampling and closed loop is illustrated in Figure 26 and Figure 27. Below SLTA = -75 km we note a clear distinction between high and low latitudes, and the mean C/No appears to be fairly tightly grouped into two different states. The reason is most likely that the thin atmosphere at high latitudes does not support bending of the ray to low SLTA.

Further we note a significant drop on C/No$_{RS}$ for the tropical region just above SLTA = -35 km. At this point we note however that the total number of occultations containing OL data is extremely low and the statistics is poor.

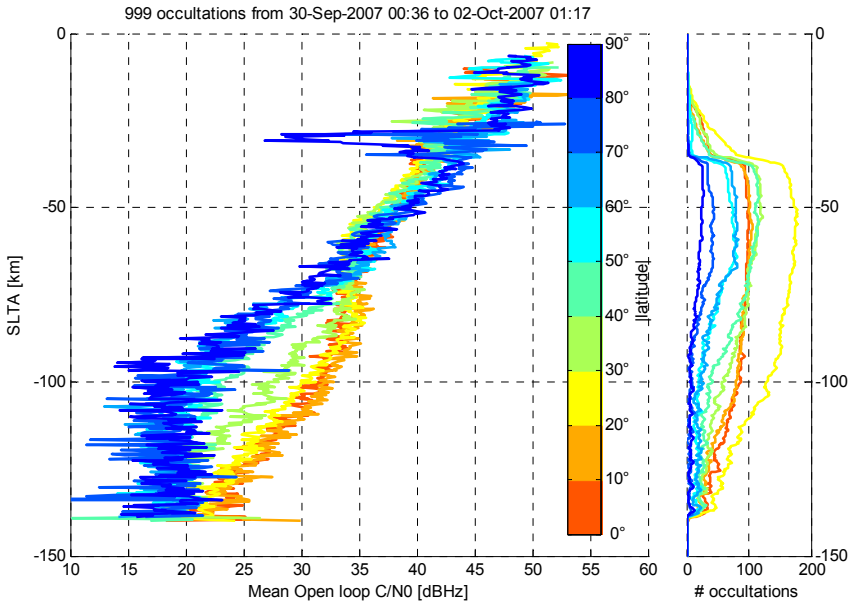

Figure 26. Mean C/N$_0$ for OL data, with latitudinal dependence. The absolute value of the latitude of the occultation point is used to sort the occultations into nine bins, and a mean value is computed for each bin. (qdata_eval.m)

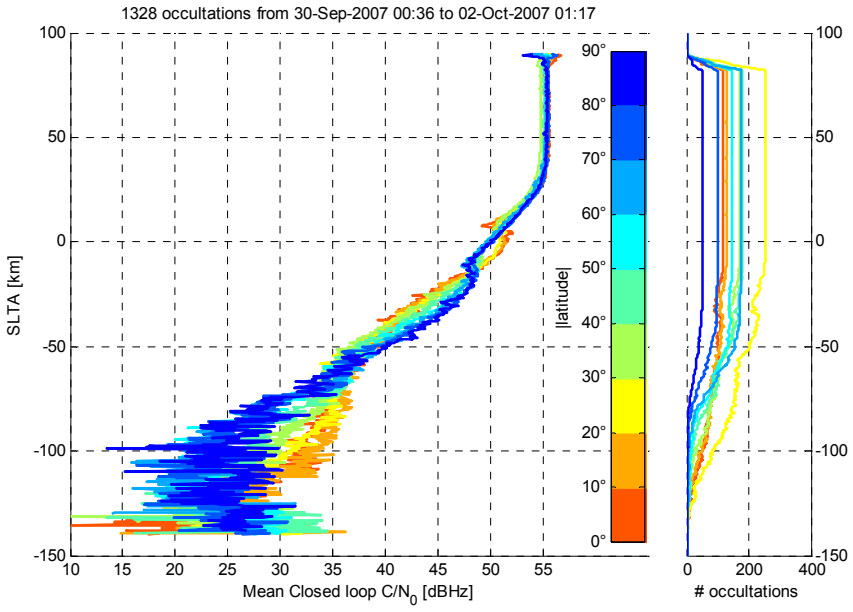

Figure 27. Mean C/N_0 for closed loop L1 C/A, with latitudinal dependence. (qdata_eval.m)

4.4.1.3 Example of False Acquisition

It is noted that the minimum C/No in the above plots are quite low and is below the tracking threshold of the receiver. Low levels of C/No can be reported during the acquisition period before the tracking loops are locked or when tracking is lost. An example, where a false acquisition results in low and widely spread C/No reports is illustrated in Figure 28.

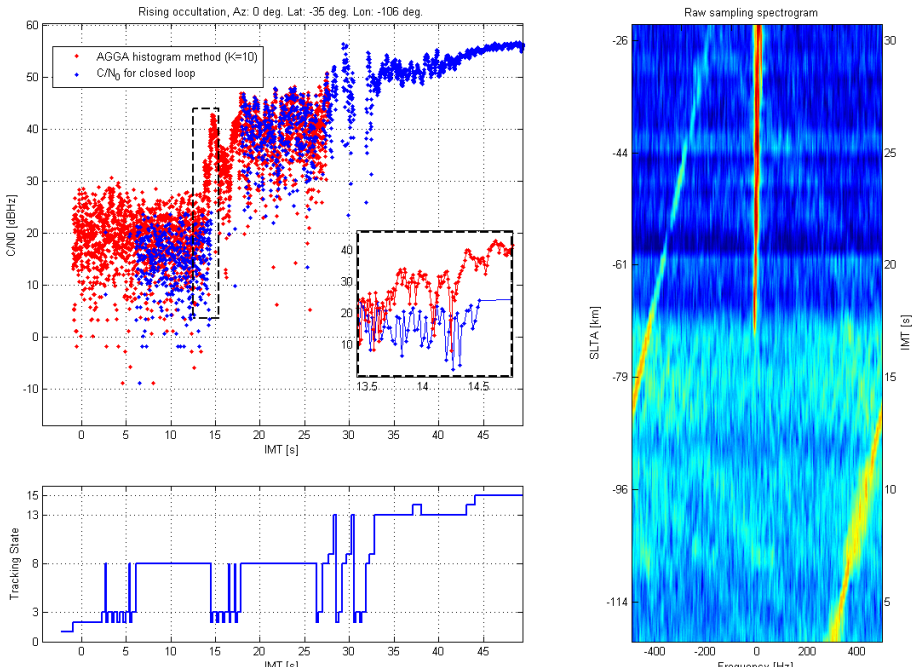

Figure 28. Example of false acquisition. The sliding spectra illustrates that the instrument has acquired false code in the beginning of the rising occultation. During the false acquisition period C/No spreads widely and differs between raw sampling and closed loop data. IMT refers here to the instrument time since the start of the occultation.

4.4.2 Data Continuity

Data continuity is a quality measure describing the maximum time gap between adjacent samples. It can serve to select how useful the data is and how much of the data that can be used for a selected retrieval process. Four different continuity measures are provided:

- **DF**: Continuity of dual frequency closed loop data.
- **L1CL**: Continuity of single frequency closed loop data.
- **RS**: Continuity of single frequency raw sampling data.
- **SF**: Continuity of single frequency data from combination of L1CL and RS data (but not DF data).

The maximum time gap represented by the continuity data corresponds to the maximum gap anywhere between the reported sample and a reference sample. The reference sample is selected as follows:

- **Close loop data:** the reference sample is defined as the sample with highest corresponding SLTA value below 50 km (or the lowest point, if no data exist below 50 km).
- **Raw sampling data:** the reference sample is any sample within the longest continuous interval of raw sampling data

With this definition the continuity measures will increase monotonically in each time direction, with starting-point at the reference sample.

The continuity vectors are demonstrated in Figure 29, where they are plotted for a typical occultation. The corresponding measurement data is shown in Figure 30. Here we see that the L1 CL data has one discontinuity of 0.7 s at SLTA -45 km, and one of 1.4 s at -60 km. RS is, however, continuous from SLTA -35 km and fills in the data gaps of the L1 CL data.

The continuity of a more complex occultation is illustrated in Figure 31, with its measurement data in Figure 32. The yellow dashed line in Figure 31 describes how we encounter longer and longer data gaps as we follow it down. RS data starts to fill out L1CL data, so that the SF vector is limited to a size of ~2 seconds, but the RS data has gaps as well.

Also note that the RS continuity is measured with the middle data part as a reference in this occultation, since it was the longest continuous section. The SF continuity, which is a combination of RS and L1CL, has the zero-level at its highest altitude. This means that SF continuity is not always the minimum of RS and L1CL continuity.

It is noted that the definition of single frequency continuity data excludes dual frequency data. In practice, we have to check both DF and SF continuity in order to find L1 continuous data.

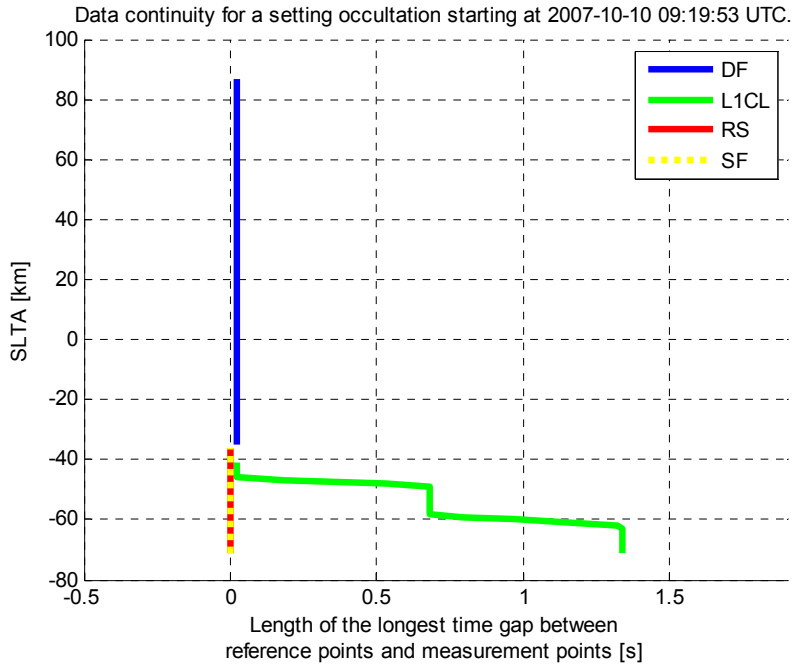

Figure 29. Data continuity for a setting occultation. When closed loop tracking on L1 is lost, raw sampling data fills out. See also Figure 30.

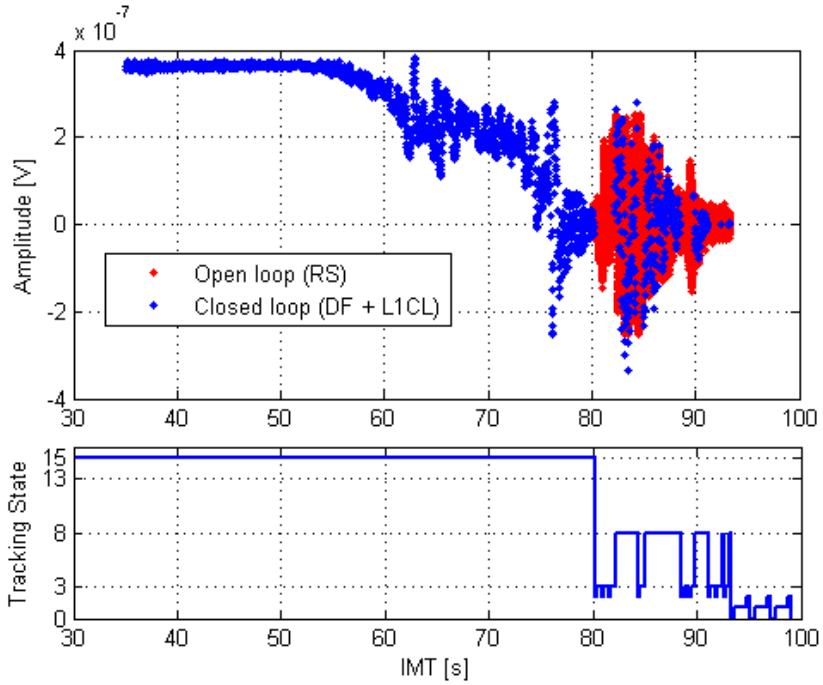

Figure 30. Amplitudes and tracking state of the occultation in Figure 29.

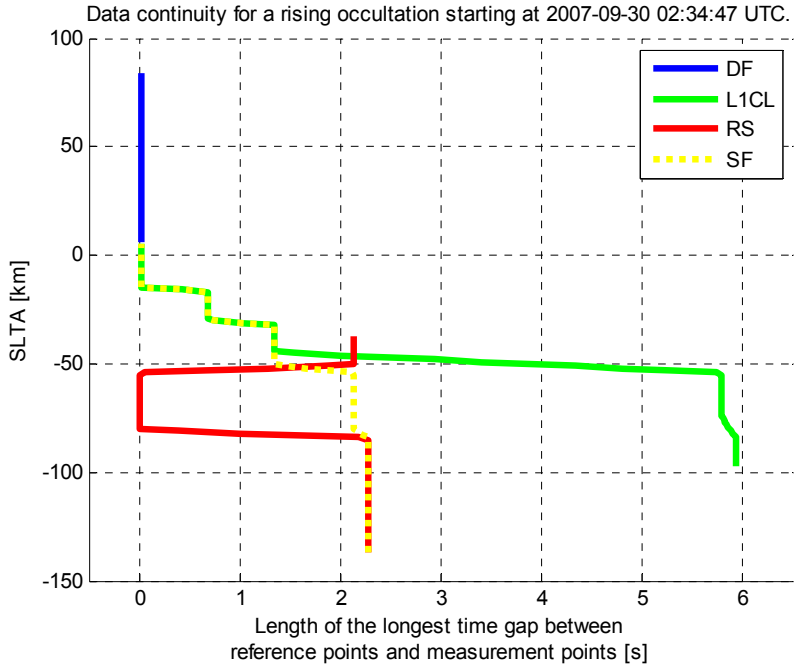

Figure 31. Data continuity for a rising occultation. One may note a complete lack of data for ~2.1 seconds at SLTA = -50 km for this specific occultation. See also Figure 32.

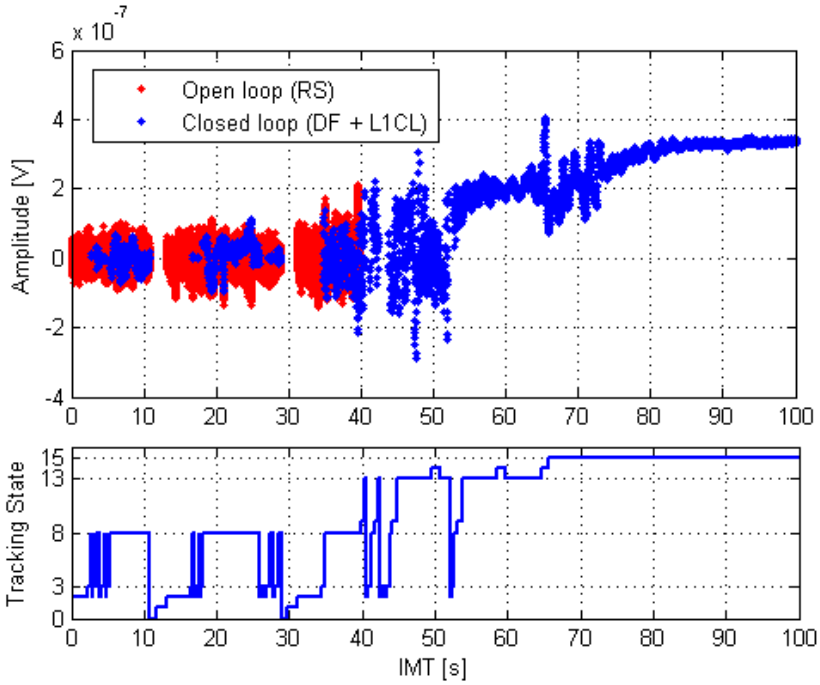

Figure 32. Amplitudes and tracking state of the occultation in Figure 31. SLTA is -50 km when (delta) IMT is 31 s.

4.4.2.1 Statistics for Data Continuity

Statistics for the data continuity measures are illustrated in Figure 33 through Figure 36 for the different continuity products. Note that continuity for all single frequency products end when dual frequency tracking starts. Consequently the distributions drop off at both ends. Further the reacquisition intervals are clearly visible for single frequency data. Two periods exist: integer 0.7 s for L1CL and 1.8 s for RS, and multiples hereof, reflecting the S/W reacquisition process.

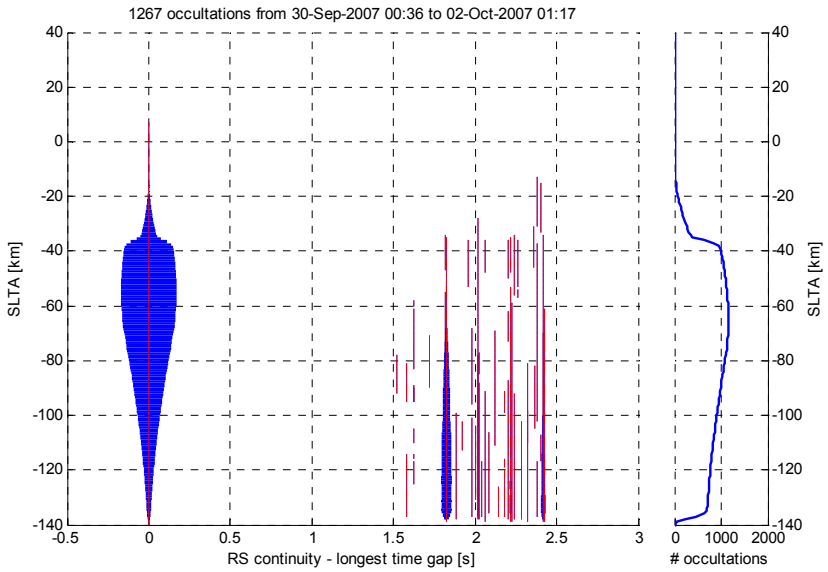

Figure 33. RS continuity (see definition). The width of a blue band is proportional to the amount of occultations that has a continuity value defined by the corresponding red line. The right graph shows the range of altitudes where RS data exists. (qdata_cont_eval.m)

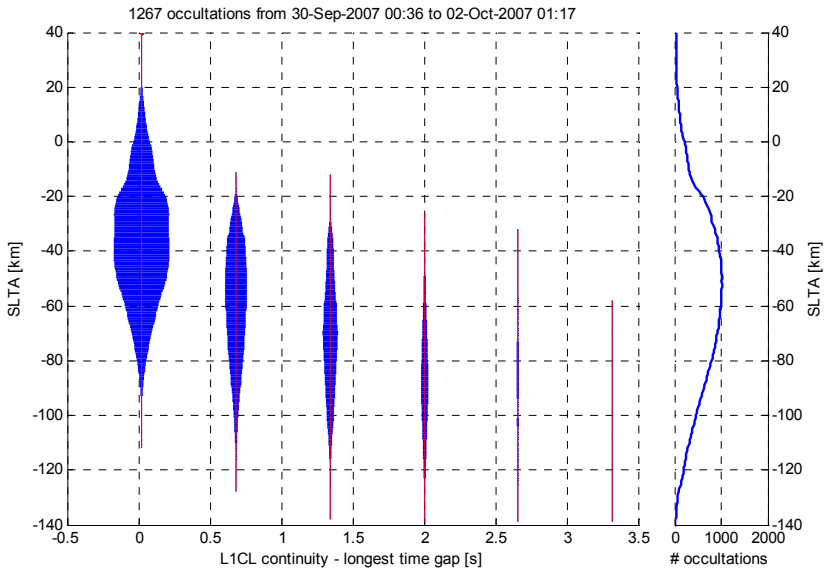

Figure 34. L1CL continuity. (qdata_cont_eval.m)

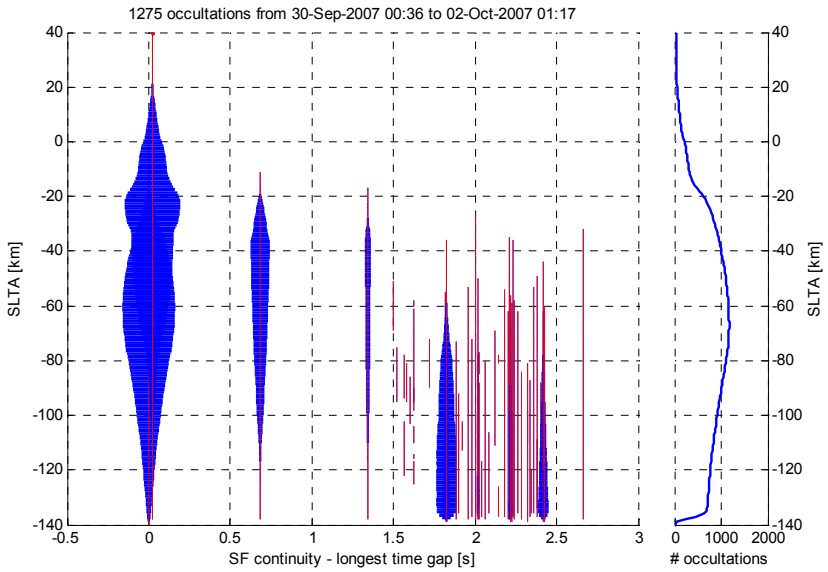

Figure 35. SF continuity (RS + L1CL). (qdata_cont_eval.m)

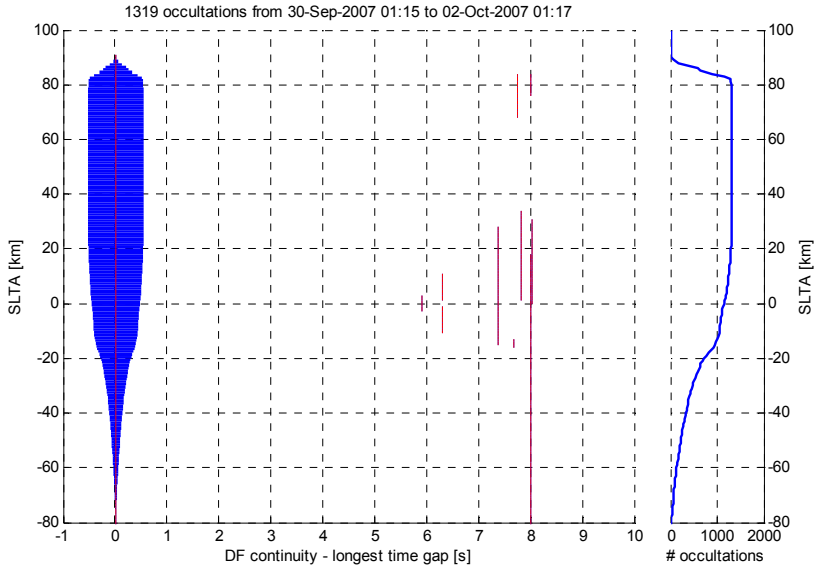

Figure 36. DF continuity. (qdata_cont_eval.m)

4.4.3 Scintillation Index

The scintillation index is calculated for closed loop data as:

$S_4 = \sqrt{\frac{\overline{P^2}}{\overline{P}^2} - 1}$ where P = (I^2 + Q^2) and running mean over 2 s intervals are used.

The scintillation index, S_4, is a measure of the atmospheric variations imposed on the occultation. S_4 saturates around 1.2 to 1.3 and does not increase further if the turbulence is increased. Normally a value of 0.8 is used to distinguish between weak and strong fluctuation [Tatarskii]. For our data set we see that about 50 % of the occultation comprises strong fluctuations below SLTA = -50 km. S_4 further gives an indication of when wave optics inversions are required to resolve the multiple signal passes behind the fluctuations.

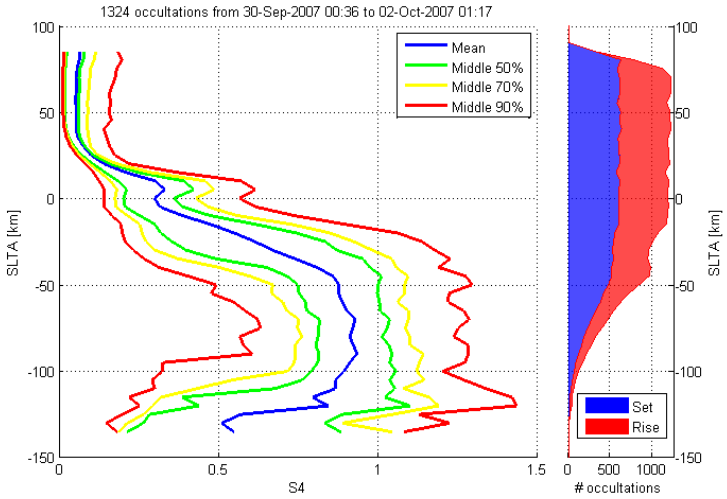

Figure 37. Scintillation index S4, as function of SLTA. (qdata_eval.m)

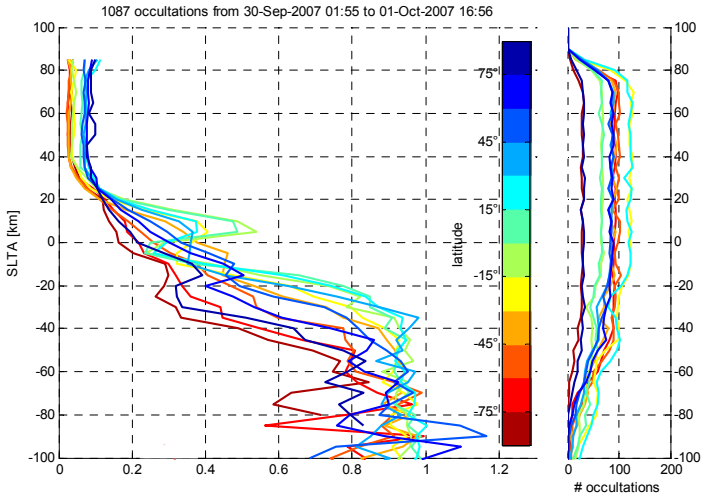

Figure 38. Mean scintillation index S4, with latitudinal bins. (qdata_eval.m)

4.4.4 Max Tracking State

The maximum tracking state reached during the occultation is most commonly the highest tracking state, TS 15. The maximum tracking state can be used as one screening parameter to identify failed occultations. The distribution of max tracking state for the Level IV occultations, as defined in 4.3.1, is estimated from ~1000 occultations to the following

TS 15 – 99.3%

TS 13 – 0.2%

TS 8 – 0.5%

4.4.5 Raw Sampling Amplitude Saturation

The RS I and Q samples are coded with 8 bits, as compared to the closed loop data that are sampled with 16 bits, this in order to save data rates at 1 kHz. It is observed that at high altitudes or severe atmospheric interference, the RS amplitudes occasionally become saturated. The saturation level, expressed in Volts, [MDID], will depend on the digital gain settings in the receiver. It should be investigated if and how much the samples that are saturated can affect the accuracy of Full Spectral Inversion (FSI) retrieval.

An example of amplitude versus time plot is shown in Figure 39 for a section at high altitude, where the RS signal gets saturated. The corresponding behaviour of the complex I/Q voltage is shown in Figure 40, where a few I/Q cycles are severely saturated.

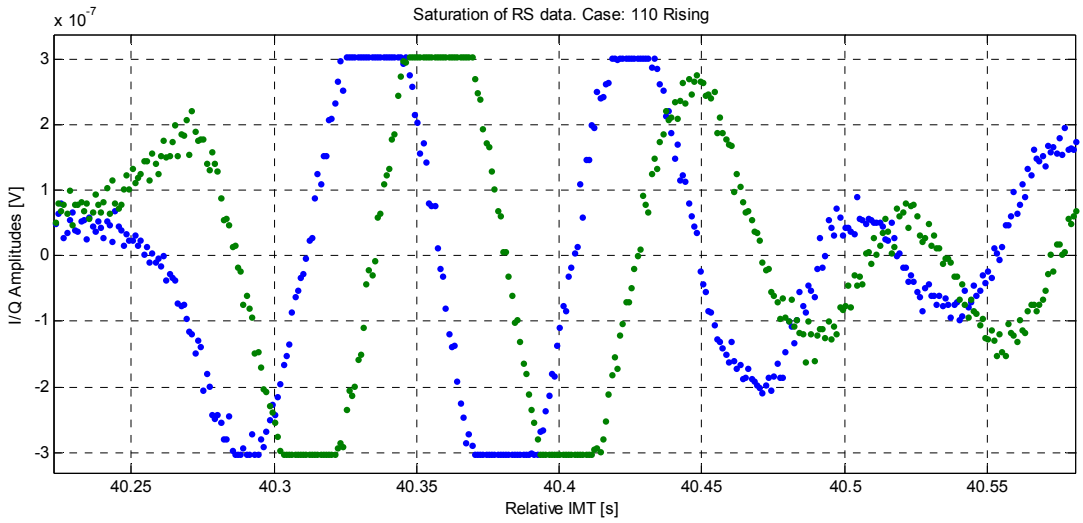

Figure 39 Example of RS data saturation. I and Q amplitudes versus IMT.

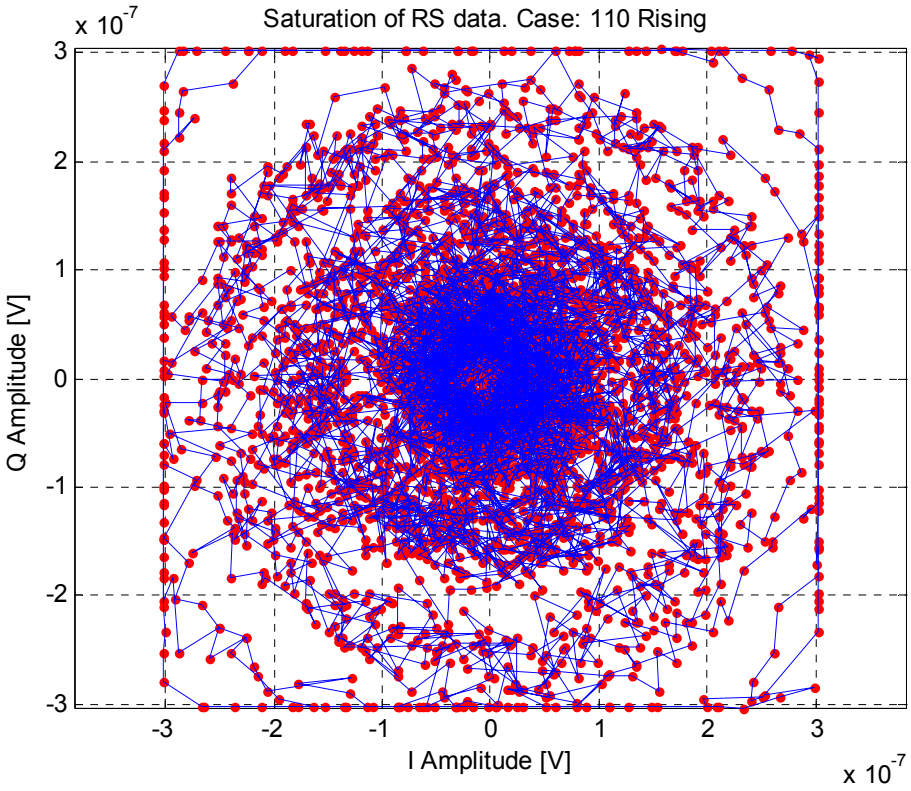

Figure 40 Example of RS data saturation. I/Q phase plot.

Data analysis shows that saturation occurs in 10-20% of the occultations, predominantly at high altitudes where also CL is available. In those cases CL data could be used and up-sampled if required to RS sampling frequency. The quality flag is defined as the lowest and highest SLTA for which RS saturation occurs. In **Figure 41** the percentage of samples that are saturated, sorted in descending order for the first 490 occultation of the data set. One occultation has more than 1% saturated samples, and 9 occultations have more than 0.5% saturated samples. It can also be concluded that in order to experience a significant saturation, quite a few sequential samples must be saturated. Hence at least for the occultations with a very small percentage of saturated samples, the amount of saturation should be negligible.

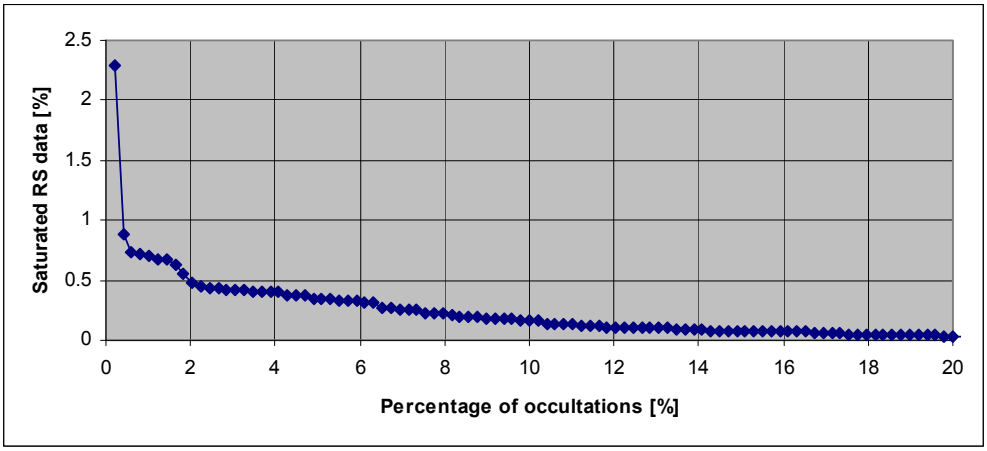

Figure 41 Percentage of saturated samples for the first 490 occultations.

4.4.6 Navigation Data Health and Signal Health

Navigation data health (NH) and signal health (SH) are also provided as a data quality measure.

Scanning the complete data set we obtain:

- NH is 0 (All navigation data OK) for 17608 of 17619 occultations
- NH is 1 (Some or all navigation data is bad) for 11 of all 17619 occultations, or 0.00624%.
- SH is distributed equally, SH is 31 (More than one combination would be required to describe anomalies) for the same 11 occultations.

These 11 occultations are with four different GPS SVs as seen in Figure 42. These occultations should be discarded from further processing due to incorrect GPS data.

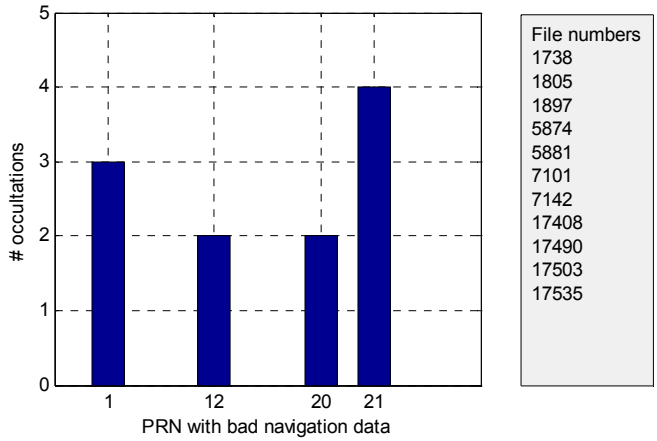

Figure 42. PRN for the 11 occultations with bad navigation data.

4.4.7 Range of Single and Dual Frequency Tracking

The lowest and highest SLTA values for continuous SF and DF data are also evaluated. The purpose of the status variables is to give a fast indication of the occultation data quality. They are defined in detail in the description of the Level IV data units. When reading the figures below, it is to be noted that SF is defined as the data where CL C/A code only is present. CL C/A signal is hence available at altitudes where either SF or DF data are present. In Figure 43 we see the altitudes for which we have dual frequency available and note the evident difference between setting and rising occultations. In Figure 44 we see the altitudes for which we have either CL C/A or RS or DF data. For rising occultations we note that above the SLTA limit -35 km we have a loss of data due to the fact that we have abandoned RS in the favour of searching for the L2 signal, and RS does not fill in for occasional loss of L1 carrier.

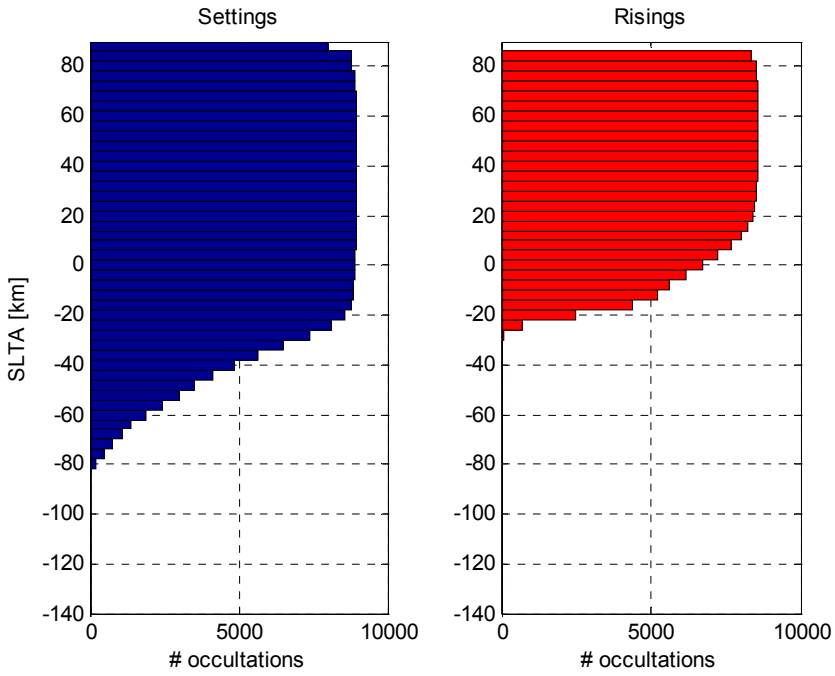

Figure 43. Distribution of continuous dual frequency data. The max and min altitudes for continuous dual frequency data are quality parameters. (qdata_eval_statusvar.m)

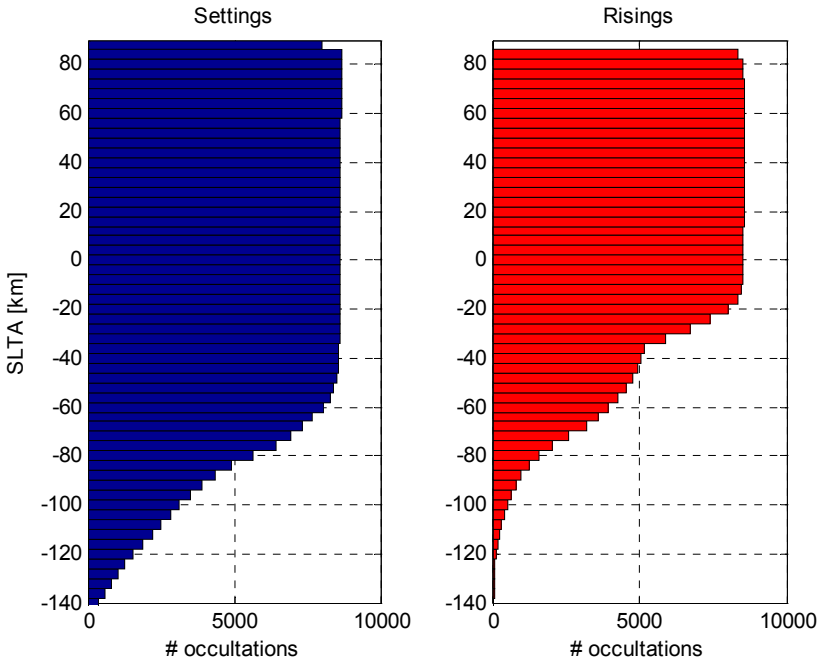

Figure 44. Distribution of continuous single frequency data (RS + L1CL+DF). The max and min altitudes for continuous single frequency data are quality parameters. (qdata_eval_statusvar.m)

4.5 Study Case Definition

A number of study cases have been identified. Each case is general and defined by the description in the following section, where it as also exemplified with one unique occultation measurement. Other similar measurements should also be analysed as part of a study case. Sliding spectrum and signal amplitude plots of the example occultations are shown in APPENDIX A.

4.5.1 Study Case Definition

The cases listed below have been identified as interesting for the study. The majority of these cases are interesting for data retrieval analyses, while some are merely interesting for the instrument tracking analyses. In case 9 for example, a false signal is tracked, which is mainly interesting from Instrument aspects, whereas it is only of concern for the data retrieval analyses to make certain that the result of such a false signal is not used.

Case	Characteristics	Description	Example ID
1	L2 tracking to low SLTA	This study case serves as a reference case to study dual frequency tracking properties under normal conditions.	431
2	OL tracking to low SLTA	A setting occultation with a considerable amount of raw sampling data. High L2 signal dynamics also at high altitude.	12
3	Ocean reflection	The impact of ocean (or ground) reflections is identified as a study case.	46
4	L2 feature at high SLTA	Some occultations show a pronounced spectral signature on the L2 signal at high SLTA, exemplified by the identified occultation.	130
5	Long fade	The L1 amplitude is reduced to a low level with duration of more than 2 seconds and then increases again. It is important that the code loop maintains lock during this type of long fades.	260
6	10 Hz disturbance	In the sliding spectrum plots one can see spectral peaks at 10 Hz intervals for a number of occultations. The impact and origin of this feature should be investigated.	409
7	Raw sampling saturation	The I and Q raw sampling values are at there maximum value for 2% of the samples as a worst case for the 30 September data. We propose to check if this has a significant effect on the results.	240
8	Weak P(Y) code signal	The P(Y) code signal amplitude is more than 20 dB lower than expected for some cases. We propose to investigate if this data is still useful and if the tracking algorithm can be improved to avoid this effect.	72
9	False tracking	The amplitude and frequency of this data indicates that the instrument has locked on incorrect SV. We believe that this data is not useful. The objective of this study case is to find an improved method for signal acquisition to increase the number of useful occultations.	172
10	Wideband signature	The bandwidth of the raw sampling signal approaches 50 Hz in some occultations and these are of particular interest for determining the minimum required raw sampling rate for future missions.	181
11	Co-channel disturbance	Interference from other GPS SVs can be noticed in many occultations. These effects will be investigated.	408
12	L1 data gap	In many rising occultations, there is a gap in the L1 closed loop data that is due to loss-of-lock being detected for the carrier NCO loop. The impact of this and ways to improve the on-board software will be studied.	23

Table 3 Description of identified study cases for processing analyses.

The example ID number refers to a file number from September 30, 2007. The time of day and other characteristics are listed in the tables below for each ID number.

Case	ID	Time(s)	hh:mm:ss	Chan	PRN#	Long (deg)	Lat (deg)	Sat (%)	RS SLTA (km)	CL SLTA (km)	P(Y) SLTA (km)
1	431	78423	21:47:03	10	5	87.4	-65.9	0	-83.1	-83.1	-81.9
2	12	1240	00:20:40	10	19	-26.5	24.5	0	-139.6	-136.1	-32.1
3	46	4955	01:22:35	8	13	3.5	-56.5	0	-138.1	-63.8	-24
4	130	16845	04:40:45	8	30	-143.4	-84.6	0	-137.6	-41.1	-19.3
5	260	56103	15:35:03	10	9	71.9	23.8	0	-83.1	-82	-39.6
6	409	75544	20:59:04	8	24	167.9	36.9	0	-138.4	-82.4	-24.6
7	240	52977	14:42:57	11	31	-69.9	-22.4	2.29	-52.8	-50.4	-23.4
8	72	8964	02:29:24	10	12	146.4	52.3	0.74	-69.6	-69.6	-12.3
9	172	44370	12:19:30	9	7	13.1	66	0	-137.3	-89.2	-16.4
10	181	45752	12:42:32	10	4	-29.4	45.2	0.14	-104.7	-99.3	-25.1
11	408	75494	20:58:14	10	3	-135.9	86.9	0	999	-76.6	-76.6
12	23	2586	00:43:06	8	21	155	27.5	0	-137.8	-115.2	-1.4

Table 4 List of example files for each study case from 30/9 2007.

Case	ID	File name
1	431	gras_occ_20070930214703Z_20070930214801Z_20090808093259Z.nc
2	12	gras_occ_20070930002039Z_20070930002203Z_20090808003906Z.nc
3	46	gras_occ_20070930012234Z_20070930012444Z_20090808004905Z.nc
4	130	gras_occ_20070930044044Z_20070930044154Z_20090808011831Z.nc
5	260	gras_occ_20070930153503Z_20070930153602Z_20090808025911Z.nc
6	409	gras_occ_20070930205903Z_20070930210104Z_20090808093231Z.nc
7	240	gras_occ_20070930144256Z_20070930144347Z_20090808025128Z.nc
8	72	gras_occ_20070930022924Z_20070930023019Z_20090808010147Z.nc
9	172	gras_occ_20070930121929Z_20070930122038Z_20090808023404Z.nc
10	181	gras_occ_20070930124232Z_20070930124336Z_20090808023427Z.nc
11	408	gras_occ_20070930205813Z_20070930205904Z_20090808090440Z.nc
12	23	gras_occ_20070930004305Z_20070930004431Z_20090808003809Z.nc

Table 5 List of file names for each study case from 30/9 2007.

5 ANALYSIS OF OCCULTATION DATA

5.1 High Stratosphere Instrument Performance

The instrument contribution to the measurement accuracy can be evaluated for the high stratosphere. The highly accurate on-board ultra stable oscillator (USO) enables evaluation of the bending angle without adding noise from single or double differencing links. Using non-differenced observations, also referred to as zero differencing, the major bending angle error contributions are the instrument thermal noise on L1 and L2, the on-board clock error, and GPS clock errors. These errors have different spectral properties as listed in Table 6, where also the properties for phase locked loop (PLL) errors are included for completeness. These spectral properties are crucial to perceive the meaning of filtering on resolution and accuracy. The precise orbits of the GPS SV and the MetOp S/C are solved for using POD, which provides low frequency GPS clock corrections at an approximate rate of once per minute.

The bending angle accuracy is modelled as proportional to the Doppler accuracy. The Doppler error of the GRAS measurements is here analyzed at measurement altitudes 50-85 km in order to remove significant impact of atmospheric modulation. The Doppler measurement error consists then of four dominant error terms with different spectral properties as listed in the Table 6.

Error Term	Description	Range spectrum	Doppler spectrum
Thermal noise	Ionosphere free dual-frequency combination of carrier phase measurements	constant	$\sim f^{2}$
GNSS clock drift	Both the Rubidium Atomic Frequency Standard (RAFS) and Passive Hydrogen Maser (PHM) have an Allan deviation proportional to $1/\sqrt{\tau}$	$\sim f^{-2}$	constant
USO clock drift	The crystal based ultra-stable oscillator (USO) is characterized by constant Allan deviation for 1s < τ < 100s	$\sim f^{-3}$	$\sim f^{-1}$
USO PLL phase noise	The local oscillator phase-locked loop generates 1/f - noise	$\sim f^{-1}$	$\sim f$

Table 6 Description of the dominating Doppler measurement error terms.

Each individual term is characterized by a spectral slope. The spectral density of the different Doppler measurement error components are shown in Figure 45 with model parameters for GRAS as listed in Table 7. The total Doppler error spectrum is obtained as the sum of these components. GRAS measurement data from the in-orbit validation campaign are shown for comparison. The GRAS data originates from the first 10 seconds of setting occultations where atmospheric effects are small. The data points correspond to the median spectral density derived from a large number of occultations after removing a best-fit third-order polynomial from the ionosphere free carrier range calculated as:

$$L_C = \frac{f_2^2}{f_2^2 - f_1^2} \cdot L1 - \frac{f_1^2}{f_2^2 - f_1^2} \cdot L2 \approx 2.54 \cdot L1 - 1.54 \cdot L2 \qquad \textbf{Eq(1)}$$

where

L1 L1 carrier phase in meter

L2 L2 carrier phase in meter

Lc Neutral carrier phase in meter, i.e. compensated for the impact from the ionosphere

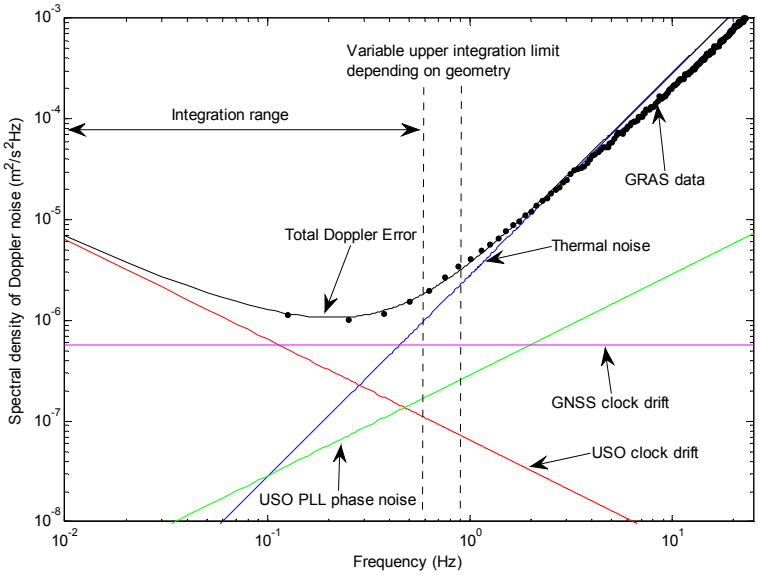

Figure 45 GRAS spectral Doppler error model. Measured (black dots) and model based (black line) errors are compared.

The model parameter value used for the GNSS Allan deviation is typical for the rubidium atomic frequency standard used in GPS Block IIR [Dass]. The C/N0 values used in the model are obtained from analysis of the GRAS measurement data.

Our model, known as the Radio Occultation Performance Estimation (ROPE) model, calculates the Doppler measurement error by integrating the spectra over the frequency range between 0.01 Hz and 1 Hz. The lower limit corresponds to the Nyquist frequency of a clock correction solution with about 50 seconds update interval. The upper limit is equal to the noise equivalent bandwidth and determines the vertical resolution of the measurements. Since the total noise density increases proportional to frequency squared, the measurement error becomes very sensitive to the upper filter band edge and hence the vertical resolution. The dependency of the measurement standard deviation σ on resolution R can be formulated as a proportional relation:

$$\sigma_n^2 \propto \int f^2 df \propto f^3 \propto \frac{1}{R^3} \qquad \textbf{Eq(2)}$$

In comparison, white noise would make the corresponding expression proportional to 1/R. The dependence of the noise equivalent bandwidth on the azimuth angle and the vertical resolution is illustrated in Figure 46, showing that in order to preserve vertical resolution the filter bandwidth will have to be adapted to the measurement altitude and azimuth angle. If a constant bandwidth is used for an entire occultation, the vertical resolution will be higher at low altitudes, since the ray moves slower at lower altitudes. With an 800 km orbit, the first Fresnel zone diameter is 1.5 km at high altitudes.

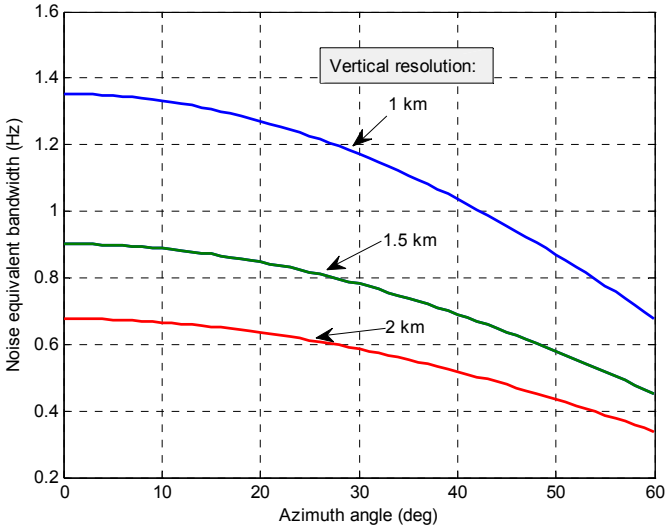

Figure 46 Noise equivalent bandwidth as a function of azimuth angle with vertical resolution at 30 km as parameter. Orbit altitude is 800 km.

The performance parameters and the results obtained for GRAS are presented in Table 7. This error model is also a valuable tool to predict performance of RO instruments based on instrument parameter performance.

Parameters	GRAS Metop
C/N_0 at L1, L1BC	55 dBHz
C/N_0 at L2, E5	48 dBHz
GNSS Allan deviation @ 1 s gate time	2e-12
USO Allan deviation @ 1-10 s gate time	1e-12
USO PLL phase noise at 1 Hz offset	-110 dBc
Results	**GRAS Metop**
Thermal Noise Error (mm/s)	0.70
GNSS Allan Deviation Error (mm/s)	0.67
USO Allan Deviation Error (mm/s)	0.53
USO PLL noise error (mm/s)	0.30
Total Doppler Meas. Error (mm/s)	**1.14**
Bending angle sensitivity to Doppler (urad mm^{-1} s)	0.4
Total Bending Angle Meas. Error (urad)	**0.46**

Table 7 Parameters and results from analysis for an azimuth angle of 30 degrees (Vertical resolution: 1.5 km, Bandwidth: 0.79 Hz)

In Table 8 a link budget for the GRAS instrument, based on parameters measured at the on ground verification, is presented in support of Table 7. We notice the low receiver noise of 225 K, but also the high C/A co-channel interference from non tracked SVs appearing in the antenna beam. The antenna temperature will vary considerably, since over oceans mainly cold space is reflected.

Item	P A R A M E T E R	Unit	L1 C/A	L1 P	L2 P
	RECEIVED SIGNAL POWER				
1	SV EIRP	dBW	29.8	26.8	24.3
2	Free space loss	dB	-185.6	-185.6	-183.5
3	Rx antenna gain	dBi	10.8	10.8	10.2
4	Received signal power Ps	dBm	-115.0	-118.0	-119.0
	NOISE AND INTERFERENCE:				
5	Antenna received noise	K	170	170	190
6	Electronics thermal noise	K	225	225	190
7	Co-channel interference	K	178	27	4
8	Total noise temperature Ntot	K	573	422	384
9	Total noise power density Ntot	dBm/Hz	-171.0	-172.3	-172.8
	C/No RESULTS				
10	Received Ps/Ntot	dB.Hz	56.0	54.3	53.8
11	Implementation loss	dB	-0.8	-2.5	-2.5
12	Codeless tracking loss on P-code	dB	-	4.3	3.8
13	**C/No**	**dB.Hz**	**55.2**	**47.5**	**47.5**

Table 8 C/No budget for the GRAS instrument.

At the bottom line of Table 7, the Doppler error is converted to a bending angle error through multiplication with the nominal relative sensitivity at an azimuth angle of 30 degrees, which is a value representative for the average over all occultations. This results in a bending angle measurement accuracy of 0.46 μrad.

For comparison, in Figure 47 GRAS bending angle noise retrieved from measurement data is shown [Marq]. This result is evaluated at the altitude 60 to 80 km and is in line with the evaluation from the error propagation model above. The GRAS data is also compared to CHAMP and COSMIC results. The differences are partly due to the high GRAS antenna gain and hence signal to noise ratio, and partly due to the GRAS capability to rely on the USO reference and do without differencing schemes to compensate on board clock errors.

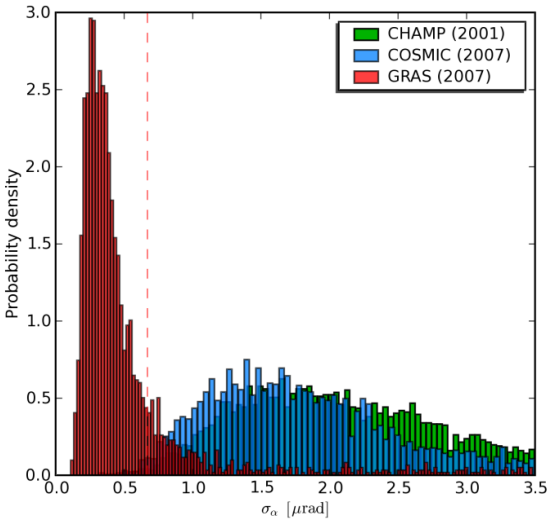

From C Marquardt, EUMETSAT

Figure 47 Bending angle noise for CHAMP, COSMIC and GRAS data evaluated [Marq]. The vertical dashed line shows GRAS bending angle requirement.

5.2 Doppler and Range Model

An on board Doppler model is extensively used in the instrument. It is used to set the frequency search range in acquisition and the carrier loop is aided by this model. In OL mode (TS 3-8), the NCO is entirely controlled by the Doppler model, and as a result of this, the Doppler calculated from RS I/Q data will directly provide the model error. The Doppler model can also be evaluated at higher altitudes where only CL data is available by combining the NCO phase and I/Q phase and compare with generated Doppler model data. An evaluation of the Doppler model accuracy using 8 000 measured occultations from low to high altitudes is seen in Figure 48. Here we can also see the variation of the signal Doppler mean and the modulation due to the atmosphere. Iso-dB contours of the power spectral densities are also shown in arbitrary units and with the peak values around -175 to -170 dB. The model is used mainly below -20 km and is accurate to better than 10 Hz. The bias seen at SLTA altitudes below 10 km is due to the wide range of anticipated atmosphere profiles the model was designed for.

The raw sampling rate of GRAS is variable in steps between 250 Hz to 1000 Hz. The model error of 10 Hz is therefore totally negligible.

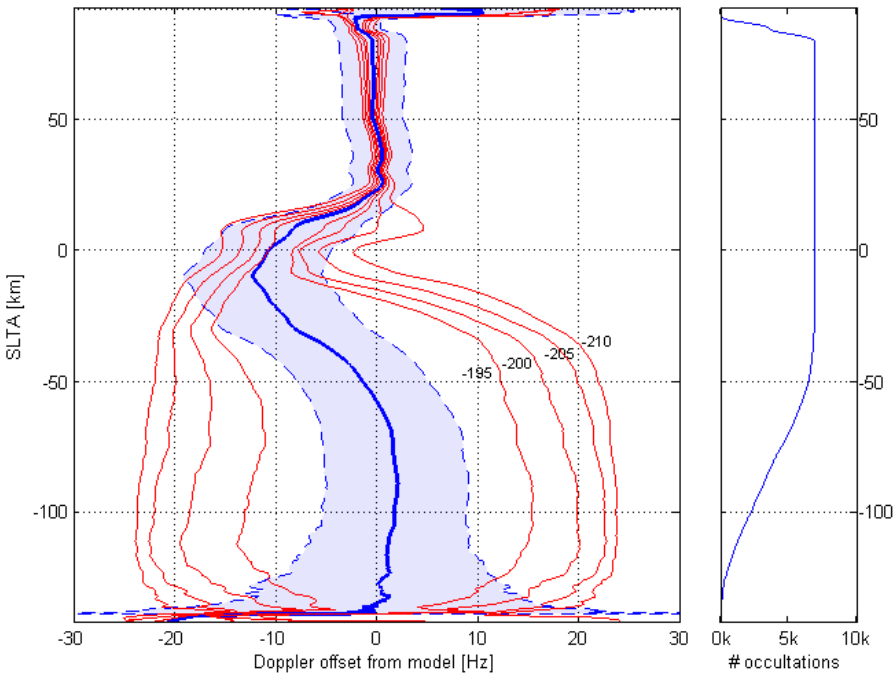

Figure 48 Doppler model error vs. SLTA. The thick blue line is the mean of the Doppler offset. The shadowed blue area is a 95% confidence interval related to the mean centre frequency. The red lines indicate the modulation bandwidth due to the atmospheric modulation.

Since the variation is smaller than the mean offset, the Doppler model can easily be improved. An accurate Doppler model becomes particularly valuable for future instruments if we wish to use it to develop a range model, since the Doppler errors will integrate when forming the range errors.

The Doppler model is controlled by a set of parameters. By modifying these parameters, we can obtain a Doppler model performance as shown in Figure 49. This can be implemented in flight by patching new parameters to the Doppler model.

A resulting budget for required raw sampling rate for a future mission is shown in Table 9 below.

#	Parameter	Contribution
1	Signal modulation	± 45 Hz
2	Doppler model	± 5 Hz
3	Instrument clock	< 1 Hz
4	Minimum required sampling rate	100 Hz
5	**Recommendation including margin:**	**100 Hz – 200 Hz**

Table 9 Compilation of signal Doppler uncertainties and recommended OL sampling rate (1 kHz default on GRAS).

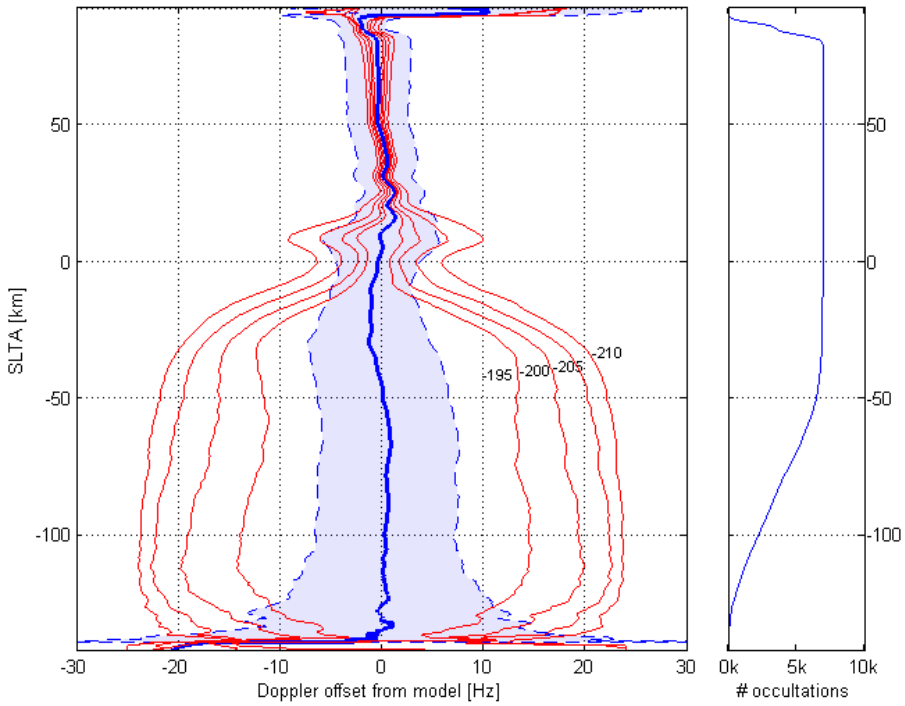

Figure 49 Performance of modified Doppler model with new values of NRIPA(SLTA). The peak offset of the mean frequency is approximately 1 Hz.

An on-board range model is used by the instrument in the acquisition process, where the code searched can be limited to a few bins in warm acquisition. It is also of importance to know the present and potential accuracy of the range model when investigating alternative tracking strategies.

This range model is here evaluated against the code range measured by the instrument.

Data from each occultation is mapped on a fixed SLTA scale so that mean values can be computed at each altitude. In order not to include pull-in phase or loss-of-lock phase, data have been omitted when:

- dR/dt > 10 meter/second

Using this screening it is unlikely that correct occultations (or parts of occultations) will be discarded, and the influence of false acquisitions will be strongly reduced.

Figure 50 below shows the difference between measured range and model range, dR, for rising occultations. The range error offset error is approximately -50 meters for all SLTA heights. The 95% limits cover the range -100 to 0 meters at low SLTA.

Figure 51 shows the corresponding range model error for setting occultations. The range offset error increases approximately from -50 meters at high SLTA to -80 meters at low SLTA. The 95% limits cover a range of 100 meters, as for the rising case.

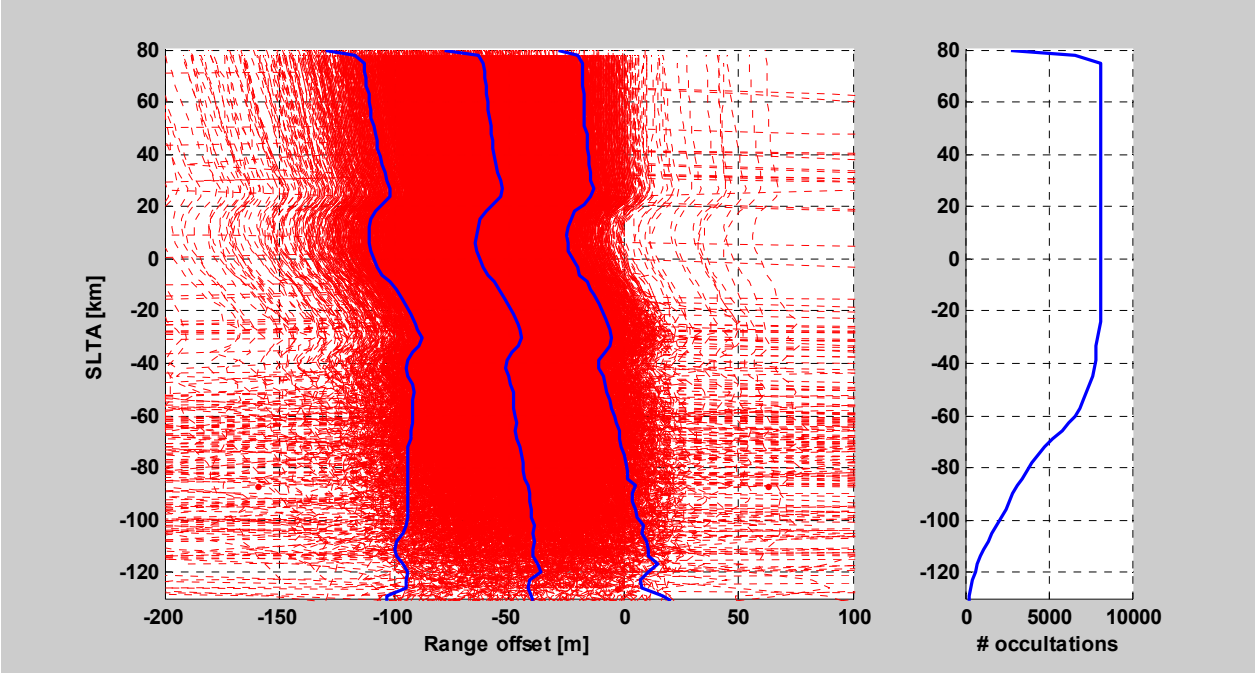

Figure 50 Range model error for rising occultations. The blue lines in the left plot indicates the mean value and 95% limits, respectively.

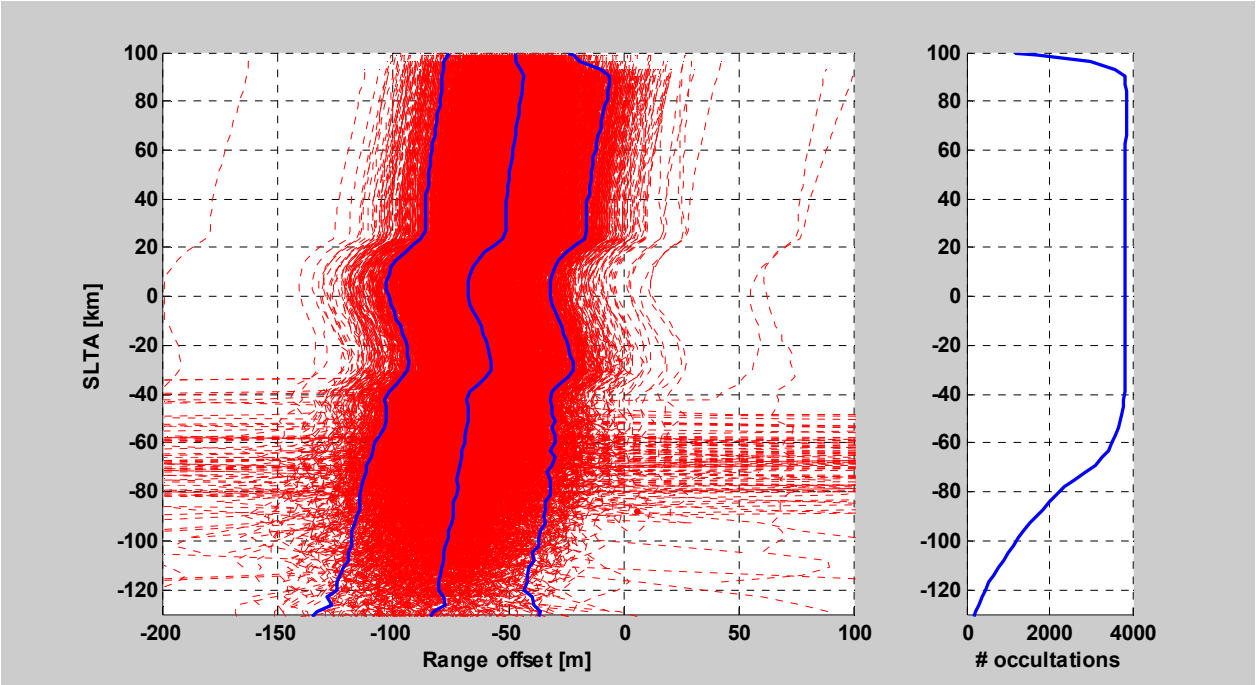

Figure 51 Range model error for setting occultations. The blue lines in the left plot indicates the mean value and 95% limits, respectively.

With a low range model error it would be possible to run the C/A code in open loop, i.e. completely model aided. Another alternative is to switch to a model based code NCO at a certain SLTA. In such case the range model is aligned to the tracked code phase at a certain SLTA. This is shown in Figure 52, where the range model is aligned to the tracked code phase at SLTA of -20 km, above the altitude where the code loop will lose lock. The range model error increases to -60 meters. This is well within the main lobe of the C/A code correlation peak, which is a triangular function with nulls at ±300 meters. On the other hand it is insufficient for a signal with higher chip rate such as L5.

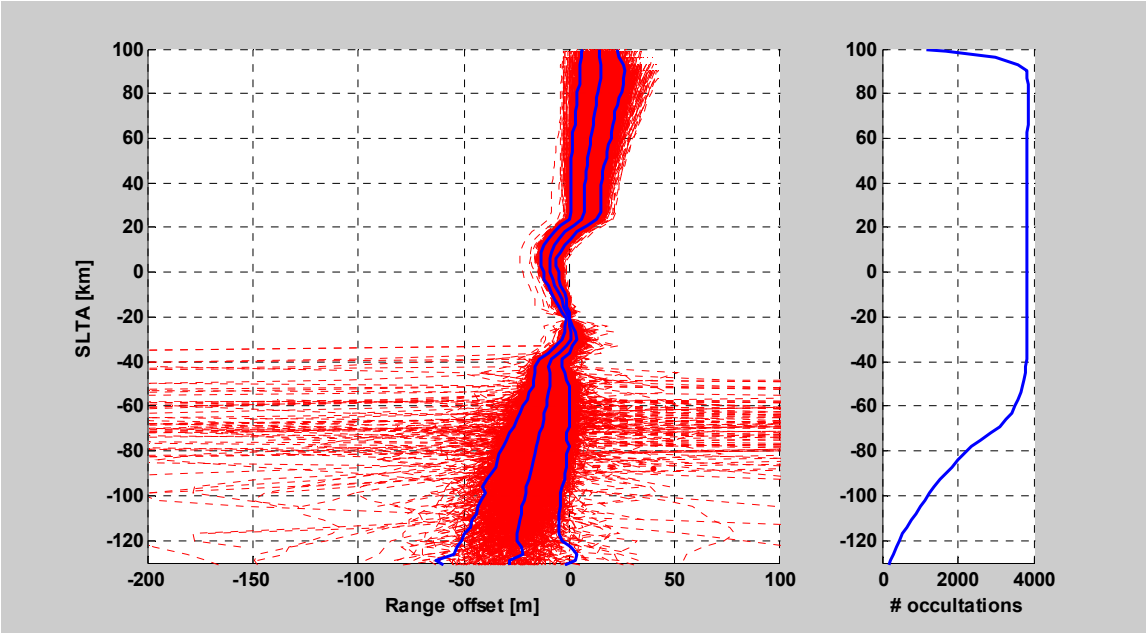

Figure 52 Range model error for setting occultations, where the range model has been aligned to tracked code phase at SLTA=-20 km. The blue lines in the left plot indicates the mean value and 95% limits, respectively.

- The range model bias is ~-50 meter.
- The range model error is within 100 meters peak-to-peak with 95% confidence (including the error of the real-time navigation solution).
- The acquisition time for C/A code in rising occultation should be possible to reduce for GRAS. The present search window is ±8 chip (±2400 meters), but according to this analysis it could be reduced to ±0.5 chip.
- Once a fix has been obtained the range model is accurate to about ±20m over a 100 km SLTA range. Consequently the code loop can be aided across large data gaps once an acquisition has occurred. This can be used to extend recordings of setting data significantly compared to the current coverage. If rising data is stored prior to dispreading and processes backwards, the lower altitude can also be extended for rising occultations.

It is noted that the absolute uncertainty of the range model is assessed under low solar activity and that the bias may shift when solar max occurs. At solar max we may approach slant path TEC around 400 TECu, for rays probing the neutral atmosphere. This corresponds to a dispersive delay of about 65 m for L1 which is small compared to the current search range during acquisition.

5.3 GRAS Interference Environment

In this section we describe the strong RF interference that has been measured by GRAS and seems to originate from ground. The correlation between the noise level in the L1 and L2 bands and the relation to actual signal quality are also investigated.

The GRAS provides the L1 and L2 histograms from the AGGA, which gives the total noise and interference power within 20 MHz bandwidth. GRAS is calibrated to provide the approximate absolute power levels.

Up to 6 dB Increased noise power density, NPD, levels are observed in the L2 band, and 3 to 4 dB in the L1 band, Figure 53. We notice a strong concentration of the increased noise to the northern hemisphere, indicating that it is interference external to the MetOp satellite. We draw the conclusion that the NPD levels measured in the southern hemisphere consist of the instrument thermal noise, the received thermal noise from Earth and GPS SV transmitted power. This strong variation in NPD was not foreseen in the GRAS design, and can have occasional impact on the tracking threshold and measurement accuracy. The tracking threshold is normalised to the input power, signal plus noise. When the received noise power is increased, the tracking threshold could invoke the loss of lock detector.

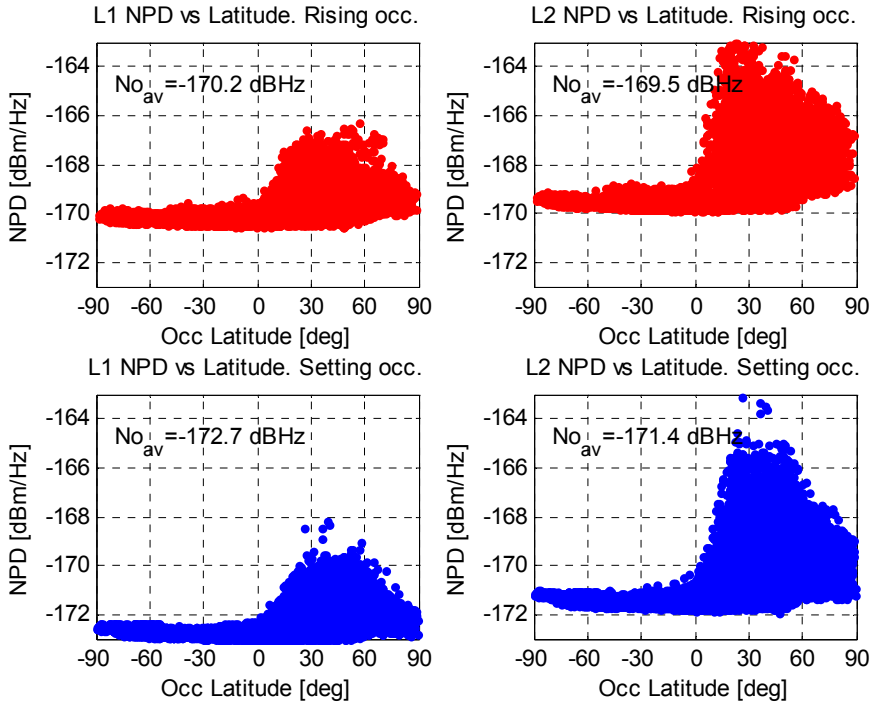

Figure 53. AGGA histogram noise power density for Rising (top), Setting (bottom), L1 (lest) and L2 (right), average NPD for the southern hemisphere are written in the plots.(Note: the written No_{av} should be in dBm/Hz)

We are here mainly interested in the NPD variations. The systematic difference between rising and setting chains is around 2.3 dB while the difference between the L1 and L2 bands is -1 dB resulting from actual differences and instrument calibration. The impact from a local terrestrial source can vary by 1.5 dB both in the L1 and L2 band due to the azimuth dependence of the antenna gain, seen in the NDP distribution in the southern hemisphere.

Plotting the occultation where the L1 NPD has increased by 2 dB or more on an earth map, Figure 54, gives a distribution that mainly coincides with industrialized and densely populated regions. It should be noted that the location cannot be pinpointed to geographical location due to the width of the occultation antenna pattern. The plotted location for the noise source is at the centre of the antenna beam, i.e. the longitude of the MetOp location and the latitude of the occultation compensated by 10° to account for the antenna elevation Beamwidth. The antenna azimuth beamwidth is ±55° which corresponds to some 50° longitude Earth coverage, measured at mid latitude.

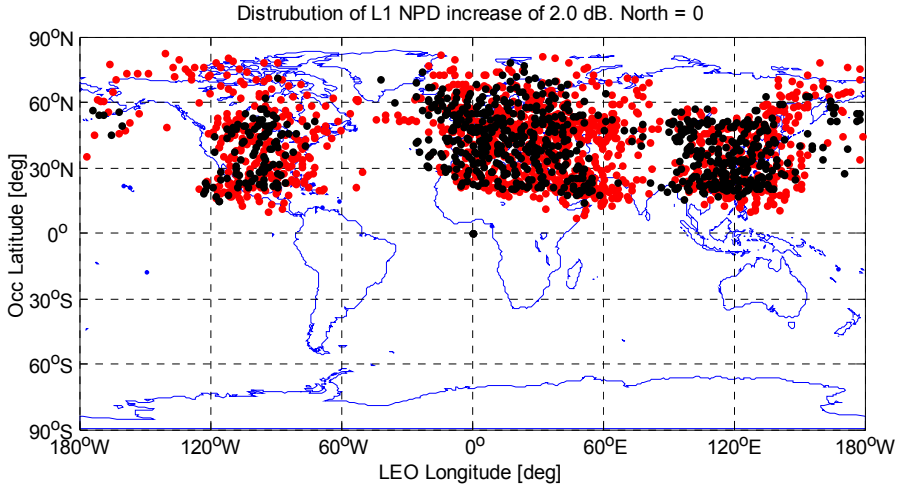

Figure 54. Location of rising (red) and setting (black) occultations where the AGGA L1 NPD has increased by more than 2 dB.

In Figure 55 and Figure 56 we show the NPD distributions for L1 and L2, and note the vast difference between the southern and northern hemispheres.

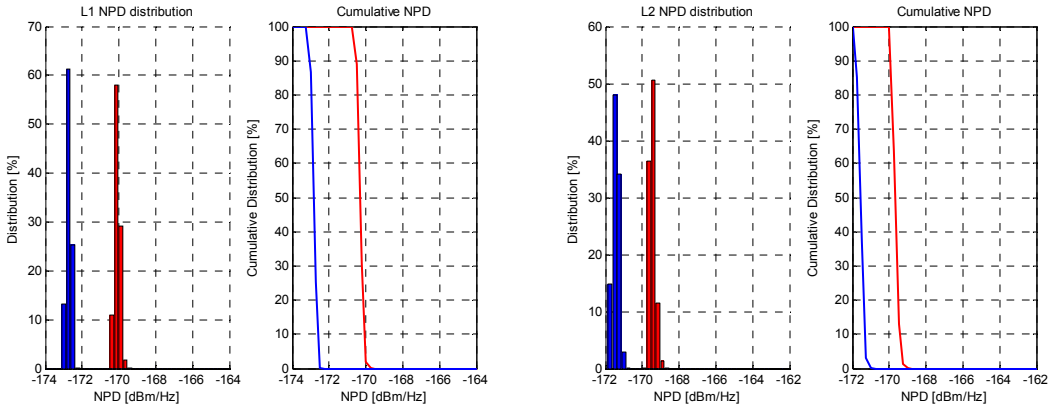

Figure 55. NPD distributions for L1(left) and L2 (right) for the southern hemisphere.

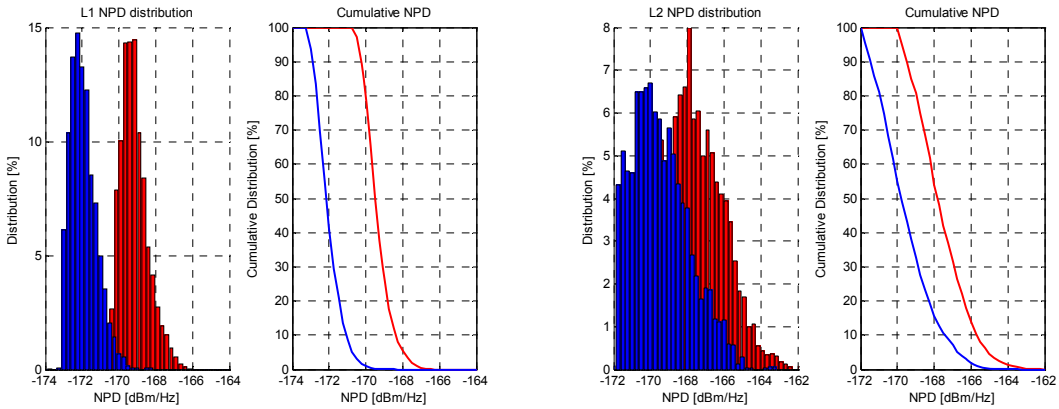

Figure 56. NPD distributions for L1(left) and L2 (right) for the northern hemisphere.

Figure 57 shows scatter plots of the NDP for set, rise and zenith channels at L1 and L2. We notice that zenith data is essentially uncorrelated, but for set and rise the L1-L2 correlation is relatively strong. Further the set-to-rise correlation at both L1 and L2 show a slight negative correlation.

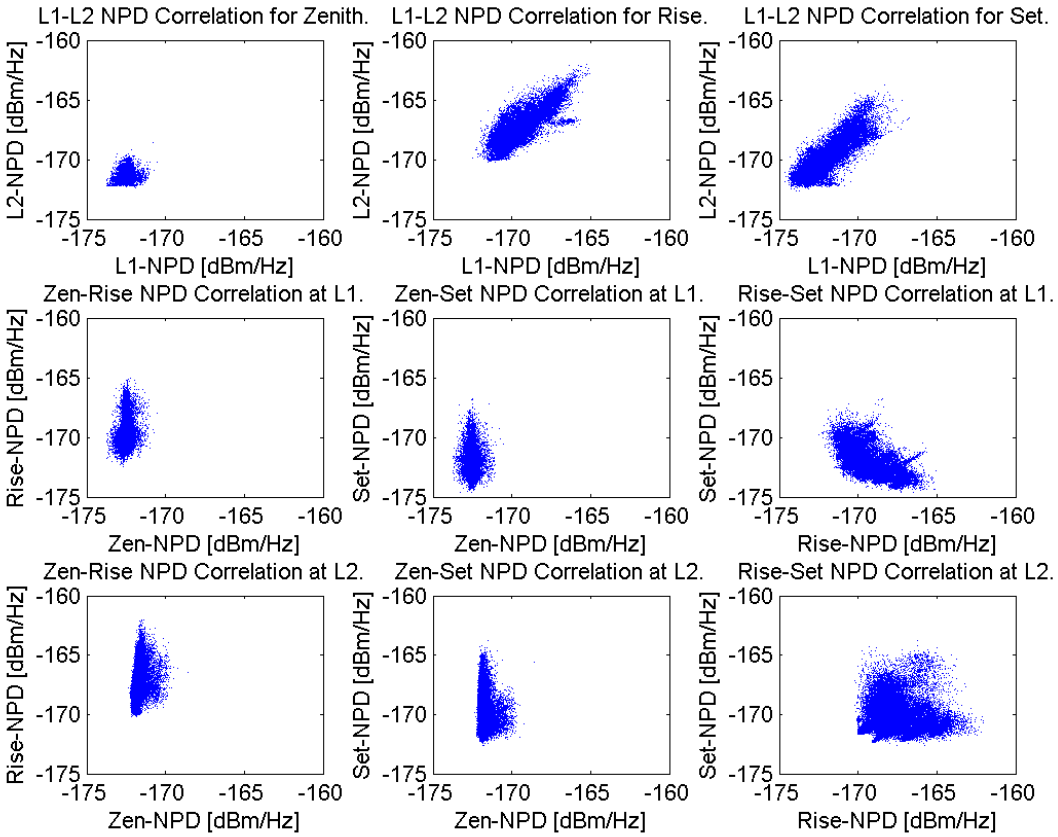

Figure 57 Correlation for NPD for set, rise and zenith channels at L1 and L2.

The correlation properties are further illustrated in Figure 58. The auto correlation peaks at orbital and daily periods with a peak magnitude at a 5 day period. MetOp revisits almost the same area on ground at 5 day intervals.

The cross correlation between set and rise peaks around 9 minutes, corresponding to the interval between set and rise viewing the same area on ground on the same pass. Peaks are also present when set and rise viewing the same area on consecutive passes.

Overall we have several indications that together provide strong evidence, that the noise power disturbance is related to interference transmitted from fixed points on ground. One example of such an interference is a pulsed transmission as identified in study case 6 (see section 5.4.2).

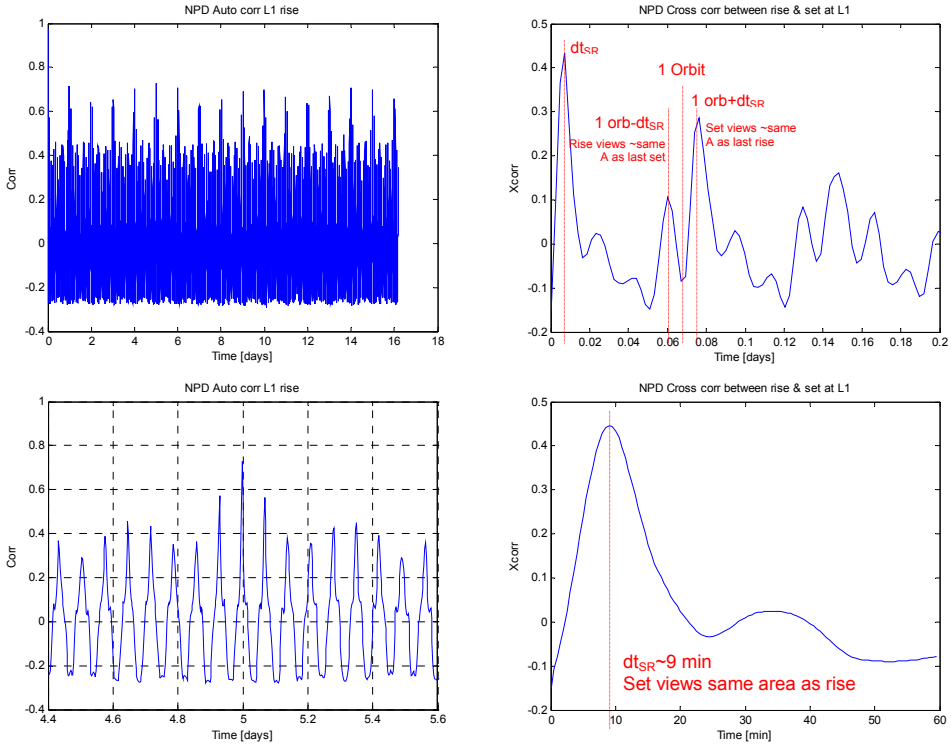

Figure 58 Autocorrelation for L1 (left) and cross correlation between rise and set (right).

5.4 Analyses of Study Cases

In this section we investigate those of the study cases anticipated in Table 3, that are of interest from the GRAS instrument point of view. The Study Cases listed in Table 10 are selected as interesting from the Instrument point of view.

Case	Characteristics	Description
3	Ocean reflection	The impact of ocean (or ground) reflections is identified as a study case.
6	10 Hz disturbance	In the sliding spectrum plots one can see spectral peaks at 10 Hz intervals for a number of occultations. The impact and origin of this feature should be investigated.
7	RS Saturation	In the 30 September data more the 0.5% of the I&Q RS data was saturated for 2% of the occultations. We propose to check if this has a significant effect on the results.
8	Weak P(Y) code signal	The P(Y) code signal amplitude is more than 20 dB lower than expected for some cases. We propose to investigate if this data is still useful and if the tracking algorithm can be improved to avoid this effect.
9	False tracking	The amplitude and frequency of this data indicates that the instrument has locked on incorrect SV. We believe that this data is not useful. The objective of this study case is to find an improved method for signal acquisition to increase the number of useful occultations.
11	Co-channel disturbance	Interference from other GPS SVs can be noticed in many occultations. These effects will be investigated.
12	L1 data gap	In many rising occultations, there is a gap in the L1 closed loop data that is due to loss-of-lock being detected for the carrier NCO loop. The impact of this and ways to improve the on-board software will be studied.

Table 10 Study cases of interest for Instrument investigations.

5.4.1 Study Case 3: Ocean reflection

Ocean reflections, OR, occur quite frequently over see ice and land. When investigating the potential impact on retrievals it is of interest to know the frequency of occurrence and the magnitude of the reflected signal. Reference is also made to the DMI retrieval of Study Case 3.

Traces of surface reflections at low altitudes can quite frequently be identified in the spectrum of the RS signal. The circular polarisation is preserved at grazing incidence reflections and the cross-polarisation loss will hence be small. Large flat surfaces must be envisaged in order to preserve the wave coherence, such as the calm sea, ice fields or possibly inversion layers close to a warm ground surface. A model has been developed predicting the Doppler and range differences, and this model is used to identify reflected signals.

An example of a sliding spectrum plot with a reflected signal and the corresponding model prediction is shown in Figure 59 below.

The impact of the ocean reflection on the bending angle processing is illustrated in Figure 61 where the bending angle intensity plot is related to the spectrum of the I/Q samples for RS and L1-C/A. When the frequency offset of the OR exceeds 25 Hz it is aliased back with a 50 Hz offset for the L1-C/A. In the bending angle plot, the aliasing is also present, but here with and altitude offset of about 16 km. This behaviour is observed, for several ocean reflections where the energy is aliased, but from the inspected samples we have not found cases where the aliased bending angle reflection crosses the main bending angle track. Increasing the sample rate to 100 Hz or more will eliminate this aliasing effect. When the range difference between the direct and reflected ray approaches the C/A chip length the signal from the two paths will de-correlate before aliasing occur.

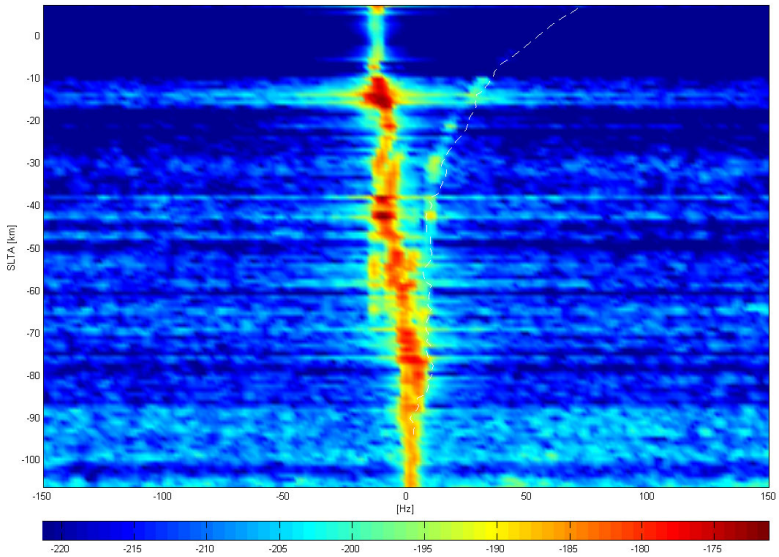

Figure 59. Setting occultation with ocean reflection. Power spectral density as function of time. Dotted line is Doppler offset predicted from model.

In order to obtain some statistics on the ocean reflection frequency, we scanned a large number of occultations and used the signal spectrum and the OR model to identify potential OR. The FFT of the raw sampling data is used to find the frequency of the spectral centre of the direct ray. We then evaluate the power spectral density within 10 Hz bandwidth at a frequency offset given by the OR model. To avoid energy from the direct ray to leak into the window of the reflected ray, a condition has been set in the analysis that the Doppler offset must be greater than 20 Hz.

10 609 occultations have been evaluated with this method, and the result is presented in Figure 60. In the figure we see land reflections added to the ocean reflections, with average power for the reflected rays some 20 dB lower than the direct rays, and land reflections slightly lower than ocean reflections as can be expected.

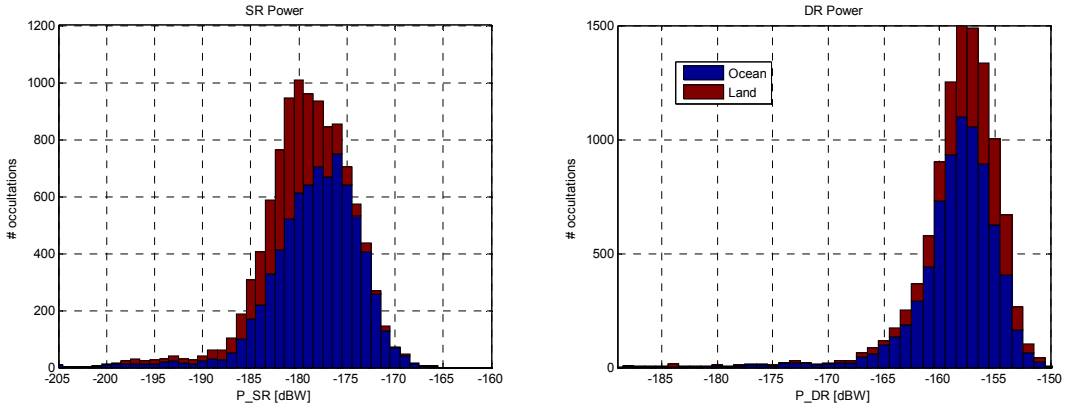

Figure 60. Distribution of mean power of potential surface reflections. Left pane: reflected rays, Right pane: direct ray.

The impact of the OR is further illustrated in Figure 61 where the bending angle intensity plot is related to the spectrum of the I/Q samples for RS and L1-C/A. When the frequency offset of the OR exceeds 25 Hz it is aliased back with a 50 Hz offset for the L1-C/A. In the bending angle plot, the aliasing is also present, but here with an altitude offset of about 16 km. This behaviour is observed, for several OR where the energy is aliased, but from the inspected samples we have not found cases where the aliased bending angle reflection crosses the main bending angle track. Increasing the sample rate to 100 Hz or more will eliminate this aliasing effect. When the range difference between the direct and reflected ray approaches the C/A chip length the signal from the two paths will de-correlate before aliasing occur.

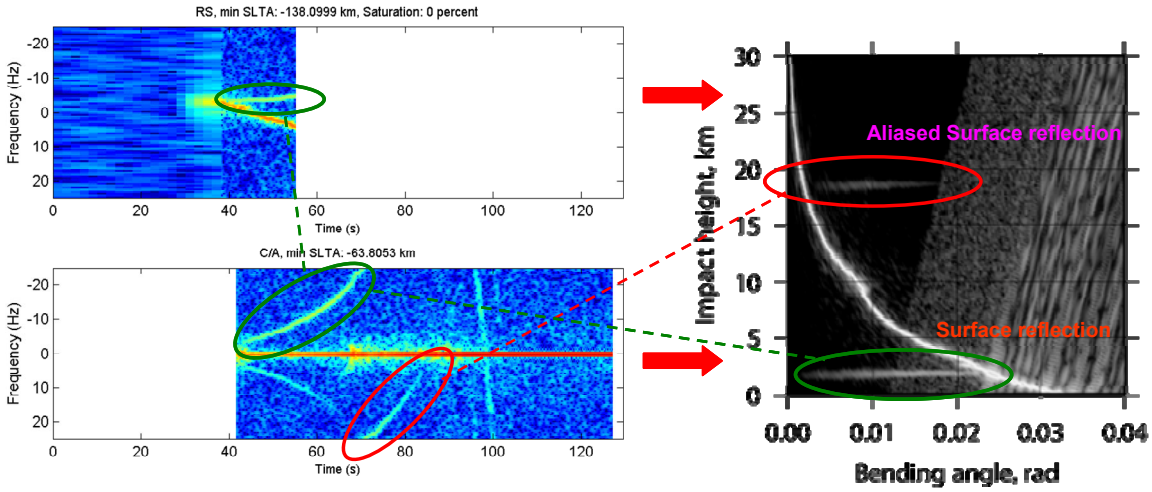

Figure 61 Relation between spectrum of measured I/Q signals and intensity of bending angle spectrum.

5.4.2 Study Case 6: 10 Hz disturbance

When analysing the frequency spectra of many occultations, several cases show evidence of disturbances at multiples of 10 Hz. One such example is shown in the figure below. The 10 Hz proved to be a 30 Hz interference convoluted at 50 Hz sampling and hence not shown in the 1 kHz spectrum.

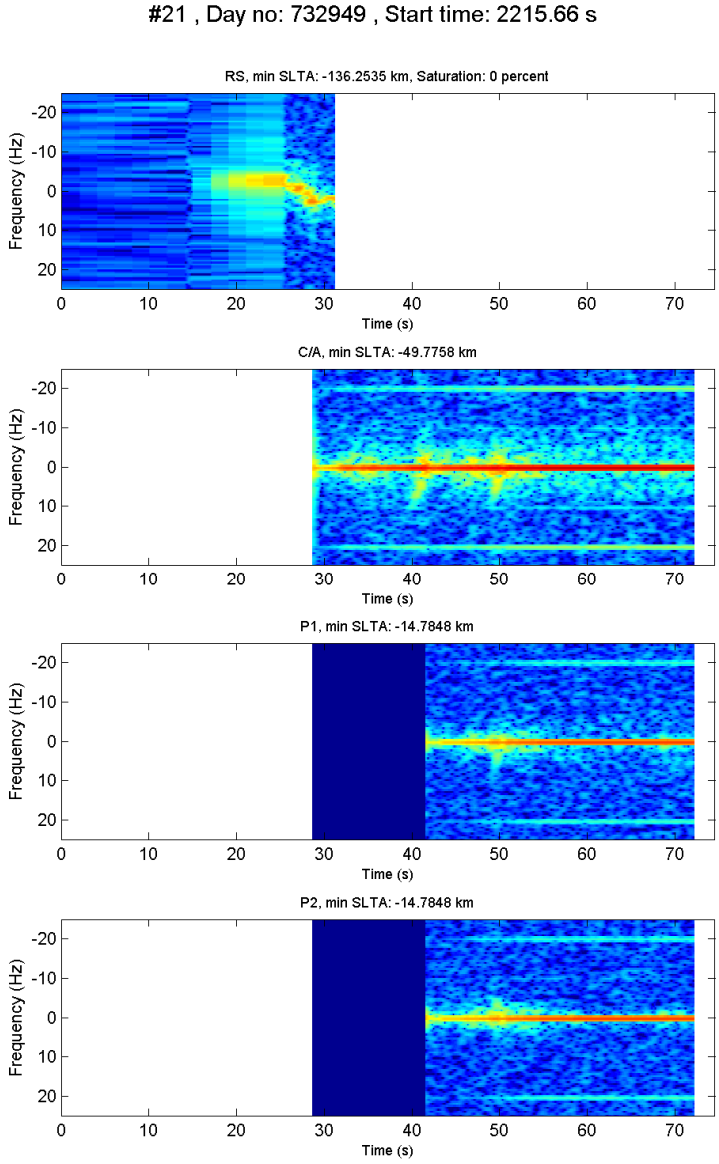

Figure 62 Sliding spectrum example with a 10 Hz disturbance.

As can be seen in this example, there are a few seconds of overlapping raw sampling data. When looking at the spectrum within +/-25 Hz as shown above, the disturbance cannot be seen in the raw sampling data. However, when analysing the data in more detail, we see that there is a disturbance also in the raw sampling data but at multiples of 30 Hz, see figure below.

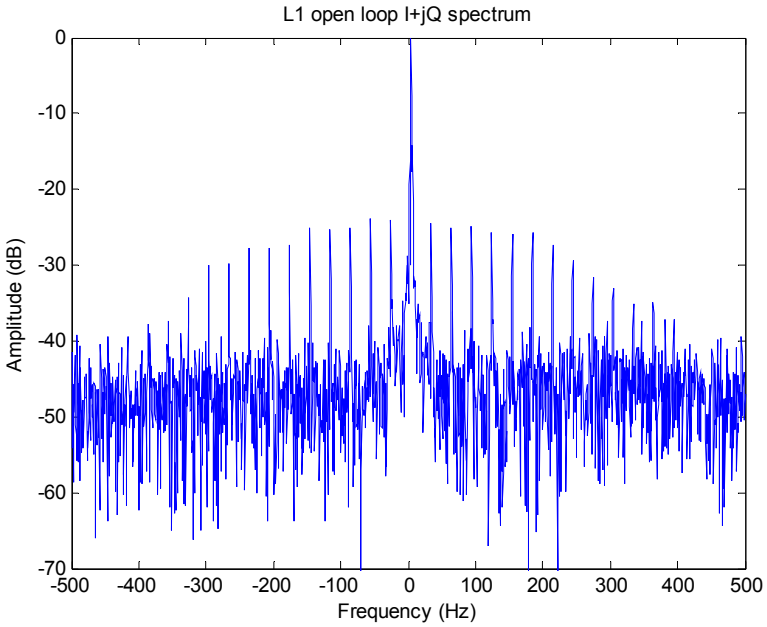

Figure 63 Power spectrum of complex amplitude open loop data.

When sampling the data at 50 Hz, the 30 Hz disturbance is aliased around 25 Hz and becomes a 20 Hz disturbance. The 60 Hz disturbance is aliased around 50 Hz and becomes a 10 Hz disturbance. This is illustrated in the power spectrum of closed loop complex amplitude data shown below.

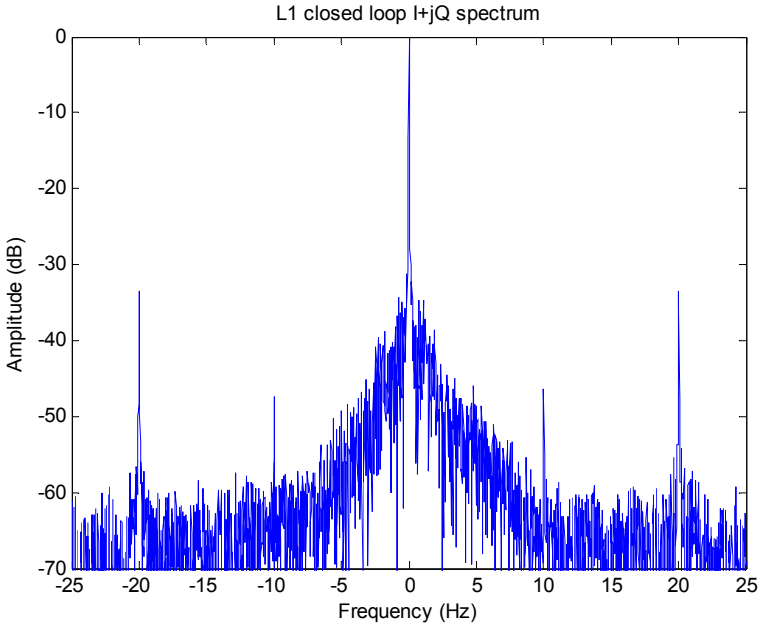

Figure 64 Power spectrum of complex amplitude closed loop data.

A time-domain plot of the open loop amplitude is shown in the figure below. It clearly shows that the signal amplitude is severely attenuated at short time intervals repeated at a rate of 30 Hz. When looking close at the individual samples, we can see that 2-3 samples are affected each time but that the repetition pattern of the disturbance is not exactly synchronized to the 1000 Hz sampling of the raw data.

In Figure 65 we have plotted the signal amplitude, and we see clearly the repetition rate of 33 ms corresponding to the 30 Hz repetition frequency.

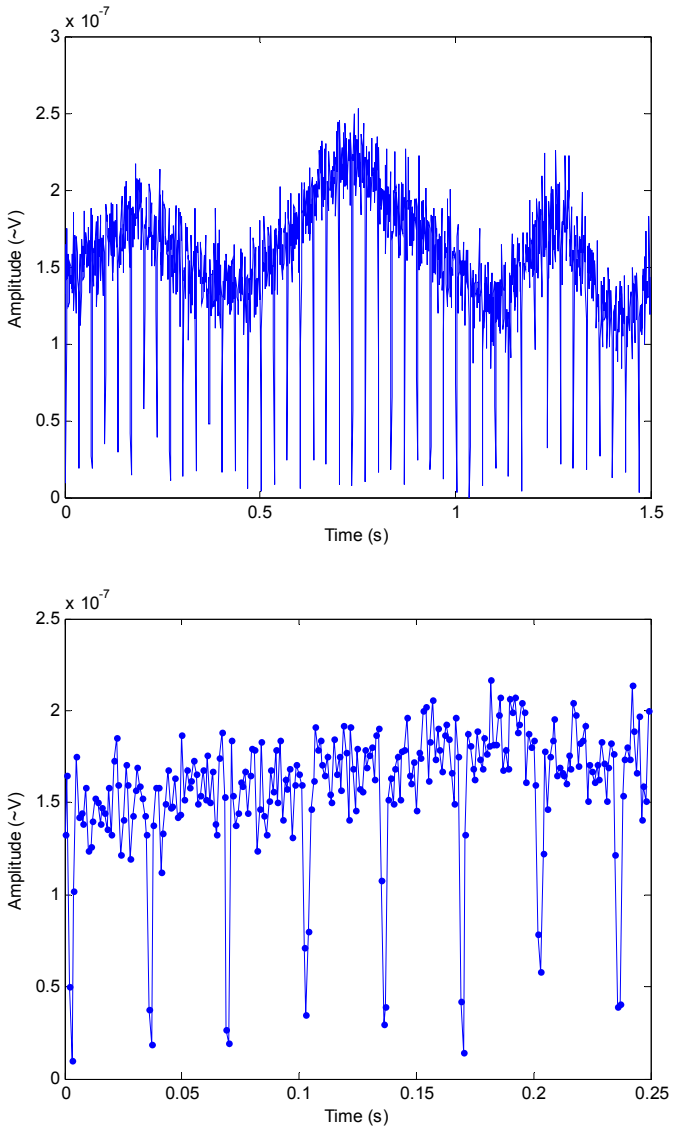

Figure 65 Open loop amplitude versus time (top) and blow-up showing individual 1-millisecond samples (bottom).

A triangular auto-correlation with a half-value width of 2 ms indicates that the disturbance can be regarded as a rectangular pulse with a duration of 2 ms.

The explanation to the attenuated signal is probably that the interference signal saturates the receiver chain and thereby causing a significant loss in gain. The digital signal processing in GRAS is two-bits and it is sensitive to presence of strong interference signals and the signal gain will drop. Due to this saturation of the receiver chain, an amplitude modulation will be present on both L1 and L2. The phase is estimated to be less affected. For this particular case, the wave optics retrieval appears to provide adequate results, but further in-depth analyses are recommended.

The geographical location of the occultations with this type of disturbance (tangent point) is plotted in the figure below. The relatively concentrated area of these occultations indicates that the origin of the disturbance is relatively few ground-based transmitters at high latitude. It should be pointed out the localisation of the interferers is very coarse, in particular in latitude, due to the wide beamwidth of the occultation antennas.

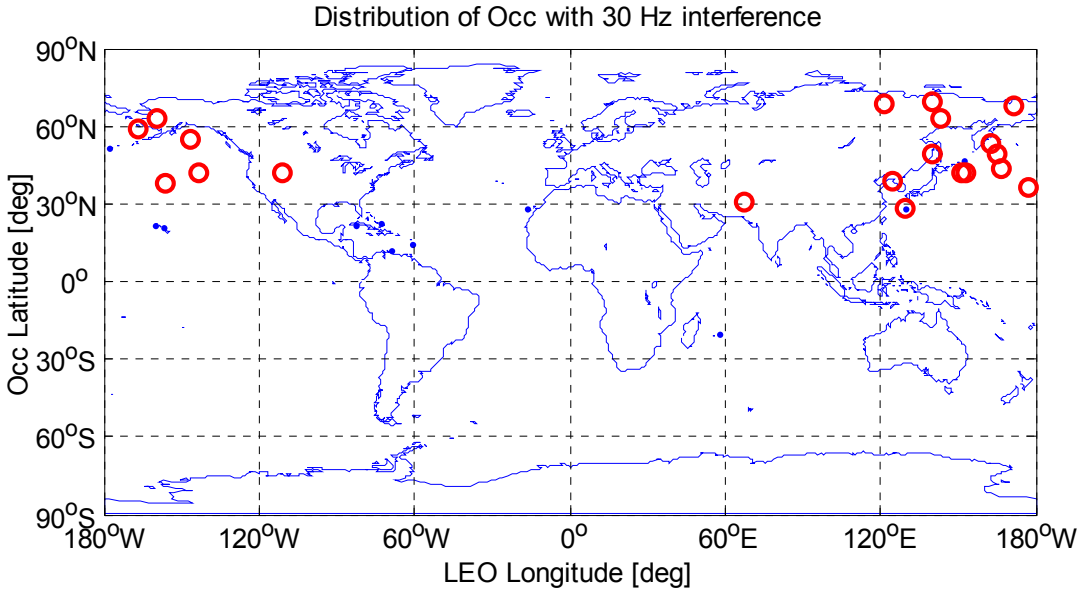

Figure 66 Geographical distribution of occultations with "10 Hz disturbance".

5.4.3 Study Case 7: Raw Sampling Saturation

Amplitude saturation of raw sampling data with example and statistics is described in section 4.4.5. In short, the RS I/Q correlator values are sampled with 8 bits in order to save data. At high altitude where the signal is strong the amplitude may saturate. In most cases, CL data is available could be used to correct the amplitude. The maximum saturation is ~3 dB and a maximum of 2% of all occultations contain 0.5% – 2.3% of saturated data. Saturation is hence rather infrequent and appears furthermore to have low impact on the BA profiles.

5.4.4 Study Case 8: Weak P(Y)-code signal

It can be observed that about 5% of all occultations suffer from more than 20 dB too low C/No on the L2 signal, see figure below.

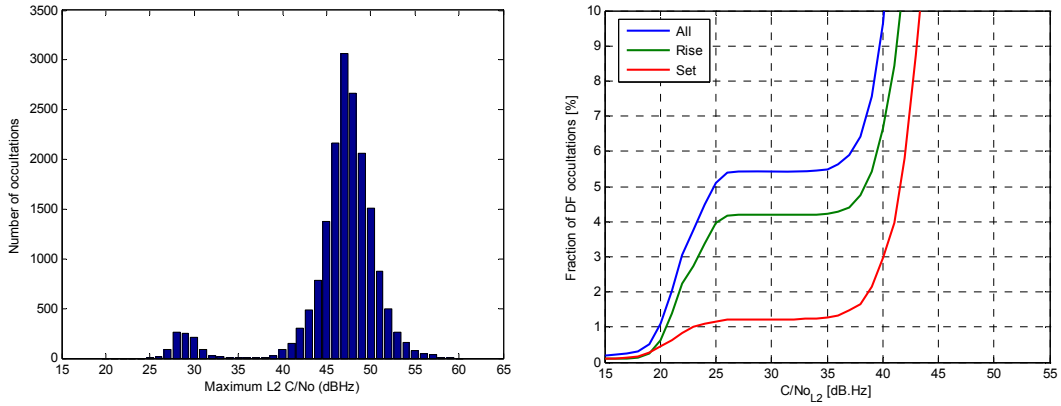

Figure 67 Histogram of maximum L2 C/No for all occultations (left) and accumulated frequency (right).

When analysing the code phase difference between different signal components, it appears as there is a random offset between the P-code and the C/A-code phase in the cases with low C/No. The reason for clustering around -30m, 0m, and +30m in the plots is that the P-code search during P-code acquisition is performed over a range of +/- 1 P-code chip and the P-code chip length corresponds to 30m in range.

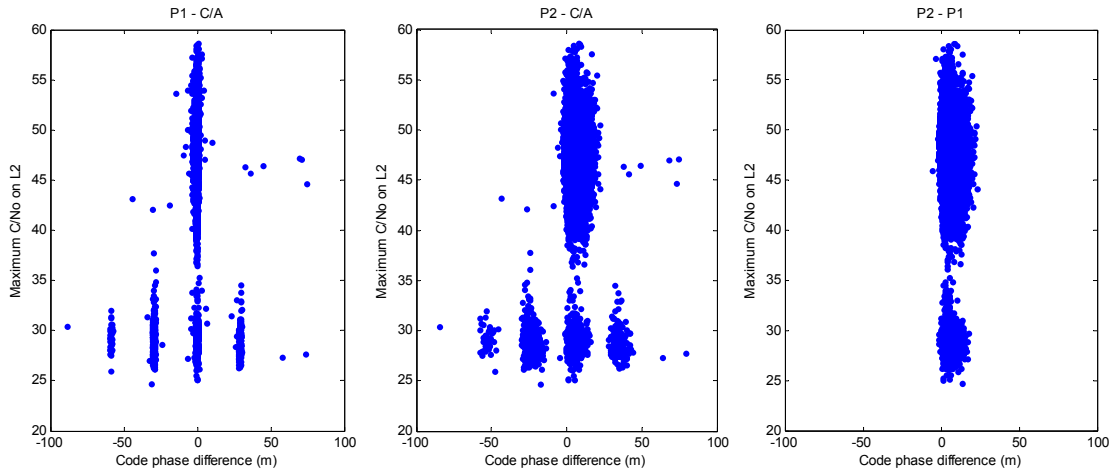

Figure 68 Maximum L2 C/No versus the code phase difference P1-C/A (left), P2-C/A (centre), and P2-P1 (right).

The most likely reason for this behaviour is that the true P-code phase is located outside the search-window and that the result of the search is that the strongest cross-correlation side-lobe peak is selected for tracking. Here, it would be possible to stop the acquisition attempt by considering the amplitude of the correlation result too low. However, it is obvious that the real-life signal amplitudes are higher than those assumed during the instrument development and therefore the lock detector approves also tracking of cross-correlation sidelobes. The case of tracking a cross-correlation sidelobe has been simulated and the result showing an amplitude loss of about 24 dB agrees well with the observed weak amplitudes.

The reason for the location of the true P-code outside the search window is believed to be due to the dynamic behaviour of the C/A code phase at the initial stages of C/A-code tracking before reducing the loop bandwidth followed by a pull-in period.

Possible solutions to this problem includes:

- increasing the threshold level of the P-code lock detector
- increasing the P-code search window
- delaying the start of the P-code acquisition allowing the C/A code phase to settle

5.4.5 Study Case 9: False Tracking

Sliding spectra for the observed case of false tracking of the L1 C/A-code signal are shown below for open loop and closed loop tracking, respectively. This is an obvious case of a false lock on an interfering co-channel SV with incorrect PRN. Since the EIRP of the GPS SV is higher than anticipated, the energy in the co-channel signal is sufficient to exceed the acquisition thresholds. When the code loop is locked, also the carrier loop can acquire the signal once the frequency offset is within the range of the FFT performed on the 1000 Hz data. The “true” signal becomes “invisible” since the code phase is here locked at an unfavourable position with very poor correlation (-60 dB).

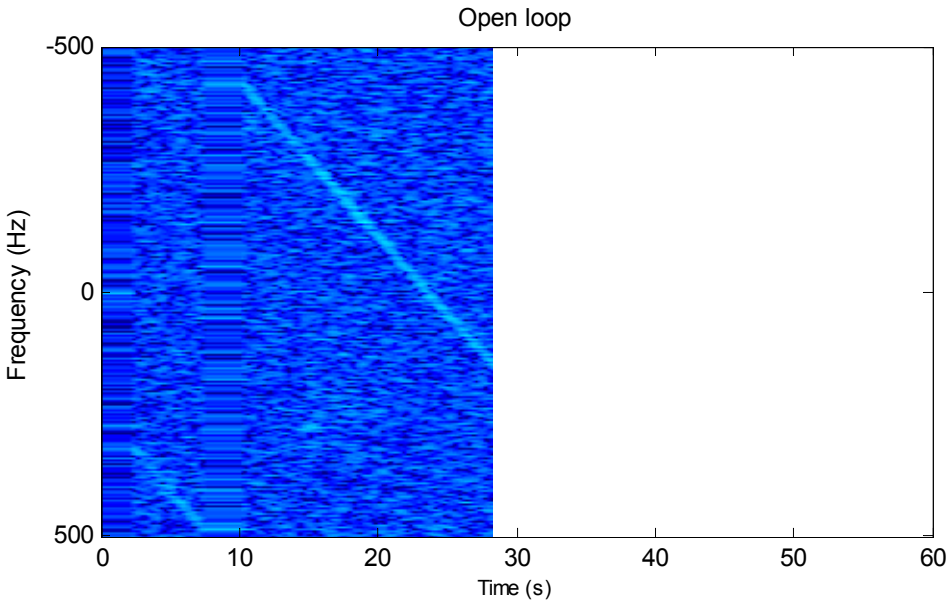

Figure 69 Sliding spectra of I/Q data for open loop tracking. Cf. next figure.

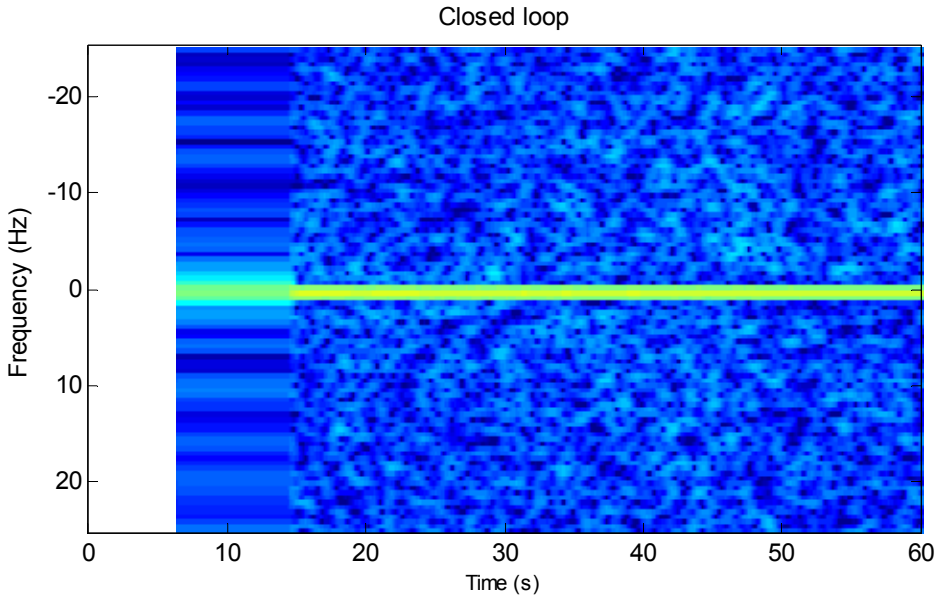

Figure 70 Sliding spectra of I/Q data for closed loop. The carrier NCO is locked to the false signal and the I/Q spectrum is focused at 0 Hz. Cf. preceding figure.

To improve the performance with respect to false-lock, a number of different solutions could be envisaged, as for example:

- Increasing the acquisition threshold values. This has the drawback of making the instrument less sensitive to acquisition of a weak (true) signal (software parameter change).
- Checking the navigation message for correct PRN identification. This has the drawback that there is quite a delay before the navigation message is acquired and decoded (software functional change).
- Using more points on the correlation function to detect acquisition of the correct correlation peak (software functional change).
- Checking the frequency of the code NCO regularly after acquisition to detect deviations from the onboard Doppler model (software functional change).

Several of this alternatives and possible others need to be investigated in more detail before a recommendation can be made for a potential MetOp-GRAS upgrade.

5.4.6 Study Case 11: Co-channel Interference

Co-channel interference is commonly seen in sliding spectrum of raw sampling data. A typical example is shown in Figure 71, where we also have indicated other visible SVs in terms of predicted Doppler offset. The co-channel interference is convoluted into the spectrum with the 1 kHz sampling rate partition.

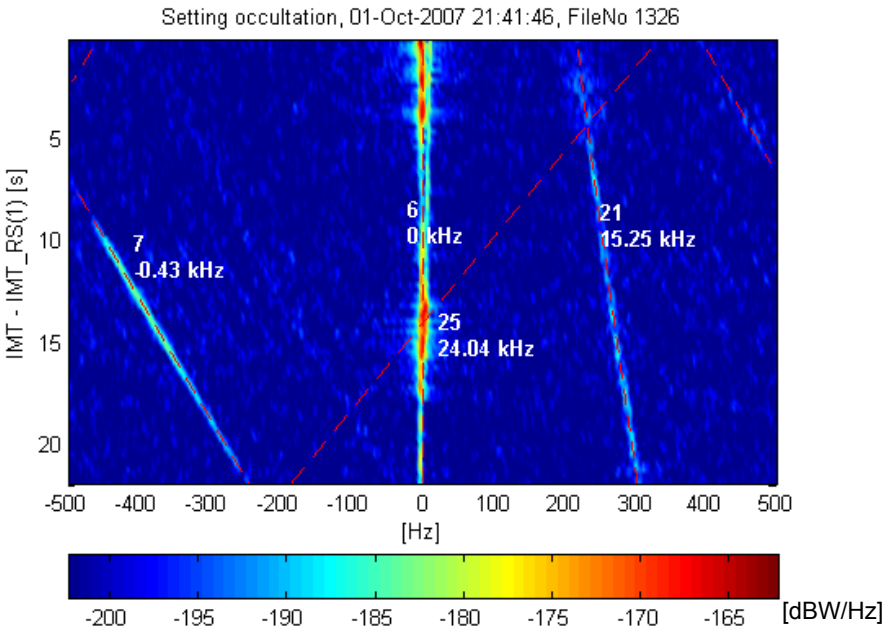

Figure 71. Setting occultation with co-channel interference. Red dashed lines are predicted. White numbers are PRNs and Doppler differences.

The Doppler difference between the occulting GPS satellite and the interfering satellites has been computed, and the result has been applied to the sliding spectra.

Ephemeris data from all GPS satellites have been used to compute satellite positions and velocities in ECEF coordinates at time of reception, and the signal propagation time is estimated assuming straight signal path. The position and velocity computation is then repeated with the approximated time of transmission.

The GRAS Doppler model has then been used to compute Doppler, with position and velocity of non-occulting satellites as input. The satellites not within the antenna field-of-view or obscured by the earth are excluded. The antenna field-of-view has been estimated roughly by azimuth bounds of ± 80°, and elevations bounds of -30° and 20°.

Generally for co-channel, no explicit retrieval problems have been identified (see also Appendix A.11 figures), but on the other hand, we have not demonstrated that the retrievals are fully resistant to co-channel interference. To determine the degree of disturbance, more in-depth analyses are needed. The worst situation is most likely for measurements at low SLTA when an interfering SV is within the antenna field of view but above the atmosphere hence having very strong amplitude.

5.4.7 Study Case 12: L1 Data Gap

A large number of rising occultations suffer from data L1 data gaps above SLTA of -35 km. At this SLTA, the raw sampling has been switched off, the AGGA integration time is changed to 10 ms and the search for the P1 and P2 codes has started. In case of an L1 carrier loss-of-lock, there is a fall-back to 1 ms integration time for L1 carrier reacquisition. The raw sampling mode is however not restarted. During the instrument specification phase it was not expected that the atmosphere conditions would be such that these events should occur above -35 km SLTA and a restart of raw sampling was therefore not considered at these altitudes.

Examples of such occultations are illustrated in Figure 72, plots generated by EUMETSAT. We note that the gaps predominately occur at low latitudes where more turbulent conditions are expected. In total about 18% of the occultations are affected by these gaps.

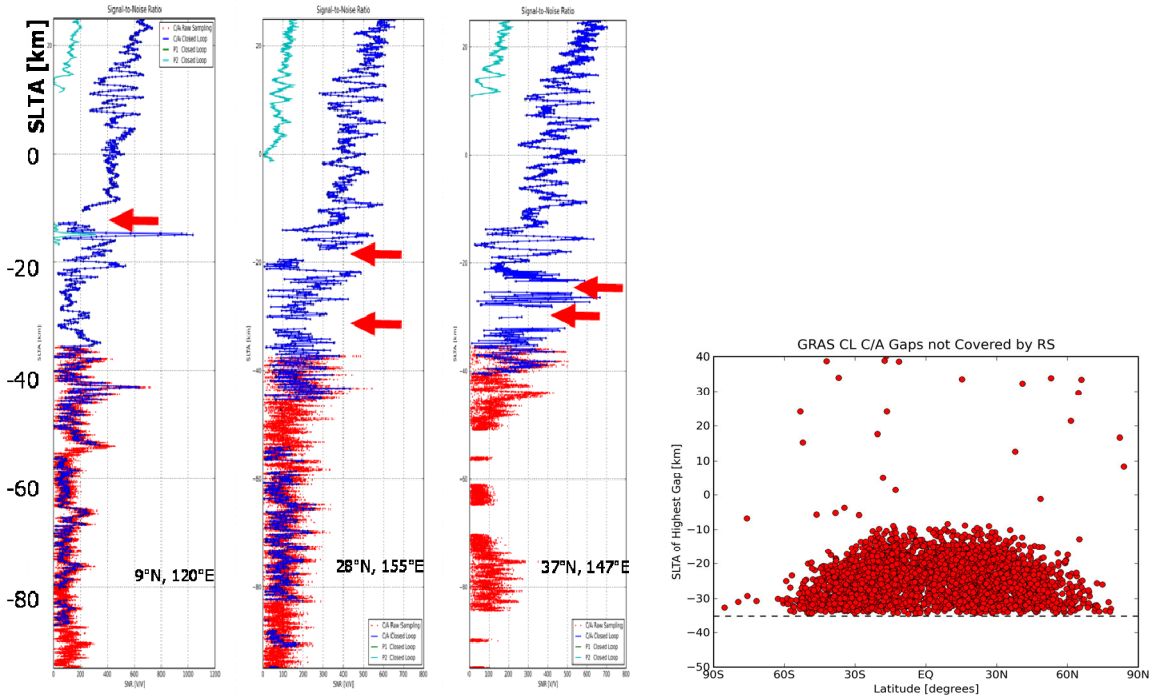

Figure 72 Examples of data gaps above SLTA of -35 km (by EUMETSAT).

The data set selected for study case 12 includes data gaps above SLTA of -35 km and is inspected in detail in this section. The RS and L1-C/A amplitude recording for study case 12 is illustrated in Figure 75. The gaps coincide with suddenly decreasing C/No as shown in the figure below.

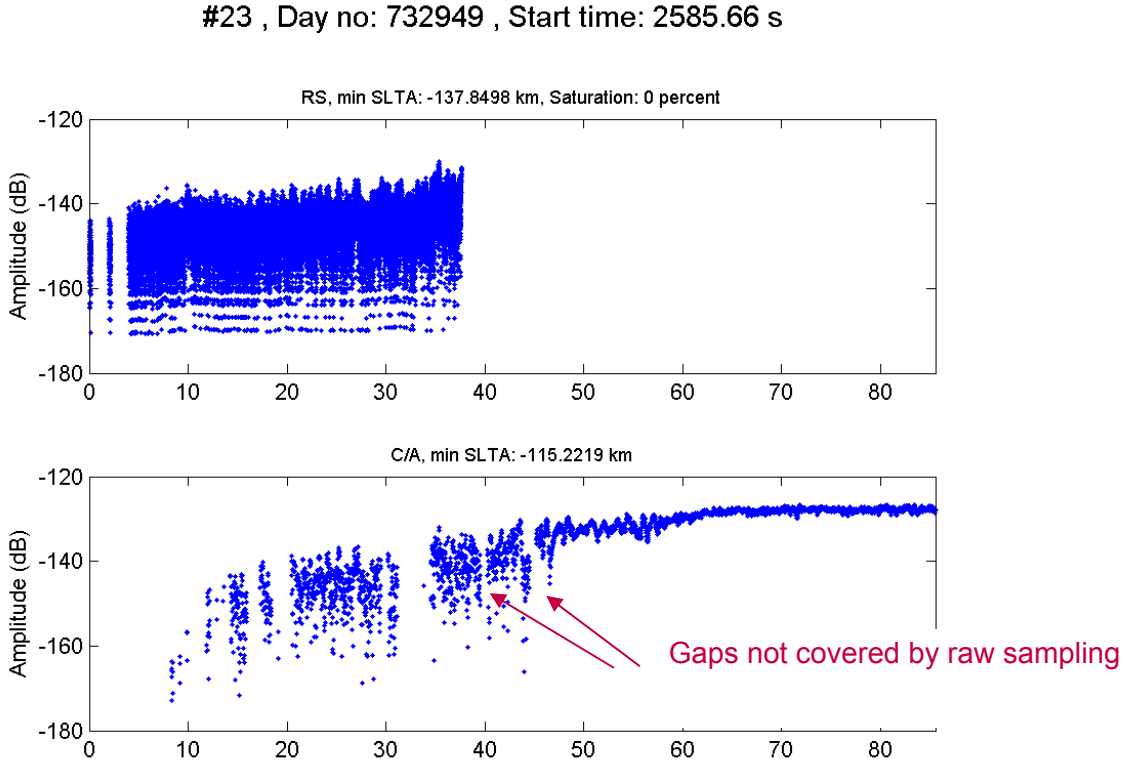

Figure 73 **Raw sampling (top) and L1 closed loop (bottom) amplitude data from a typical rising occultation. A number of data gaps can be seen in the closed loop data, two of which are not covered by raw sampling data.**

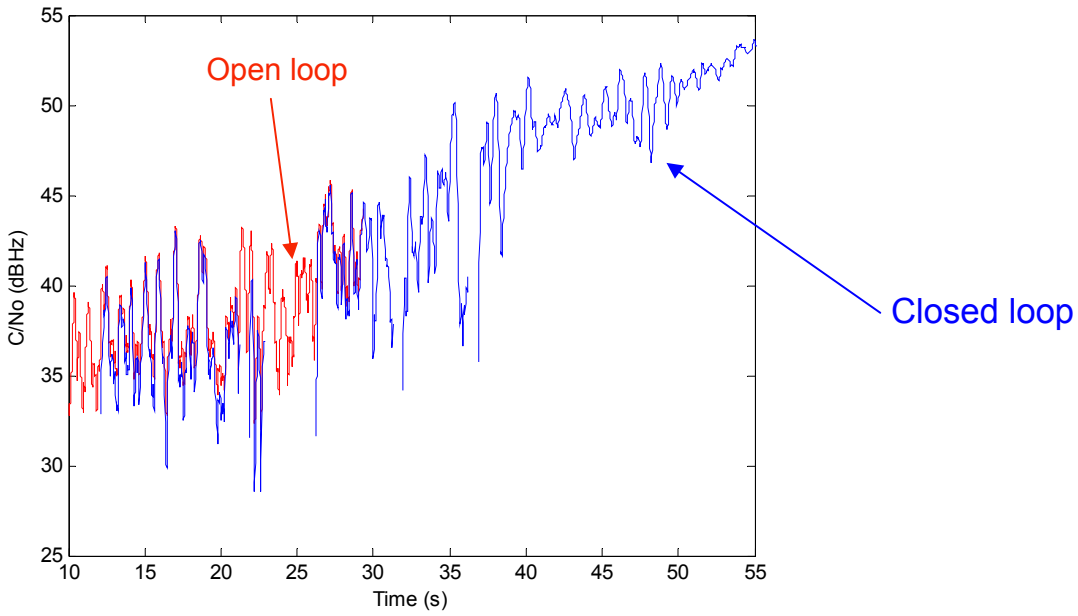

Figure 74 **C/No for open loop and closed loop data with gaps.**

The reason for a data gap in the L1 closed loop data is that the L1 carrier lock detector has detected a loss-of-lock. This can be due to that the carrier loop actually has lost the signal. This can be checked by analysing the carrier frequency and comparing it with the Doppler model. Another reason can be that the carrier lock detector is too sensitive and therefore generates false alarms.

In order to check if there is a true loss-of-lock, the total measured carrier frequency (NCO plus I and Q phase) data have been analysed and are plotted in the figure below. We see that the frequency is well behaved also around the data gaps with only the expected variation du to the atmosphere. The frequency, however, seems to be correctly measured when comparing to the Doppler model (red line). The conclusion is therefore that the signalled loss-of-lock is a false alarm.

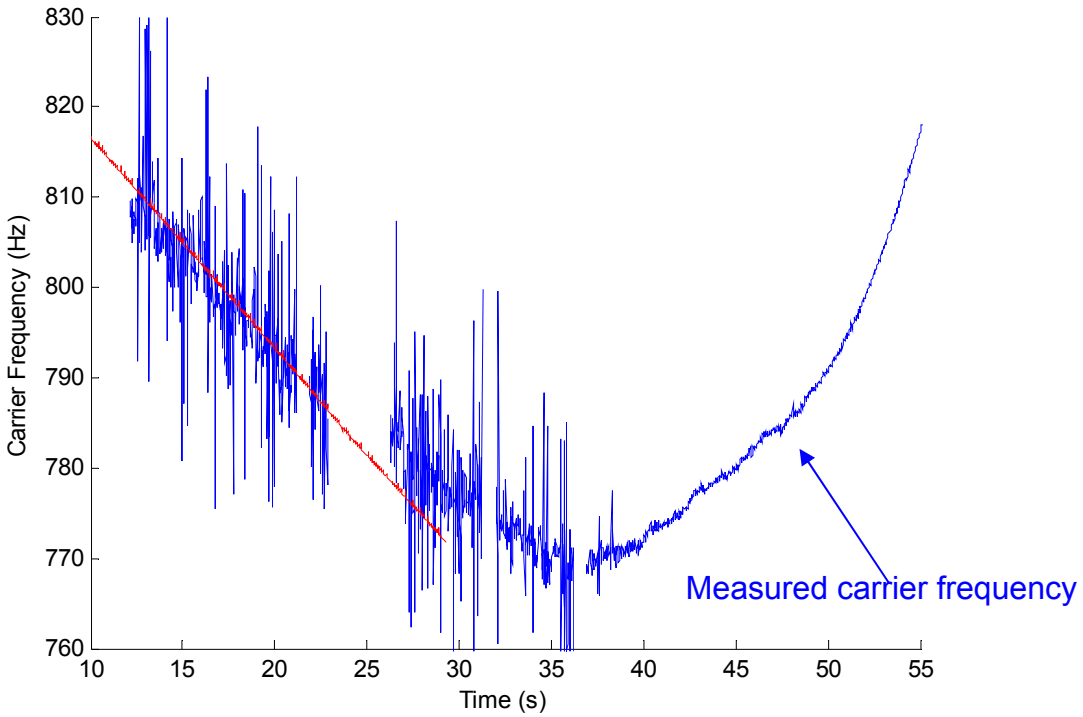

Figure 75 Measured carrier frequency (blue) plotted together with the open loop NCO frequency (red) as controlled by the Doppler model.

The amplitude of the lock detector as calculated from the I and Q data is plotted in the figure below. We see that the amplitude varies rapidly at the beginning of the rising occultation when the C/No is low. This is caused by the signal amplitude fluctuations being stronger and more dynamic than anticipated when designing the lock-detector.

A possible and very simple method of reducing the false-alarm rate of the lock detector is to increase the value of the integration time constant (single parameter value that can be patched). The resulting behaviour of the lock-detector amplitude can be seen in the figure below. This would result in much fewer false alarms from the lock detector. The capability to detect true loss-of-lock would remain but the reaction time is expected to increase somewhat.

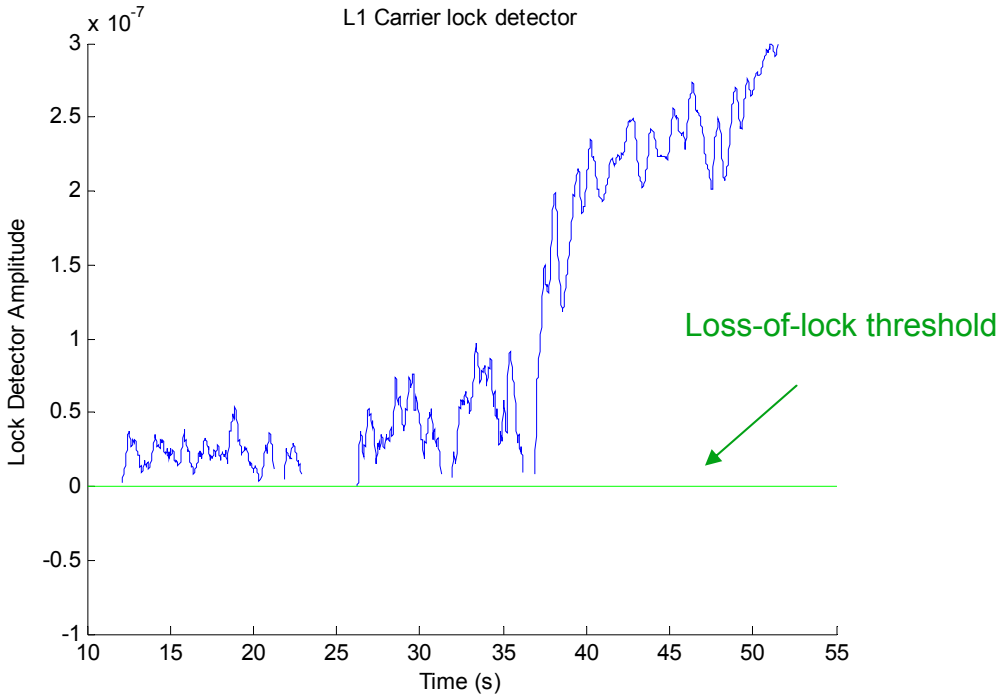

Figure 76 The L1 carrier lock detector amplitude versus the threshold.

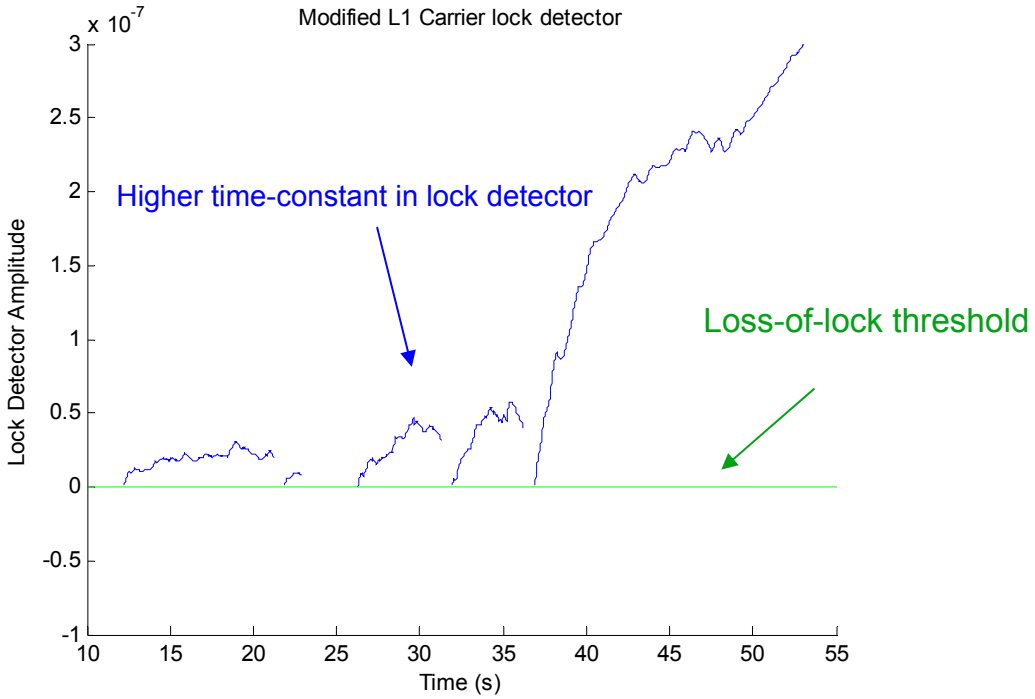

Figure 77 The modified L1 carrier lock detector amplitude versus the threshold. The modification consists of increasing the value of the integration time constant.

Another (more complex) modification of the tracking software is to provide raw sampling data in the case of loss-of-lock detection during L1 closed loop tracking, which is possible as long as the C/A-code loop is not affected. Another alternative is to increase the SLTA limit by command (now -35 km), forcing the OL mode (TS 3-8) to remain until a higher altitude but at the cost of a delayed L2 tracking.

5.5 GRAS Code Loop Tracking Performance

The code loop tracking performance is generally good. A potential for additional improvement exists in the case of dynamic amplitude conditions at low altitude as described below.

About 3-4% of the setting occultations show large data gaps in RS data. This is related to loss of C/A code phase tracking at low altitudes before the end of a setting occultation and code phase tracking can be improved to mitigate the problem.

The instrument behaviour for setting occultations is as follows:

- When code loop tracking is lost below SLTA = -90 km the tracking is aborted and the track is terminated.
- When code loop tracking is lost above SLTA = -90 km reacquisition is attempted. Restart of acquisition from TS 0 invokes the setting acquisition sequence. This means that RS is never started, but the search for L2 carrier starts as soon as L1 carrier tracking is achieved. It is only after the loss of L1 carrier tracking and the instrument falls back to TS 3, that RS is engaged.

In the following plots the presented behaviour is illustrated for two cases that also include false tracking of the P1 and P2 signals. We plot C/A amplitude in the 1st panel; P2 and RS amplitudes in the 2nd panel; TS for CL C/A and raw TS (time and TS when TS shifts) in the 3rd panel; and C/A code phase in the 4th panel. We have subtracted a 3:rd order polynomial fit from the code phase in order to see the dynamics. The time when SLTA is -90 km is marked in the 3rd panel. Time for start of the occultation and order of polynomial subtracted from thee code phase are indicated in the figure headings.

Among these cases RS frequently occurs relatively early in the occultation, sometimes due to false tracking of the P1 and P2 signals. The code tracking is more vulnerable during RS due to the 1 ms coherent integration time in the AGGA and we have RS for a longer time in these cases.

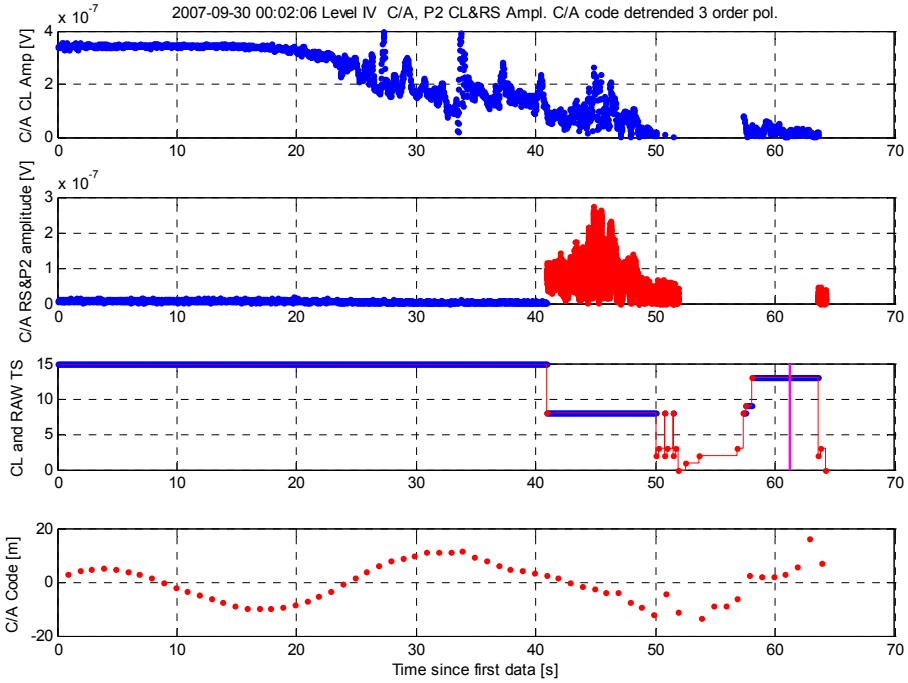

Figure 78 Example of loss of code phase. Top down: CL C/A amplitude, P2 (blue) and RS (red) amplitudes, TS, and Code phase.

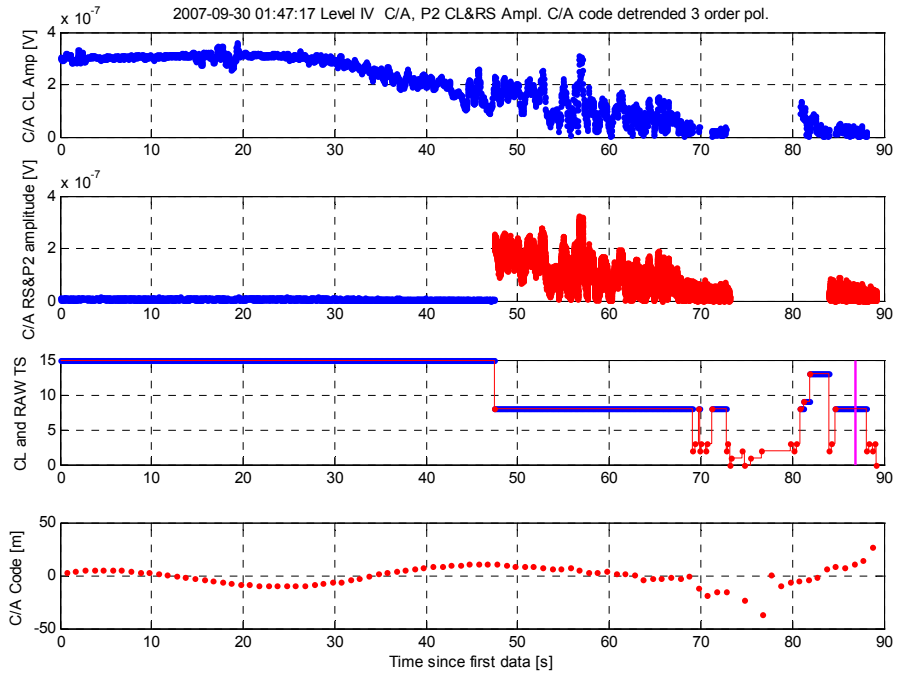

Figure 79 Example of loss of code phase. Top down: CL C/A amplitude, P2 and RS amplitudes, TS, and Code phase.

A minor modification to GRAS software could be to disregard the code lock detector below a certain SLTA and continue tracking to a fixed SLTA limit. The obvious advantage is that the probability to obtain longer setting tracks increases down to lower SLTA. The drawback is that re-acquisition of the code is no longer possible for the cases where code loop loses track.

To improve the tracking threshold we suggest increasing the incoherent and/or coherent integration times for the code loop. Thanks to the good Doppler model, most of the signal spectrum energy lies within ±50 Hz and therefore could a coherent integration time of 10 ms or 20 ms be possible to use which will increase the SNR. The RS data can still be sampled at 1 ms, because the coherent integration is performed in SW.

Both alternatives above will improve the lower altitude coverage for setting measurements and altitude coverage below SLTA = -140 km is expected if the settable parameter SLTA_AV is reduced below -140 km.

An improved code lock detector function would probably improve the performance for the situations where the C/No is good enough but tracking is aborted. This covers 20-25% of all rising occultations. By comparing the punctual (P) correlator value to the early (E) and late (L) correlator values, it is possible to estimate the deviation from centre of the correlation function and thereby achieving a true lock detector. The strength with this method is that there is no need of the measured noise level, i.e. the value is normalised to the present signal strength and present noise level. This improvement would probably not be possible to implement for GRAS, and should be considered for the next generation.

Based on the demonstrated accuracy of the Doppler and range models in section 5.2, the acquisition search volume can be reduced significantly allowing both faster acquisition cycles and/or more robust decisions based on longer integration times. In this case, parameters for the acquisition cycle should be defined to maximize the probability of detection after accounting also for the signal statistics of the interference patterns related to turbulent conditions.

The situation for rising occultations is similar to that for setting. In almost all occultations, a number of short periods of RS is obtained, but are immediately aborted. Analysing the code phase, we see that the signal is often correctly acquired, but discarded by the tracking lock detector. The same mitigation as for the setting occultation would make the also the rising acquisition more robust and will enable measurements at lower altitudes.

5.6 New GNSS Signals for the Next Generation

We compile the signal properties for the GPS modernisation and for the GALILEO signal in Table 11.

We note that the E5 signal having a chip rate of 10 Msps will be more difficult to acquire than the E1 signal, due to the shorter chip length and hence the larger amount of search bins.

The Pilot tone will enable long coherent integration times, and hence very robust tracking and high confidence in the SNR estimates. The modulated signal component must, however, also be decoded in order to access the Navigation message. Also the additional signal energy will improve the SNR.

Signal	Carrier [MHz]	Chip rate [Msps]	Chip Length [m]	Prim Code length	Sec Code length	Data mod [sps]	Modulation
GPS							
L1 C/A	1575.42	1.023	293.05	1 023		50	BPSK
L2 C	1227.6	1.023	293.05	150x10 230		-	BPSK
L2 CM	1227.6	0.5115	586.1	10 230		50/25	BPSK
L2 CL	1227.6	0.5115	586.1	75x10 230		Pilot	BPSK
L1 P	1575.42	10.23	29.305	1 week		50	BPSK
L2 P	1227.6	10.23	29.305	1 week		50	BPSK
L5-I	1191.795	10.23	29.305	10 230	10	100/50	
L5-Q	1191.795	10.23	29.305	10 230	20	Pilot	
L1C D	1575.42	1.023	293.05	10 230		100	BOC(1,1)
L1C P	1575.42	1.023	293.05	10 230	1 800	Pilot	BOC(1,1)
GAL							
E1-B	1575.42	1.023	293.05	4 092		250/125	BOC(1,1)
E1-C	1575.42	1.023	293.05	4 092	25	Pilot	BOC(1,1)
E5b-I	1207.14	10.23	29.305	10 230	4	250/125	BPSK
E5b-Q	1207.14	10.23	29.305	10 230	100	Pilot	BPSK
E5	1191.795	10.23	29.305	10 230	all E5	all E5	AltBOC (15,10)
E5a-I	1176.45	10.23	29.305	10 230	20	50/25	BPSK
E5a-Q	1176.45	10.23	29.305	10 230	100	Pilot	BPSK

Table 11 Overview of GPS modernisation and GALILEO signals.

5.7 Observations and Instrument Improvements

In the table below we summarise the analysed problems and other made observations that have been analysed in this report. The last column discusses possible follow-on activities which cover GRAS instrument updates.

Description	Ref §	Observations and possible solutions for improvement
1. High RF interference over northern hemisphere (25% occurrence)	5.3 5.4.2 5.4.6	It is suggested to analyse the performance of the GRAS breadboard in presence of interference. Assess the criticality of AM/PM effects. Possibly also implement an in-flight experimental S/W patch to better understand the characteristics and property of the interference and from that suggest adequate measures for GRAS / next generation RO. For some cases it may be necessary to identify and discard data in the post-processing (possibly ~3%). The noise increases up to 6 dB on L2 and 3 dB on L1, increases the thresholds accordingly. Data should be flagged and the distortion mechanism and user impact should be further assessed. **Suggestions:** **-** Possibly disable or slow-down the analogue/digital gain change activity. - Increase robustness of lock detectors. - Further evaluations of the distortion mechanisms and consequences are recommended.

Description	Ref §	Observations and possible solutions for improvement
2. L1 data gaps in closed loop data (18% occurrence)	5.4.7	**Suggestions:** **-** A simple change could be to increase the time constant of the L1 carrier lock-detector. This implies only a change of the value of a constant in the software. It is also possible to modify the state machine such that open loop data is provided directly when the carrier lock-detector signals a loss-of-lock. This implies a software modification. **-** Other software improvements are also possible.
3. Weak P(Y)-code signal (5% occurrence)	5.4.4	**Suggestions:** **-** A simple change is to increase the P-code acquisition threshold (value of a constant). **-** It should also be considered to increase the search window or to delay the start of P-code acquisition. **-** Other software improvements are also possible.
4. Acquisition/ tracking on co-channel signal	5.4.5	**Suggestions:** **-** The easiest improvement is to increase the incoherent averaging in the second dwell verification and adapt the acquisition lock detector threshold (values of constants). **-** The code search window can also be decreased. **-** A solution for improved sensitivity (lower threshold) is to also increase the coherent integration time up to 10 ms for the code loop (still possible to maintain 1 kHz RS data). **-** Other software improvements such as relying heavier on the Doppler and range models and/or additional track verification steps are also possible.
5. Data gaps in RS data, and extended altitude coverage	5.5	**Suggestions:** **-** For rising - Improve acquisition code lock detector performance. **-** For setting - Disable the tracking code lock detector and output RS data until lower SLTA limit is reached or switch over to range model below certain SLTA limit. - Lower the -140 km SLTA altitude limit. - Other software improvements are also possible.
6. Acquisition time	5.2	The acquisition time for rising is critical since it determines the start of RS data. The range model error analysis shows that 95% of all occultations lie within -100 and 0 meters relative to the range model. **Suggestions:** the present code search range in rising is ±8 chip (±2400 meters) can be reduced. The non-coherent integration time during search can be increased to improve the probability but the acquisition time should in total be possible to reduce. Improve the acquisition threshold setting, try to remove the dependence to AGGA noise data (which is disturbed by interference). Other software improvements are also possible.
7 Sampling rate	5.2	**Suggestions:** - OL sampling rate could be reduced if required for data load reasons.
8. Measurement at low SLTA	5.2 6 5.4 5.5	Comparison of EGOPS analysis and measured data indicates that strong signals can reappear at low SLTA altitudes and should be measured. This is also a conclusion in [WP1500]. **Suggestions:** - Extend measurements to lower limits by reducing lower SLTA limit below -140 km. - For setting - Revise the loss of lock detector - Increase coherent integration time - Increase reliance on on-board aiding models. - For rise: - Revise threshold and loss of lock settings - Reduce acquisition search volume - Increase coherent integration times.

Table 12 Summary of the analysed problems and way forward.

Several of the solutions and improvements described above can be handled in a step-wise approach where incremental improvements are implemented. We propose that a plan for incremental improvements is established based on mutual agreement between EUMETSAT, ESA and RUAG as well as other relevant parties. Further we recommend that this plan is executed in incremental steps to allow revision of the plan as we learn more about the actual possibilities, needs and effects.

In some cases we can predict the outcome of a given change fairly accurately, but in other cases or aspects we may need feed-back from actual trials to determine how to proceed. For this purpose we propose to define trial periods for MetOp-A, where potential changes can be evaluated. Such periods could be during or around orbit manoeuvres when the GRAS data is not used operationally. I.e. we patch a test version during this period, and review the results before a decision to use the patch operationally. The initial step of each increment should be to assess the impact of the change on GRAS and balance this against the user benefit.

Further we propose to discriminate between improvements for MetOp-A and the ones on ground (MetOp-B & C), where larger S/W updates not restricted to a few memory locations are feasible. Improvements for next generation RO receivers are also treated separately.

6 EGOPS WOP SIMULATIONS AND EVALUATION

EGOPS wave-optics (WOP) forward modelling simulations of GNSS phase and amplitude observables were selected in order to find interesting i.e. highly dynamic occultations to simulate. The EGOPS simulations by the University of Graz are made from the ECMWF profiles of physical data obtained from the ECMWF data closest in space and time to the set of selected occultations to be simulated. No ionosphere is included. All simulations are made as setting occultations in head-on geometry. The total occultation time is close to 60 seconds.

The simulations were made for three frequency bands, L1 L2 and L5. Two additional frequencies within each band were simulated in order to enable the calculation of the code phase equal to the group delay. The three centre frequencies and delta frequencies are listed in Table 13.

GPS band	Centre frequency [MHz]	Delta frequencies [MHz]
L1	1575.42	±10.0
L2	1227.6	±10.0
L5	1191.795	±15.345

Table 13 Summary of frequencies used in the simulations.

The ten WOP cases were selected among the GRAS occultation events to simulate strong multipath situation. All EGOPS cases were chosen from the Sep 30, 2007 measurements, just as the Study Cases selected for detailed analysis. In three cases these cases coincide with the Study Cases defined in Table 3 for further analysis by RUAG and DMI. A summary of the time and position of the EGOPS cases and the Study cases with corresponding time and position are compiled in Table 13.

EGOPS CASE	Time	Lat	Long	CASE Table 3	Time	Lat	Long
1:	00:01:55	50.1S	38.3W				
2:	00:09:26	30.6N	26.8W				
3:	00:12:57	4.7S	25.3W				
4:	00:13:54	46.1N	57.7W				
5:	00:20:39	24.6N	26.7W	2	00:20:40	24.5N	26.5W
6:	00:21:39	20.4N	43.1W				
7:	00:43:05	27.7N	154.8E				
8:	00:52:27	2.6S	149.4E				
9:	12:42:32	45.4N	29.3W	10	12:42:32	45.2N	29.4W
10	15:35:03	23.9N	71.9E	5	15:35:03	23.8N	71.9E

Table 14 Summary of the simulated EGOPS cases and corresponding Study Cases. Time is given as hh:mm:ss, all on 30-Sep-2007.

6.1 EGOPS WOP Simulations by University of Graz

The set of GNSS frequencies in the L1, L2, L5/E5 bands was defined together by the University of Graz and RUAG and quasi-realistic atmospheric conditions were adopted by utilizing ECWMF analysis fields at high resolution (T511L91) so that also typical multipath situations are encountered in the lower troposphere. The need was to provide a set of realistically simulated GNSS observables so that RUAG can further analyze the data characteristics, including of carrier and code phases or also in form of complex signals. Here we summarize the simulation setup and the data then delivered to RUAG as well as show an illustrative example of the simulation results, the evaluation of which is described in the following subsection 6.2.

The radio occultation simulation software EGOPS was used to perform the simulations, where in particular the forward modelling part was employed. The EGOPS multiple phase screen wave-optics propagator (WOP; developed by M. Gorbunov/IAP Moscow) was the key tool used to obtain quasi-realistic phase and amplitude observables.

In order to construct a small ensemble of example cases, ten representative occultation event locations were chosen from the 30 September 2007 “test day dataset” of MetOp/GRAS data, see Table 14. For this choice also aspects were considered which occultation events might yield some multipath in the lower troposphere and boundary layer..

The first eight events of Table 14, made use of the atmospheric refractivity field: *ECMWF T511L91 00:00 UTC ,* and events 9 and 10 : *ECMWF T511L91 12:00 UTC*

In this way the time separation of the analysis time and event time is as close as within 1 hour for nine of the events, only the 10^{th} event is about three hours separated (not critical in this simulation context).

The representative frequencies simulated in the L1, L2, and L5/E5 bands were defined together with RUAG, where the concept was that each band is covered by its nominal frequency and two additional lower and higher frequencies separated by about 10 MHz from the nominal one. These additional frequencies served in RUAG’s analysis to estimate and analyze code ranges in addition to the carrier phases and amplitudes.

Using the definitions of locations and atmospheric fields, the EGOPS WOP simulations were carried through for the representative frequencies at a 1 kHz sampling rate to allow detailed evaluation. Figure 80 shows example results for the centre frequency of the three frequency bands for one case, indicating the quasi-realistic nature of the output. The simulations clearly captured multipath features such as near the top of boundary layer. Corresponding complex signals and their spectra showed multiple-peak spectral behaviour typical for multiple ray propagation conditions. When zooming into small time intervals with peaks of strong multipath, also expected local deviations of code range from carrier range that occur under strong multipath became visible. The data of all cases were delivered to RUAG for their analyses summarized in the following subsection.

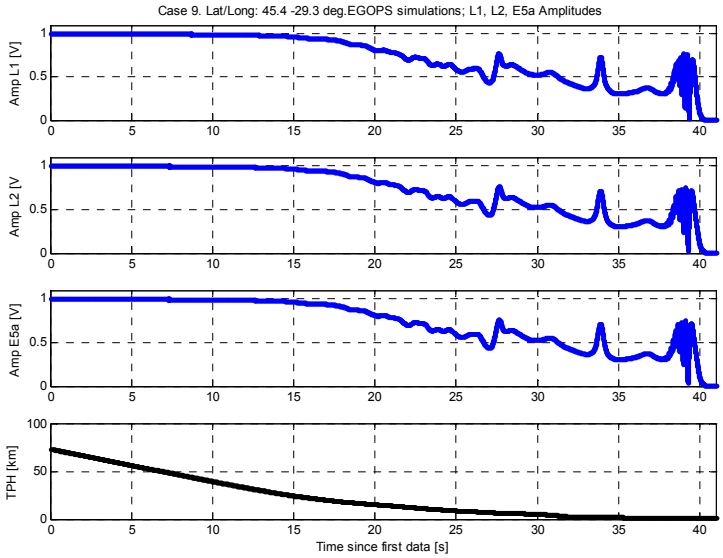

Figure 80 Example EGOPS WOP simulation results – amplitude profiles at the L1, L2, L5/E5 centre frequencies for occultation event no. 9 (occ9) (top three panels) and corresponding relation of tangent point height vs. time (bottom panel).

6.2 Evaluation of EGOPS WOP Simulations by RUAG

In the multipath situations, a ray propagates multiple paths in the atmosphere, recombines differently at different frequencies, and the atmosphere is experienced as dispersive. From simulations we find that the code and carrier ranges follow closely except in strong multipath situations, where they differ locally, rarely more than one meter. We examine case 9 in a region of strong multipath (around 39 s), where we see the code and carrier ranges in Figure 81.

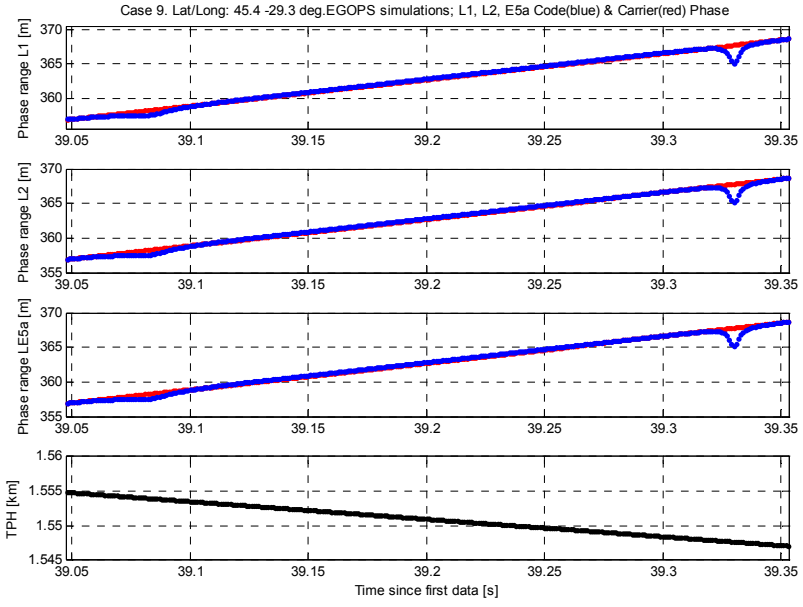

Figure 81 EGOPS Case 9 2nd simulation. Carrier (red) and code (blue) range plots of L1, L2, L5 and tangent point height, RTH.

We expect the code phase obtained from the phase slope and the accumulated carrier phases to track each other within a few meters in the absence of an ionosphere. We plot the difference between the code and carrier ranges in Figure 82. This difference is attributed to the atmospheric multipath.

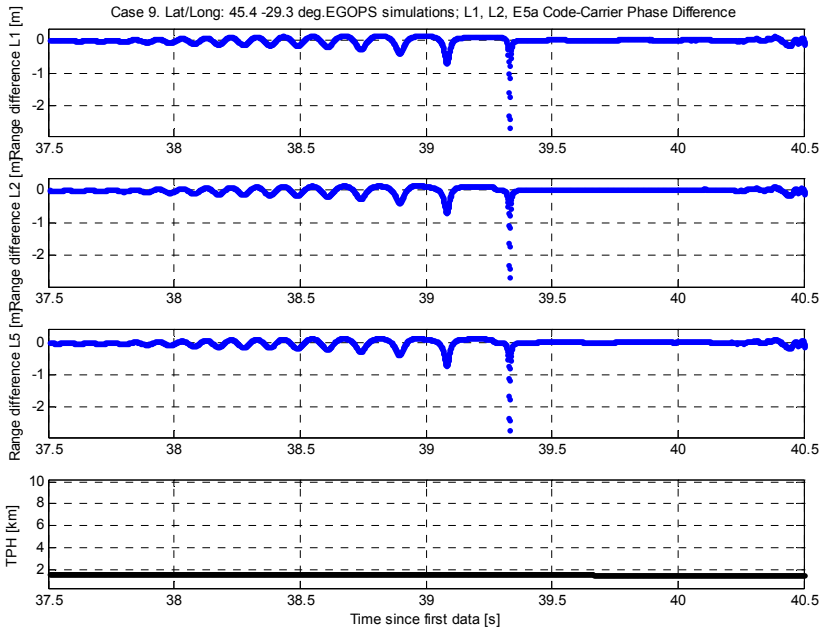

Figure 82 EGOPS Case 9 2:nd simulation. Difference between code and carrier range for L1, L2, L5 and tangent point height, RTH.

The major advantages of using modernized GNSS signals, defined as signals with open codes at three frequencies, are:

- No codeless tracking is required and hence more robust tracking and two signals available at low altitudes.
- Open loop tracking can be used for all signals – no carrier tracking is required (but code tracking is retained).
- E5/L5 is a protected band, less RF interference than in the L2 band can be expected

Apart from the obvious benefit from collecting more signal energy with three signals, there is no indication that tracking should be improved. Figure 83 shows a typical multipath situation, where the nulls of the L2 and L5 signals occur within one milli-second. The L1 signal differs more from L2 or L5 in that the nulls occur in a fraction of a second apart and not necessarily correspond. Mutual aiding between the signal chains can be made with the two signals.

We conclude hence that three frequency tracking has no definite advantage over two frequency tracking. It is, however, worth pointing out that the data is obtained during a period with low ionospheric activity. The presented patterns could differ more with a stronger ionospheric delay.

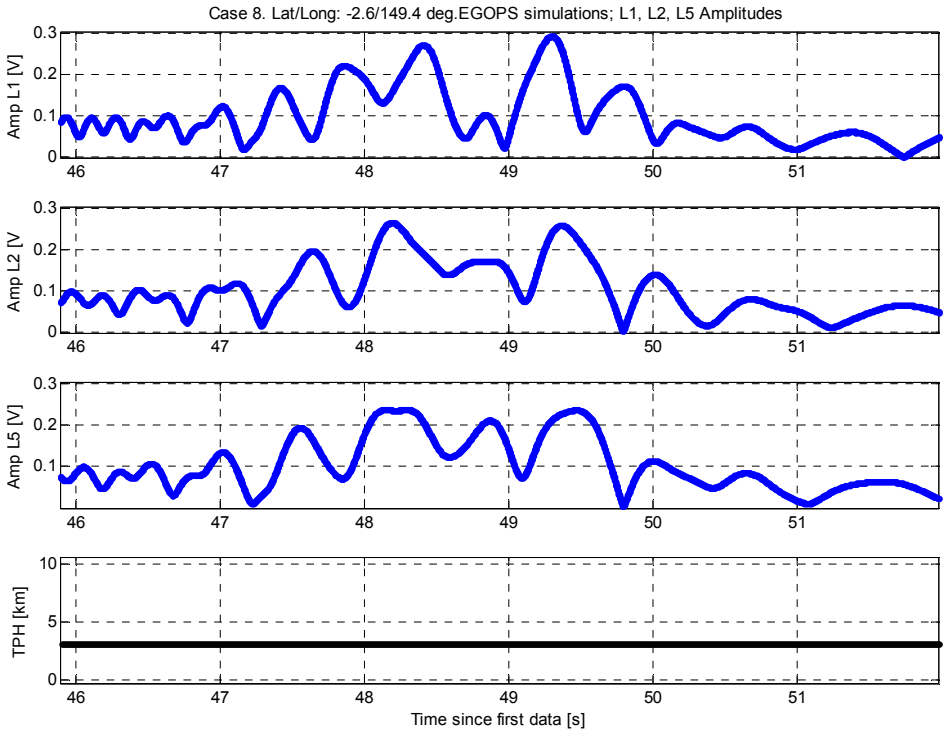

Figure 83 EGOPS Case 8 2:nd simulation. Amplitudes of L1, L2, L5 and tangent point height, RTH.

7 RETRIEVAL PROCESSING

Independent retrieval results from Danish Meteorological Institute (DMI), University of Graz (UoG) in Austria, GFZ in Potsdam (Germany) and EUMETSAT are presented in this section.

This study focuses on the retrieval performance of the GRAS radio occultation measurements when the raw sampling measurements are performed by the GRAS instrument. The period from 30 September 2007 until 31 October 2007 has been selected. During this period the GRAS receiver did perform the radio occultation measurements with the raw measurements also included.

The raw sampling of the L1 signal allows for measurements closer to the surface. Radio occultations are a limb sounding measurement and in particular close to the surface the signal dynamics make the close-loop tracking difficult. Hence raw sampling measurements extend the measured profiles. For NWP users the measurements close to surface are important as the atmosphere is denser.

The processing is performed at DMI, UoG, GFZ and EUMETSAT. The DMI have performed retrievals for the full study period and statistics are presented for both one day and for the full data set (one month). Results are presented as a statistical comparison against the ECMWF model, to show the performance of the radio occultation measurements. The ECMWF is used as a reference for the state of the atmosphere; however deviations may also reflect that the ECMWF does not exactly represent the real atmosphere.

Analysis of individual profiles are also presented, as is done e.g. for the twelve selected study cases.

7.1 DMI Retrieval Processing

Note that references are provided in section 7.1.10.

7.1.1 L1 Preprocessing

The measurements in L1 channel ($f_1 = 1.57542\ \mathrm{GHz}$) are performed in two receiver modes: CL and OL. Closed loop mode is used for tracking signals corresponding to rays with perigee heights above 4–10 km. This height varies for different occultations, it depends upon the region. OL mode is ideal for tracking signals with strong variations of the phase, which are characteristic for the tropospheric propagation.

OL mode is used for ray perigee heights below 4–10 km. The processing of open-loop mode signals requires the navigation bits (NB) removal (wipe-off) and phase re-accumulation. Our procedure follows the guidelines of the navigation bits removal outlined in [**1**, **2**].

When using externally supplied (external or alternative) navigation bits, the standard demodulation procedure is employed. According to the navigation bit states, 0 or 1, we add 0 or π to the excess phase samples, then subtract the phase model, re-accumulate the phase, and add the phase model to restore the phase variation. The phase model used for the phase re-accumulation is based on the MSIS climatology with addition of a simple model of humidity: we assume a constant relative humidity of 90% below a height of 15 km, and humidity is set to 0 above 15 km. If necessary, this model is extrapolated using smoothed measurements of the L1 excess phase. As shown in [**1**], even a rough model of the atmosphere allows for the prediction of the Doppler frequency within 10–15 Hz. This indicates that even for the COSMIC data having the sampling rate of 50 Hz, the ±25 Hz interval around the phase model will cover the spectrum of the signal. For the GRAS data that have a sampling rate of 1000 Hz, even a rougher phase model can be used.

To check the quality of the navigation bits, we apply the correlation approach [**4**] and form the following two functions (normalized derivatives of the phase and navigation bits):

$$F_i^{\varphi} = \left| \frac{\left(\pi + \varphi_{1,i} - \varphi_{1,i-1}\right) \bmod 2\pi - \pi}{\pi} \right|, \qquad (1)$$

$$F_i^{B} = \left| B_i - B_{i-1} \right|,$$

where $\varphi_{1,i}$ are the L1 phases including the navigation bits modulation and B_i are the navigation bits. The first function, F_i^{φ}, visualizes the changes of the navigation bits in the area where the phase variations between samples are significantly smaller than π, and the large phase variations can be attributed to navigation bits changes. The function should equal 1, where the navigation bit sequence switches from 0 to 1 or from 1 to 0, and it equals 0, where navigation bits do not change. The second function, F_i^{B}, has the same property, but it operates on the recorded navigation bits. We compute the following correlation function:

$$C^{B}(\Delta i) = \frac{\left\langle F_i^{\phi} F_{i+\Delta i}^{B} \right\rangle}{\sqrt{\left\langle \left(F_i^{\phi}\right)^2 \right\rangle \left\langle \left(F_{i+\Delta i}^{B}\right)^2 \right\rangle}}, \qquad (2)$$

where averaging is performed with respect to index i over the time interval of 4 seconds below the upper height of the OL mode region. The correlation maximum position is equal to the eventually necessary shift of the navigation bits sequence. Shifting the navigation bits sequence was found necessary for some of COSMIC events. If the maximum correlation is below some specified level (which can be specified by a command-line option, the default value being 0.4), then the internal navigation bits removal [**2**] is activated.

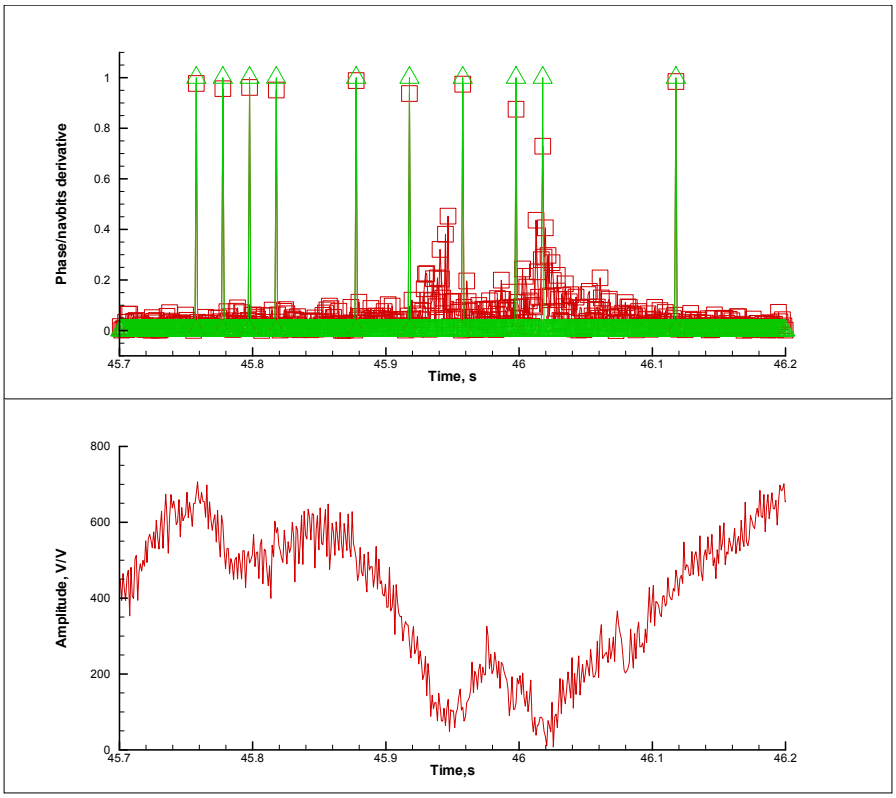

Figure 84. Occultation event at 38.6°S 9.0°W, 2007/09/30, UTC 00:02. Upper panel: normalized derivatives of the phase [radian/sample] (red line) and navigation bits (green line). Lower panel: Signal-to-Noise Ratio (SNR) [Volt/Volt].

The external navigation bits are not always present in the files. This indicates the necessity of an internal navigation bits demodulation procedure. We follow the guidelines laid-out in [**2**], with the modifications necessary for processing 1000 Hz data.

Navigation bits have a frequency of 50 Hz, so we find the samples, between which the GPS time crosses an integer number of 0.02 second periods, and only perform the identification of the navigation bits flips here. We implemented the internal navigations bits removal where they are absent or marked as non-reliable, and use the externally-supplied navigation bits otherwise. The internal navigation bits removal imitates the 2-quadrant detector that is insensitive to navigation bits, but cannot effectively track the signal in presence of severe multipath conditions [**3**]. The internal navigation bits removal consists in a half-cycle re-accumulation of the phase, i.e. in addition of an integer number of half-cycles (π) to the samples of the phase so as to minimize the phase variation between the samples.

In addition to the navigation bits removal, we also apply the half-cycle re-accumulation to L1 phase recorded in the CL mode. There are examples of COSMIC occultations with extra half-cycles between samples in the CL mode (which is equivalent to ±25 Hz addition to the Doppler frequency). The half-cycle phase accumulation treats half cycles as zeros, and restores the corrupted phase.

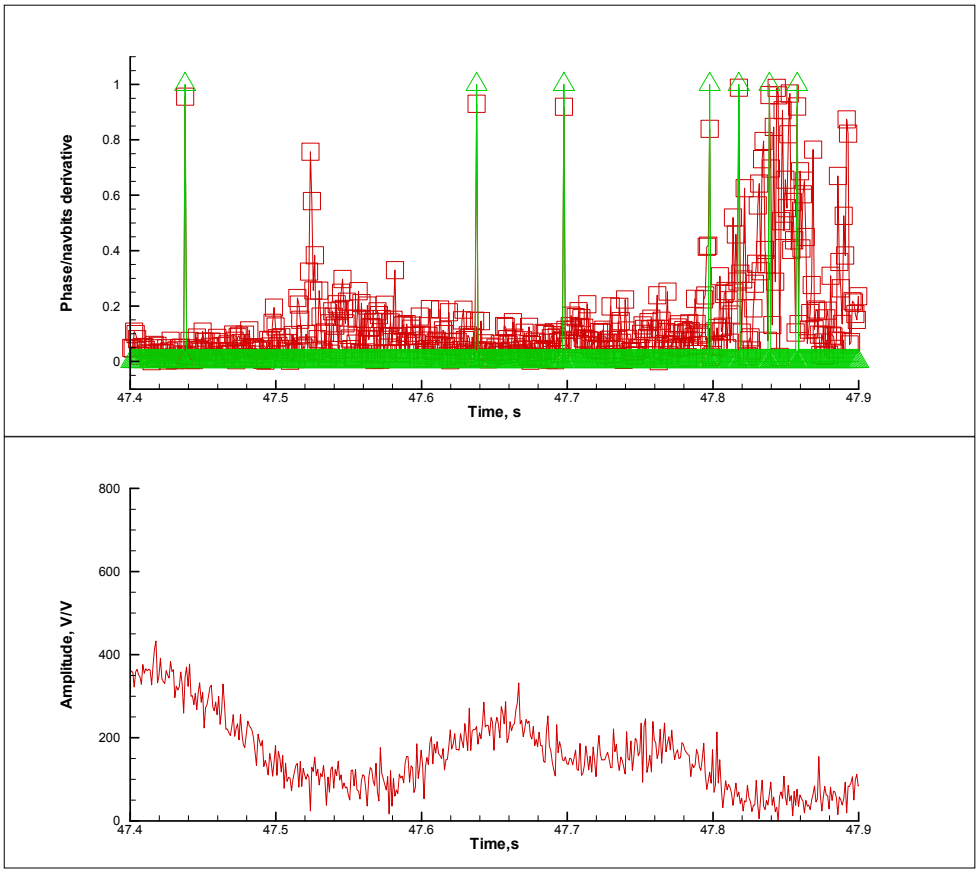

Figure 85. Occultation event at 38.6°S 9.0°W, 2007/09/30, UTC 00:02. Upper panel: normalized derivatives of the phase [radian/sample] (red line) and navigation bits (green line). Lower panel: Signal-to-Noise Ratio (SNR) [Volt/Volt].

Figure 84 and Figure 85 show examples of normalized derivatives of the phase and navigation bits and the corresponding fragment of the amplitude (SNR) record. The correlation between the phase and navigation bits derivatives depends on the amplitude. For high amplitude the correlation is very good. Where the amplitude drops below the level about 200 V/V, the correlation gets poorer, because the relative noise level increases.

The relatively good navigation bit identification also shows in the retrieved refractivities shown in Figure 86, where the comparison between retrieval using internal an external NB is made.

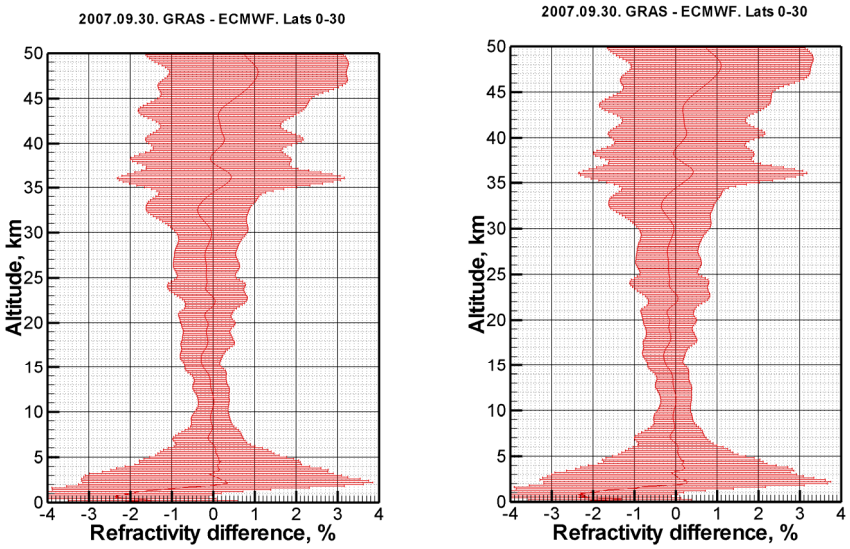

Figure 86. Relative difference of GRAS and ECMWF refractivities, 30 September 2007, tropics (0–30° North + South). Left panel: based on external navigation bits, right panel: based on internal navigation bits from the netCDF input file.

7.1.2 L2 Preprocessing and Quality Control

Processing of L2 (f_2=1.22760 GHz) excess phase is completely different from processing L1 data due to the following reasons: 1) L2 channel is not operated in OL mode. When the receiver switches to the OL mode, there is no L2 data, some rough phase model is substituted instead. 2) L2 data are much noisier than L1 data. We use the following scheme of the noise reduction and extrapolation of L2 data.

L2 amplitude is replaced by the smooth geometric optical (GO) amplitude computed for the MSIS model. This is done for the wave-optical processing of data in the OL mode, where there is no L2 amplitude. L2 data is subjected to the radio holographic (RH) filtering in the time domain as described in [**5**], the L2 excess phase is then pre-filtered with a window 0.25 km. We compute the badness estimate of the L2 signal using the procedure described in [**5**] with some modifications. Using the radio holographic analysis, we retrieve the smoothed profiles of L1/L2 impact parameter $\overline{p}_{1,2}(t)$, bending angle $\overline{\varepsilon}_{1,2}(t)$, corresponding relative Doppler frequency shift $\overline{d}_{1,2}(t)$, excess phase $\overline{S}_{1,2}(t)$, and the impact parameter spectral widths $\delta p_{1,2}(t)$ [**5**]. We form the following L2 badness estimate:

$$Q^{L2}(t) = \left(\frac{\left| \overline{p}_1(t) - \overline{p}_2(t) \right|}{\Delta p_A} + \frac{\delta p_2(t)}{\Delta p_D} \right)^2, \qquad (3)$$

where $\Delta p_A = 0.2$ km and $\Delta p = 0.15$ km (these values were found empirically). The badness parameter penalizes data where L1 and L2 impact parameters diverge too much from each other (this corresponds to lost L2 signal track or missing L2 data) and where L2 signal has a large spectral width (this corresponds to noisy L2 data). The discrepancy between L1 and L2 (here represented by the first term in (3) is also employed in the other RO data processing systems [**6**, **7**]. The L2 cut-off point is defined as the highest point of the CL record where $Q^{L2}(t)$ exceeds some threshold Q_0, but not higher than the point with the straight-line perigee height of 20 km.. The

threshold has a generic empirical value of 15. This value was optimized for processing CHAMP and COSMIC data and it was also found to work well for GRAS instrument.

Below the cut-off point, the L2 data are replaced by extrapolated values. We estimate the ionospheric difference of the bending angles $\Delta\varepsilon_I$ by averaging $\overline{\varepsilon}_2(p)-\overline{\varepsilon}_1(p)$ over the 2 km interval above the cut-off point. The L2 bending angles below the cut-off point are estimated as $\overline{\varepsilon}_1(p)+\Delta\varepsilon_I$, and from them we compute the extrapolated smoothed L2 excess phase $\overline{S}_2^{ext}(t)$. The ionospheric difference of the excess phase is estimated as $\Delta S_I = \overline{S}_2^{ext}(t) - \overline{S}_1(t)$. The corrected L2 excess phase $S_2^{cor}(t)$ below the cut-off point is computed as follows: the finite differences of $S_2^{cor}(t)$ are formed as a linear combination of finite differences of $S_1+\Delta S_I$ and finite differences of S_2 with weights $W(t)$ and $(1-W(t))$, respectively [**5**], where the weighting function $W(t)$ smoothly increases from 0 to 1 in the vicinity of the cut-off point. The L2 amplitude is also multiplied with $(1-W(t))$ and it is used for the determination of the cut-off point within the CT algorithm. In numerical simulations, where we added random noise to the simulated RO data and deleted L2 signal below the height of 11 km, we found that this extrapolation procedure did not introduce any significant error or biases.

7.1.3 Wave Optical Retrieval of Bending Angles

Our wave optical (WO) retrieval of bending angles has three choices: Back Propagation (BP) [**9**], Canonical Transform of the 1st type (CT) applied after BP [**10**], and Canonical Transform of the 2nd type (CT2) applied directly to the measurements of the complex field along the LEO orbit [**11**]. The latter method combines the numerical efficiency of the Full-Spectrum Inversion (FSI) method [**12**] and the high accuracy approaching that of the Phase Matching (PM) method [**13**], which provides the most accurate solution. CT2 is our method of choice and it is applied in this study. WO processing is activated below some height specified by a command-line option. In this study, the height equals 25 km. The GO profiles above this height and WO profiles below this height are merged into a single profile. It was found that for all instruments (Microlab-1, CHAMP, COSMIC, and GRAS) GO and WO profiles at this height can be seamlessly integrated.

The core of the CT2 approach is a transform of the measured complex wave field into the representation of the impact parameter, which is implemented by a Fourier Integral Operator (FIO) of the second kind:

$$\hat{\Phi}_2 u(\tilde{p}) = \sqrt{\frac{-ik}{2\pi}} \int a_2(p,t)\exp\left(ikS_2(p,t)\right)u(t)\,dt, \qquad (4)$$

where $u(t)$ is the measured complex wave field, $S_2(p,t)$ is the phase function, $a_2(p,t)$ is the amplitude function, or the symbol of the FIO, and $\hat{\Phi}_2 u(\tilde{p})$ is the wave field in the transformed space.

The exact expressions for the amplitude and phase functions were established in the framework of the PM method [**11**, **13**]. However, the exact operator defies a fast numerical implementation. To reduce the FIO to a composition of a Fourier transform, a non-linear scaling of the coordinate and the superimposing of a phase model, we introduce the representation of the approximate impact parameter. For this purpose, we introduce a smooth model of ray structure without multi-path propagation and linearize the expression for the impact parameter as follows:

$$\tilde{p}(t,\sigma) = p_0(t) + \frac{\partial p_0}{\partial \sigma}\left(\sigma - \sigma_0(t)\right) = f(t) + \frac{\partial p_0}{\partial \sigma}\sigma,$$
$$f(t) = p_0(t) - \left.\frac{\partial p_0}{\partial \sigma}\right|_{\sigma=\sigma_0(t)} \sigma_0(t), \tag{5}$$

where $\tilde{p}(t,\sigma)$ is the approximate impact parameter, $\sigma = d\Psi/dt$ is the momentum corresponding to wave field $u(t) = A(t)\exp\left(ik\Psi(t)\right)$, $\sigma_0(t)$ is a smooth model of the phase, and $p_0(t) = p\left(t,\sigma_0(t)\right)$ is the impact parameter computed for the smooth model of the ray manifold. We introduce a new coordinate Y instead of time and the corresponding momentum η as follows:

$$dY = \left(\frac{\partial p_0}{\partial \sigma}\right)^{-1} dt = \frac{\partial \sigma}{\partial p_0} dt,$$
$$\eta = \frac{\partial p_0}{\partial \sigma}\sigma. \tag{6}$$

The canonical transform from (Y,η) to $(\tilde{p},\xi)$, where ξ is the new momentum, can be written in the following form:

$$\tilde{p} = f(Y) + \eta,$$
$$\xi = -Y, \tag{7}$$

where $f(Y) \equiv f\left(t(Y)\right)$. The corresponding phase function can the be written as the sum of a bi-linear term and a phase model being a function of Y:

$$S_2(\tilde{p},Y) = -\tilde{p}Y + \int_0^Y f(Y')dY', \tag{8}$$

and $f(t)$ evaluates as follows:

$$f(t) = p_0 - \left(\dot{\theta} - \frac{\dot{r}_G}{r_G}\frac{p_0}{\sqrt{r_G^2 - p_0^2}} - \frac{\dot{r}_L}{r_L}\frac{p_0}{\sqrt{r_L^2 - p_0^2}}\right)^{-1} \sigma_0. \tag{9}$$

The corresponding amplitude function reads [**11**]:

$$a_2(\tilde{p},Y) = \left(\sqrt{r_L^2 - \tilde{p}^2}\sqrt{r_G^2 - \tilde{p}^2}\left\{\frac{r_L r_G \sin\theta}{\tilde{p}}\right\}_{3D}\right)^{1/2}. \tag{10}$$

Finally, we arrive at the following expression for the FIO projecting the measured wave field into the representation of the approximate impact parameter:

$$\hat{\Phi}_2 u(\tilde{p}) = \sqrt{\frac{-ik}{2\pi}}\, a_2\left(\tilde{p},Y_s(\tilde{p})\right)\int \exp(-ik\tilde{p}Y)\exp\left(ik\int_0^Y f(Y')dY'\right)u(Y)\,dY, \tag{11}$$

where $u(Y)$ is understood as $u\left(t(Y)\right)$. We replaced $a_2(\tilde{p},Y)$ by its value $a_2\left(\tilde{p},Y_s(\tilde{p})\right)$ at the stationary point $Y_s(\tilde{p})$ and factored it out from within the integral. Function $Y_s(\tilde{p})$ equals $-\xi(\tilde{p})$, where momentum $\xi(\tilde{p})$ is defined as the derivative of the eikonal of the field $\hat{\Phi}_2 u(\tilde{p})$ in the transformed space. For the computation of the eikonal we first substitute $a_2 \equiv 1$ and evaluate the integral, then evaluate $a_2\left(\tilde{p},Y_s(\tilde{p})\right)$ and multiply the transformed field with it. The bending angle as a function of p is determined from the following relation:

$$\varepsilon(p) = \theta\left(t\left(Y_s(p)\right)\right) - \arccos\frac{p}{r_G\left(t\left(Y_s(p)\right)\right)} - \arccos\frac{p}{r_L\left(t\left(Y_s(p)\right)\right)}. \quad (12)$$

where the satellite radii r_G, r_L (in the system of the Earth's local curvature centre) and the satellite-to-satellite angle θ are functions of time t, which can be expressed as a function of Y from (6). Expression (11) allows for a fast numerical implementation based on the FFT.

Our WO processing includes the RH filtering in the impact parameter domain [**5**]. After the RH filtering the cut-off height is determined from the CT amplitude. For this purpose we determine the maximum of the correlation of the CT amplitude with the step function. RH filtering makes this procedure more stable and improves the quality of the shadow border determination. In the L2 channel, the cut-off height determined from the L2 CT amplitude corresponds to the L2 cut-off height defined above. Below the L2 cut-off height, the L2 CT bending angle is extrapolated in the same way as in GO processing.

If one of the WO processing options is activated, the bending angles from GO processing and from WO processing steps are merged as discussed above, producing profiles of L1 and L2 bending angles $\varepsilon_{1,2}(p)$. In the framework of WO processing, we also compute the RH error variances $\left\langle \left(\delta\varepsilon_1^{WO}(p)\right)^2 \right\rangle$ of the bending angles.

7.1.4 Ionospheric Correction and Noise Reduction

The ionospheric correction and noise reduction follows the Optimal Linear Combination (OLC) technique described by [**14**]. The computation of the background profile of bending angle has the following options: 1) bending angles computed by Abel integral from the local refractivity profile from MSIS climatology, 2) global search of MSIS bending angle profile [**15**] (initially suggested by Stig Syndergaard, 1999), and 3) bending angles obtained by Abel integral from the local refractivity profile extracted from global fields of analyses of ECMWF or NCEP in the GRIB format.

7.1.5 Inversion of Bending Angles

The retrieval of refractivity and dry temperatures follows the standard procedure based on the Abel inversion. Using the error variance of the bending angle, we also retrieve the error variances of refractivity and dry temperature [**17**].

7.1.6 Processing of CL+OL Data

The results presented in this draft report so far include the processed data by the OCC code implementation.

In the processing of GRAS data we observe all the typical features that we can also see in COSMIC data: multipath structures and reflected rays.

Below we present diagnostic plots for selected cases. The plots have 9 panels organized as table with 3 rows and 3 columns, which legend is explained in APPENDIX B, where the 12 study cases listed in Table 3 are also analysed.

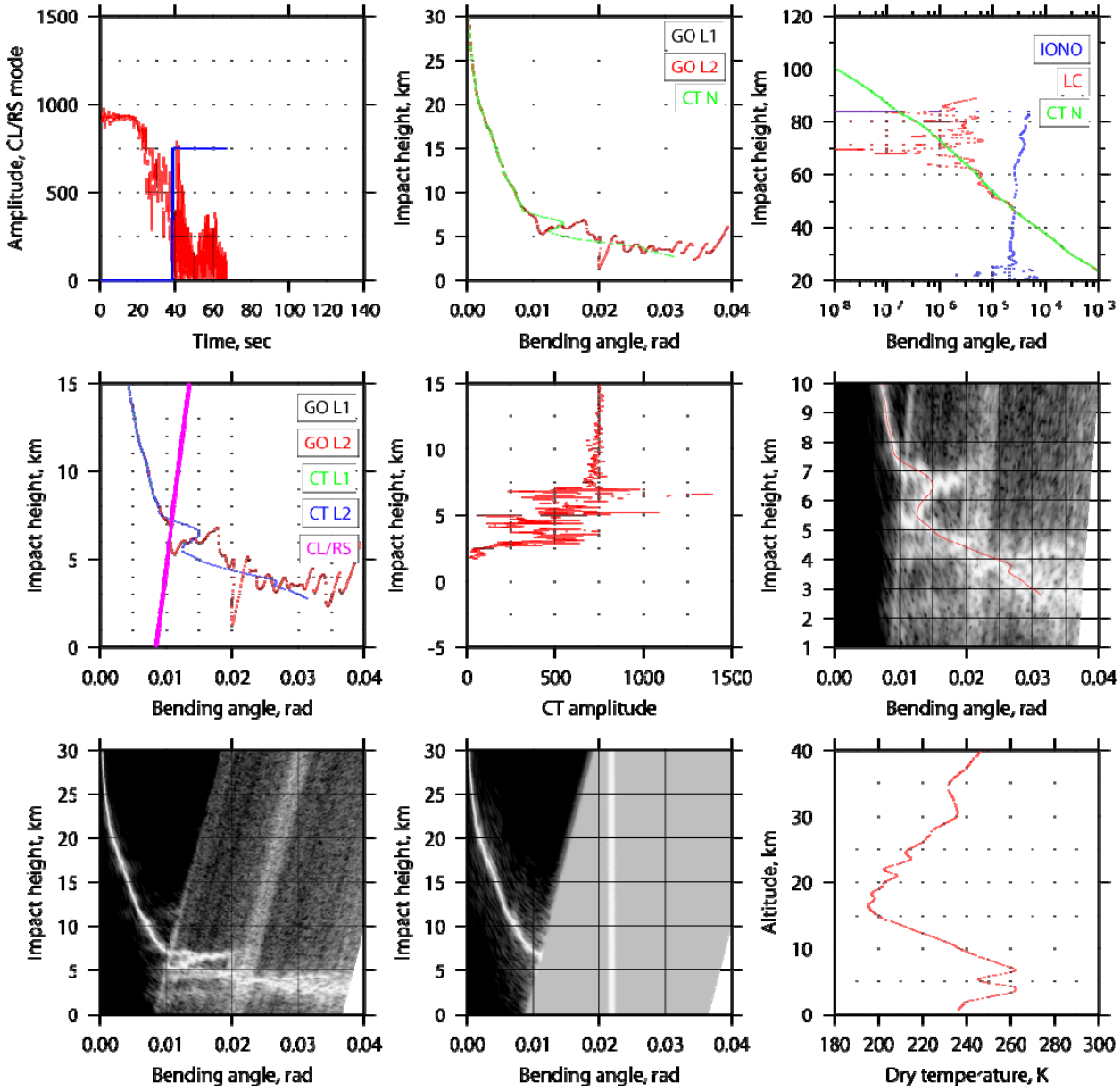

Figure 87 Occultation event observed on 2007/09/30 at UTC 00:12, 4.7°S 25.3°W, badness score 28.102. This is an example of a tropical event with a pronounced multipath structure.

Figure 87 shows an example of a tropical occultation with a pronounced multipath structure. The interfering rays are observed in the impact parameter range of 5–7 km. The CT amplitude indicates strong scintillations which are typical for a turbulent atmosphere. The multipath structure must originate from a strong humidity layer located at a height of 5 km. This is a setting event. The receiver switched to the OL mode at a height of 7 km.

The 12 study cases listed in Table 3 are presented in Appendix B.

7.1.7 FSI Used to Process the GRAS Radio Occultation Data

The FSI radio occultation retrieval chain used to process the GRAS radio occultation data consist of the following main processing steps. Each of these steps is important for the final results.

1) The open and closed loop data records found in a NetCDF file must first be merged into a common data file. Michael Gorbunov has merged the closed and open loop part of the measurement and saved the result in an ASCII file. We will in the 12 case examples show plots of the amplitude and phases as a function of the time for the 2 frequencies.

2) Low pass filtering of the radio occultation data is needed before it can be feed to the FSI algorithm. A FIR filter of order 20 and with an effective zero phase response has been used.

3) The FSI algorithm is applied to each of the 2 complex fields expressed in amplitudes and phases. The FSI then delivers bending angle and transmission profiles as a function of impact parameter for the L1 and L2 frequencies. When FSI is used, the transmission can be calculated as the amplitude of the Fourier transformed field. This amplitude must then be corrected by the electromagnetic field found in a vacuum. We will in the 12 case examples show plots of bending angle and transmission as a function of the height for the 2 frequencies.

4) The L2 radio occultation signal often stops before the L1 signal. The bending angle for the L2 signal will therefore stop at a higher height, called the cut point height for L2, than the corresponding L1 bending angle. Extrapolation of the L2 bending angle is therefore needed. The difference between the L2 and L1 bending angles are calculated from the cut height and 5 km up. A first order polynomial is fitted to these differences and the L2 bending angle below the cut height is calculated by adding the L1 bending angle to an extrapolated value of the bending angle difference. This extrapolated value is calculated from the first order polynomial. The corresponding L2 profile is called the corrected L2 bending angle. If the difference between the L1 and L2 bending angles exceed a certain threshold value from a certain height, this height would then be selected as the cut point.

5) An ionospheric corrected bending angle is calculated from the L1 and L2 bending angles with the use of the following equation

$$\alpha_{LC}(a) = \frac{f_1^2 \alpha_1(a) - f_2^2 \alpha_2(a)}{f_1^2 - f_2^2} \tag{13}$$

where $\alpha_1(a)$ is the bending angle of the signal with frequency f_1 and $\alpha_2(a)$ is the bending angle of the signal with frequency f_2. Both of the bending angles are functions of the impact parameter a. We will in the 12 case examples show plots of the extrapolated L1 and L2 bending angles together with the ionospheric corrected LC bending angle. The L1 and L2 bending angles calculated using geometric optics will also be shown as a reference.

6) Statistical optimization is applied on the ionospheric corrected bending angle. The bending angle will in the neutral in the atmosphere decreases exponentially as function of height. When the bending angle becomes dominated by noise terms then the bending angle must be extrapolated. The noise on the measured bending angle is obtained by the linear deviation from a model bending angle α_m and the expected magnitude of climatological variations of 20% on the signal. This defines σ_{noise} and σ_{signal} as,

$$\sigma_{noise} = \alpha - \alpha_m \quad \text{and} \quad \sigma_{\text{signal}} = 0.2\alpha_m \tag{14}$$

Statistical optimization is implemented applying a smooth transition from real measured data to model data by the weighting coefficient *C*, defined as,

$$C = \frac{1}{1 + |\frac{\sigma_{noise}}{\sigma_{signal}}|} \tag{15}$$

The new bending angle α_{stat} is now computed by the following expression,

$$\alpha_{stat} = \alpha_m + C\sigma_{noise} \tag{16}$$

At initial heights of 100 km the noise dominates completely over the signal, $C \approx 0$ and the bending angle α_{stat} equals the model α_m . As the occultation descends through the neutral atmosphere the noise terms decrease with respect to the signal, $C \rightarrow 1$ hence $\alpha_{stat} \rightarrow \alpha$. Bellow a certain height (determined by the level of noise on the signal) statistical optimization is deactivated and only the measured bending angle α is used to compute the temperature profile.

To constrain the statistical optimization we have used a modified version of the MSIS90 atmosphere model which equals a 1D approximation of the neutral atmosphere. To assign the correct model bending angle to the real data, the model bending angle is adjusted to match the true bending angle profile for the height limit of 25 km up to approximately 35 km. The model bending angle is re-scaled by computing a χ^2 fit to the measured bending weighted according to noise as in the equation above.

7) The refractivity can now be calculated as a function of height from the ionospheric corrected bending angle with the use of the Abel transform. The ionospheric index of refraction μ_i can be found from the Abel transform [Fjeldbo] and [MEL94] assuming spherical symmetry.

$$\mu_i(a) = \exp\left(\frac{1}{\pi}\int_a^\infty \frac{\alpha(x)dx}{\sqrt{x^2 - a^2}}\right) \tag{17}$$

The refractivity *N* as a function of height *h* can be found by combining the following equations.

$$N = (\mu_i - 1)10^6, \quad h = \frac{a}{\mu_i(a)} - R_{curve} \tag{18}$$

where R_{curve} is the curvature radius of the Earth at the tangent point.

8) The pressure and dry temperature are finally calculated using the standard equations. We will in the 12 case examples show plots of the retrieved refractivity, pressure and temperature as a function of height.

7.1.7.1 Examples of the FSI processing

The FSI retrieval chain has been applied to the 12 challenging cases selected by RUAG Space. In the following pages we present the results for two of these cases. The first case is the ocean reflection case. The two figures below show the amplitude and phase for the two frequencies as a function of time. The next figure show the positions of the GPS (red circles) and LEO (blue circles) during the radio occultation event. It is seen from the first plot that the radio occultation signal for the L2 signal stops after approximately 65 seconds.

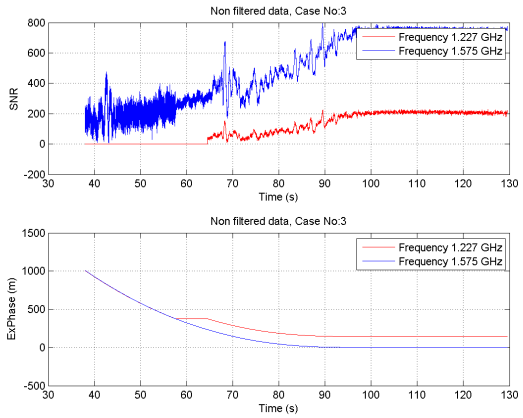

Figure 88 The plots picture shows the amplitude and phase for the L1 and L2 frequencies as a function of time.

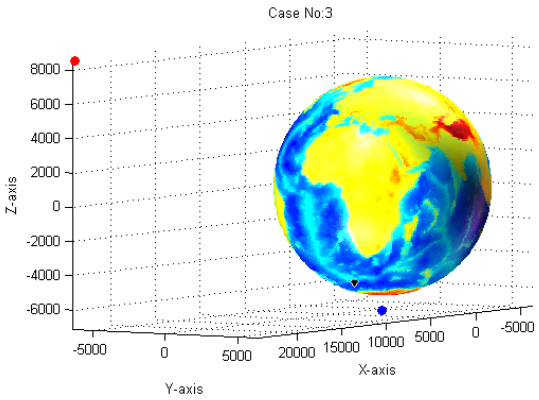

Figure 89 Satellite positions for the transmitting GPS (red circles) and receiving (blue circles) LEO satellite. It is a raising radio occultation. The black diamond show the location of the mean tangent point. The latitude and longitude for the mean tangent point is -56.51 degrees and 3.51 degrees respectively.

The short time Fourier transform has been applied to the radio occultation signals for the L1 and L2 frequencies. The figures below show the corresponding results. The figure for the L1 case show clear signs of ocean surface reflections. The figure above also confirms that the radio occultation event is indeed taking place over the southern ocean.

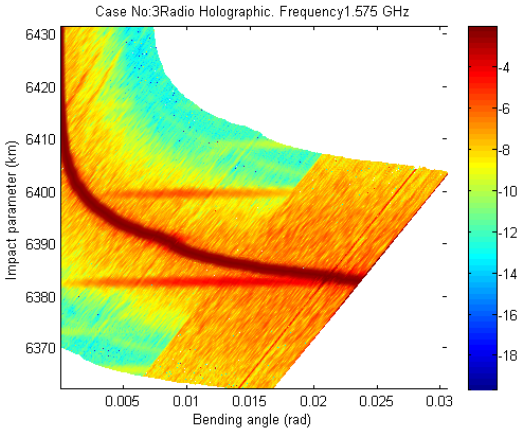

Figure 90 Bending angle versus impact parameter calculated using short time Fourier transformation. The radio wave frequency is 1.575 GHz.

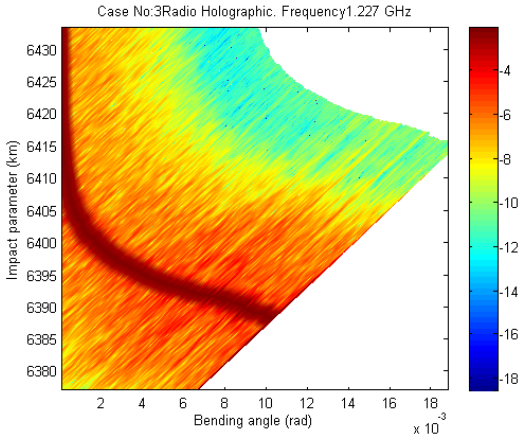

Figure 91 Bending angle versus impact parameter calculated using short time Fourier transformation. The radio wave frequency is 1.227 GHz.

The two figures below show plots of bending angle and transmission as a function of the height for the 2 frequencies. These profiles are direct outputs of the FSI routine. The FSI has no problem (as it can be seen from the figures) processing this event with ocean surface reflections this is because the frequencies of the surface reflections are not close to the frequencies of the radio occultation signal.

The two figures below show plots of bending angle and transmission as a function of the height for the 2 frequencies. These profiles are direct outputs of the FSI routine. The FSI has no problem (as it can be seen from the figures) processing this event with ocean surface reflections this is because the frequencies of the surface reflections are not close to the frequencies of the radio occultation signal.

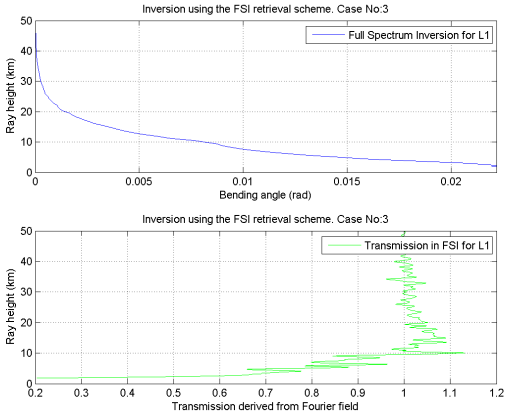

Figure 92 Bending angle and transmission versus ray height calculated using FSI. The radio wave frequency is 1.1575 GHz.

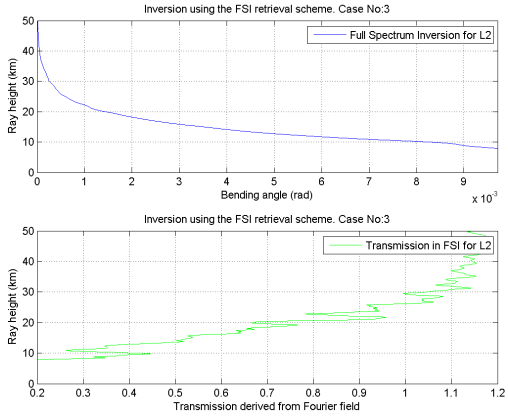

Figure 93 Bending angle and transmission versus impact parameter calculated using FSI. The radio wave frequency is 1.227 GHz.

The extrapolated bending angle profiles for L1, L2 and LC are shown in the lower part of the left panel plots. The upper part of the panel show L1 and L2 bending angle profiles calculated with the use of geometric optics. The right panel show plots of the retrieved refractivity, pressure and temperature as a function of height.

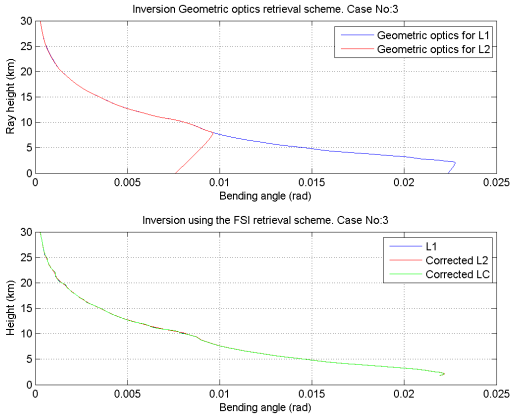

Figure 94 Top graph: Bending angle versus ray height for the L1 and L2 frequencies calculated using Geometric optics. Bottom graph: Bending angle versus ray height for the L1, L2 and LC calculated using FSI and extrapolated to same height interval.

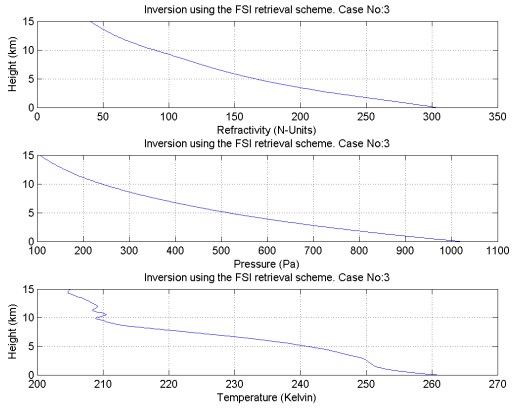

Figure 95 Refractivity, pressure and temperature versus height calculated using FSI.

The second case is the long fade case. The two figures below show the amplitude and phase for the two frequencies as a function of time. The next figure show the positions of the GPS (red circles) and LEO (blue circles) during the radio occultation event. It is seen from the amplitudes of the radio occultation signals that the noise level for this case is relatively high.

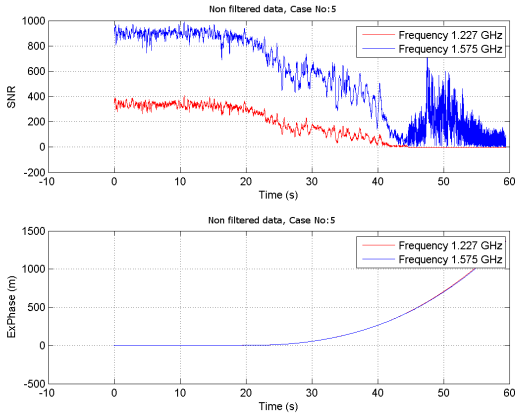

Figure 96 The plots picture shows the amplitude and phase for the L1 and L2 frequencies as a function of time.

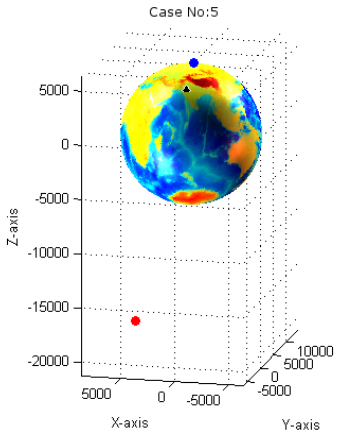

Figure 97 Satellite positions for the transmitting GPS (red circles) and receiving (blue circles) LEO satellite. It is a setting radio occultation. The black diamond shows the location of the mean tangent point. The latitude and longitude for the mean tangent point is 24.14degrees and -45.91 degrees respectively.

The short time Fourier transform has been applied to the radio occultation signals for the L1 and L2 frequencies. The figures below show the corresponding results.

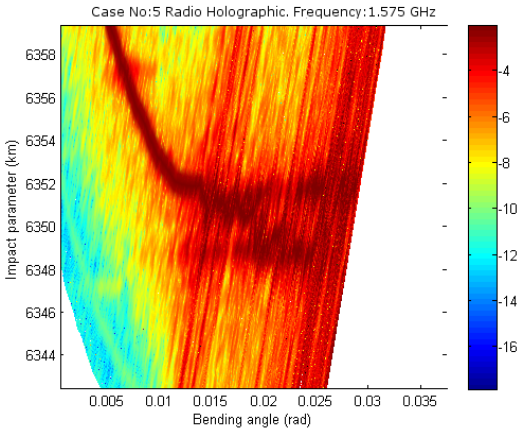

Figure 98 Bending angle versus impact parameter calculated using short time Fourier transformation. The radio wave frequency is 1.1575 GHz.

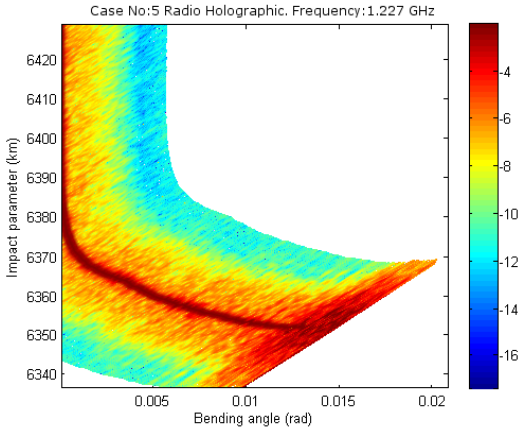

Figure 99 Bending angle versus impact parameter calculated using short time Fourier transformation. The radio wave frequency is 1.227 GHz.

The two figures below show plots of bending angle and transmission as a function of the height for the 2 frequencies. These profiles are direct outputs of the FSI routine. It is seen from these figures that there is a very strong spike in the L1 bending angle profile at ray height at around 5 km.

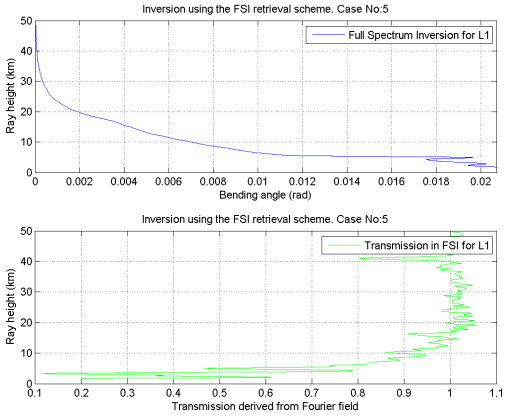

Figure 100 Bending angle and transmission versus ray height calculated using FSI. The radio wave frequency is 1.1575 GHz.

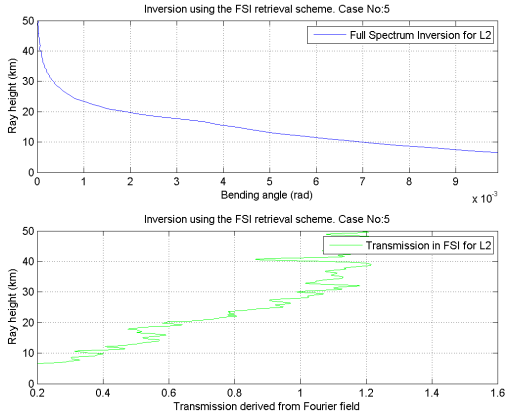

Figure 101 Bending angle and transmission versus impact parameter calculated using FSI. The radio wave frequency is 1.227 GHz.

The extrapolated bending angle profiles for L1, L2 and LC are shown in the lower part of the left panel plots. The upper part of the panel show L1 and L2 bending angle profiles calculated with the use of geometric optics. The right panel show plots of the retrieved refractivity, pressure and temperature as a function of height.

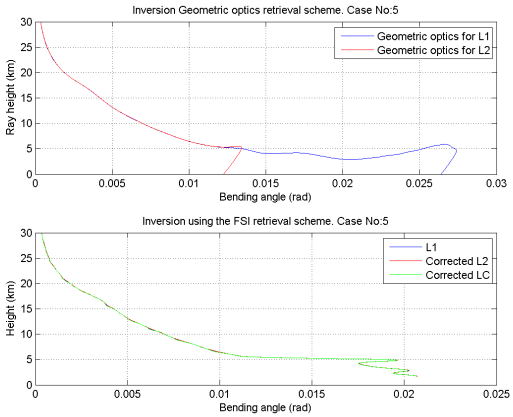

Figure 102 Top graph: Bending angle versus ray height for the L1 and L2 frequencies calculated using Geometric optics. Bottom graph: Bending angle versus ray height for the L1, L2 and LC calculated using FSI and extrapolated to same height interval.

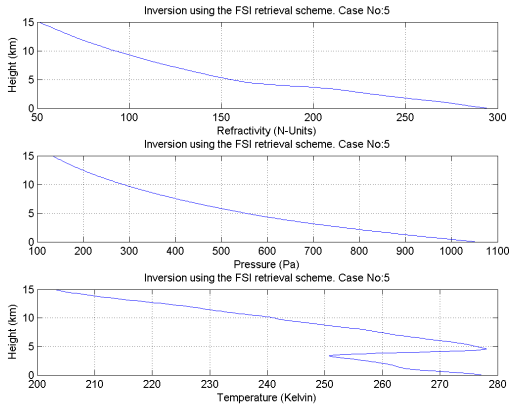

Figure 103 Refractivity, pressure and temperature versus height calculated using FSI.

The statistics based on one day of processing with the FSI retrieval chain can be found in APPENDIX C.

7.1.8 Statistical comparison of CL+OL Data with ECMWF

The main result of the comparison of all processed occultations against ECMWF is presented here. The period covering October 2007 including 30 September 2007 is analyzed. The statistics are divided into setting and rising occultations. All results here are processed using the OCC retrieval software as described above.

7.1.8.1 Statistics on Penetration

Setting

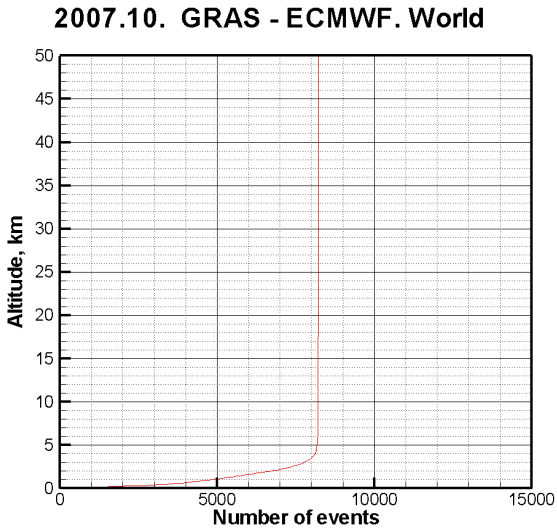

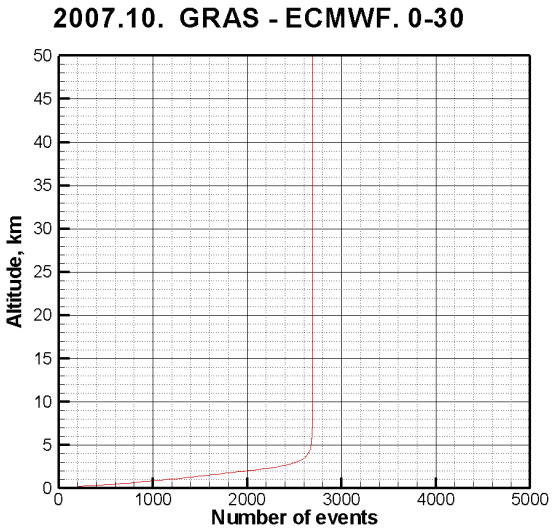

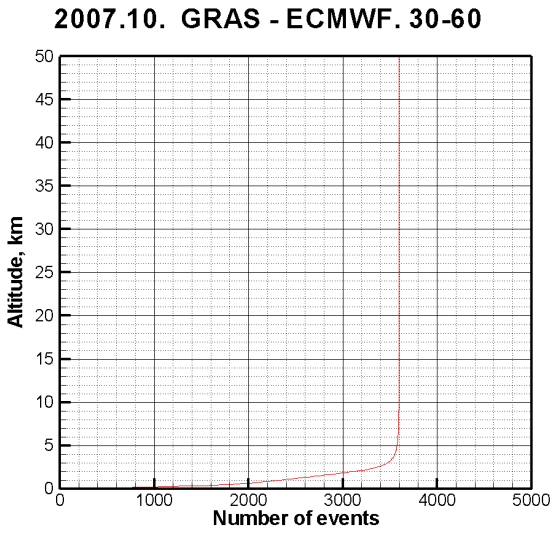

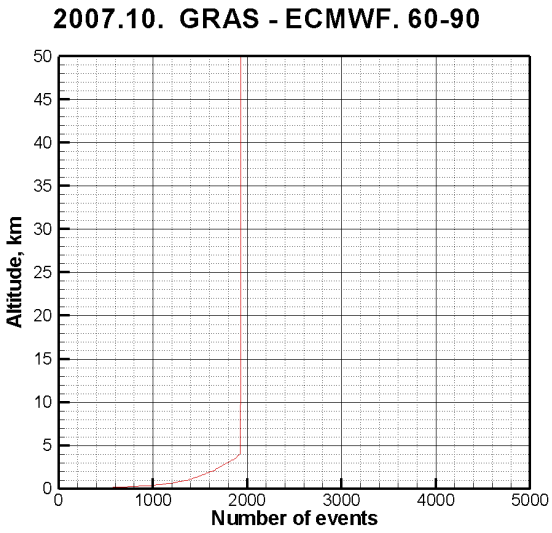

Rising

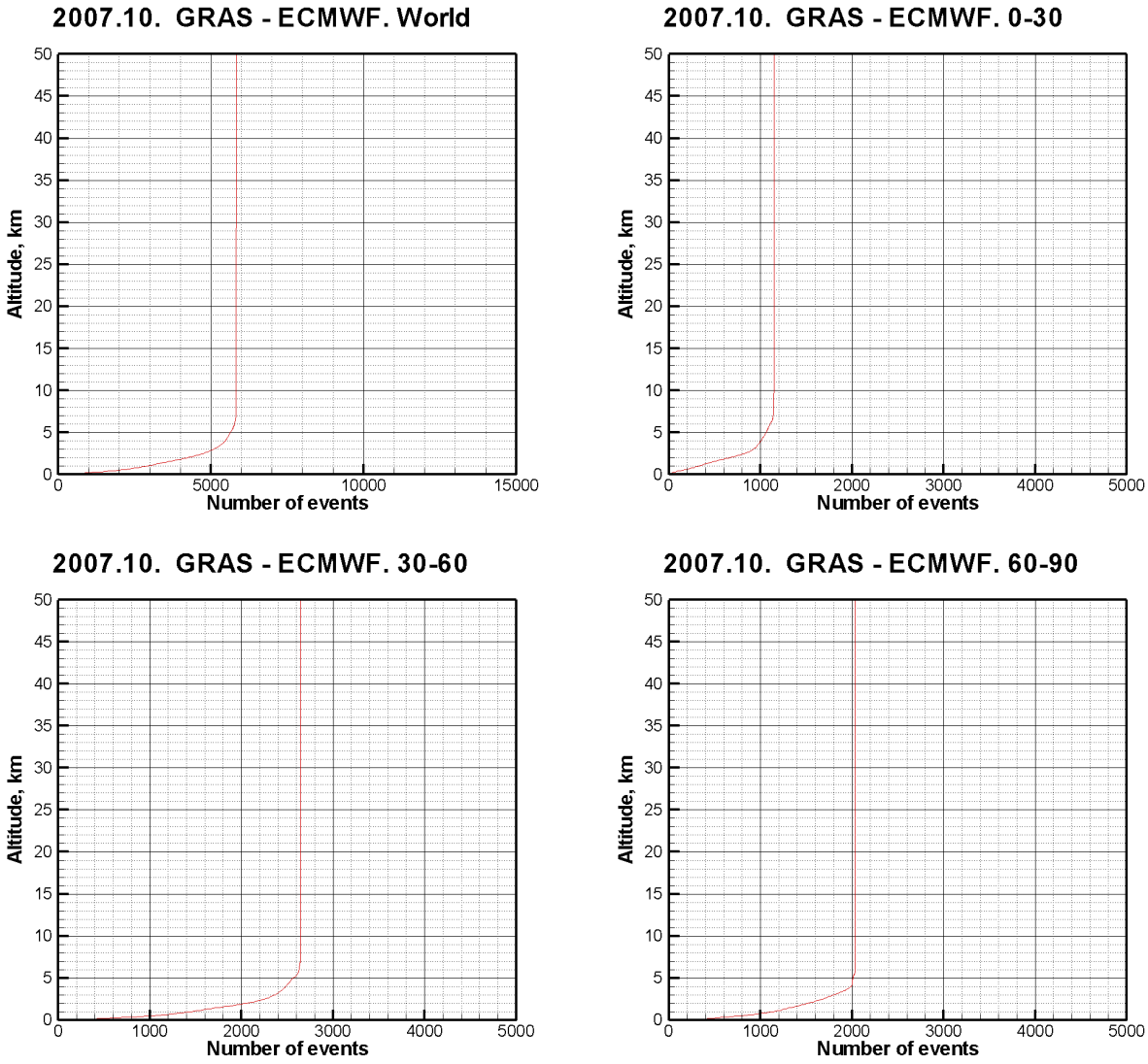

Figure 104. . Numbers of GRAS (CL+OL) events for different height levels, 1–27 October 2007, separated into setting and rising. Upper left panel: world, upper right panel: tropics (0–30° North + South), lower left panel: middle latitudes (30–60° North + South), lower right panel: polar latitudes (60–90° North + South).

7.1.8.2 Statistics on Bending Angle Retrieval

Setting

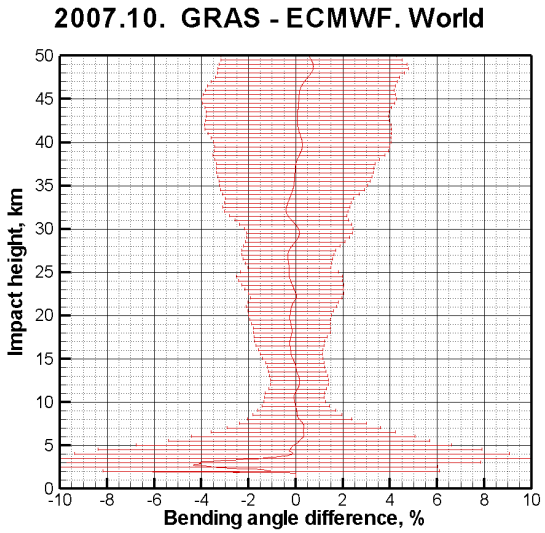

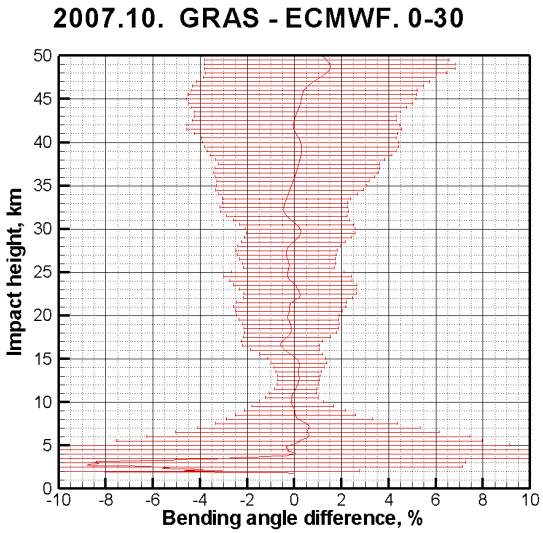

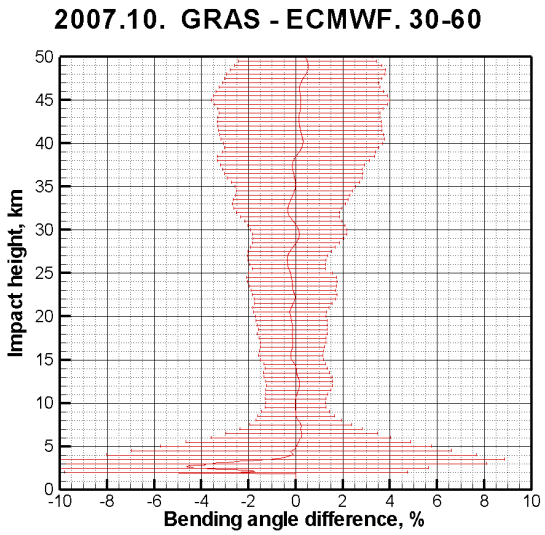

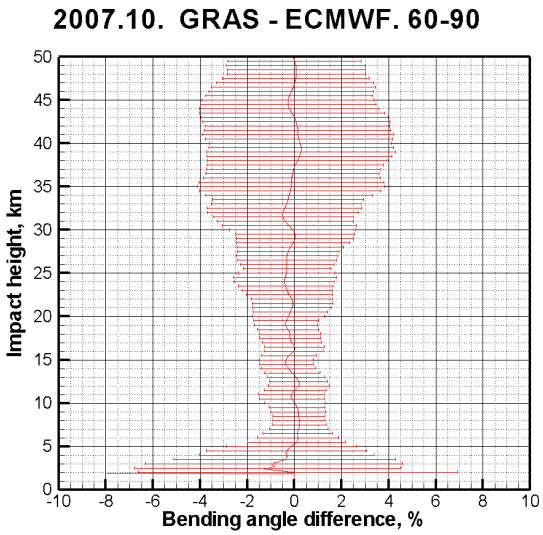

Rising

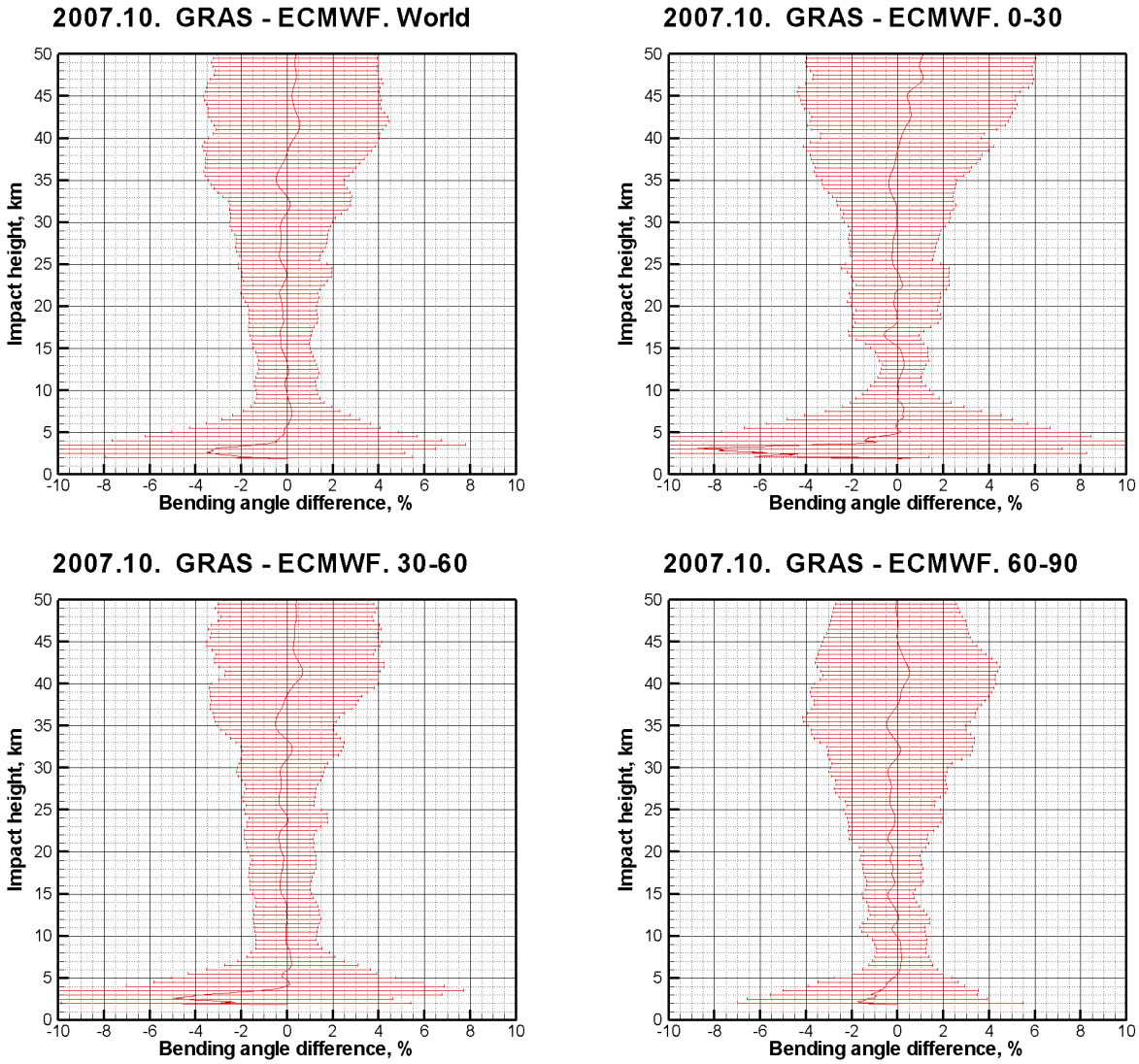

Figure 105. Relative difference of GRAS (CL+OL) and ECMWF bending angles, 1–27 October 2007, separated into setting and rising. Upper left panel: world, upper right panel: tropics (0–30° North + South), lower left panel: middle latitudes (30–60° North + South), lower right panel: polar latitudes (60–90° North + South).

7.1.8.3 Statistics on Refractivity Retrieval

Setting

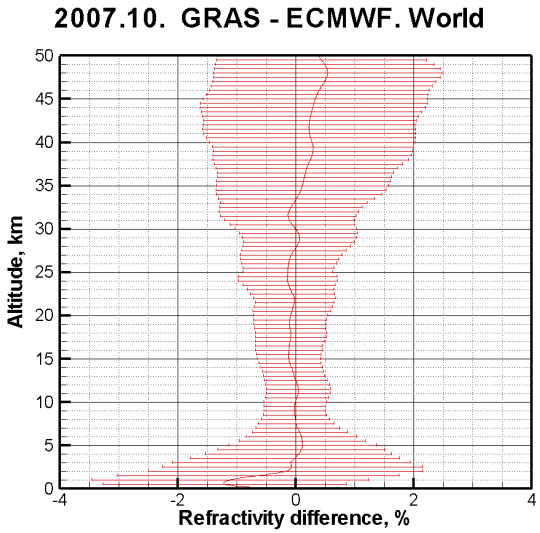

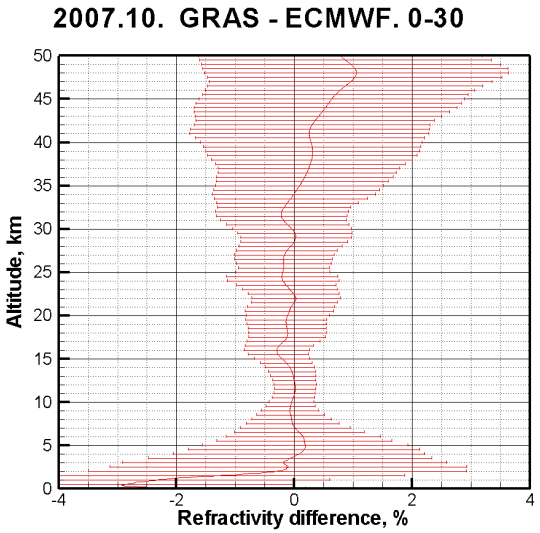

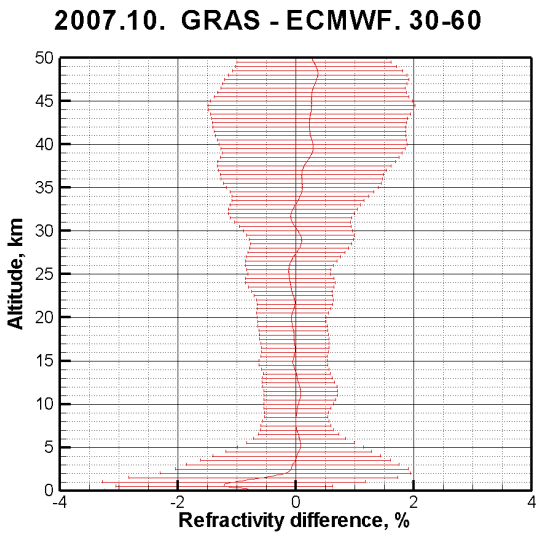

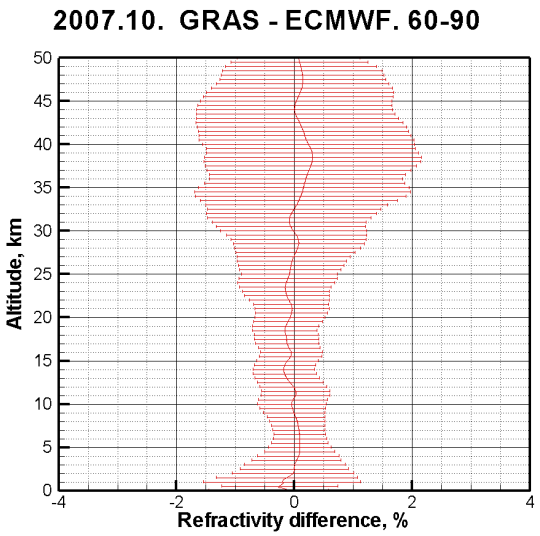

Rising

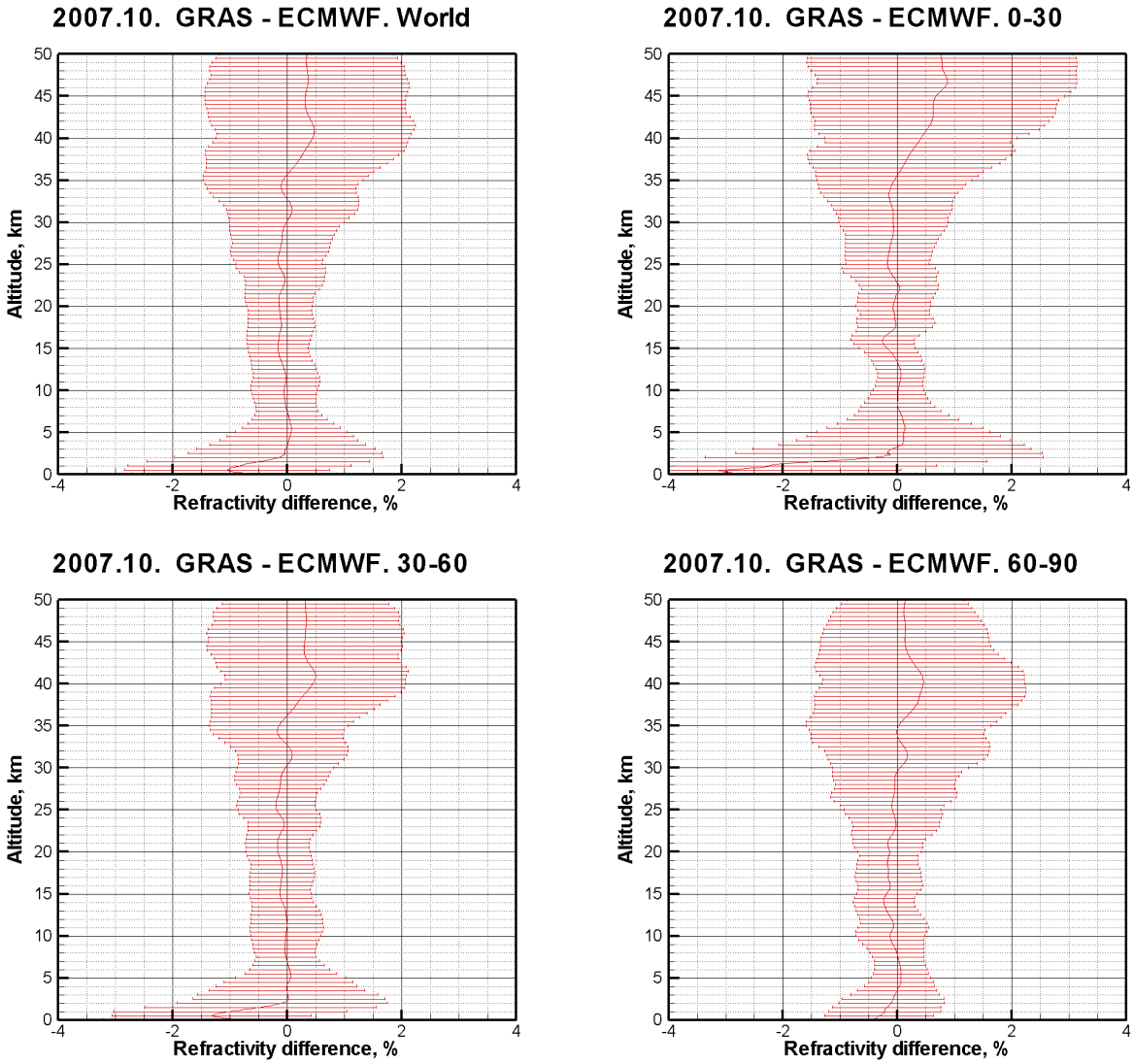

Figure 106. Relative difference of GRAS (CL) and ECMWF refractivities, 1–27 October 2007, separated into setting and rising. Upper left panel: world, upper right panel: tropics (0–30° North + South), lower left panel: middle latitudes (30–60° North + South), lower right panel: polar latitudes (60–90° North + South).

7.1.9 Conclusions

7.1.9.1 Recommended Baseline for GRAS Open Loop Data Processing

Based on this study as well as on the previous experience of processing open loop data from the COSMIC mission, we recommend the following updated baseline for processing GRAS open loop data. A system of RS data processing should include the following modules:

1. **Visualization of radio-holographic spectra, which is useful for the data diagnostics.**
   This proves to be very useful for selected cases studies and can be use to analyze individual profiles. The visualization tool is not necessary for the data processing.
2. **Reading and preprocessing of original data files with options that allow different modes of merging CL and RS data and choice of different navigation bits removal modes.**
   In particular, we found that the use of internal navigation bits (NB) does not significantly change the statistical comparison against ECMWF, as compared to the use of external navigation bits (see Figure 86).

   Even though the results show that NBs obtained from the 1000 Hz signal yields results similar to those obtained from external NBs some comments are relevant. As discussed, GRAS signals do not penetrate far into the shadow zone, thus parts of the signals where we can expect correct NBs to be important are not present. The data gaps also mean that some of the occultations do not extend as far down as they could, and a similar comment may apply here. Examining spectra for individual profiles it is also possible to see small improvements when using external NBs compared to internal ones.
3. **Identify data with degraded L2 quality. Quality control for the specific instrument that can identify degraded L2 data and exclude them from the further processing;**
   It is beneficial to include a quality control related to the quality of the L2 signal. This can be done in different ways (and is done in different ways by different processing centers). In this study we define the quality as discussed in chapter 7.1.2 (i.e. from the noise on the L2 signal and from the deviations of impact parameters obtained from the L1 and L2 signals).
4. **Use retrieval of bending angles based on Fourier integral operators (also sometimes referred to as "wave optics" methods).**
   Any of the existing algorithms, including Canonical Transform (CT), Full-Spectrum Inversion (FSI), Canonical Transform of 2nd kind (CT2), and Phase Matching (PM) can be used. All these algorithms are expected to give similar results. However, results will depend on screening of input data, choice of cut-off of output data, and how the noise filtering is done. The reaction of these algorithms to random noise, including ionospheric residuals and non-linear receiver errors, is not fully understood and requires further investigation;
5. **It is recommended to use Radio-holographic filtering for noise reduction [5, 17].**
6. **Use dynamical error estimates based on different variants of radio-holographic analysis [5, 17, 18, 19].**
7. **Use the ionospheric correction on bending angles and statistical optimization [14].**

This recommended baseline will process the GRAS open loop data into bending angles. The following processing step will be identical as for bending angles retrieved using the geometrical optics method.

7.1.9.2 Range of Usefulness of OL Data

Based on the comparison of processing CL and OL data in the troposphere, we conclude that involving OL data significantly improves the penetration and reduces a negative bias of retrieved bending angles and refractivities. This effect is strongest in the tropics, but it also is observed in middle and polar latitudes.

7.1.9.3 Factors Limiting Retrieval Performance

We can identify the following factors limiting the retrieval performance:

1. Ionospheric noise
2. Receiver noise
3. Loss of weak parts of the signal corresponding to strongly refracted rays.
4. Gaps in the data

Data from rising occultations contain data gaps that limit the performance. Small gaps of about 0.04 seconds can be included in the parts of the signal used in the analysis without causing any disturbance. We have found that gaps up to 0.8 seconds can be filled with a phase model and processed without having any noticeable effect on the results. The phase model used for this is obtained from the MSIS climatology, supplemented with a fixed relative humidity of 90% below 15 km (cf. section 7.1.1).

The ionospheric noise may in most cases be treated as a weak noise not resulting in biases. Its reduction is based on the use of statistical optimization [14] and optimal filtering [21]. The receiver noise may be subdivided into thermal noise and signal tracking effects.

Thermal noise of the receiver is in most cases weaker than the ionospheric noise. But unlike the multiplicative ionospheric noise, the thermal noise is additive, and it may influence very weak signals, as pointed out below.

Tracking effects may manifest themselves in CL mode. This effect should result in negative bias in the phase measured in lower troposphere. This is inferred from our CL data inversion which indicated a larger negative bias as compared to CL+OL data.

A negative bias, although weaker than that in the inversion CL data, also exists in the processing of OL data. Currently, we lack full understanding of this bias. We can, however, identify its correlation with complicated lower-tropospheric structures typical for the tropics. Because the negative bias is common to the COSMIC and GRAS receiver having different technical implementations, we assume that the bias is not due a technical failure, but rather due to principal physical limitations.

We believe that improved OL data and tracking that leads to higher signal to noise data should help to further understand the bias. Here, we suggest an explanation of the negative bias by the loss of weak parts of the signal corresponding to strongly refracted rays. Such a possibility is inferred from the example of occultation event presented in Figure 146, Appendix B. The event indicates a sharp spike of the bending angle, which is abruptly cut-off by a data gap (in the interpolation the gap is filled-in by our rough phase model). A part of the signal corresponding to the spike tip may have been lost and the spike may be underestimated. This indicates the importance of performing measurements deeply in the shadow zone [22]. Large spikes of bending angle result in signals with low amplitude near the shadow zone border. Identifying weak signals in rising events is less probable than in setting ones. Even in setting events the weak

signal will be contaminated with noise. Therefore, we may expect a negative bias, but it is not straightforward to estimate the expected magnitude of this effect.

Recently, it was shown for COSMIC data [22] that the use of the measurements made deep in the shadow zone can affect the negative bias. The GRAS data selected for investigation did not provide such measurements, so in this study it was not possible to check the influence of cut-off to potential biases. On the other hand, for COSMIC data change of cut-off altitudes does not eliminate the strong negative bias structure observed for tropics. Figure 107 shows how changing the lower cutoff based on the SLTA value changes the negative bias structure for the processing of COSMIC data. The results can be summarized as follows:

- using a lower SLTA value for the cutoff of the data results in a smaller negative bias below 500 m. GRAS investigated data did not penetrate below -140 km SLTA, but the control parameter is presently set to -300 km SLTA.
- using a lower SLTA value for the cutoff of the data results in a small positive bias around 2 km. This positive bias can however be almost fully eliminated by doing a radio holographic filtering of the CT2 amplitude before the determination of the impact parameter cutoff height by correlating the CT2 amplitude with a step function. The impact parameter cutoff height determines the vertical coverage of the retrieved profile.

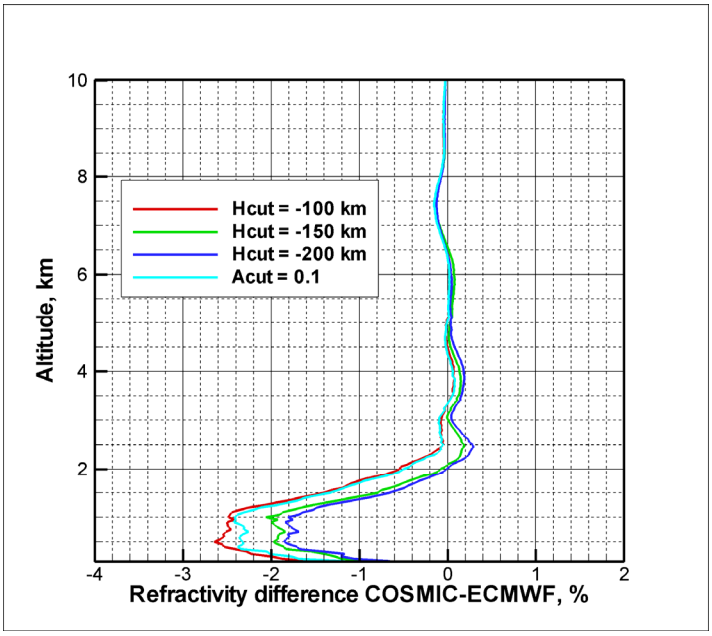

Figure 107. Relative refractivity deviations compared to ECMWF as function of height for different cutoff of the measured signals: cutoff for different SLTA heights and cutoff when the amplitude falls to a value below 0.1.

7.1.9.4 Recommendations for Future Instruments and Methods

- Data gaps should be avoided. However it is show in this report that gaps of up to 0.8 sec can be successfully handled.
- A sampling rate of 200 Hz should be sufficient, we have not observed sign of need for higher sampling. A follow up study is necessary to analyse if this is correct.
- External NBs are still needed. Further study should confirm this.
- Strong refraction and occultations affected by super refraction shall be measured. The instrument shall allow measurements down to -250 km in the shadow zone (as is done for COSMIC, and today also for GRAS). A follow-up

study is needed to determine how many occultations that may be influenced by this and quantify the benefit to the users. This will put higher demands on the instrument especially for rising occultations.

- Wave optics should be used for the entire profile. To be able to handle also scintillations in the ionosphere.
- The data that cannot be processed may contain information on the limitations of the current processing and instrument. It is suggested to investigate such data further, in particular to identify the reasons why the data cannot processed.

The users have a strong demand for RO profiles all the way down through the troposphere and the open loop data do allow for such measurements. It is shown in the study that the GRAS open loop data already provides very useful information in the troposphere, and that with future enhancement these measurements provide the users with high precision profiles that reach down to just above the surface.

7.1.10 References

1. Sokolovskiy, S., Y.-H. Kuo, C. Rocken, W. S. Schreiner, D. Hunt, and R. A. Anthes, Monitoring the atmospheric boundary layer by GPS radio occultation signals recorded in the open-loop mode, Geophys. Res. Lett., 33, L12,813, doi:10.1029/2006GL025,955, 2006.
2. Sokolovskiy, S., C. Rocken, W. Schreiner, D. Hunt, and J. Johnson, Postprocessing of L1 GPS radio occultation signals recorded in open-loop mode, Radio Science, 44, RS2002, doi:10.1029/2008RS003,907, 2009.
3. Beyerle, G., M. E. Gorbunov, and C. O. Ao, Simulation studies of GPS radio occultation measurements, Radio Sci., 38, 1084, doi: 10.1029/2002RS002,800, 2003.
4. Ziedan, N. I., GNSS Receivers for Weak Signals, Artech House, Norwood, Mass., 2006.
5. Gorbunov, M. E., K. B. Lauritsen, A. Rhodin, M. Tomassini, and L. Kornblueh, Radio holographic Filtering, error estimation, and quality control of radio occultation data, Journal of Geophysical Research, 111, D10,105, doi: 10.1029/2005JD006,427, 2006.
6. Kuo, Y., T. Wee, S. Sokolovskiy, C. Rocken, W. Schreiner, D. Hunt, and R. Anthes, Inversion and error estimation of GPS radio occultation data, J. Meteor. Soc. Japan, 82, 507–531, 2004a.
7. Beyerle, G. S., J. Wickert, T. Schmidt, and C. Reigber, Atmospheric sounding by global navigation satellite system radio occultation: An analysis of the negative refractivity bias using CHAMP observations, J. Geophys. Res., 109, doi:10.1029/2003JD003,922, 2004.
8. Ustinvov, E. A., To the solution of the problem of the numerical differentiation by the statistical optimization method, Cosmic Research (Kosmicheskie issledovaniya), 28, 545–554, 1990, in Russian.
9. Gorbunov, M. E., and A. S. Gurvich, Microlab-1 experiment: Multipath effects in the lower troposphere, Journal of Geophysical Research, 103, 13,819–13,826, 1998.
10. Gorbunov, M. E., Canonical transform method for processing GPS radio occultation data in lower troposphere, Radio Sci., 37, 9-1–9-10, doi:10.1029/2000RS002,592, 2002a.
11. Gorbunov, M. E., and K. B. Lauritsen, Analysis of wave fields by Fourier Integral Operators and its application for radio occultations, Radio Sci., 39, RS4010, doi:10.1029/2003RS002,971, 2004.
12. Jensen, A. S., M. S. Lohmann, H.-H. Benzon, and A. S. Nielsen, Full spectrum inversion of radio occultation signals, Radio Sci., 38, 6-1–6-15, doi: 10.1029/2002RS002,763, 2003.
13. Jensen, A. S., M. S. Lohmann, A. S. Nielsen, and H.-H. Benzon, Geometrical optics phase matching of radio occultation signals, Radio Sci., 39, RS3009, doi: 10.1029/2003RS002,899, 2004.
14. Gorbunov, M. E., Ionospheric correction and statistical optimization of radio occultation data, Radio Sci., 37, 17-1–17-9, doi: 10.1029/2000RS002,370, 2002b.
15. Gobiet, A., and G. Kirchengast, Advancements of Global Navigation Satellite System radio occultation retrieval in the upper stratosphere for optimal climate monitoring utility, Journal of Geophysical Research, 109, D24,110, doi:10.1029/2004JD005,117, 2004.
16. Lohmann, M. S., Analysis of global positioning system (GPS) radio occultation measurement errors based on Satellite de Aplicaciones Cientificas-C (SAC-C) GPS radio

occultation data recorded in open-loop and phase-locked-loop mode, J. of Geophys. Res., 112, D09,115, doi:10.1029/2006JD007,764, 2007.

17. Gorbunov, M. E., K. B. Lauritsen, A. Rodin, M. Tomassini, and L. Kornblueh, Analysis of the CHAMP experimental data on radio-occultation sounding of the Earth's atmosphere, Izvestiya, Atmospheric and Oceanic Physics, 41,726–740,2005.
18. Lohmann, M. S., Dynamic Error Estimation for Radio Occultation Bending Angles Retrieved by the Full Spectrum Inversion Technique, Radio Science, 2006, 41, RS5005, doi:10.1029/2005RS003396.
19. M. S. Lohmann, Application of Dynamical Error Estimation for Statistical Optimization of Radio Occultation Bending Angles, Radio Science, 2005, 40, RS3011, doi:10.1029/2004RS003117.
20. Kursinski, E. R., S. B. Healy, and L. J. Romans, Initial Results of Combining GPS Occultations with ECMWF Global Analyses Within a 1DVar Framework, Earth Planets Space 52 (11) pp. 885-892 (2001).
21. Sokolovskiy, S., W. Schreiner, C. Rocken, and D. Hunt, Optimal Noise Filtering for the Ionospheric Correction of GPS Radio Occultation Signals, Journal of Atmospheric and Oceanic Technology, 2009, 26, July, 1398–1403.
22. Sokolovskiy, S., Structural uncertainty and biases of radio occultation inversions in the lower troposphere, Presentation at Fourth FORMOSAT-3/COSMIC Data Users Workshop, 27-29 October 2009: Boulder, Colorado U.S.A.
23. Gorbunov, M. E., K. B. Lauritsen, S. S. Leroy, Application of Wigner distribution function for analysis of radio occultations, 2010RS004388, 2010, in press.

7.2 UoG Retrieval Processing

Note that references are provided in section 7.2.4.

At Wegener Center/University of Graz MetOp/GRAS retrieval performance for the "test day dataset" of 30 September 2007 processed by the EGOPS OPSv5.4 and OPSv5.5 systems was assessed. Here we give a brief introduction to the EGOPS OPS software and shows an example of validation results of MetOp/GRAS data relative to ECMWF analysis data. In addition the quality of MetOp/GRAS data was assessed relative to other radio occultation (RO) data provided by different satellite missions (CHAMP, GRACE, and COSMIC); we summarize below main results also to this end.

7.2.1 EGOPS Occultation Processing System (OPS) Retrieval Algorithm

The WEGC OPSv5.4 RO retrieval (*Steiner et al*., 2009; *Pirscher*, 2010) is a dry-air geometric optics (GO) retrieval, which uses profiles of atmospheric excess phase and precise orbit information (position and velocity vectors of LEO and GPS satellites) for generating profiles of atmospheric parameters like refractivity or dry temperature. Currently, the OPSv5.4 retrieval is the "operational" RO retrieval utilized at WEGC. Derived atmospheric profiles and climatological products are disseminated by https://www.globclim.org. Recently, we have integrated a wave-optics (WO) retrieval for the lower and middle troposphere in the OPSv5.5 retrieval (*Fritzer et al*., 2009, section 3.4 therein; developed by M. Gorbunov/IAP Moscow based on the so-called CT2 method described by *Gorbunov and Lauritsen*, 2004). We applied this one as well.

OPS input data were provided by EUMETSAT for MetOp/GRAS and by UCAR/CDAAC Boulder for CHAMP, GRACE, and COSMIC.

7.2.2 Validation of Refractivity and Dry Temperature Profiles

Refractivity is one of the parameters which is closest to the observed data. For that reason it is of high importance to validate refractivity profiles of MetOp/GRAS. The second atmospheric parameter used in the validation procedure was dry temperature, which results from the refractivity when using dry-air atmospheric profiles retrieval.

The validated MetOp/GRAS test data were used from 30 September 2007. Phase and orbit data have been processed in offline-mode with processing version 0.6 by *Marquardt* (2009). Due to a small code deficiency these GRAS level 1 data did not contain L2 excess phase delay of rising occultation measurements (need proper reconstruction from raw data) and WEGC therefore utilized only the 340 setting GRAS measurements of 30 Sept. 2007 in the OPS retrieval.

Co-located ECMWF profiles were extracted from operational ECMWF analysis fields, which were used at a resolution of T42L91 (horizontal resolution T42: spectral representation with triangular truncation at wave number 42, vertical resolution L91: 91 vertical levels). The horizontal resolution of T42 was chosen to match the horizontal resolution of RO data (approximately 250-300 km).

The statistical parameters inspected in the validation were the systematic difference between RO and co-located ECMWF analysis profiles as well as the standard deviation about the systematic difference. Figure 108 shows example validation results for refractivity when using the OPSv5.5 output (i.e., including the WO retrieval in the troposphere). Main conclusions from the WEGC processing are summarized below.

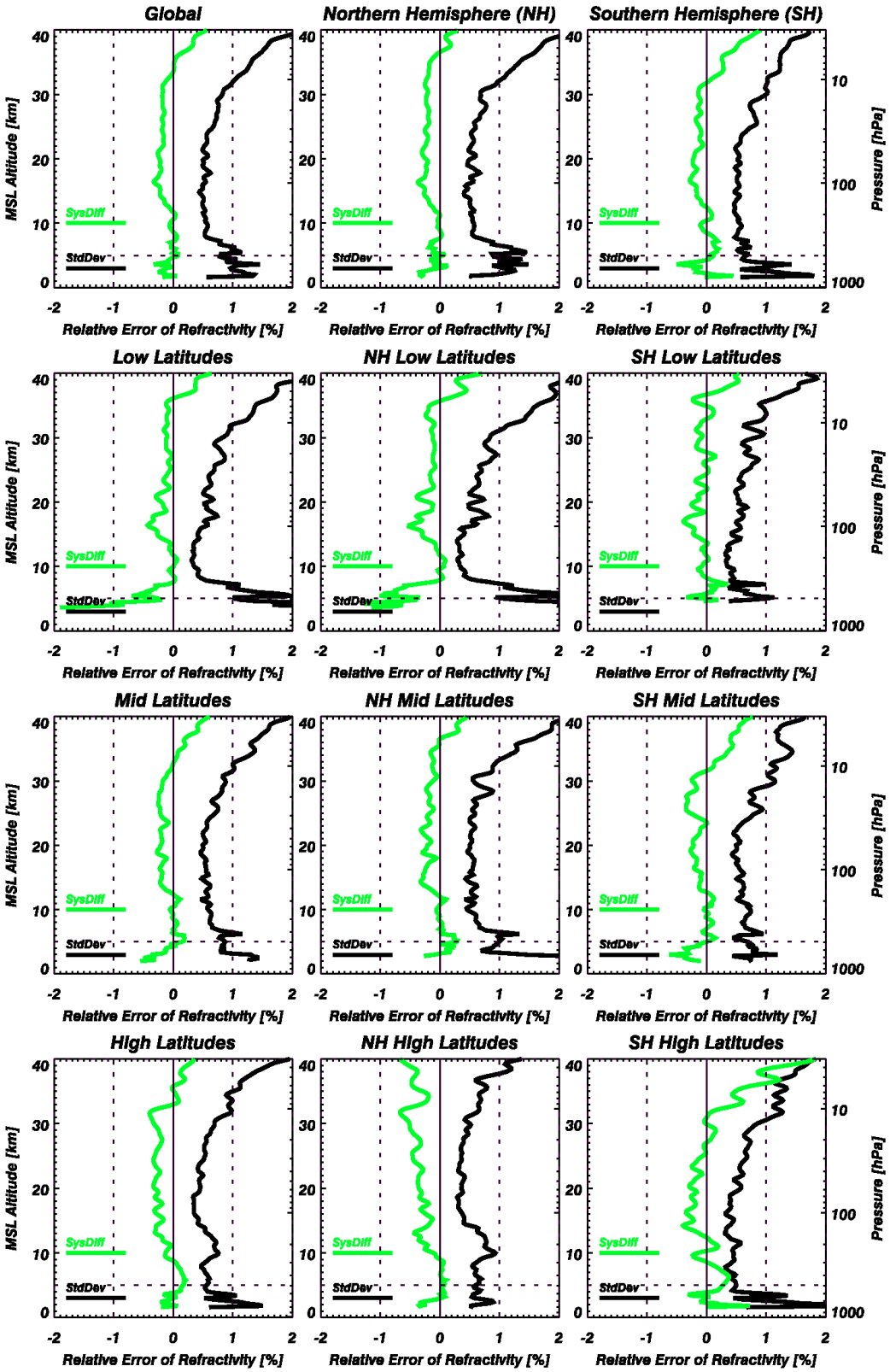

Figure 108 GRAS refractivity validation results using the OPSv5.5 (revision 2050) processing (shown are systematic difference, SysDiff, and standard deviation, StdDev, profiles).

7.2.3 Conclusions from the WEGC Processing and Validation Analysis

MetOp/GRAS refractivity and dry temperature data, derived for 30 September 2007, are in very good agreement with ECMWF and other RO satellite data. Below an altitude of about 37 km, the systematic difference between global mean RO refractivity and ECMWF refractivity is always smaller than 0.3 %. Global mean difference of GRAS and ECMWF dry temperature exceeds 1 K above 30 km altitude but always keeps smaller than 1.5 K. Compared to RO data provided by CHAMP, GRACE, and COSMIC, MetOp/GRAS systematic difference and standard deviation relative to ECMWF are slightly larger but show similar characteristics.

One interesting feature in the present MetOp/GRAS data is observed at high northern latitudes. Both refractivity and dry temperature systematic differences were found negative relative to ECMWF at nearly all altitude levels. Latitude regions except high northern latitudes show a predominantly positive dry temperature systematic difference. Such a latitude-dependent systematic difference in dry temperature has not been observed before. The reason remained unclear for the time being and deserves further check in future work respectively a tracking whether it is still visible in future GRAS processing versions.

7.2.4 References

Fritzer, J., G. Kirchengast, and M. Pock (2009), End-to-End Generic Occultation Performance Simulation and Processing System Version 5.5 Detailed Design Document (EGOPS5.5/DDD). *Tech*. *Rep. for ESA/ESTEC No. 2/2009*, Wegener Center, Univ. of Graz, Graz, Austria.

Gorbunov, M. E., and K. B. Lauritsen (2004), Analysis of wave fields by Fourier integral operators and their application for radio occultations, *Radio Sci*. 39, RS4010, doi:10.1029/2003RS002971.

Marquardt, C. (2009), GRAS prototype data format description. *Doc-ID EUM/OPS/TEN/ 09/2483*, 1–13, EUMETSAT, Darmstadt, Germany.

Pirscher, B. (2010), Multi-Satellite Climatologies of Fundamental Atmospheric Variables From Radio Occultation and Their Validation, *PhD Thesis*, Wegener Center and IGAM/Inst. of Physics, Univ. of Graz, Graz, Austria.

Steiner, A. K., G. Kirchengast, B. C. Lackner, B. Pirscher, M. Borsche, and U. Foelsche (2009), Atmospheric temperature change detection with GPS radio occultation 1995 to 2008, *Geophys*. *Res*. *Lett*. 36, L18702, doi:10.1029/2009GL039777.

7.3 GFZ Retrieval Processing

Note that references are provided at the end of this section 7.3.

7.3.1 Results

At the GFZ Potsdam the experimental processing software POCS-X is used to retrieve bending angle/refractivity profiles from GRAS OL data. The software includes FSI (Full Spectrum Inversion) in order to cope with multi-path regions and enables in connection with OL data to retrieve atmospheric profiles down to the Earth's surface. CL/OL data necessary for the inversion of a RO event is read from EUMETSAT NetCDF file. The processing consists of two stages, hereinafter referred to as Level 2 and Level 3 processing.

Level 2 processing: The phase and amplitude of the entire signal is assembled from CL data recorded at 50 Hz and OL data recorded at 1 kHz. The residual phase extraction (four-quadrant inverse tangent applied to in- and quadrature-phase samples) requires knowledge of the navigation data bits. External navigation data bits, collected by GFZ's ground station network, are used (Beyerle et al. 2009). Internal navigation data bits (contained in EUMETSAT NetCDF file) are used if external navigation data bits are not available (25% of all occultation events). We select the longest contiguous CL and OL records and require an overlap between CL and OL in order to determine the phase-offset between the contiguous CL and OL records. The processing system uses zero differencing (Beyerle et al. 2005a) to retrieve excess paths.

Level 3 processing: The implementation of the FSI closely follows Beyerle et al. 2005b. The ionospherically corrected excess path is calculated from the L1 and L2 excess paths by the standard linear combination (Beyerle et al. 2004). Frequency variations caused by radial variations in the radius vectors of the GPS and the LEO satellite are accounted for (Jensen et al. 2003). The signal in the time domain is not truncated and not subject to any filtering. The bending angle as a function of the impact parameter follows from the derivative of the FSI phase. The valid impact parameter range is determined from the FSI amplitude. Specifically, the bending angle profiles are truncated at that impact parameter value where the FSI amplitude drops below 50% of the maximum value. The resolution of the bending angle profile is reduced from 0.5 m to 50 m using a running mean. Above 12 km ray-height bending angles are replaced by corresponding standard Doppler retrieved bending angles. For the low-pass filtering of the excess paths and the simultaneous calculation of the excess path rates we apply a local polynomial regression of degree 3 using 71 samples (Savitzky-Golay smoothing filter). Above 40 km ray-height statistical optimization using auxiliary data (MSIS climatology) is performed. The bending angle profiles are inverted to refractivity profiles using the Abel transform.

Quality Control (QC): QC is applied at different stages of the processing. The early stage QC (applied at Level 2 and Level 3) examines CL/OL data gaps, the CL/OL overlap, SNRs, and L1/L2 excess path ratios. The final stage QC compares the retrieved refractivity profiles to the ECMWF refractivity. Profiles with a fractional refractivity deviation exceeding 10% at any altitude between 5 km and 30 km are rejected.

Retrievals are validated against ECMWF (European Centre for Medium-Range Weather Forecasts) profiles. ECMWF refractivity is computed from pressure, temperature and water vapour partial pressure (Bevis et al. 1994). Interpolation between grid points and linear interpolation in time is performed between 6 h analyses fields. The focus is on data from September/October 2007; Day Of Year (DOY): 273-300. From 18878 occultation events, 12678 occultation events pass the QC. 60% of successfully retrieved profiles stem from setting occultation events. The discrepancy between the retrieved refractivity from an occultation event and ECMWF refractivity is measured in terms of the fractional refractivity deviation:

Figure 109 to Figure 111 show the fractional refractivity deviation versus altitude for different latitude bands; the northern hemisphere (30°N-90°N), the southern hemisphere (30°S-90°S) and the tropics (30°S-30°N). The number of successfully retrieved data points at a given altitude is attached to all figures. In the northern/southern hemisphere biases are insignificant from 2 km to 10 km. Close to the ground a negative bias exists reaching 1.5% in the northern hemisphere and 2% in the southern hemisphere. The standard deviation reaches 2% at 2 km for both hemispheres. The 50% altitude, i.e. the altitude where the number of successfully retrieved data points is reduced to 50%, is 838 m for northern hemisphere and 631 m for the southern hemisphere. In the tropics a negative bias exists reaching 3% close to the ground. The mean deviation in the altitude range 2-6 km tends to be positive, reaching about 0.5% at 2 km. The standard deviation reaches 3% at 2 km. The 50% altitude is 817 m.

7.3.2 Conclusions

The statistical comparison shows that refractivity profiles derived from OL data indicate good quality. It is concluded that OL data and the application of an advanced retrieval algorithm allow retrieving profiles that extend deep into the lower troposphere. Biases present in the lower troposphere need to be investigated in more detail (retrievals derived from different RO missions show similar biases). A possible explanation of the enhanced negative bias in the lower troposphere is the presence of critical refraction. In addition recent investigations by S. Sokolovskiy (presentation at the 4th COSMIC Data Users Workshop) point to that the truncation and filtering of RO signals have a large influence on both, positive and negative, biases in the lower troposphere. We also note that there are significantly more (successfully retrieved) profiles from setting occultation events than rising occultation events. This is due to the fact that in rising occultation events data gaps in the signal are frequent. Since our retrieval algorithm relies on the longest contiguous CL and OL records a large number of rising occultation events are rejected by our QC. An increased yield of the retrievals, i.e. a method to fill data gaps, is work in progress.

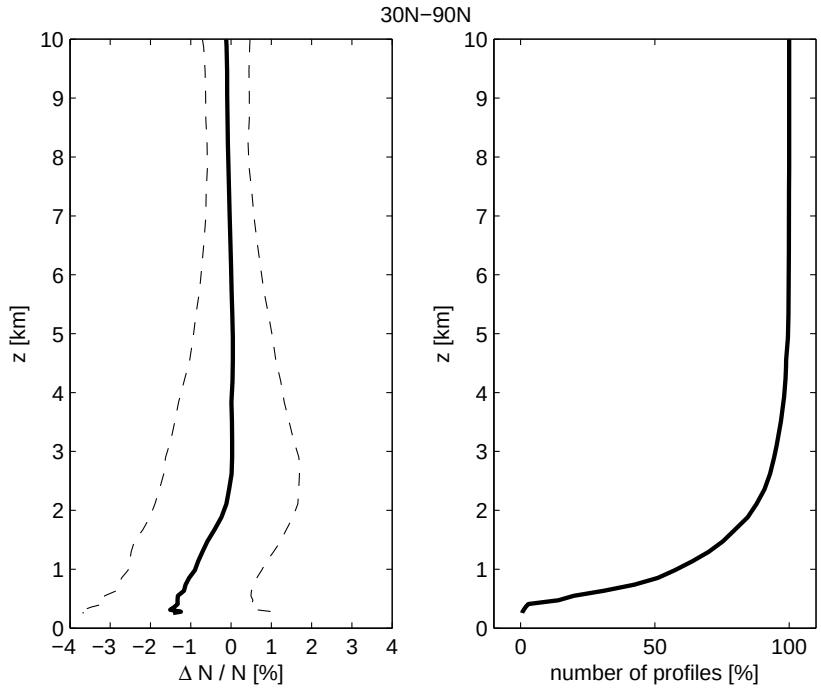

Figure 109 Fractional refractivity deviation (left) and number of retrieved data points (right) versus altitude (northern hemisphere: 30°N-90°N). The solid line indicates the mean and the dashed lines indicates the ± one-sigma standard deviation from the mean.

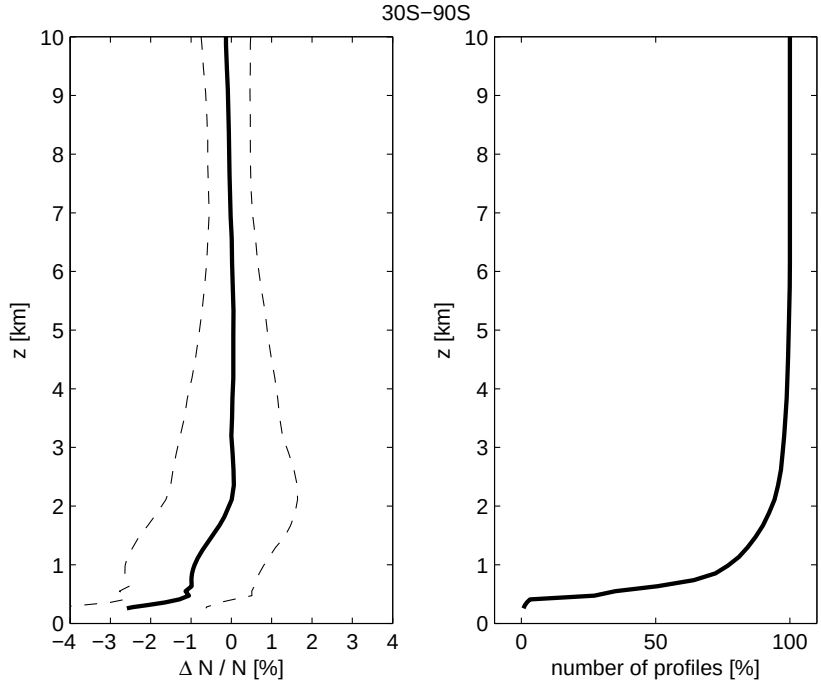

Figure 110 Fractional refractivity deviation (left) and number of retrieved data points (right) versus altitude (southern hemisphere: 30°S-90°S). The solid line indicates the mean and the dashed lines indicates the ± one-sigma standard deviation from the mean.

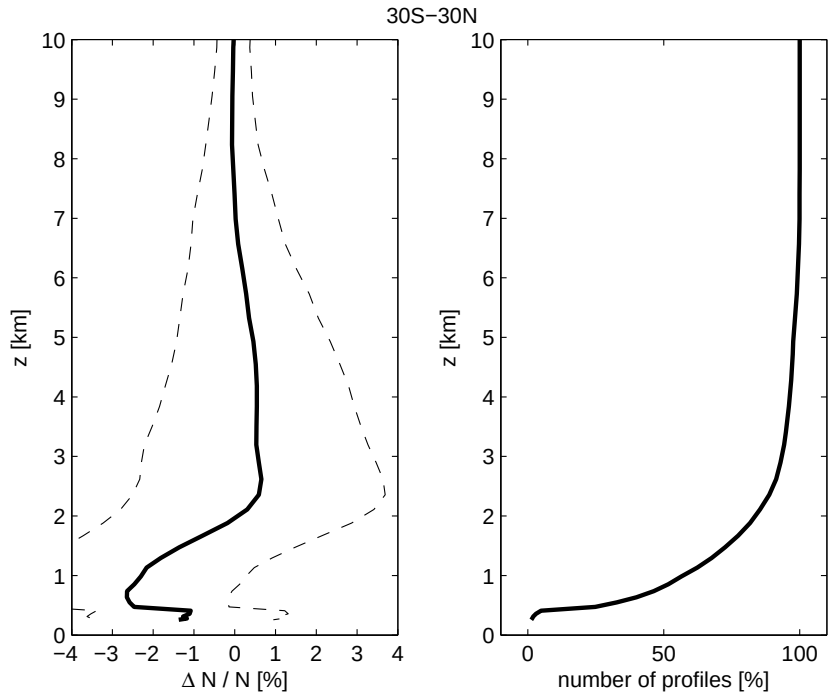

Figure 111 Fractional refractivity deviation (left) and number of retrieved data points (right) versus altitude (tropics: 30°S-30°N). The solid line indicates the mean and the dashed lines indicates the ± one-sigma standard deviation from the mean.

References:

Bevis, M., S. Businger, S. Chiswell, T. A. Herring, R. A. Anthes, C. Rocken, and R. H. Ware: GPS meteorology: Mapping zenith wet delays onto precipitable water, J. Appl. Meteorol., 33(3), 379–386, 1994.

Beyerle, G., J. Wickert, T. Schmidt, and C. Reigber: Atmospheric sounding by global navigation satellite system radio occultation: An analysis of the negative refractive bias using CHAMP observations. J. Geophys. Res., 109, D01106, doi:10.1029/2003JD003922, 2004.

Beyerle, G., Wickert, J., Schmidt, T., and Reigber, C.: GPS radio occultation with GRACE: Atmospheric profiling utilizing the zero difference technique, Geophys. Res. Lett., 32, L13806, doi:10.1029/2005GL023109, 2005a.

Beyerle, G.: Simulating GPS radio occultation events, Scientific Report, 05-09, Danish Meteorological Institute (DMI), 1-38, 2005b.

Beyerle, G., T. Schmidt, J. Wickert, S. Heise, M. Rothacher, G. König-Langlo, and K. B. Lauritsen: Observations and simulations of receiver-induced refractivity biases in GPS radio occultation, J. Geophys. Res., 111, doi:10.1029/2005JD006673, 2006.

Beyerle, G., Ramatschi, M., Galas, R., Schmidt, T., Wickert, J., and Rothacher, M.: A data archive of GPS navigation messages, GPS Solutions, 13, 35–41, doi:10.1007/s10291-008-0095-y, 2009.

Jensen, A. S., Lohmann, M. S., Benzon, H.-H., and Nielsen, A. S.: Full spectrum inversion of radio occultation signals, Radio Sci., 38, 1040, doi:10.1029/2002RS002763, 2003.

7.4 EUMETSAT GRAS Data Characteristics and Retrieval Processing

7.4.1 Introduction

The current operational processing of GRAS data is focusing on atmospheric altitudes above 8 km, exploiting carrier phase measurements obtained in a closed loop tracking mode of the instrument along with “geometrical optics” retrieval algorithms (Vorob’ev and Krasil’nikova, 1994). It is well known that the complicated signal propagation in the troposphere causes large amplitude and phase variations of the signal, which cannot be successfully tracked by phase-locked tracking loops typically implemented in GNSS receivers. Instead, “open loop” tracking algorithms are required (Sokolovskiy, 2001). The GRAS receiver in particular implements a unique 1 kHz “raw sampling” measurement mode. The retrieval of geophysical parameters in the mid and lower troposphere under such atmospheric multipath conditions requires advanced retrieval algorithms like FSI (Full Spectrum Inversion, Jensen et al., 2003), CT (Canonical Transform, Gorbunov, 2002a)) or more generally FIO (Fourier Integral Operator, Gorbunov and Lauritsen,2004)) algorithms.

Section 7.4.2 describes the data set used by the study team. Section 7.4.3 addresses the data characteristics of the GRAS instruments and briefly discusses the low level data reconstruction required for GRAS data. It also introduces three issues in the current instrument configuration which are relevant for the data processing: low L2 SNR (Signal-to-Noise Ratio) values for a small, but significant part of the data set; data gaps in closed loop data which are not covered by raw sampling measurements in a significant part of rising occultations; and frequent data gaps in all raw sampling measurements. The current EUMETSAT implementation of the FSI algorithm for the retrieval of bending angle profiles is used in section 7.4.4 to discuss some of the issues related to the data gaps observed in the GRAS data.

References are provided in section 7.4.6.

7.4.2 Dataset

The study is based on GRAS observations taken between September 30 and October 31 2007. EUMETSAT provided a level 1a data set (i.e., amplitude, SNR and carrier phase data reconstructed from level 0 GRAS measurements) along with precise Metop-A orbits derived from GRAS zenith antenna measurements. For the GPS constellation, final GPS orbits and clocks from the IGS processing performed by CODE (Center for Orbit Determination in Europe) were used. Raw observations of the navigation bit data transmitted by the satellites of the GPS constellation were kindly provided by UCAR, GFZ Potsdam and JPL, and were applied for the demodulation of the navigation bits from the GRAS raw sampling data during the level 1a processing.

The level 1a data set, §7.4.3.2, consists of 22105 globally distributed occultations, equally split between rising and setting events. We note that the (successful) validation of the data reconstruction as implemented by EUMETSAT was also undertaken as part of the study, see §4.3. While the same level 1a data was used by all participants of the study apart from UCAR, level 1b (bending angle) processing was performed by individual groups using their choice of advanced retrieval algorithms. Differences in retrieval results between the study participants therefore highlight structural uncertainties in the level 1b processing applied by the various centres.

In contrast to the other participants, UCAR also implemented their own version of the low level data reconstruction, using EUMETSAT's source code as a reference. Differences in reconstructed level 1a data, §7.4.4, however, have turned out to be comparatively small, similar to impacts from different precise orbit solutions provided by EUMETSAT and UCAR. Differences in the level 1b processing are therefore assumed to be the major contributor to structural uncertainty in the UCAR data.

7.4.3 GRAS Data Characteristics and Issues

The GRAS receiver is the first GPS receiver designed specifically for operational radio occultation soundings. There is no common heritage with the line of GPS receivers based on JPL (Jet Propulsion Laboratory) designs as used in, e.g., the GPS/MET, CHAMP, GRACE and COSMIC RO missions. As a consequence, a number of differences exist in the design and data characteristics of the GRAS and JPL based receivers. We note that both hardware and software design and implementation of the GRAS instrument were completed before the first open loop and rising occultation data became available from other receivers (Ao et al., 2009).

7.4.3.1 Measurement Modes

For individual occultations, GRAS provides data from three distinct measurement modes:

Dual Frequency Closed Loop Tracking: If SNR values are sufficiently high, the receiver tracks carrier phases transmitted by the occulting GPS satellite for C/A, P1(Y) and P2(Y) codes (the latter by exploiting a codeless tracking technique) using a Phase-Locked-Loop (PLL). In this mode, GRAS produces 50 Hz carrier phase and SNR measurements, similar to other spaceborne RO receivers. In addition to the phase estimated by the PLL, the receiver also reports the real and complex components I and Q of the signal's residual with respect to the PLL controlled phase estimate, which allows the reconstruction of the full electromagnetic field measured by the instrument.

Single Frequency Closed Loop Tracking: If SNRs are too low for P1/P2 carrier phase tracking, the receiver may still be able to successfully track C/A carrier phase data in a closed loop mode. The data is also reported at 50 Hz, again with I/Q correlator output alongside the PLL phase estimate.

Single Frequency Raw Sampling: In raw sampling (or open-loop) mode, the PLL-controlled carrier phase estimate is replaced with an empirical model of the carrier phase progression, which is reported along with the I and Q residuals of actual measurement at a 1 kHz rate. Note that this high sampling rate distinguishes GRAS raw sampling data from the 50 Hz open loop measurements taken by receivers with a JPL heritage.

Due to hardware constraints, GRAS is only able to provide either dual frequency tracking or raw sampling data. Closed loop C/A carrier phase measurements may occur simultaneously with raw sampling measurements, and generally show a high level of consistency (not shown). For setting occultations, the receiver dynamically switches to raw sampling mode as soon as P1/P2 carrier phase tracking is lost. In rising occultations, a configurable threshold altitude for the Straight Line Tangent Altitude (SLTA) triggers the termination of the raw sampling mode in favour of attempting to achieve dual frequency tracking. This threshold is currently set to -35 km SLTA, representative for geometrical altitudes in the mid-troposphere.

In all measurement modes, the GRAS receiver requires the C/A code to be tracked in order to be able to demodulate the C/A modulation from the carrier signal; if the C/A code tracking fails, no measurements will be reported to the ground. This is another difference between GRAS and receivers with a JPL heritage which exploit a range model for the code phase tracking. The design was chosen on purpose in order to maximize SNR during raw sampling measurements; its drawback is the potential loss of measurement data in case C/A code tracking is lost.

7.4.3.2 Level 1a Reconstruction

Usually, GPS receivers provide time-stamped pseudo-range, carrier phase and amplitude data which simply need to be unpacked. GRAS differs from this traditional approach by delivering a collection of integer and fractional code phase cycles, various components of carrier phase measurements, histograms of noise measurements and receiver gain setting parameters, all time stamped with integer clock ticks. Ordinary GPS observables and their time referencing have to be reconstructed from these data sets, taking into account instrument characterization data, e.g. delays caused by the various electronic components of the instrument, or GRAS' high gain antennas. While the reconstruction process has the disadvantage of being significantly more elaborate than that for ordinary GPS receivers, it also offers the benefit that some critical raw data handling which otherwise has to be carried out in the receiver's firmware can be performed as part of the ground processing, potentially reducing the need for frequent firmware updates and data losses due to firmware problems.

7.4.3.3 Signal-to-Noise Ratios (SNR)

Figure 112 shows frequency histograms of C/A and P2 SNR averaged over altitudes above 60 km SLTA. At these altitudes, the closed loop tracking characteristics of the GRAS instrument are not affected by atmospheric effects as the latter are very weak; the averaged SNR at high altitudes therefore provides a proxy for assessing the overall closed loop tracking performance of the instrument. According to Figure 112, the bulk of C/A carrier phase measurements exhibits SNRs in the order of 750 – 950 V/V, while P2 carrier phase measurements cantered in the range between 200 – 350 V/V (which is lower due to the SNR losses related to the codeless tracking of the encrypted P-codes). For both C/A and P1/P2 carrier phase measurements, SNR values are nearly symmetrically distributed around their respective mode values.

For comparison purposes, an experimental processing of the COSMIC data available during the study period was performed at EUMETSAT. Figure 113 shows the distribution of averaged SNR values from the six COSMIC satellites. Overall, COSMIC C/A SNR values are slightly lower (with the maximum of the distribution located between 700 and 800 V/V) compared to GRAS, and also exhibit a heavier tale towards lower SNR values. For P2 SNR values larger than 200 V/V, the COSMIC distribution shows a similar shape as the one for GRAS; in addition, the distribution exhibits a bimodal shape with a second maximum located below 200 V/V.

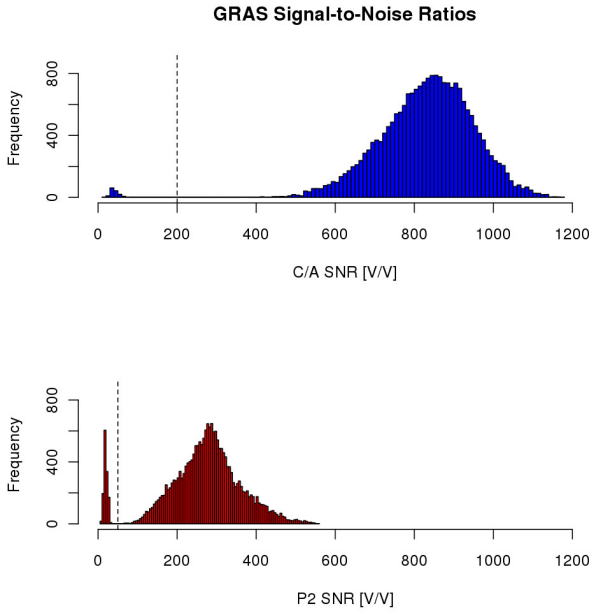

Figure 112 Histograms of GRAS SNR values averaged over altitudes above 60 km SLTA for L1 (top) and P1/P2 (bottom) carrier phase measurements. Vertical dashed lines show thresholds for the automated quality control implemented in the GRAS prototype processing at EUMETSAT.

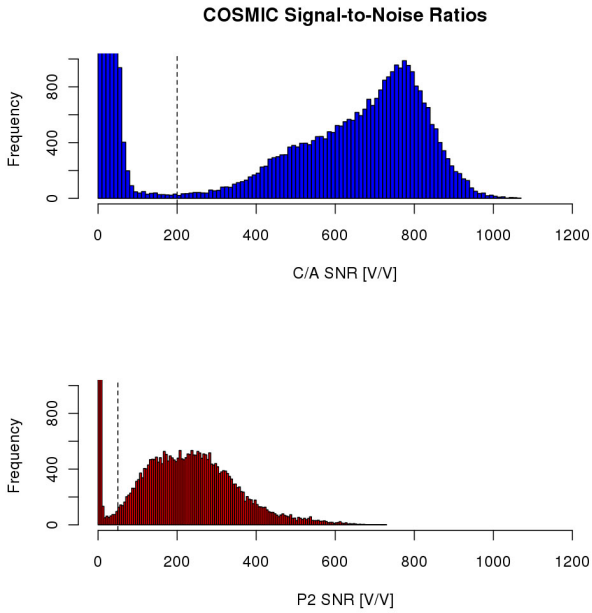

Figure 113 As preceding figure, but for the COSMIC constellation. The vertical axis has been cut in order to show the shape of the frequency distribution for the "good" cases. Quality control criteria were chosen to be the same as for GRAS.

The visual comparison of the figures suggests that the Q/C criteria applied to GRAS processing would also be well suited to separate the very low SNR cases at the very left end of the SNR scale from the higher SNR cases in the COSMIC data set. Note that the vertical axis had to be cut off at 1000 cases in order to be able to show the shape of the frequency distributions for the high SNR occultations; see below for a more detailed discussion on this.

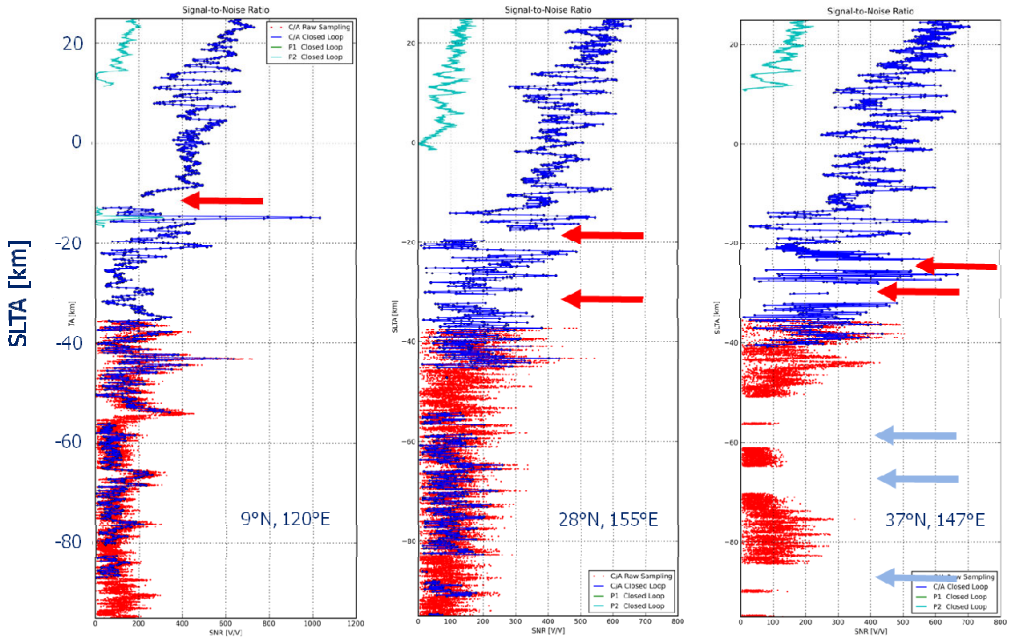

Figure 114 SNR of closed loop (dark blue for closed loop, red for raw sampling measurements; see legend for other colours) for three example occultations taken on 30. September 2007 as function of SLTA. Light blue arrays indicate location of data gaps in raw sampling data (rightmost example only), while red arrays indicate closed loop data gaps not covered by raw sampling data.

7.4.3.4 Low L2 SNR Values in Closed Loop Tracking

Figure 112 identifies a first issue in GRAS data related to SNR values in L2 closed loop data. There is only a very small part (< 1% of all occultations in the study period) with low (< 200V/V) C/A SNR values, confirming that that the C/A carrier phase tracking is highly reliable. However, a significant part (7%) of occultations exhibits low (< 50V/V) SNRs for the P2 carrier phase tracking; the majority of cases occurs for rising occultations. An initial analysis of the data indicates that the search procedure for the correlation peak of the codeless P1/P2 tracking is occasionally terminated somewhat prematurely, resulting in instable tracking behaviour and frequent cycle slips in the P2 carrier phase data in these cases.

Bending angle profiles retrieved from this data often show strong unphysical oscillations at upper altitudes, and the experience from the operational processing at EUMETSAT is that most profiles being rejected by NWP data quality control system in NWP centres belong to these low P2 SNR cases. At EUMETSAT, the GRAS prototype processing therefore uses these thresholds (200 V/V and 50 V/V for L1 and L2 carrier phase measurements, respectively) for flagging individual profiles as bad.

To put the low P2 SNR issue into perspective, we note that other RO receivers also suffer from poor P2 tracking performance. For example, about 50 % of the COSMIC level 1a occultation data available during the same period suffer from SNR values of less 50 V/V for P2 carrier phase measurements. With this in mind, the overall performance of the GRAS C/A code and P1/P2 codeless tracking loops turns out to be excellent. Nevertheless, some improvement of the tracking behaviour for P1/P2 codeless tracking appears desirable in order to achieve the 95% availability target of the instrument.

7.4.3.5 Raw Sampling Data Gaps

The requirement to always track the C/A code even for raw sampling measurements gives rise to a second issue in the GRAS data. With C/A code tracking being lost under low SNR conditions, data gaps in the raw sampling time series occur for more or less all rising occultations, and the majority of setting occultations. An example is shown in the subtropical (rightmost) example in Figure 114, where several interruptions of the raw sampling data can be seen around -55 km, -70 km and below -85 km in SLTA. The example also demonstrates that signals were successfully measured earlier on below these data gaps, in particular between -70 km and -85 km SLTA. This suggests that the loss-of-lock indicators for the C/A code tracking might be set to overly conservative values in the GRAS firmware, i.e. cause a loss-of-lock earlier than really necessary. In any case, not taking the lower parts of the measurements into account would mean to exclude measurements from strongly bent signals, i.e. to systematically underestimate lower tropospheric bending angles (see Sokolovskiy et al., 2010).

7.4.3.6 Closed Loop Data Gaps in Rising Occultations

A third tracking problem, also demonstrated in Figure 114, is related to the fixed SLTA threshold for switching from raw sampling to Dual Frequency measurements in rising occultations; setting occultations are not affected. For a significant part of rising occultations (33%, or 16% of all occultations), amplitude and phase variations in closed loop data undergo sufficiently strong variations even above the current raw sampling cut-off threshold altitude for the C/A carrier phase tracking loop to loose lock. Note that loss-of-lock events in the Closed Loop data do occur frequently at lower SLTAs (see the second example in Figure 114), but can be fixed if raw sampling data is available at the same time. For the data gaps indicated by the red arrows, however, no raw sampling data is available because the receiver has already terminated its raw sampling mode for the occultation in question.

Similar to the data gaps in the raw sampling data, lock-of-loss indicators for the closed loop C/A carrier phase tracking appear to be overly sensitive to short term variations, and parameter settings could potentially be optimized to reduce the number of data gaps.

7.4.4 Level 1b (Bending Angle) Processing

7.4.4.1 Algorithms

Bending angles as function of impact parameter – and from there on, other geophysical parameters – are calculated from the signal's Doppler frequency shift caused by the signal's propagation and bending through the atmosphere, using precise position and velocity data together with principles of geometrical optics and the assumption of spherical symmetry (see, e.g., Vorob'ev and Krasil'nikova (1994)). If an occultation is characterized by a single Doppler frequency at any moment in time, it is known from both optics (e.g., Born and Wolf, 1999) and time–frequency analysis (e.g., Cohen, 1995; Flandrin, 1998; Boashash, 2003) textbooks that the instantaneous frequency of the signal can be calculated as time derivative of the phase of the signal, i.e. directly from the GPS phase as observed by the RO receiver. In the RO literature, this is known as "geometrical optics" (GO) retrieval. If a measurement exhibits more than a single frequency occurring simultaneously at the same time – e.g., due to atmospheric multipath caused by the complex signal propagation characteristics in the troposphere – the instantaneous frequency is not representative for the actually contained frequency components in the signal. In signal processing and time–frequency analysis, the next simple approach is to calculate the group delay, i.e. the time at which a certain frequency is observed. Group delay can be calculated by time differentiating the Fourier transformed observed signal (Cohen, 1995; Flandrin, 1998; Boashash, 2003), and carries physical meaning as long as each frequency is only observed at a single moment in time.

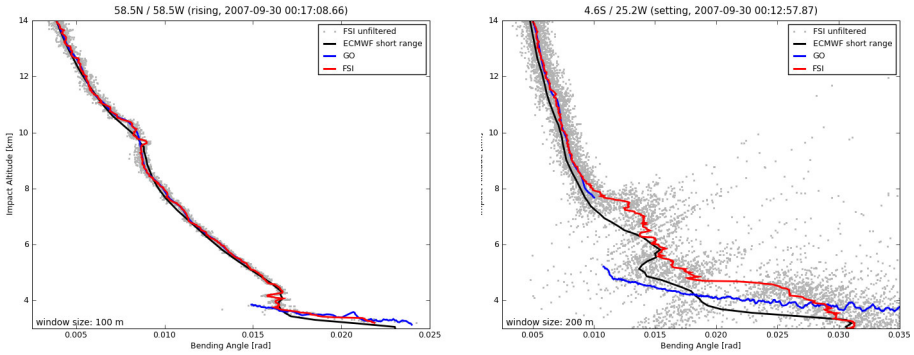

Figure 115 Comparison of EUMETSAT prototype bending angle profiles in high latitudes (left, rising) and the tropics (right, setting) calculated using the FSI (red) with a geometrical optics retrieval (blue) as well as bending angle profiles forward modelled from ECMWF short range weather forecast data (black). Grey dots indicate bending angle values obtained from the FSI prior to downsampling and filtering. The retrievals utilize both closed loop and raw sampling data; both profiles were observed on 30. September 2007. Note that impact height is used as vertical coordinate; the Earth's surface is typically located at 2 – 3 km impact height.

The approach is known as “Full Spectrum Inversion” (FSI; Jensen et al., 2003) in the RO literature; in order to ensure the uniqueness of observed frequencies, a transformations to the orbit and time coordinates are occasionally applied before the calculation of arrival times (or group delays) is performed. Bending angle profiles are then calculated as in the “geometrical optics” retrieval. Alternatively, geometry transformations following the “Canonical Transform” (CT) methodology known from classical and quantum mechanics (Gorbunov, 2002a; Gorbunov and Lauritsen, 2004) have been proposed, combining frequency and bending angle estimation in a single step. Both FSI and CT appear to be mathematically equivalent, at least in the context of radio occultation retrievals (Gorbunov et al., 2004). Regardless of the details of each of these algorithms, the measured signal is usually upsampled and Fourier transformed, before arrival times, Doppler frequencies and eventually bending angles and impact parameters are calculated. In a final step, some kind of downsampling and smoothing is applied before the final bending angle profiles are produced. In the RO literature, these retrieval algorithms are often referred to as “wave optics” methods.

Figure 115 shows two examples of tropospheric bending angle profiles obtained from GRAS soundings on 30. September 2007. The profiles were retrieved at EUMETSAT using an FSI-based algorithm, and are shown as function of impact height; note that the Earth’s surface is typically located between 2 and 3 km in impact height coordinates. Thus, both profiles reach into the lowest kilometre of the Earth’s atmosphere. The figure also shows a GO retrieval along with a bending angle profile forward modelled from short range ECMWF forecast data.

For the extratropical profile (Figure 115, left), the agreement between the GRAS and ECMWF profiles is excellent. The FSI retrieval reveals some high vertical resolution structures around the tropopause (10 km in impact height) and in the lower troposphere boundary layer (4 km in impact height). The geometrical optics profile is somewhat smoother compared to the FSI retrieval, and (expectedly) unable to resolve the boundary layer structures where the FSI clearly performs better. Finally, the gray data points also shown in the figure indicate raw (or unfiltered) bending angle values calculated from the FSI without applying the final filter step. The compact correlation between unfiltered bending angle and impact height values reflects the very favourable noise characteristics of this particular occultation.

The second example (Figure 115, right) shows a tropical occultation exhibiting somewhat noisier measurement data. The scatter of the unfiltered (gray) bending angle data is significantly larger than in the extratropical example, suggesting that the final FSI retrieval drawn in red depends more critically on the filter and other processing options applied. Note that the raw data values are probably not even normally distributed around the final retrieval. Many of the small vertical scale structures visible in the FSI bending angle profile may actually not carry physical information, but simply represent noise which hasn’t been smoothed out sufficiently. The FSI retrieval shows large deviations from its geometrical optics counterpart, which can again be explained by the presence of atmospheric multipath which cannot be resolved in the traditional approach. The agreement between GRAS bending angle retrieval and the co-located ECMWF profile is also poorer than in the extratropical case, although it cannot be determined which profile is closer to the true atmospheric state without performing a more rigorous validation which is outside the scope of this study.

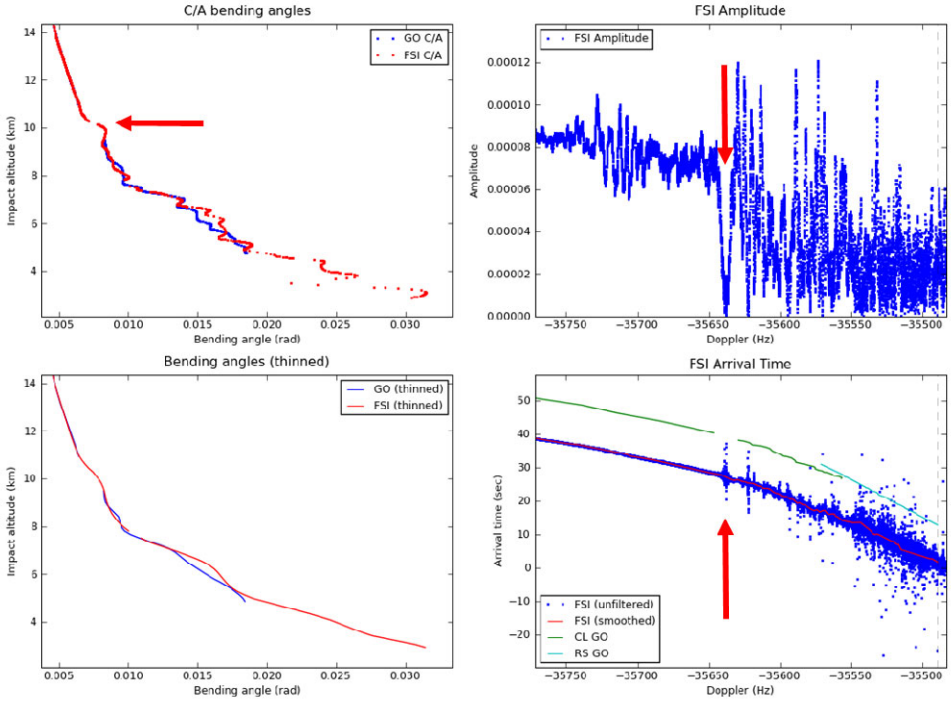

Figure 116 Tropospheric bending angle profiles (left) and FSI diagnostics (right) for the first (tropical) data gap case presented in Figure 114 after zeroing amplitude and phase data during the data gap. Both high resolution (top left) and thinned (lower left) bending angles are shown for comparison. FSI diagnostics include FSI amplitude (top right) and arrival time vs. Doppler frequency (lower right). In the lower left subfigure, geometrical optics Doppler calculated from both closed loop (light green) and raw sampling (light blue) data is also shown, but shifted by 10 seconds in time for clarity. The location of the data gap is indicated by the red arrows. See text for details.

7.4.4.2 Data Gap Handling

The data gaps described previously have been handled in different ways by the participating groups. In the processing of the University of Graz, data is cut off below the highest data gap. Other groups (DMI and GFZ) decided to interpolate amplitude and phase data over sufficiently short gaps. For example, the DMI processing interpolates over data gaps shorter than 0.8 seconds, and cuts data off if gaps extend over longer periods. A similar approach is implemented in the UCAR processing. Processing centres favouring the interpolation approach then process the interpolated data as if observations had been made during the data gaps.

Cutting off data below data gaps has the drawback to significantly reduce the penetration of bending angle retrievals into the troposphere. On the other hand, the interpolation of missing data over gaps without indicating their existence in the final bending angle profiles falsely suggests information in the retrieved data which is not backed by real observations. EUMETSAT therefore took yet another approach, aiming at identifying measurement data gaps also in bending angle profiles. The resulting bending angle profiles contain data gaps, which can easily be handled in present day variational retrieval and data assimilation algorithms for higher level geophysical parameters like temperature and moisture.

Technically, the initial implementation of EUMETSAT's bending angle retrieval consisted of zeroing amplitude and phase data during data gaps and performing a usual FSI retrieval. This approach is based on the observation that the FSI amplitude of a signal prepared this way shows localized drops in the presence of data gaps; it was hoped that the latter would allow identifying data gaps in the bending angle space. As a practical example, Figure 116 shows FSI diagnostics for the first example case presented in Figure 114. The amplitude drop related to the measurement data gap is indicated by a red arrow (Figure 116, upper right).

These figures also demonstrate the shortcomings of this approach: lower tropospheric data very often exhibit an overall decrease in FSI amplitude data, and the objective identification of data gaps based on FSI amplitude alone is difficult. In practice, data gaps tend to be only partially discovered, and artefacts from the gap boundaries add to systematic and random errors of the bending angle profiles. This is apparent in Figure 116 (upper left), where FSI bending angles from the EUMETSAT processing are compared with the geometrical optics retrieval derived from the same measurements. The latter handles the available continuous data segments individually, and provides a way to indicate the extent of data gaps as long as atmospheric multipath can be neglected. The FSI, as implemented at EUMETSAT for this study, adds a small positive bump to the bending angle profile at impact heights around 10 km which is not supported by measurements. When producing thinned bending angles (Figure 116, lower left), the remaining bending angle data gap is erroneously smaller than the vertical level separation, and hence does not even appear as gap any more in the thinned bending angle, still exhibiting a (probably non-physical) positive bump around an impact height of 10 km.

We note that the drop on FSI amplitude goes along with an increase in the scatter of the Doppler vs. arrival time distribution (Figure 116, lower right). Inasmuch as the width of this distribution can be taken as a proxy for the uncertainty of the bending angle profile calculated from it, one can hardly avoid observing that the information content of the lower tropospheric measurements does not appear to significantly exceed the information content of the data gap. One would therefore expect to observe a high structural uncertainty in lower tropospheric bending angle retrievals. We will see in section 7.5 that this is indeed the case.

7.4.5 Conclusions

The GRAS receiver provides a 50 Hz closed loop measurement mode, along with a 1 kHz raw sampling mode for tropospheric data. Closed loop and raw sampling data are – apart from different noise levels due to the varying sample rates – highly consistent. The receiver provides either closed loop carrier phase data at both GPS frequencies (from both C/A and P(Y) codes), or C/A carrier phase closed loop data along with "raw sampling" measurements. Raw sampling measurements employ an open loop carrier phase tracking, but require C/A code locking, and are provided at a high (1 kHz) sampling rate.

In its present configuration, GRAS data suffers from three issues:

(i) For a small part (about 6 %) of (predominantly rising) occultations, L2 tracking does not work as expected, resulting in low L2 SNR values and frequent L2 full cycle slips for the occultations affected. Full cycle slips must be handled in the GO processing, but not when using spectral methods and are not even well defined for multipath situations. We note that, compared to other radio occultation receivers, GRAS' L2 performance can still be regarded as excellent.

(ii) Open loop data regularly suffers from data gaps in lower tropospheric data. These data gaps can last for several seconds.

(iii) A significant part of rising occultations (33 % or about 16 % of all occultations) suffers from data gaps in the mid troposphere. The problem occurs for rising occultations located in the tropics and subtropics.

7.4.6 References

Ao, C. O., G. A. Hajj, T. K. Meehan, D. Dong, B. A. Iijima, A. J. Mannucci, and E. R. Kursinski (2009). Rising and setting GPS occultations by use of open-loop tracking. Journal of Geophysical Research 114.

Boashash, B. (Ed.) (2003). Time Frequency Signal Analysis and Processing. Elsevier Science.

Born, M. and E. Wolf (1999). Principles of Optics. Cambridge University Press.

Cohen, L. (1995). Time-Frequency Analysis (1st ed.). Prentice Hall.

Flandrin, P. (1998). Time-Frequency/Time-Scale Analysis (1st ed.). Academic Press. Gorbunov, M. E. (2002a). Canonical transform method for processing radio occultation data in the lower troposphere. Radio Sci. 37, 10.1029/2000RS002592.

Gorbunov, M. E., H.-H. Benzon, A. S. Jensen, M. S. Lohmann, and A. S. Nielsen (2004). Comparative analysis of radio occultation processing approaches based on Fourier integral operators. Radio Science 39 (6).

Gorbunov, M. E. and K. B. Lauritsen (2004). Analysis of wave fields by Fourier integral operators and their application for radio occultations. Radio Science 39 (4).

Jensen, A. S., M. S. Lohmann, H.-H. Benzon, and A. S. Nielsen (2003). Full Spectrum Inversion of radio occultation signals. Radio Science 38 (3).

Sokolovskiy, S., C. Rocken, W. Schreiner, and D. Hunt (2010, November). On the uncertainty of radio occultation inversions in the lower troposphere. Journal of Geophysical Research 115 (D22),1–19.

Sokolovskiy, S. V. (2001). Modeling and inverting radio occultation signals in the moist

Vorob'ev, V. V. and T. G. Krasil'nikova (1994). Estimation of the accuracy of the atmospheric refractive index recovery from doppler shift measurements at frequencies used in the NAVSTAR system. USSR Phys. Atmos. Ocean, Engl. Transl. 29, 602–609.

7.5 Intercomparison of Retrieval Results

7.5.1 Data Processing Differences

This GRAS RO Performance Study was set up to analyse the overall GRAS data quality, to investigate the potential of the raw sampling measurement mode, and to evaluate different processing options for tropospheric GRAS data. In parallel, EUMETSAT funded a joint study with UCAR (University Cooperation for Atmospheric Research, USA; contract no. EUM/CO/4600000677/AVE) in which a retrieval chain for GRAS data based on the EUMETSAT prototype for the low level data reconstruction and the COSMIC processing suite for higher level products was implemented. This section summarizes some of the preliminary findings of these studies relevant for tropospheric observations from the GRAS receiver.

The four centres participating in the ESA study each provided one day (30th September 2007) of bending angle profiles retrieved from the test data set compiled by EUMETSAT; UCAR provided data for the same day, but processed from level 0. Some of the key differences in the various level 1b implementations used for the GRAS data are summarized in Table 15, and are discussed in more detail in the following. We note that all processing centres chose to downsample the available 1 kHz raw sampling data to 50 Hz to make it compatible to the closed loop data; potential benefits of the high raw sampling data rate therefore have not yet been fully exploited.

Centre	Algorithms	Filtering	Data Gap Handling	Other
DMI	CT2 < 25 km, GO above	radioholographic filtering; combined ionospheric correction & statistical optimisation	Interpolation over data gaps < 0.8 sec	Internal navigation bits if needed
GFZ	FSI < 12 km, GO above	GO: 0.8 sec polynomial filter	Cutting off below highest data gap	Internal navigation bits if needed
UoG	CT in troposphere, GO above	1.5 sec polynomial filter	Cutting off below highest data gap	Setting occultations only
UCAR	FSI in troposphere, GO above	1 sec polynomial filter	Interpolation over data gaps < 1 sec	Internal navigation bits if needed
EUM WO	FSI (all altitudes)	Kaiser & altitude dependent polynomial filter in impact parameter space (Fresnel radius)	Zeroing with data gap identification	Internal navigation bits if needed
EUM GO	GO (all altitudes)	1.5 sec polynomial filter (Fresnel radius)	Cutting off below highest data gap	Closed loop data only

Table 15 Retrieval options implemented by the various participating processing centres.

Generally, all centres apart from EUMETSAT implement a split altitude retrieval scheme, where tropospheric bending angles are retrieved using an advanced (wave optics) method, while stratospheric retrievals are based on the traditional geometrical optics approach. The partial retrievals are then merged over some altitude range, with details of the implementation and split altitude selection varying between the centres (some details can be found in Table 15). EUMETSAT is an exception, using an advanced retrieval algorithm for the entire altitude range in order to avoid a transition region and potential inconsistency issues due to filtering and data merging in the affected altitude region.

DMI and the University of Graz implement a Canonical Transform (CT) method (Gorbunov, 2002a; Gorbunov and Lauritsen, 2004) based on code maintained by the original author of this method. All other retrievals are based on mutually independent implementations of the Full Spectrum Inversion (FSI) algorithm (Jensen et al., 2003). For the purpose of this study, EUMETSAT also provided a pure geometrical optics retrieval. While this is not considered state-of-the-art for the processing of tropospheric radio occultation data, it serves as a proxy for EUMETSAT's operational retrievals.

Filter options vary considerably between the centres: At DMI, a combined ionospheric correction and statistical optimisation procedure is applied using profile dependent settings Gorbunov (2002b), while UCAR uses a different optimal noise filtering approach (Gorbunov et al., 2004). Both treat tropospheric data with a radio-holographic filter with profile specific, but varying settings (Gorbunov et al., 2006). GFZ, the University of Graz and EUMETSAT apply the traditional ionospheric correction of bending angles (Vorob'ev and Krasil'nikova, 1994) after having smoothed the observed (excess) carrier phase measurements with a polynomial filter (e.g., Hocke, 1997); the width of smoothing windows is different for each centre. EUMETSAT's FSI retrieval uses a two-stage filtering approach: First, a short Kaiser-Filter is applied to the numerically differentiated phase of the Fourier-transformed signal controlling the high frequency numerical noise introduced by the finite differencing. Next, bending angles are smoothed by local polynomial regression in impact parameter space using altitude dependent smoothing windows. The width of these windows is in the order of the local Fresnel radius and roughly equivalent to the excess phase smoothing window in EUMETSAT's geometrical optics window.

The handling of data gaps was already discussed previously (see section 7.4.3). In three retrievals (GFZ, University of Graz, and EUMETSAT's geometrical optics), data is cut off below the highest data gap. DMI and UCAR interpolate over sufficiently short data gaps, while EUMETSAT's FSI zeros phase and amplitude of the signal during data gaps, aiming at identifying them later on in the processing.

Finally, bending angle profiles were provided by all centres without statistical optimization being applied, avoiding systematic a priori effects influencing statistical comparisons in the stratosphere. All processing centres also used externally provided navigation data bits in the preprocessing of the raw sampling data if available, and fall back to the navigation bit data estimated from the raw sampling data by EUMETSAT if needed. Unfortunately, one centre (University of Graz) was only able to process setting occultations due to some format problems in the data files delivered by EUMETSAT.

7.5.2 Number of Profiles

While all data centres used the same GRAS level 1a (amplitude and phase) data set for the retrieval of their bending angles, the number of successful retrievals provided back to the intercomparison varied significantly. Most profiles were produced by the two EUMETSAT processing chains (685 and 683 for geometrical and wave optics, corresponding to 97% of a total of 705 profiles available on that day). DMI provided 613 profiles (87% of all available profiles), UCAR 543 (77%) GFZ 442 (63%), and University of Graz 190 profiles (27%).

Different bending angle profile numbers are mostly due to different overall quality control algorithms implemented in the various processing centres; for example, UCAR performs a quality control against NWP data and does not provide profiles which deviate too strongly from a short range forecast. The different numbers may also reflect bugs in the software which are triggered by GRAS' specific low level data characteristics (and hence do not allow for the successful processing of affected occultations). As pointed out before, the University of Graz could unfortunately only process setting occultations. Nevertheless, the number of profiles from this centre is particularly low and represents the lowest return of successful retrievals from all participating centres. The reasons for this are under investigation.

The number of occultations may have an impact on comparison statistics, as very stringent quality control approaches resulting in a low number of accepted profiles may select only those cases which also agree exceptionally well with ECMWF data. In order to account for this in the intercomparisons to follow, the calculation of biases and standard deviations use robust M-estimators for scale (bias) and spread (standard deviation) using Tukey's biweight as weight function. This ensures that large deviations against ECMWF found in a small number of individual profiles do not affect the overall statistics. The algorithm also returns an effective number of profiles being used for the calculation of the respective statistics for each level. A data set containing a significant number of outliers might therefore exhibit a robust bias and standard deviation which is similar to a second data set without outliers, but the effective number of observations will be reduced according the number of outliers. We finally note that for all comparisons, bending angle profiles were thinned to the operational 247 level set also used by the operational GRAS data using the ROPP software package, unless the data wasn't provided on these levels anyway.

7.5.3 Stratospheric Intercomparisons

Figure 117 shows a comparison of the bending angle profiles with co-located ECMWF data, focussing on stratospheric bending angles. ECMWF short range forecast data was forward modelled to bending angles using the ROPP software package by the GRAS SAF. We emphasize that ECMWF data is not seen as truth, but rather as a transfer data set providing a convenient way to intercompare data sets with different number of available occultations. Note that in the vertical altitude scale ("impact height") used here, Earth's surface corresponds to an altitude between 2 and 3 km.

Above impact parameters of 8 km, bending angle profiles from all participating centres agree very well to each other, with biases typically in the order of 0.1% or less between each other. Biases against ECMWF are larger, with a negative bias in the order of -0.2% between 15 and 35 km impact altitude, and a more variable structure exhibiting larger biases above. The vertical bias structure above 10km is consistent with earlier data validation studies undertaken for GRAS data (von Engeln et al., 2010), and both size and vertical structure of the bending angle bias against ECMWF are usually attributed to shortcomings of the forecast system (Healy, pers. comm.).

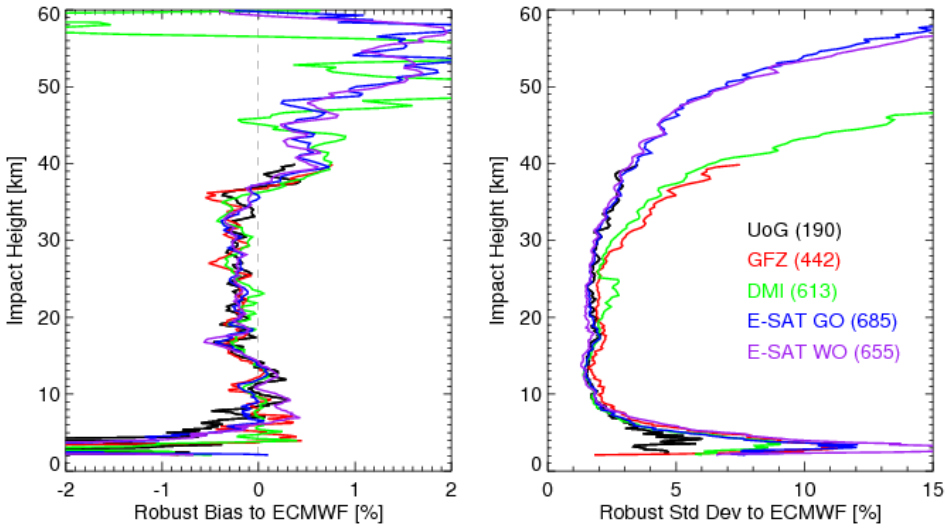

Figure 117 Bias (left) and standard deviation (right) over altitude with respect to ECMWF for different wave optics processing streams. All results based on EUMESAT reconstructed data for 30th of Sep. 2007. The number of successfully processed occultations is given in brackets.

As for the standard deviations, lower and mid (8–30 km) stratospheric values are in the order of 2–3% for all participating data centres, with GFZ's data exhibiting a marginally larger standard deviations. An interesting feature in the DMI data is the blob of increased standard deviations at the top end of the CT retrieval just below 25 km impact parameter altitude, marking the transition between tropospheric wave optics and stratospheric geometrical optics retrieval methodologies in this data set. Later versions of the DMI retrieval system address this particular issue by fine tuning filter parameters for the transition region.

Above 30 km in impact altitude, the standard deviations of two centres (DMI and GFZ) increase more quickly than for the remaining ones. Experimentation at one centre (GFZ) confirmed that the size of the upper stratospheric spread against ECMWF is mainly driven by the choice of the excess phase smoothing usually undertaken as part of the geometrical optics retrieval applied in the stratosphere, consistent with earlier findings by Marquardt and Healy (2005). The differences in the standard deviations shown by the various retrievals are considered to be fully understood as consequences of the various centre's decisions on filter options applied during the preprocessing of the data.

Note that the two EUMETSAT retrievals maintain consistent noise characteristics at all stratospheric altitudes, exhibiting standard deviations against ECMWF very similar to those from the University of Graz data. This confirms that a split-and-merge approach for stratospheric radio occultation retrievals (as implemented in all retrievals apart from EUMETSAT's wave optics) is not required to achieve good stratospheric retrieval performance. As the EUMETSAT retrieval demonstrates, wave optics retrievals can be applied successfully in the stratosphere as well, provided consistent filter methods are implemented.

Overall, our findings are in good agreement with earlier results of radio occultation centre intercomparisons for stratospheric data based on CHAMP data (Ho et al., 2009). In particular, they confirm the high level of maturity of processing algorithms and their implementations for stratospheric radio occultation data at all participating centres.

We note that the comparison statistics in the stratosphere are not strongly affected by the number of available occultations. The effective profile numbers output by the robust bias and standard deviation algorithm do not differ by more than 5% between centres, suggesting that the number of profiles provided by the various data centres has no significant impact on the comparison statistics. In particular, the bulk of data from the high number of retrievals provided by EUMETSAT exhibits a very similar statistics to that obtained from the lower profile number data sets. Thus, the lower number of successfully retrieved bending angle profiles provided by all centres compared to EUMETSAT does not lead to significantly "better" data quality, at least not as far as comparisons against ECMWF is concerned.

7.5.4 Tropospheric Intercomparisons

A closer look at tropospheric statistics is provided in Figure 118, along with the penetration statistics of profiles into the lower troposphere. In contrast to the stratospheric data, where all retrievals more or less exhibit the same comparison statistics against ECMWF (and even share small vertical scale details in their bias and standard deviation structures), it is apparent that both biases and standard deviations become more diverse between the different processing centres in the troposphere.

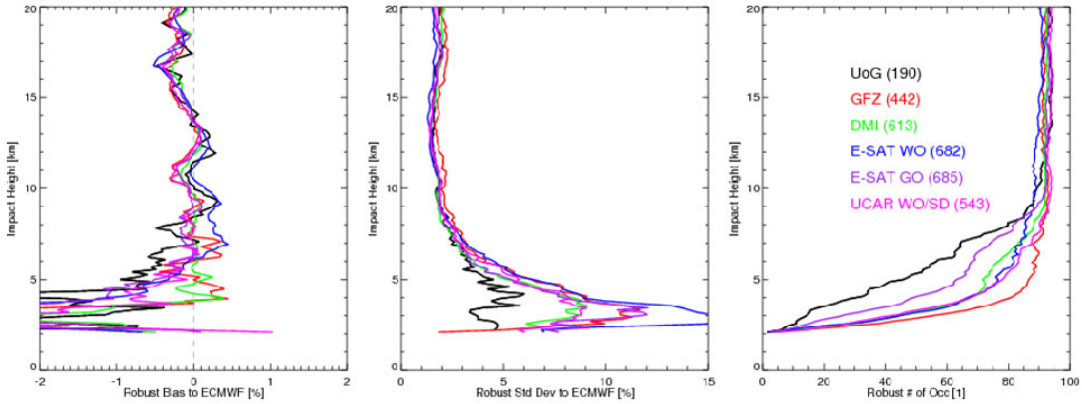

Figure 118 Robust bias (left), robust standard deviation (middle) and penetration depth (right) in the troposphere for of different processing streams. The number of successfully processed occultations is given in brackets.

Two centres (DMI and GFZ) produce bending angle profiles which appear to be unbiased (within 0.5%) against ECMWF down to 4 km impact altitude. Wave optics retrievals from the other three centres (University of Graz, UCAR and EUMETSAT) exhibit negative biases against ECMWF for impact altitudes below 6 km. Around 4 km impact altitude, both the UCAR and EUMETSAT wave optics bias is in the order of - 1%, with Graz retrievals showing slightly larger negative biases. The EUMETSAT wave optics retrieval also suffers from a small (0.2-0.3%) positive bias against ECMWF and all other retrievals between 6 and 10 km in impact altitude. We note that the high consistency in the vertical bias structures between centres observed in the stratosphere breaks down below about 10 km impact altitude.

In addition to the absolute number of profiles available from each processing centre, statistics in the troposphere is also dependent on how far down bending angle profiles reach. Penetration depth is also shown in Figure 118 (right), represented by the number of profiles reaching down to a given altitude and normalized by the number of available occultations within the respective processing stream. Penetration depth is primarily influenced by the cut off criteria for tropospheric data implemented by the various retrieval schemes. It therefore represents another quality control measure applied during the retrieval. With SNR decreasing with altitude, extending radio occultation observations deeper down into the troposphere results in increased noise and uncertainty, potentially causing larger deviations against the reference ECMWF data set. With the exception of the University of Graz and the geometrical optics EUMETSAT retrieval, all processing centres have tuned their processing to deliver data down to the lowest km of the atmosphere (corresponding to altitudes below 3 km in impact altitude) for at least 50% of all processed profiles. On one hand, this demonstrates that GRAS raw sampling data allows the sounding of the Earth's atmosphere down to the lowest km. On the other hand, the inclusion of low SNR data means that smoothing and filtering of the data becomes even more important, with subtle differences between the implementations potentially having significant impacts on the comparison statistics. In case of the University of Graz retrievals, the figure also shows the practical impact of data gaps on the retrieval performance, as this processing centre chose not to use data below the first data gap. This might be part of the reason why the same data set also exhibits the smallest standard deviations against ECMWF, as the statistics in effect has been cleaned from the majority of low SNR tropospheric measurements.

The other extreme with respect to standard deviations is found for the EUMETSAT wave optics data, which is even larger than the standard deviations for the geometrical optics retrieval from the same provider. EUMETSAT's penetration depth is comparable to those from DMI and UCAR, suggesting that the poorer statistics of the EUMETSAT retrievals is not related to significantly different penetration behaviour. An initial analysis of the data set indicates that it is the particular way of dealing with data gaps (as discussed in section 4.2) that causes artefacts in the profile retrievals and larger random deviations against ECMWF in the lower troposphere. Work is underway to address these issues, and to make standard deviations of the EUMETSAT retrieval more consistent with the better results from DMI and UCAR.

While DMI, UCAR and EUMETSAT retrievals exhibit comparable penetration depth statistics, GFZ stands out by providing more bending angle retrievals below 6 km impact altitude than all other centres, at the same time exhibiting larger standard deviations in these altitude regions. As discussed above, the inclusion of more low SNR data points could contribute to the increased standard deviations in the GFZ data set compared to DMI and UCAR.

A direct comparison of bending angle profiles successfully processed by GFZ, DMI and EUMETSAT is shown in Figure 119, stratified into low, mid and high latitudes. No systematic tropospheric biases are found between GFZ and DMI retrievals, while tropospheric standard deviations are larger than in the stratosphere, and depend on the latitude band. Smallest standard deviations are found in high latitudes (< 2%), increasing towards mid and low latitudes (< 3 and < 5%, respectively). Even tropical standard deviations are smaller than the global standard deviations against ECMWF profiles, confirming that an important contribution in the standard deviations between bending angle profiles from radio occultation measurements and NWP data as shown in Figure 118 are the uncertainties in the NWP data.

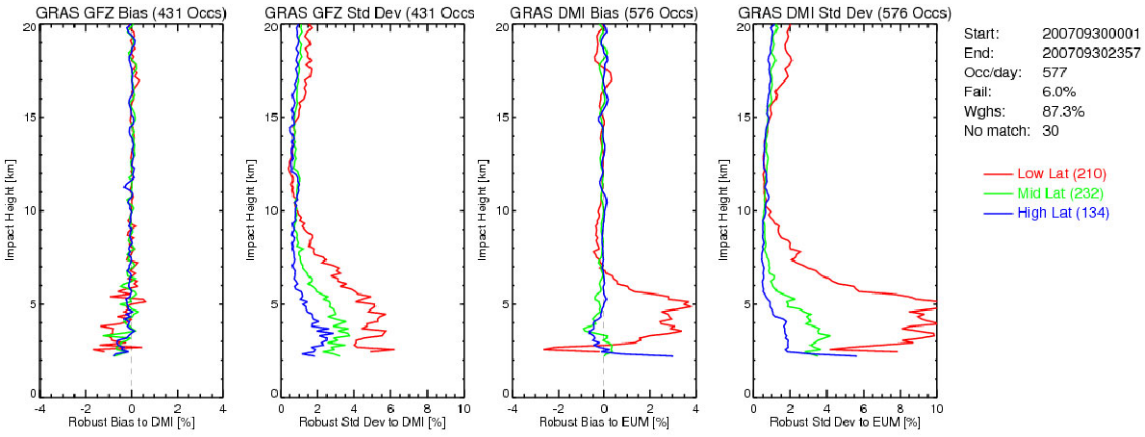

(a) GFZ vs. DMI (b) DMI vs. EUM

Figure 119 Matched profile intercomparison between (a) GFZ and DMI as well as (b) DMI and EUMETSAT retrievals for low (30' S – 30' N, red), mid (30' – 60', green) and high (60' – 90', blue) latitudes. Each subfigure shows robust biases (left) and robust standard deviations (right).

It is interesting to note that the EUMETSAT bending angle retrievals do not show systematic biases against DMI in mid and high latitudes; the standard deviations obtained for those regions are also similar to those obtained from comparing GFZ and DMI data. Tropical retrievals in the lower troposphere, however, differ significantly in both bias and standard deviation. Given that low SNR data as well as quality control issues like data gaps predominantly occur in the tropics, the finding suggests that it is not the choice of the main retrieval algorithm itself (e.g., CT in case of DMI or FSI in case of EUMETSAT) that causes large structural uncertainty issues in tropospheric retrievals, but rather other processing choices implemented around that particular core algorithm - predominantly quality control measures, filtering and – for GRAS data – the handling of data gaps. A similar conclusion can be drawn from the fact that the core retrieval algorithms in both the University of Graz and DMI processing systems are exploiting the same CT algorithm based on code written by the original author.

We would finally like to point out that a single day of data as used in this preliminary study certainly provides a useful basis to identify structural uncertainty issues, but does not allow for a decision on which implementation is “best”. The study team will therefore continue its efforts to develop a better understanding of the role of processing and quality control options in the processing of tropospheric radio occultation data based on a larger data set.

7.5.5 Conclusions

Based on the FSI bending angle retrieval implemented at EUMETSAT, we showed some impacts of these data gaps on retrieval diagnostics. When zeroing measurements over data gaps, the latter show up as drops in the FSI amplitude, allowing in principle to identify their location in the transformed Doppler space. On the other hand, lower tropospheric measurements obtained under low SNR conditions are characterized by similarly low values in the FSI amplitude. This suggests that the information content of radio occultation measurements in the lower troposphere is limited; retrievals of geophysical parameters like bending angles may thus depend strongly on a priori information used during the processing. Different implementations of retrievals might therefore cause differences in the retrieved bending angles despite using identical raw measurements, a problem also known as “structural uncertainty”.

As part of this study, we also performed a first intercomparison of both stratospheric and tropospheric bending angle retrievals from all participating centres. As all retrievals (apart from the UCAR data) are based on the same level 1a data set, differences in the retrievals of bending angles and other geophysical products are solely related to differences in the processing setup of the participating centres, i.e. structural uncertainties. Results presented in this study refer to data covering a single day. This is not considered to be a representative data set well suited for an extensive data analysis and validation, but it should be sufficient to detect structural uncertainty issues in bending angle retrievals.

Stratospheric retrievals were found to agree within 2–3% at altitudes between 8 and 30 km, without significant biases between the retrievals of the various centres. Small systematic deviations between bending angle retrieval and ECMWF profiles are known from other studies, and are usually attributed to shortcomings in the NWP analyses or short range forecasts. Thus, the study confirms previous results regarding retrievals from other radio occultation receivers.

Significantly larger deviations were found in tropospheric retrieval results. For the majority of the processing centres, lower tropospheric global bending angle standard deviations against ECMWF data are as large as 8–11% in the lowest few kilometres of the troposphere. The EUMETSAT retrievals stand out by exhibiting the largest standard deviations; manual inspection of several sample cases suggests that the cause for the large deviations is an imperfect treatment of the data gaps after zeroing the measured signal causing spurious fluctuations in the retrieved bending angles. This interpretation is confirmed by another data set provided by the University of Graz, consisting of profiles only above tropospheric data gaps, and showing significantly smaller standard deviations.

With respect to biases against ECMWF short range forecasts, the retrieval data sets can be separated into two groups: one being unbiased even in the lowest few km (two data centres), and a second data set showing a small negative bias in the order of - 1% in the lowest 2–3 km. Given the limited size of the data set, it is not possible to draw conclusions on which data sets are better reflecting the true atmospheric state being observed, especially as NWP analyses and forecasts are also known to have problems with the representation of humidity. More detailed conclusions would require a more detailed analysis, using a longer period of test data, and possibly also independent measurements of lower tropospheric humidity content.

The direct comparison of matching bending angle profiles between processing centres, stratified by latitude, further shows that both biases and standard deviations between different retrievals are largest in tropics and decrease towards mid and high latitudes. In particular, the comparatively poor performance of EUMETSAT's tropospheric retrievals in terms of standard deviations is limited to the tropics, while its statistics cannot be distinguished from that of data from other processing centres in the remaining latitude bands. On the other hand, data gap issues in the GRAS data are mostly prevalent in the tropics. This suggests that it is not the selection of any particular kind of advanced retrieval algorithm (i.e., FSI or CT) that causes the observed differences in the comparison statistics, as retrievals from the various participating centres all perform similarly well in mid and high latitudes. Instead, the quality control and data cleaning (or interpolation) methodologies implemented in the various retrieval chains appear to cause the majority of differences between tropospheric bending angle retrievals. Overall, the zeroing approach originally chosen at EUMETSAT appears to perform worst, producing the largest random deviations compared to ECMWF. But different ways to implement interpolation over data gaps also seem to cause increased standard deviations in regions where data gaps often occur, i.e. in the tropics.

Major differences between data sets also related to different quality control and data editing approaches exist in the number of available data, both in terms of numbers of profiles being available (ranging from little more than 50% to more than 95% of all available occultations), and in the penetration depth of profiles into the lower troposphere. It could not be demonstrated that those centres providing fewer profiles produce consistently better stratospheric results in terms of agreement with ECMWF data, at least not in the context of robust statistical methods applied in this study. In the troposphere, most processing centres achieve a penetration down to the lowest km, although different cut-off criteria employed by the various centres cause slightly different penetration statistics. With standard deviations in the troposphere varying significantly more between processing centres compared to the stratosphere, no conclusions on the impact on different penetration depths on the agreement with ECMWF could be drawn. However, it is noted that a data set restricted to gap-free data shows the lowest standard deviations against ECMWF (and the poorest performance in terms of penetration depth), while the data set exhibiting the deepest penetration suffers from the highest standard deviations (apart from the EUMETSAT data set) against ECMWF in the lower troposphere.

7.5.6 References

Gorbunov, M. E. (2002a). Canonical transform method for processing radio occultation data in the lower troposphere. Radio Sci. 37, 10.1029/2000RS002592.

Gorbunov, M. E. (2002b). Ionospheric correction and statistical optimization of radio occultation data. Radio Sci. 37, 10.1029/2000RS002370.

Gorbunov, M. E., H.-H. Benzon, A. S. Jensen, M. S. Lohmann, and A. S. Nielsen (2004). Comparative analysis of radio occultation processing approaches based on Fourier integral operators. Radio Science 39 (6).

Gorbunov, M. E. and K. B. Lauritsen (2004). Analysis of wave fields by Fourier integral operators and their application for radio occultations. Radio Science 39 (4).

Gorbunov, M. E., K. B. Lauritsen, a. Rhodin, M. Tomassini, and L. Kornblueh (2006). Radio holographic filtering, error estimation, and quality control of radio occultation data. Journal of Geophysical Research 111 (D10), 1–10.

Ho, S.-p., G. Kirchengast, S. Leroy, J. Wickert, A. J. Mannucci, A. Steiner, D. Hunt, W. Schreiner, S. Sokolovskiy, C. Ao, M. Borsche, A. von Engeln, U. Foelsche, S. Heise, B. Iijima, Y.-H. Kuo, R. Kursinski, B. Pirscher, M. Ringer, C. Rocken, and T. Schmidt (2009, December). Estimating the uncertainty of using GPS radio occultation data for climate monitoring: Intercomparison of CHAMP refractivity climate records from 2002 to 2006 from different data centers. Journal of Geophysical Research 114 (D23), 1–20.

Hocke, K. (1997). Inversion of GPS meteorology data. Ann. Geophys. 15, 443–450.

Jensen, A. S., M. S. Lohmann, H.-H. Benzon, and A. S. Nielsen (2003). Full Spectrum Inversion of radio occultation signals. Radio Science 38 (3).

Marquardt, C. and S. B. Healy (2005). Measurement noise and stratospheric gravity wave characteristics obtained from GPS occultation data. J. Met. Soc. Jap. 83 (3), 417–428.

von Engeln, A., S. Healy, C. Marquardt, Y. Andres, and F. Sancho (2010). Validation of operational GRAS Radio Occultation Data. Geophysical Research Letters 36.

Vorob'ev, V. V. and T. G. Krasil'nikova (1994). Estimation of the accuracy of the atmospheric refractive index recovery from doppler shift measurements at frequencies used in the NAVSTAR system. USSR Phys. Atmos. Ocean, Engl. Transl. 29, 602–609.

8 ZENITH DATA ANALYSIS

8.1 Background

GRAS performance related to POD and navigation has been reported in [RD1, RD2]. Two outstanding issues related to the findings in [RD1, RD2] are further assessed in this report:

- Distance between MetOp Centre of Mass and zenith antenna phase centre.

  Here [RD2] reports that kinematic positioning results show a 2–4 cm radial offsets with respect to the reduced dynamic solutions and suggest that the radial offsets are most likely related to a systematic bias of the assumed vector between the spacecraft centre-of-mass and antenna phase centre locations and suggest that the distance in the +Z direction should be reduced accordingly.

- Codeless tracking losses:

  Here [RD2] reports findings that suggest that the code-less tracking losses of the GRAS instrument compared to the PolarRx2 receiver may be on the order of 2.5 dB higher.

8.2 Distance Between COM and Antenna Phase Centre

The analysis of the radial distance between Centre of Mass (COM) and the zenith Antenna Phase Centre (APC) has been refined by O. Montenbruck (DLR), by comparing Reduced Dynamic Orbit solutions and the Kinematic Orbit solutions, based on the one-month (September 2007) data set used for this study.

The current data set is about 10 times longer than the data set used in [RD1, RD2]. From this data set, the Z-distance between actual COM and the actual APC, is estimated to be 3.7 cm longer, than the distance between COM and APC values applied to the POD processing.

Estimation of the distance between COM and APC from POD solutions are illustrated in Figure 120 and are explained by:

- A Dynamic POD solution ties the estimated orbit to the COM (green left dot)
- A Kinematic POD solution ties the estimated orbit to the APC (green right dot)
- The distance between APC and COM can be estimated from the difference between the Dynamic, and the Kinematic POD solution (green to black).
- This distance is compared to the distance defined by the GRAS Instrument Characterization Data Base (ICDB) – (green to red).
- The discrepancy is about 3.7 cm in the radial direction

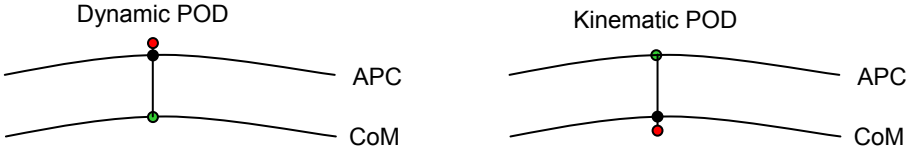

Figure 120 Distance CoM - APC determined from Dynamic and Kinematic POD.

To identify potential causes of the detected radial offset the alignment between the electrical phase centre of the two zenith antenna elements and the COM of MetOp has been broken down into the sub-alignment steps illustrated in Figure 121 and each step has been reassessed to the best possible accuracy based on the available data. The breakdown includes reassessment of the:

- Electrical antenna phase centre positions in the antenna reference frame (ARF)
- Alignment between antenna and payload module reference frames
- Alignment between payload module and the space craft reference frames
- Centre of mass in the space craft reference frame

The assessments are summarised in the next section and further details are found in later sub-sections and in annexed documents.

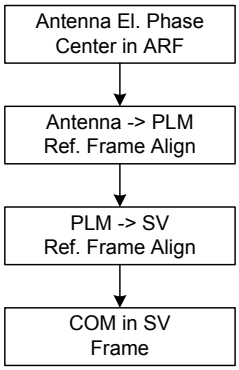

Figure 121 Alignment between antenna phase centre and MetOp COM.

Information about the distance between centre of mass (CoM) and antenna phase centre (APC) is comprised in the ICDB. This information is in part carried by geometrical vectors and in part by phase mapped vectors (mapped across azimuth and elevation). The information is treated slightly different in the ICDB and during the POD processing, see Figure 122.

For the ICDB, the distance between

- CoM and ARP (Antenna Reference Point) is described by geometrical vectors
- ARP and APC of the L1 and L2 antenna is defined as a phase mapped vectors

For POD processing, the phase mapped vector between ARP and zenith antenna phase centre (APC) is transformed to ANTEX file representation, where two new physical reference points are defined close to the physical centre of the L1 and L2 antenna. The ANTEX file then comprises:

- Two geometrical vectors from ARP to the added reference points, ANTEX-REF.
- Two phase mapped vectors from ANTEX-REF to APC

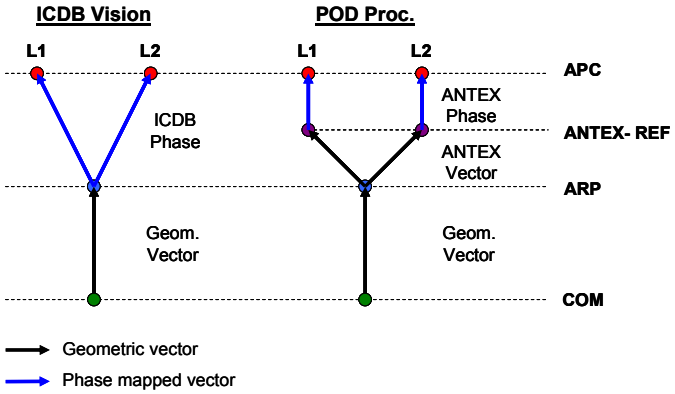

Figure 122 Vector definition between CoM and APC used for ICDB and POD.

8.2.1 Summary of Assessments

8.2.1.1 Antenna Phase Centre in Antenna Reference Frame

Based on measured data, the best-fit electrical phase centre of the Gras Zenith Antenna (GZA) L1 and L2 elements has been estimated to be positioned 10 mm above (Z_ant = 10 mm) the centre of the radiating apertures. Data was obtained from the ICDB which is generated from isolated antenna pattern measurements at RUAG.

For POD processing the antenna phase corrections of the ICDB are transformed to separate reference points for the L1 and L2 element, and formatted into an ANTEX file. Also this representation is consistent with a phase centre 10 mm above the centre of the radiating apertures, see §8.2.3.1.

Antenna measurement data has been reviewed in order to identify potential errors for the best-fit electrical phase centres, but no error has been identified.

Further POD residuals has been compared to simulated multipath based on GTD (Geometrical Theory of Diffraction) analysis, in order to assess the potential of using simulate MP to compensate and potentially improve the POD solution. Based on the result presented in §8.2.3.2, the POD solution would be degrade by such a compensation and this method will not be perused further.

8.2.1.2 Alignment: Antenna to Payload Reference Frames

The antenna alignment in the PLM reference frame has been reviewed and we have high confidence that the alignment is correct based on [RD4] pp 141 & 147:

- x-y positions is directly measured; [x,y] = [-635, -913.2] mm.
- z position is measured to 900 mm at antenna-PLM interface and 67.4 mm are added according to RES drawing.
- GZA origin in PLM frame: [x,y,z] = [-635, -913.2, 967.4] mm
- Measurement error < ± 1 mm

8.2.1.3 Alignment: Payload to Space Craft Reference Frames

The best information we have available here is drawing based information from EADS, see §8.2.3.3. The dominating error is a rotational misalignment and the estimated uncertainty in the z-direction is below 0.5 mm.

8.2.1.4 Centre of Mass in Space Craft Reference Frame

The Centre of Mass (COM) in the SV frame (SVF) has been revised by EADS as a result of the reassessment of WP2000, see [RD5]. The revised values are summarised in Table 16 along with the original estimate comprised in the ICDB. With respect to the Z-direction, COM has moved approximately 18 mm closer to the GZA antenna, This corresponds to about half of the bias observed by POD. The revised value of COM is inline with independent estimates performed by EUMETSAT, see [RD5].

COM in SVF	X	Y	Z
Current DB	-1871.0 mm	81.0 mm	51.0 mm
COM April 2009	-1882.5 mm	79.4 mm	68,8 mm
Delta	-11.5 mm	-1.6 mm	17.8 mm

Table 16 Revision of centre of mass (COM)

Reassessment of COM has also revealed that COM is fuel dependant and will vary with space vehicle SV lifetime. In the Z-direction a variation of about 5 to 6mm is foreseen between beginning of life BOL and end of life EOL. This variation can be predicted based on fuel consumption, and EADS has agreed to update the ICDB to include information that facilitates this.

Further COM will exhibit an orbital variation (approximately sinusoidal shape) of ±2mm in the Y and Z direction. The variation is predictable and is related to the orientation of the solar panels. With respect to POD performance insignificant impact is foreseen.

8.2.2 Conclusion

The alignment between the electrical phase centre of the two zenith antenna elements and the centre of mass COM of MetOp has been broken down into the following sub-alignment steps:

- Electrical antenna phase centre positions in the antenna reference frame (ARF)
- Alignment between antenna and payload module reference frames
- Alignment between payload module and the space craft reference frames
- Centre of mass in the space craft reference frame

Each step has been reassessed to the accuracy possible based on the available data. The radial bias between COM and the Antenna Phase Centre (APC) which was observed by the POD processing has been reduced from 3.7 cm to approx 2 cm. Two cm is still larger than expected but no further explanation has been identified.

8.2.3 Sub-assessments

8.2.3.1 Electrical Phase Centre (EPC) Used for POD

During POD processing the ICDB antenna phase characteristics were represented separately for the L1 and L2 elements in an ANTEX files. The reference positions used in the ANTEX file are shown in Table 17, where the X, Y coordinates are located within 1 mm of the centre of the radiating apertures.

The average range correction of the ANTEX file versus elevation is illustrated in Figure 123, where the parabolic shape indicates that the electrical phase centre includes an additional offset in the Z-direction.

The best-fit electrical phase centre is estimated to be positioned with an additional Z offset of 9.7 mm and 3.8 mm for L1 respectively L2 and the corresponding best-fit estimate of the electrical phase centre is listed as Z_EPC in Table 17. The antenna phase corrections corresponding to Z_EPC are illustrated in Figure 123 as the average correction versus elevation.

	X_ant	Y_ant	Z_ant	Z_corr	Z_EPC
L1	-47.38 mm	-47.38 mm	1.20 mm	9.7 mm	10.9 mm
L2	47.38 mm	47.38 mm	6.29 mm	3.8 mm	10.0 mm

Table 17 Reference positions used in the ANTEX file

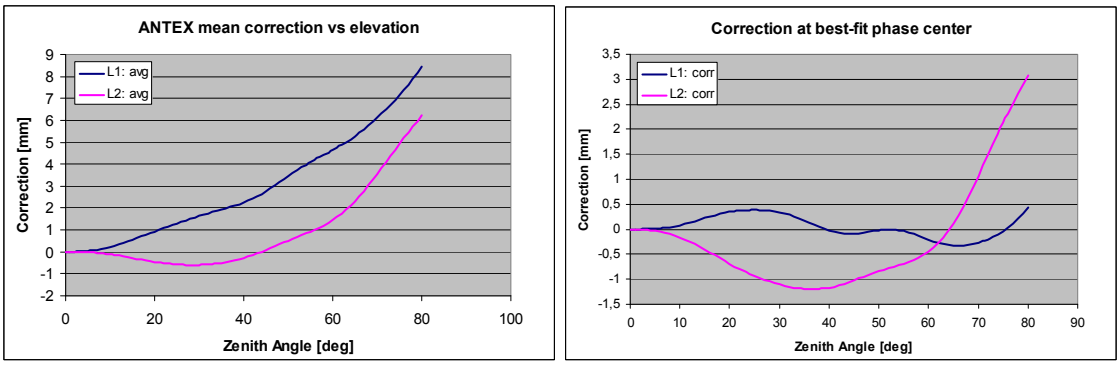

Figure 123 Left: ANTEX mean correction vs. zenith angle. Right: Transformed corrections at best fit phase centres.

8.2.3.2 POD Residuals Versus Simulated Multipath

In this section simulated multipath residuals are compared to POD residuals, in order to assess if the simulate multipath error can be used to compensate and potentially improve the POD processing.

8.2.3.2.1 Simulated Multipath Patterns.

During the Gras Zenith Antenna (GZA) development, the S/C impact was assessed using GTD S/W based on ray tracing and diffraction. This is adequate for calculating the scattering of the radiation from an isolated source from a large object. It is less accurate when the scattered field is reacting with the source as can be expected for the GZA antenna placed on the S/C zenith deck.

The impact of local multipath, LMP, is estimated from the difference between on-farm simulations and the measured isolated antenna pattern, i.e. the phase is calculated for the antenna on the S/C relative to the phase for the isolated antenna. This calculation is made for L1 and L2, and then the ionosphere free combination is formed, see Figure 124 and Figure 125.

In the GTD analysis, patterns are given in the S/C coordinate system with Z-axis in the Zenith direction, and the S/C flying in the -Y direction, and the solar array in the direction of the X-axis. The analyses are made for a number of Solar Array, SA, positions. We chose here to present the result for a solar array position where the interference from solar array reflections is relatively small. This is deemed to best represent an antenna pattern obtained from averaging over long time periods.

Isolated patterns represent the pattern provided in the GRAS ICDB. Subtracting the isolated antenna phase corresponds hence approximately to compensating the antenna pattern with the reference pattern provided in the ICDB.

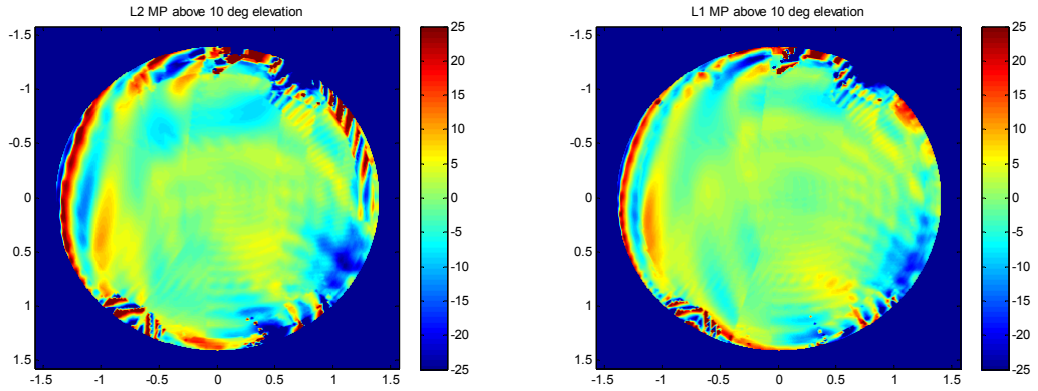

Figure 124 Local multipath residual above 10° elevation estimated from GTD analysis. Left: L1; Right: L2. (Angular scale in radians)

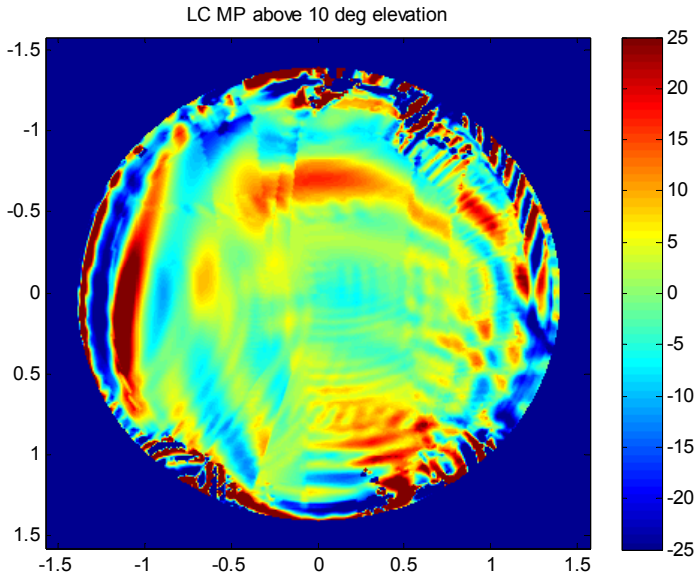

Figure 125 Ionosphere free combination (LC) formed from plots in Figure 124. (Angular scale in radians)

8.2.3.2.2 Ionosphere Free Residual from POD Analysis.

POD ionosphere range residuals, has been mapped to azimuth and elevation and averaged for the one-month data set by DLR, see Figure 126.

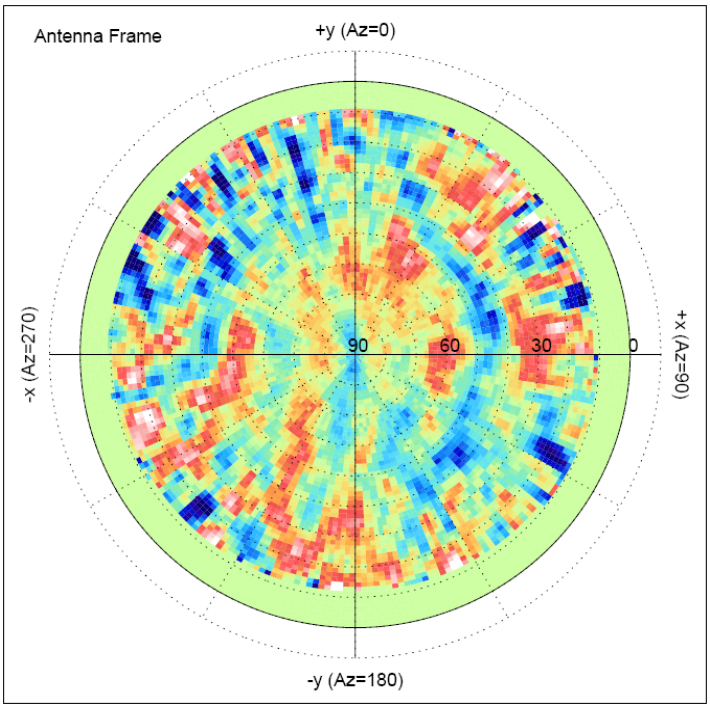

Figure 126 Ionosphere free range residuals from POD as determined by DLR.

8.2.3.2.3 Comparison of Residuals

The two maps shown in Figure 125 and Figure 126 are compared in Figure 127 in order to assess if the simulate MP error can be used to compensate and potentially improve the POD processing. It is seen that the POD residuals appears to be essentially uncorrelated with the GTD based estimates. The mean residual/error of the two data sets are -0.3 mm and 0.3 mm for POD respectively GTD.

The difference map is shown in Figure 128. Here we observe that the POD residuals appear to dominate for elevation angle above approximately 30°, while the GTD residuals dominate for elevation angle below approximately 20° deg

If the POD processing were to be compensated by the GTD based map the POD results would likely degrade. This is further illustrated by the RMS errors plotted in Figure 129.

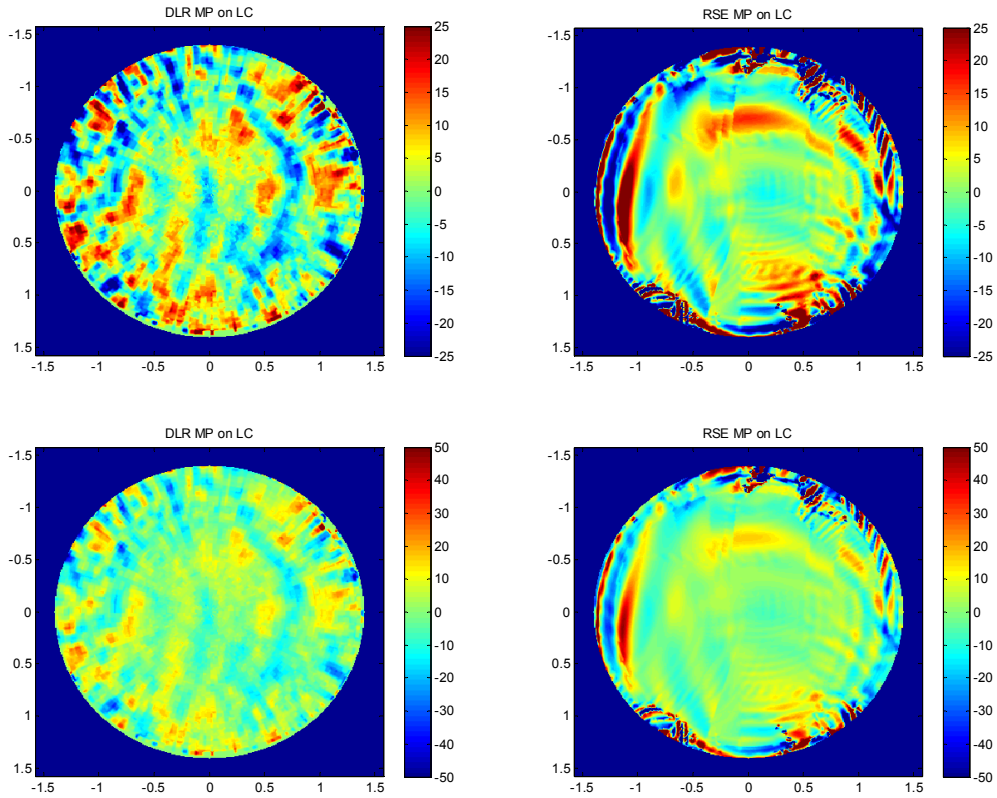

Figure 127 Comparison between POD residual errors (left) and simulated multipath error (right). Images scale is ±25 mm (top) and ± 50 mm (bottom). (Angular scale in radians)

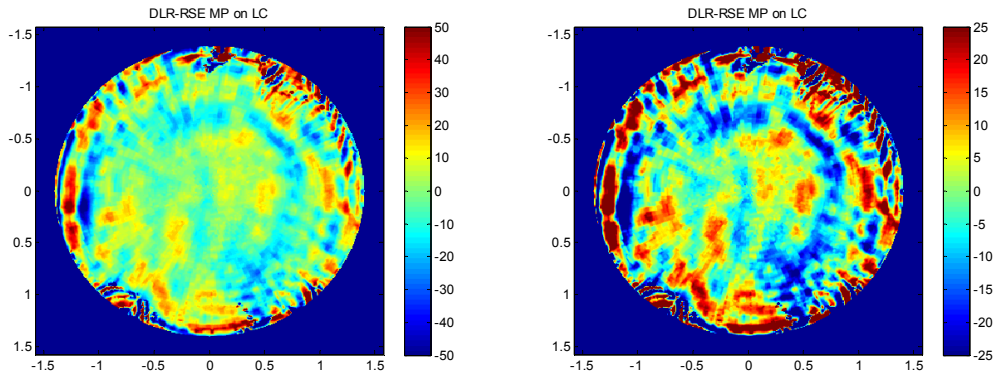

Figure 128 Difference between POD residuals and simulated multipath. (Angular scale in radians)

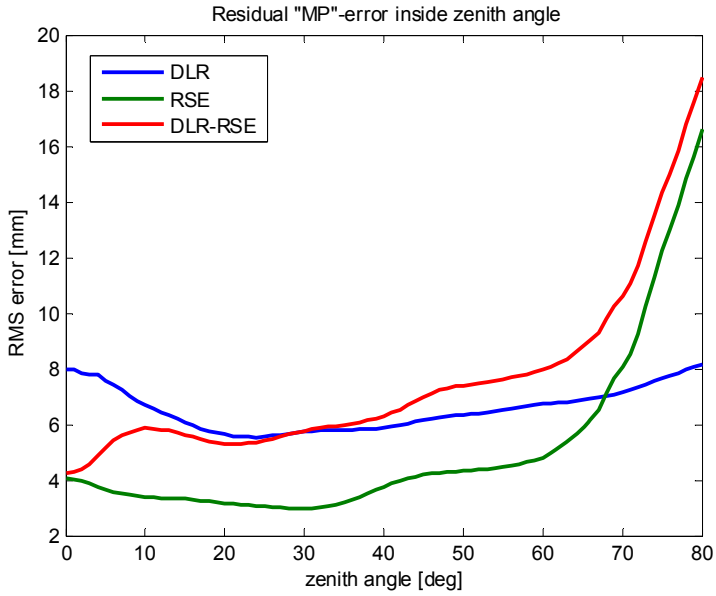

Figure 129 RMS error for POD residuals (DLR), simulated multipath (RSE) and difference (DLR-RSE). RMS is calculated versus zenith angle for all angles above the stated zenith angle.

8.2.3.3 PLM-SVM Alignment

The alignment of the GZA on MetOp was checked with EADS. The conclusion was that the Y- and Z- position error at the GZA will be below 0.5mm.

8.3 Codeless Tracking Loss

Also as part of the zenith data analysis, the difference in reported C/No and codeless tracking loss between GRAS and IGOR receiver has been studied.

8.3.1 Expected Codeless Tracking Loss

In the Anti-Spoofing (AS) mode of operation, the P-code is encrypted into the Y-Code. The encryption is performed by modulating a classified W-code on the P-code. The Y-code is modulated on both the L1 and L2 carriers. Carrier phase measurements in the presence of the Y-code can be based on a number of different techniques. The GRAS instrument implements the Ashtech Z-technique, which relies on the fact that the Y1- and Y2-codes are the same. The sign of the underlying encryption code is estimated for both Y1 and Y2 by pre-integration of the despread signals over W-code chip duration. These encryption estimates (E1 and E2) are then cross-multiplied with the despread and pre-integrated signals of the opposite channel to form the correlation result:

C1 = E1 <Y2>

C2 = E2 <Y1>

where <Y1> and <Y2> represents Y-code despread by P-code and integrated over a W-code chip. This applies to punctual, early, and late integrator chains.

This results in a codeless tracking loss L_{CL1} and L_{CL2} for the Y1 and Y2 chain respectively

$$L_{CL1} = -20 \cdot \log\left(erf\left(\sqrt{\frac{C/N_0\big|_{P2}}{B}} \right) \right) \quad [\text{dB}]$$

$$L_{CL2} = -20 \cdot \log\left(erf\left(\sqrt{\frac{C/N_0\big|_{P1}}{B}} \right) \right) \quad [\text{dB}]$$

where B is the equivalent noise bandwidth associated with the pre-integration, which is given by the W-code chip length, estimated to 10.23 MHz / 22 bits =0.465 MHz. $C/N_0\big|_{P1}$ and $C/N_0\big|_{P2}$ are the carrier-to-noise ratios for P1 and P2 signals in coded tracking mode at the correlator output.

For low signal levels, the codeless tracking loss can be approximated asymptotically as

$$L_{CL1} = 56.7 - C/N_0\big|_{P2dB} \quad [\text{dB}]$$

$$L_{CL2} = 56.7 - C/N_0\big|_{P1dB} \quad [\text{dB}]$$

8.3.2 Data Evaluation Method

The codeless tracking loss can be estimated from measurement data by calculating the carrier-to-noise-density ratio from the received correlation amplitudes and the (wideband) AGGA noise estimates. This noise estimate is not affected by co-channel interference noise on any signal component. Since the P1 signal has a carrier-to-noise-density-ratio (CNR) that is 3.8 dB lower than the C/A signal on L1 (including difference in transmit power and implementation loss), the codeless tracking loss can be estimated as

$$L_{CL1} = C/N_0\big|_{P1dB} - C/N_0\big|_{Y1dB} = C/N_0\big|_{CAdB} - 3.8 - C/N_0\big|_{Y1dB} \quad [\text{dB}]$$

or if we define the measure

$$CNR_{Y1-CA} = C/N_0\big|_{Y1dB} - C/N_0\big|_{CAdB} \quad [\text{dB}]$$

this is expected to equal

$$CNR_{Y1-CA} = -3.8 - L_{CL1} \quad [\text{dB}]$$

and asymptotically for low CNR

$$CNR_{Y1-CA} = -3.8 - 56.7 + C/N_0\big|_{P2dB} \quad [\text{dB}]$$

According to the GRAS link budget, the carrier-to-noise-density ratio of the P2 signal is about 5.5 dB lower than for the L1 C/A signal (when co-channel interference effects are not included). This ratio depends on the relation between the transmitted power levels as well as the antenna gain on the two frequencies. The expected asymptotic behaviour of the evaluated parameter therefore becomes (without co-channel effects)

$$CNR_{Y1-CA} = -3.8 - 56.7 + C/N_0\big|_{CAdB} \text{-}5.5 \quad = C/N_0\big|_{CAdB} - 66.0 \quad [\text{dB}]$$

If we account for the co-channel interference influence on the L1 C/A CNR, the CNR-difference between L1 C/A and L1P is reduced to 1.6 dB, and the CNR-difference between L1 C/A and L2P is reduced to 3.7 dB. The expected behaviour would then become (with co-channel effects)

$$CNR_{Y1-CA} = -1.6 - 56.7 + C/N_0\big|_{CAdB} - 3.7 = C/N_0\big|_{CAdB} - 62.0 \ [\text{dB}]$$

The expected Y1-CA CNR ratio is plotted both with and without co-channel interference in Figure 130.

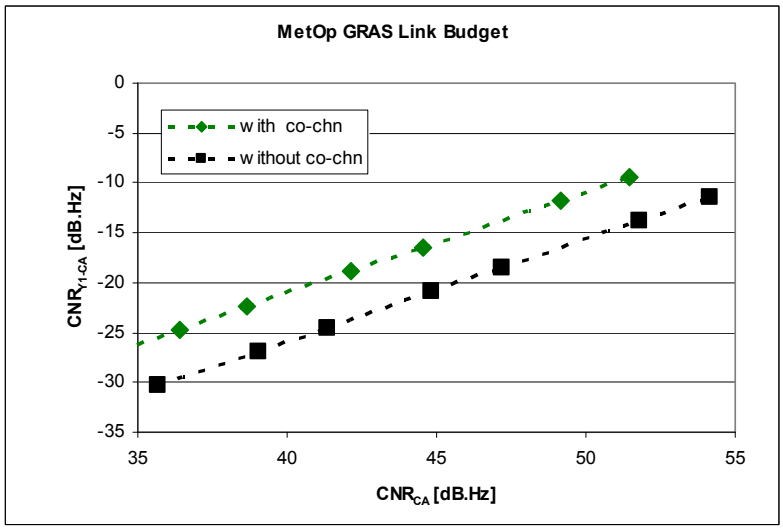

Figure 130 Comparison of carrier-to-noise-density ratio for MetOp GRAS link budget when co-channel interference is included/excluded.

8.3.3 Data Evaluation

The semi-codeless tracking loss of the GRAS instrument was analysed and compared to the IGOR receiver by Montenbruck et al., see [RD2]. These results are shown in Figure 131 below together with the expected theoretical behaviour of the Z-tracking technique. We can observe that the GRAS results agree with the expected asymptotic behaviour but slightly on the positive side since co-channel effects should not be expected in the GRAS results that are based on wideband AGGA noise estimates.

A likely reason that the IGOR data points agree better with the expected behaviour when co-channel effects are included than when they are not, is that CNR on IGOR is measured based on the punctual correlated outputs and hence includes the effect of co-channel interference. Other reasons can be differences between the antenna gain at L2 and L1. It is also possible that the data is normalized to a different reference, which may include a calibration bias.

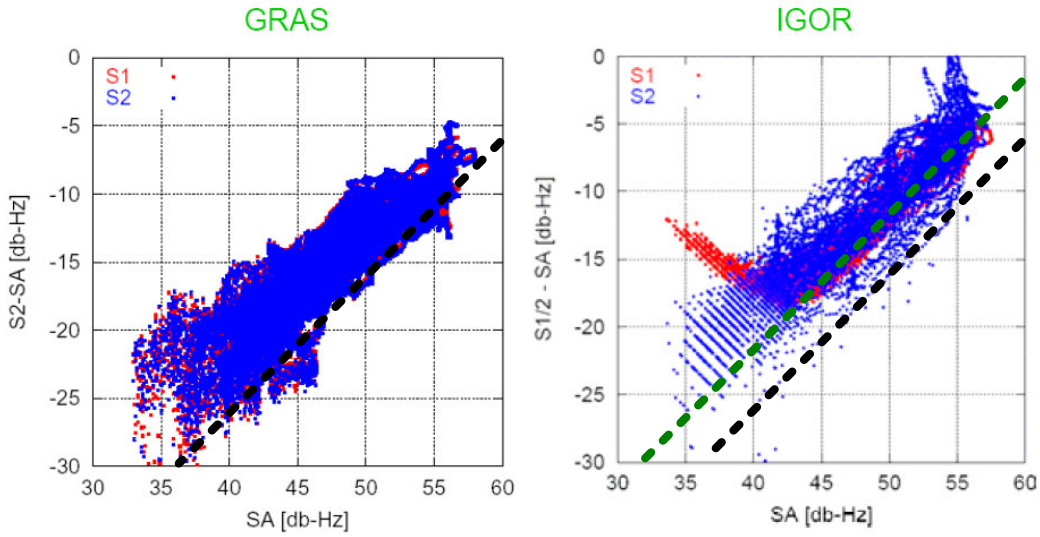

Figure 131 Comparison of carrier-to-noise-density ratio differences between GRAS and IGOR with data as presented in [RD2]. SA, S1, and S2, are the carrier-to-noise-density ratio on L1 C/A, L1P(Y), and L2P(Y), respectively. Expected asymptotic behaviour is shown with the dashed line without co-channel (black) and with co-channel (green) effects.

A corresponding data plot for 4 orbits from the GRAS data used in this study is shown in Figure 132 below. It agrees well with the results presented in [RD2]. Straight line fits to the data show a somewhat smaller slope (0.83) than predicted (1.0).

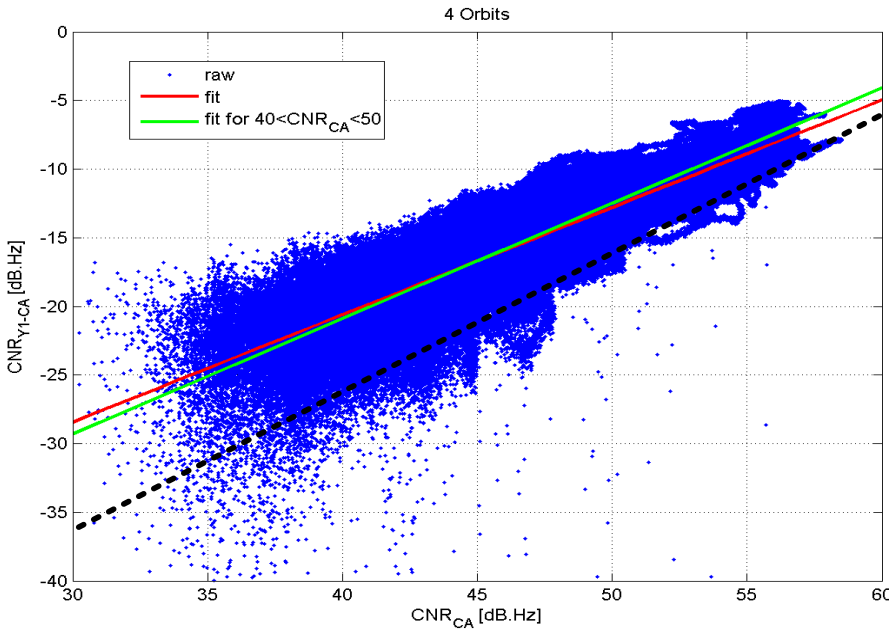

Figure 132 Carrier-to-noise-density ratio of Y1-CA versus CA. Expected asymptotic behaviour (without co-channel effects) is shown with dashed line.

One explanation for the large spread of the values above the expected curve is given in Figure 133 below which shows burst-wise increases of the noise density as the satellite passes over the Northern hemisphere probably caused by man-made interference.

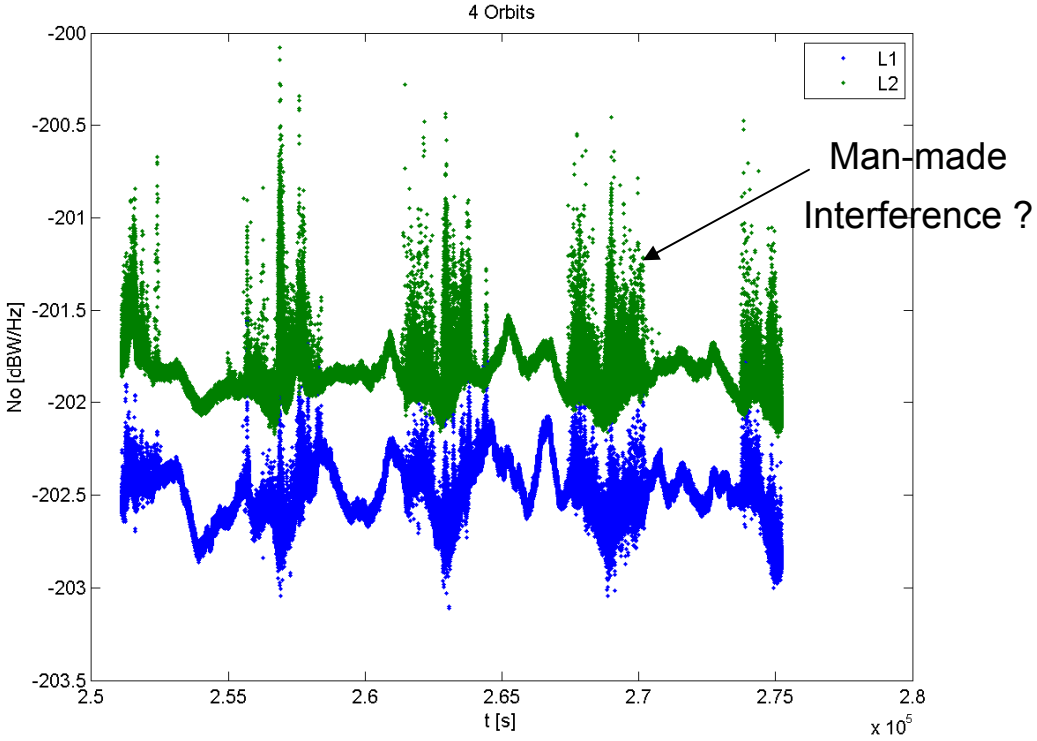

Figure 133 Noise-density (N_0) variation as a function of time during four orbits. The location of the bursts of increased noise corresponds to the Northern hemisphere.

8.3.4 Results Summary

The observed codeless tracking losses are found to agree with the predicted behaviour. It is especially noted that co-channel interference effects shall not be accounted for when calculating the expected behaviour for GRAS and that the co-channel effect may be included in the IGOR data.

A straight-line fit to the data points show a bias towards a lower code-less tracking loss than expected for weak signals. A possible explanation is that the C/A code signal is more affected by man-made interference than the P(Y) code is.

9 SUMMARY AND CONCLUSIONS

9.1 Conclusions on the GRAS Instrument Performance

The study has led to an increased understanding of atmospheric influence and measurement conditions, which can be used to improve the present MetOp instrument.

The following can be concluded from the presented analyses:

- GRAS bending angle accuracy is well within the specification.
- Doppler (±25 Hz) and Range models (±50 m) can be trusted to reduce search windows and use stronger aiding of tracking loops. This will lead to faster acquisitions, fewer false acquisitions, and more robust tracking through fades and to lower altitudes for both rising and setting occultations
- It is sufficient to use 200 Hz sampling rate even in open loop.
- We have gained an increased knowledge of signal dynamics (larger amplitude but smaller spectral and range variations than expected)
- Acquisition and tracking algorithms can be tuned, e.g. loop bandwidths, loss-of-lock detection and search windows, and increased coherent integration can be employed.
- Open loop carrier tracking is sufficient for open signals
- The ground interference noise varies considerably.
- Based on study conclusions the parameter controlling the low SLTA limit has been changed from the initial setting -140 km to -300 km.

9.2 Recommended GRAS Instrument Improvements

The following actions are foreseen and proposed for GRAS on MetOp:

- A S/W parameter patch for GRAS on MetOp-A is planned to mitigate data gaps, and false P(Y) code acquisitions

Additional potential improvements for later implementation can be:

- MetOp-A/B: Parameter patches to fine tune robustness & extend altitude coverage
- MetOp-C: Functional Changes to improve robustness & extend altitude coverage
- MetOp-SG (Second Generation): Updated functionality to incorporate modernized GNSS signals and fully benefit from gained understanding of the environment.

Considering to introduce short non-operational trial periods once MetOp-B is in orbit is also recommended. This can be used to exploit further improvements without requirement for operational quality data.

Improved prediction / understanding of atmospheric impact at low altitude is needed:

- To refine on-board modelling
- To refine retrieval processing
- Further exploitation of retrieval benefit from1 kHz data
- Further mitigation of GRAS issues, mainly data gaps

- Extend the measurements deep into the shadow zone. As shown in section 7.1.9 reference [22], this may reduce the biases in the retrieved bending angles and refractivity.

9.3 Conclusions on GRAS Open Loop Retrieval

Based on the comparison of processing closed loop (CL) and raw sampling (RS) data in the troposphere, we conclude that involving RS data significantly improves the penetration and reduces a negative bias of retrieved bending angles and refractivities. This effect is stronger in the tropics, but it also is observed in middle and polar latitudes.

The retrieval results from the different centres (DMI, Univ. Graz, GFZ, EUM) are very similar, but not identical. The main reasons for the differences are believed to be occultations selection/screening mechanisms, interpolations across data gaps and filtering, see §7.5. Further dedicated studies will be required to answer this.

The conclusions can be summarised:

- Processing capability at many European and US centres
- Stratosphere: good agreements, std. dev. differences mostly understood
- Troposphere, RS data:
    - Structural differences are present. This is due to different choices in preprocessing and quality control, different handling of data gaps, and difference in filtering.
    - Handling of data gaps, filtering and data screening varies
    - SLTA coverage needed down to -250 km (TBC)
    - Navigation data bits needed and likely to be more important at lower SLTA
- Data continuity is essential
- RS prototype processor in place
- Operational RS processor development on-going at EUMETSAT
- Visualization of radio-holographic spectra is useful for the data diagnostics. This proves to be very useful for selected cases studies and can be use to analyze individual profiles. This tool allows for the identification of complicated multipath structures, noise properties, parasitic modulation, effect of signal gaps, interference etc. The visualization tool is not necessary for the data processing, because it is problematic to formalize the visual analysis of the data (see examples in Appendix B).

The following aspects need also further investigations/studies:

- Structural uncertainties needs to be better understood and processing should be better coordinated
- Improved prediction / understanding of atmospheric impact at low altitude is needed, with possible impact on retrieval processing.
- Optimize processing at low altitude, extract best methods from different centres, ECMWF processing should be used as evaluation

9.4 Conclusions on Zenith Data Analysis

The radial bias between the space craft Centre of Mass (CoM) and the Antenna Phase Centre (APC) which was observed by the POD processing has been reduced from 3.7 cm to approx 2 cm. The residual error of about 2 cm is still larger than expected but no further explanation has been identified.

The codeless tracking losses in the GRAS and IGOR receivers are found to be equivalent when co-channel interference effects are accounted for.

APPENDIX A IDENTIFIED STUDY CASE EXAMPLE PLOTS

The Table below has been copied from section 4.5 for the sake of facilitating the reading.

Case	Characteristics	Description
1	L2 tracking to low SLTA	This study case serves as a reference case to study dual frequency tracking properties under normal conditions.
2	OL tracking to low SLTA	A setting occultation with a considerable amount of raw sampling data. High L2 signal dynamics also at high altitude.
3	Ocean reflection	The impact of ocean (or ground) reflections is identified as a study case.
4	L2 feature at high SLTA	Some occultations show a pronounced spectral signature on the L2 signal at high SLTA, exemplified by the identified occultation.
5	Long fade	The L1 amplitude is reduced to a low level with duration of more than 2 seconds and then increases again. It is important that the code loop maintains lock during this type of long fades.
6	10 Hz disturbance	In the sliding spectrum plots one can see spectral peaks at 10 Hz intervals for a number of occultations. The impact and origin of this feature should be investigated.
7	Raw sampling saturation	The I and Q raw sampling values are at there maximum value for 2% of the samples as a worst case for the 30 September data. We propose to check if this has a significant effect on the results.
8	Weak P(Y) code signal	The P(Y) code signal amplitude is more than 20 dB lower than expected for some cases. We propose to investigate if this data is still useful and if the tracking algorithm can be improved to avoid this effect.
9	False tracking	The amplitude and frequency of this data indicates that the instrument has locked on incorrect SV. We believe that this data is not useful. The objective of this study case is to find an improved method for signal acquisition to increase the number of useful occultations.
10	Wideband signature	The bandwidth of the raw sampling signal approaches 50 Hz in some occultations and these are of particular interest for determining the minimum required raw sampling rate for future missions.
11	Co-channel disturbance	Interference from other GPS SVs can be noticed in many occultations. These effects will be investigated.
12	L1 data gap	In many rising occultations, there is a gap in the L1 closed loop data that is due to loss-of-lock being detected for the carrier NCO loop. The impact of this and ways to improve the on-board software will be studied.

Table 18 Description of identified study cases for processing analyses.

In the following the 12 study cases are presented with two plots each. The first plot contains sliding spectra as function of time since the first data is available for (top-down); Raw sampling with spectral window limited to ±25 Hz, C/A closed loop, P1 and P2 signals. The second plot contains the amplitudes as function of time for (top–down); Raw sampling, C/A closed loop, P1 and P2 signals.

Appendix A.1 Case 1: L2 tracking to low SLTA

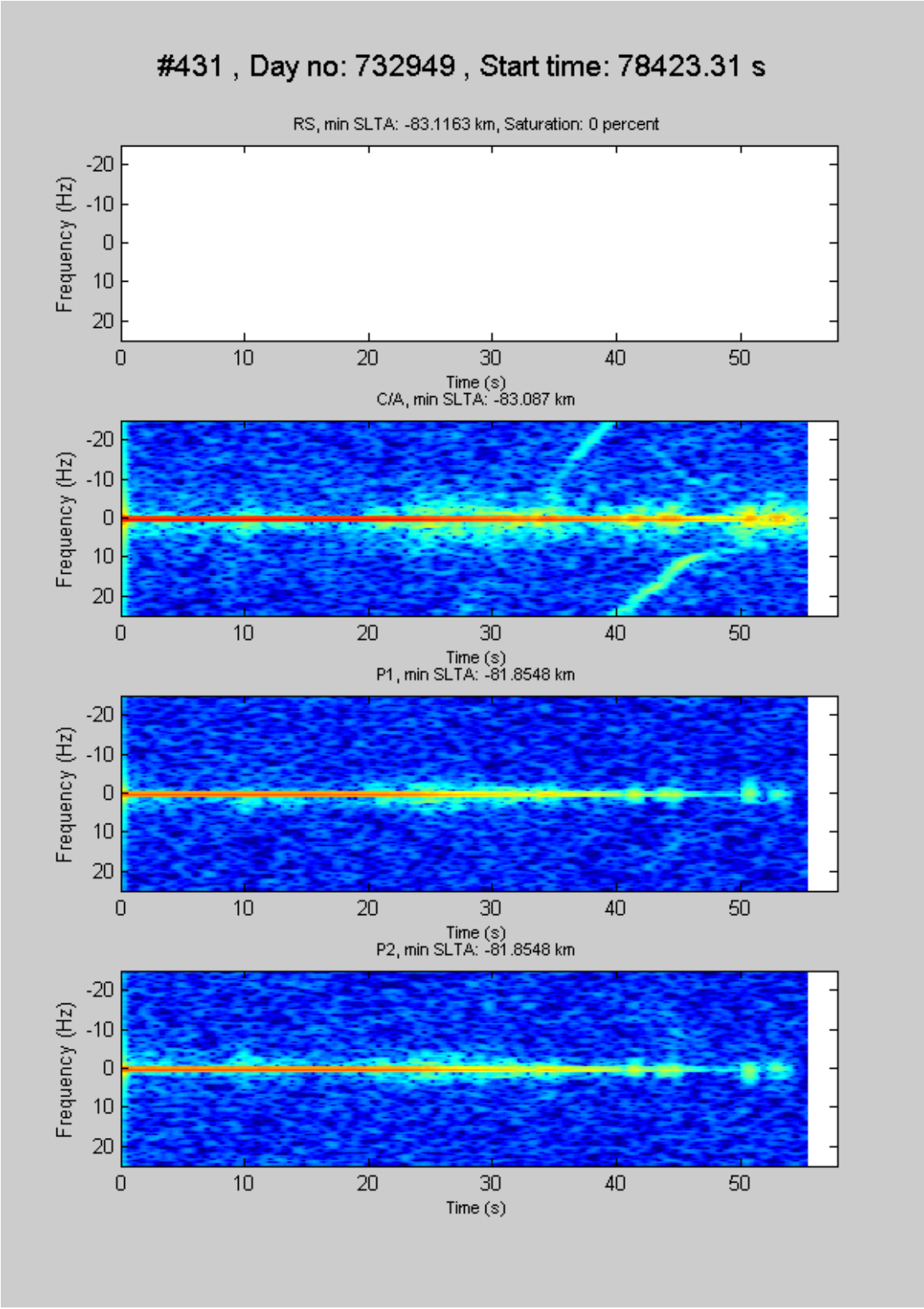

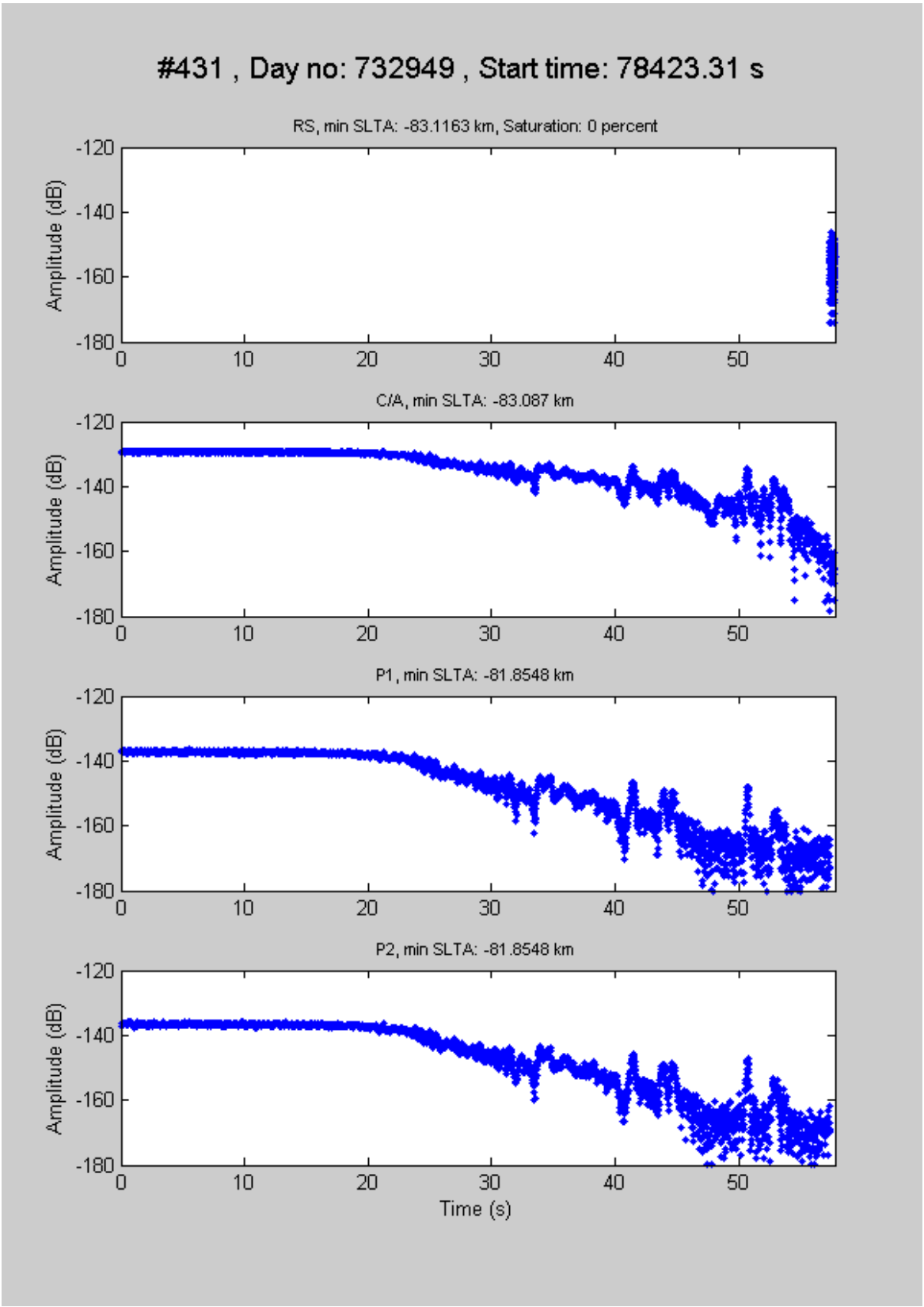
#431 , Day no: 732949 , Start time: 78423.31 s
RS, min SLTA: -83.1163 km, Saturation: 0 percent
C/A, min SLTA: -83.087 km
P1, min SLTA: -81.8548 km
P2, min SLTA: -81.8548 km
Amplitude (dB)
-120
-140
-160
-180
0
10
20
30
40
50
Time (s)

Appendix A.2 Case 2: OL tracking to low SLTA

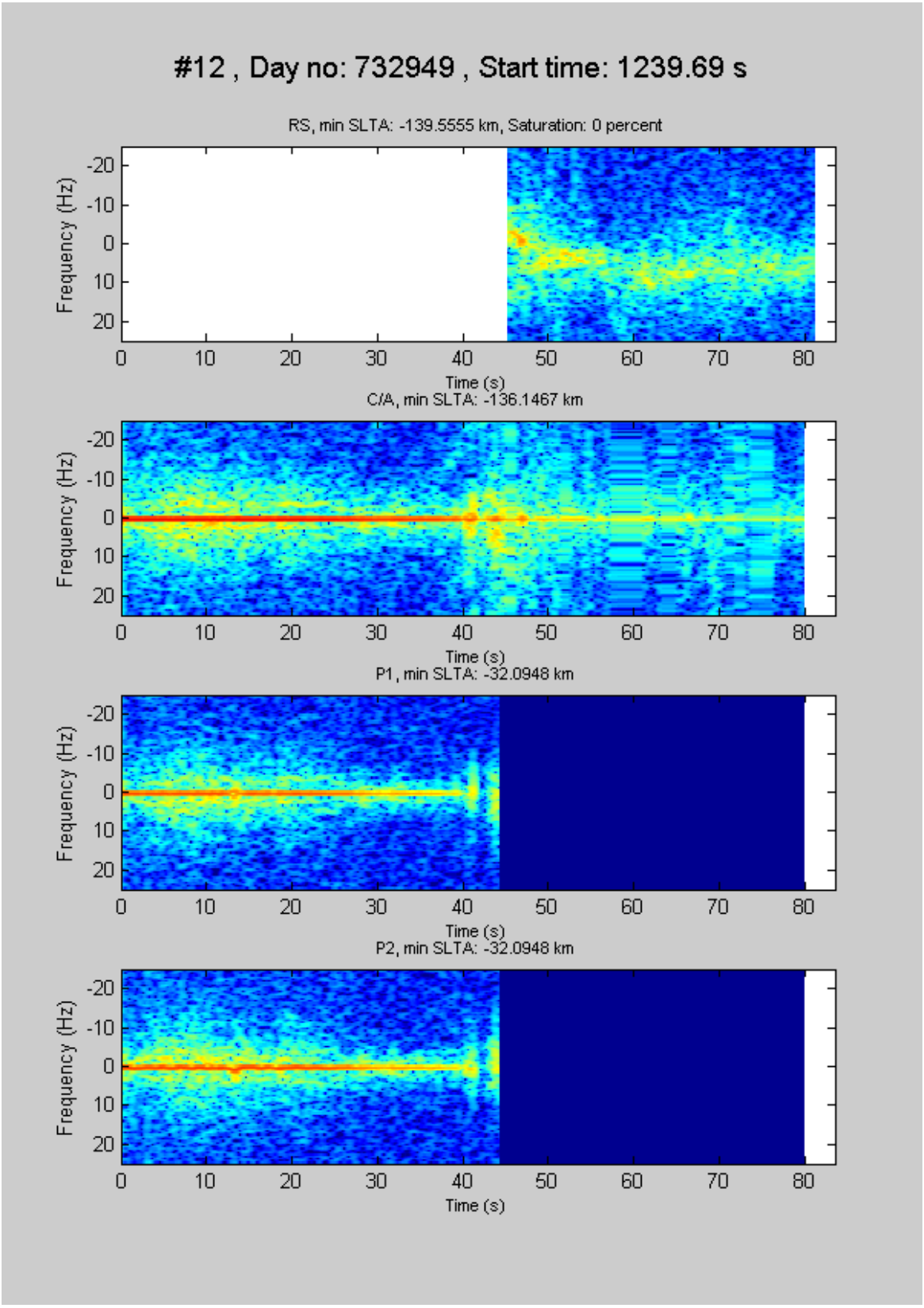

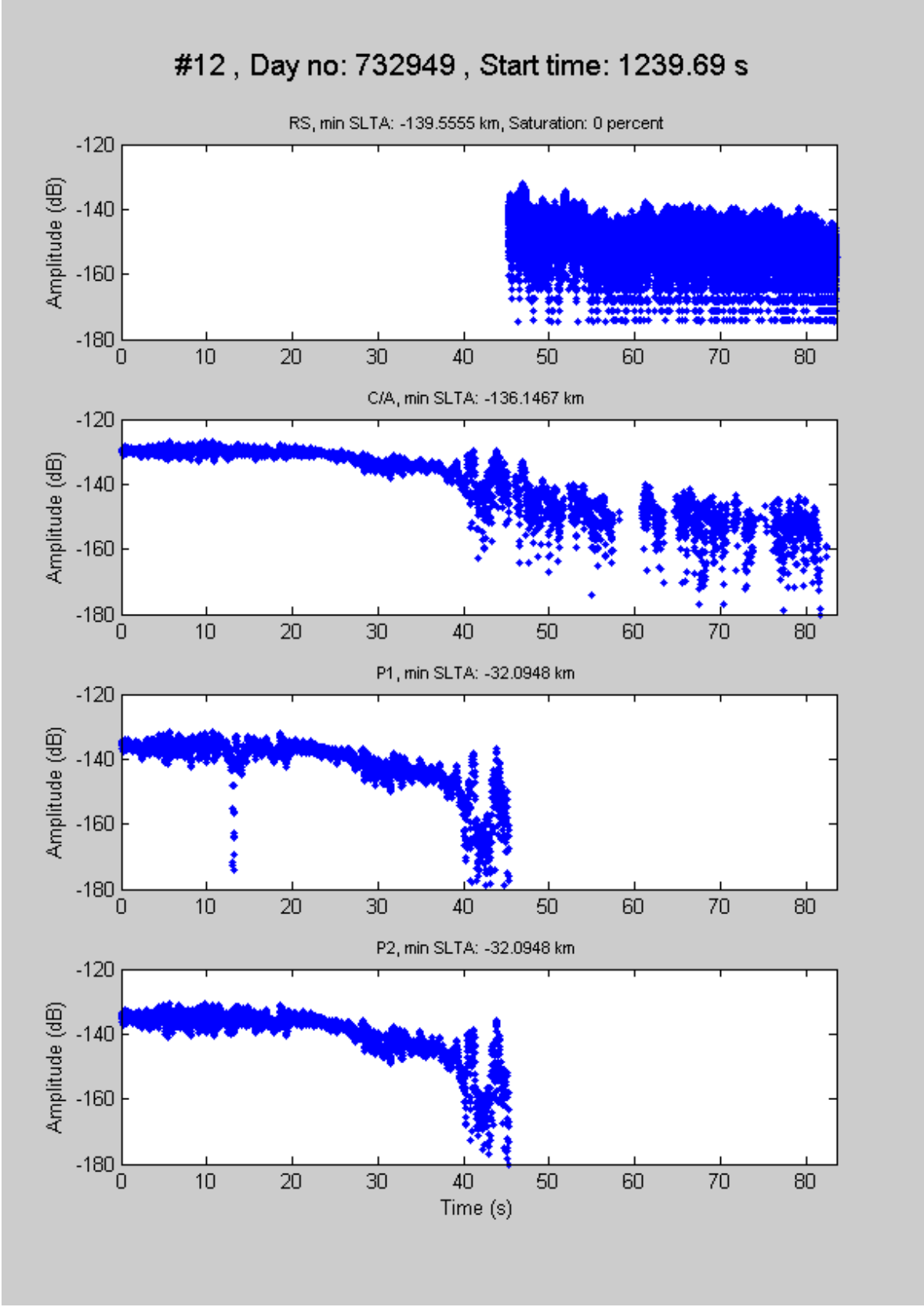
#12 , Day no: 732949 , Start time: 1239.69 s
RS, min SLTA: -139.5555 km, Saturation: 0 percent
C/A, min SLTA: -136.1467 km
P1, min SLTA: -32.0948 km
P2, min SLTA: -32.0948 km
Amplitude (dB)
-120
-140
-160
-180
0
10
20
30
40
50
60
70
80
Time (s)

Appendix A.3 Case 3: Ocean reflection

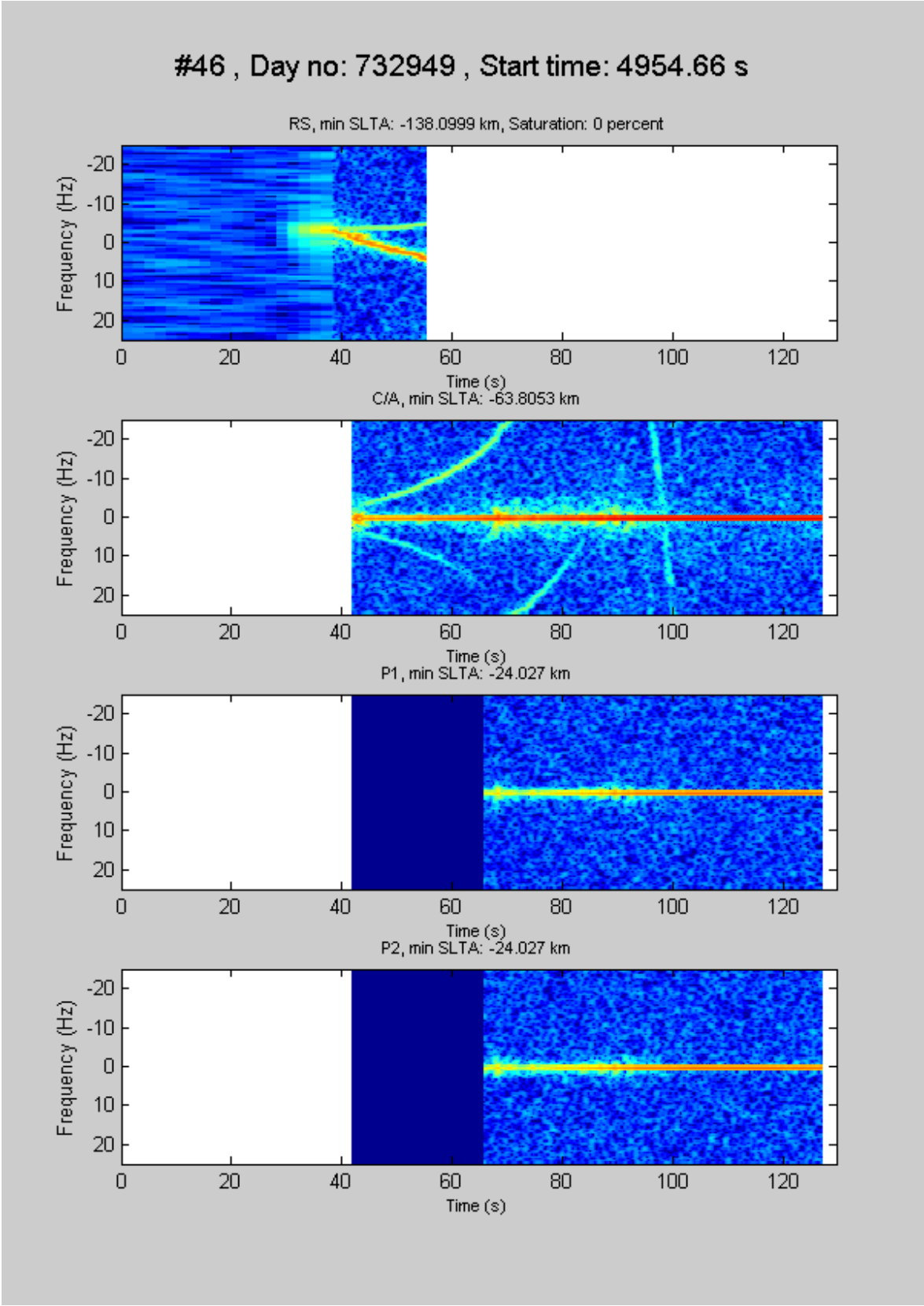

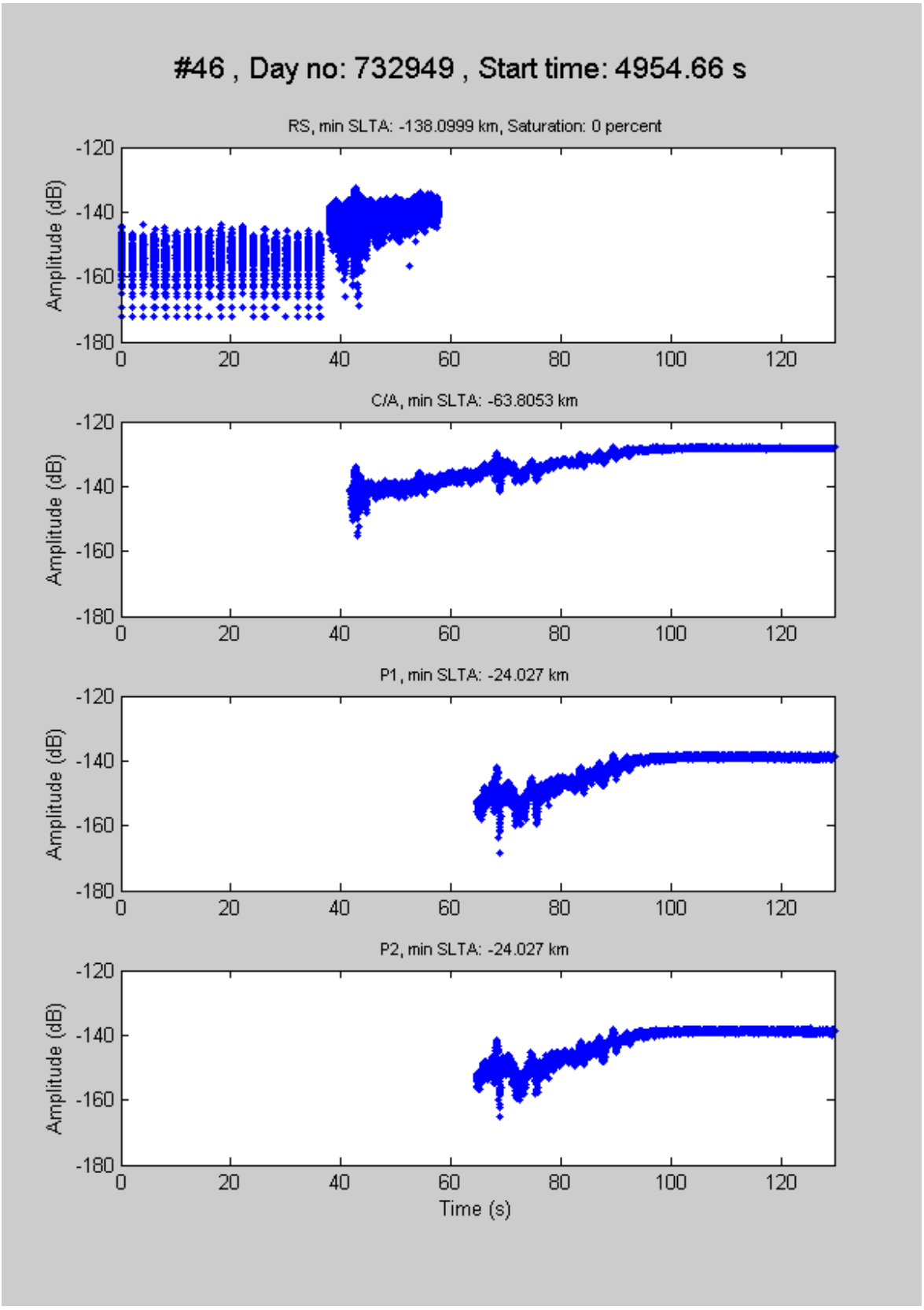
#46 , Day no: 732949 , Start time: 4954.66 s
RS, min SLTA: -138.0999 km, Saturation: 0 percent
C/A, min SLTA: -63.8053 km
P1, min SLTA: -24.027 km
P2, min SLTA: -24.027 km
Amplitude (dB)
-120
-140
-160
-180
0
20
40
60
80
100
120
Time (s)

Appendix A.4 Case 4: L2 feature at high SLTA

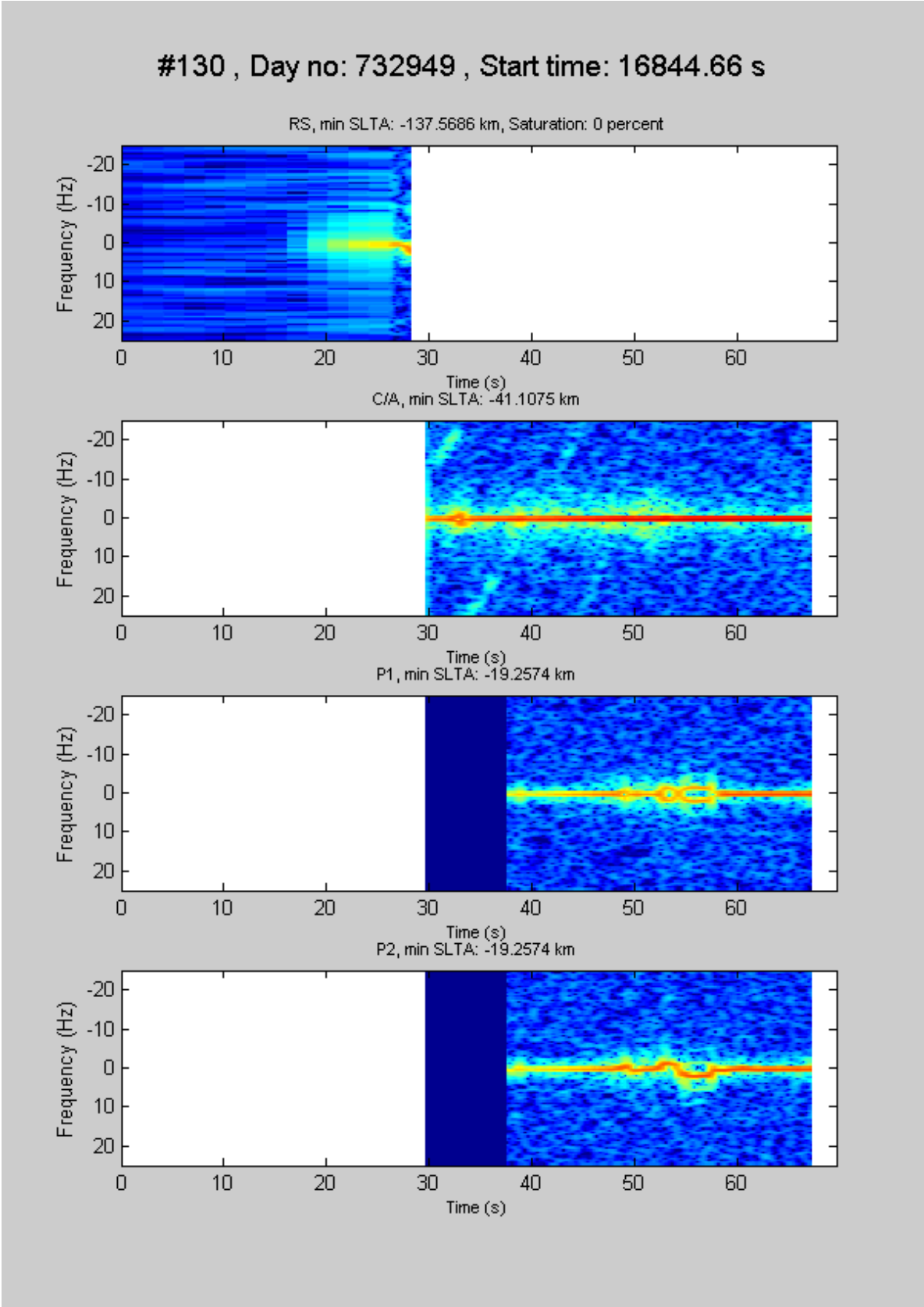

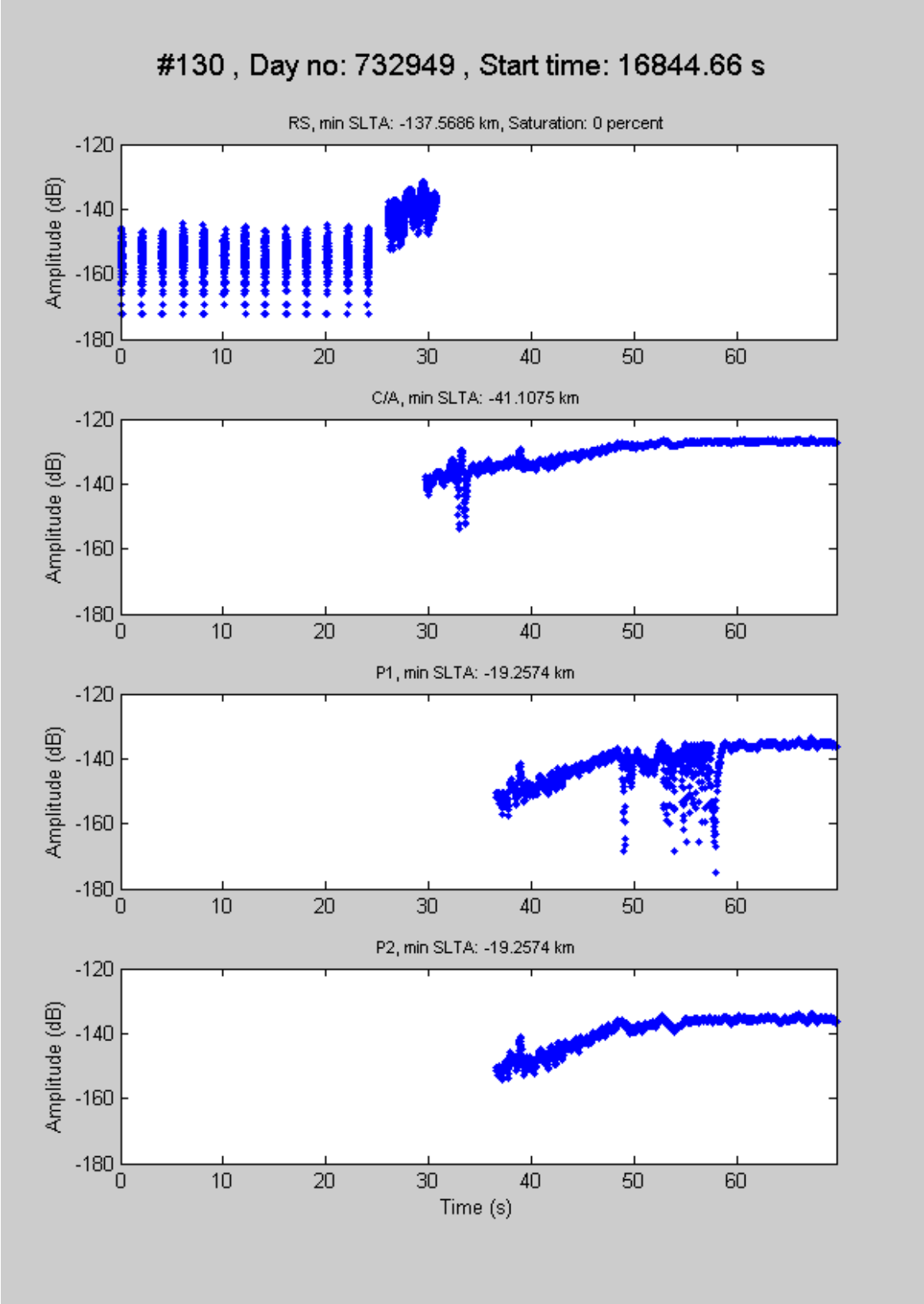
#130 , Day no: 732949 , Start time: 16844.66 s
RS, min SLTA: -137.5686 km, Saturation: 0 percent
C/A, min SLTA: -41.1075 km
P1, min SLTA: -19.2574 km
P2, min SLTA: -19.2574 km
Amplitude (dB)
-120
-140
-160
-180
0
10
20
30
40
50
60
Time (s)

Appendix A.5 Case 5: Long fade

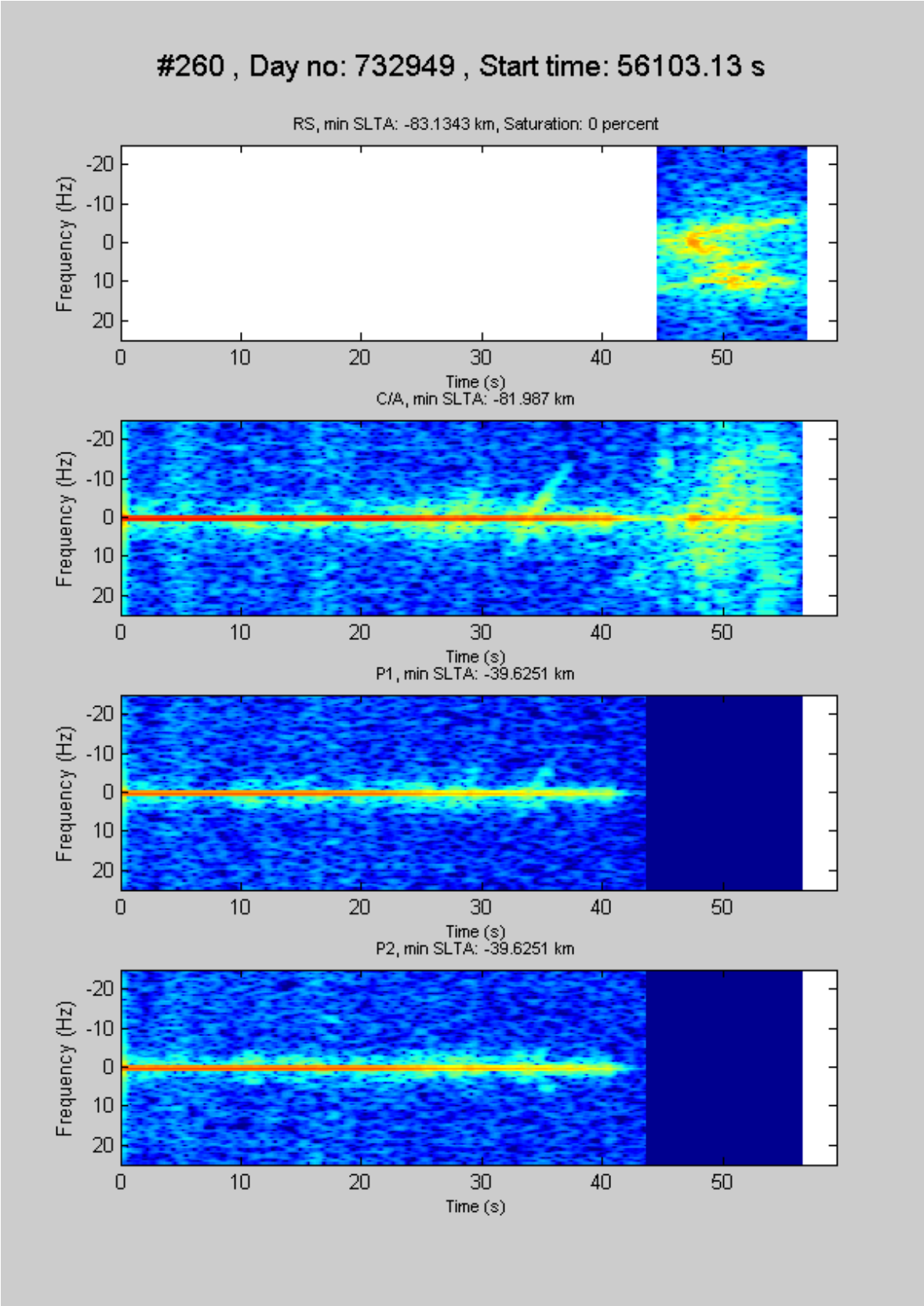

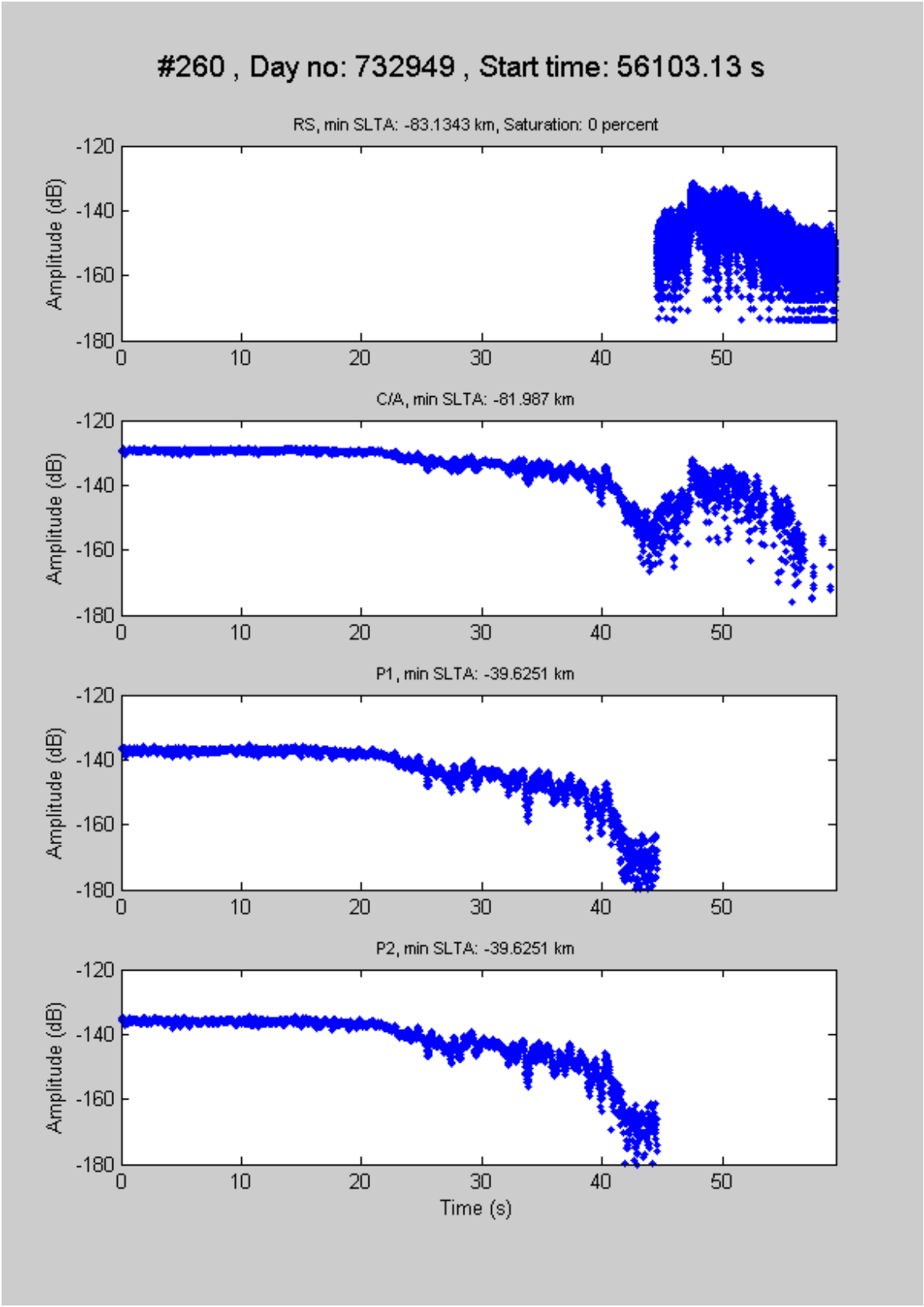
#260 , Day no: 732949 , Start time: 56103.13 s
RS, min SLTA: -83.1343 km, Saturation: 0 percent
C/A, min SLTA: -81.987 km
P1, min SLTA: -39.6251 km
P2, min SLTA: -39.6251 km
Amplitude (dB)
-120
-140
-160
-180
0
10
20
30
40
50
Time (s)

Appendix A.6 Case 6: 10 Hz disturbance

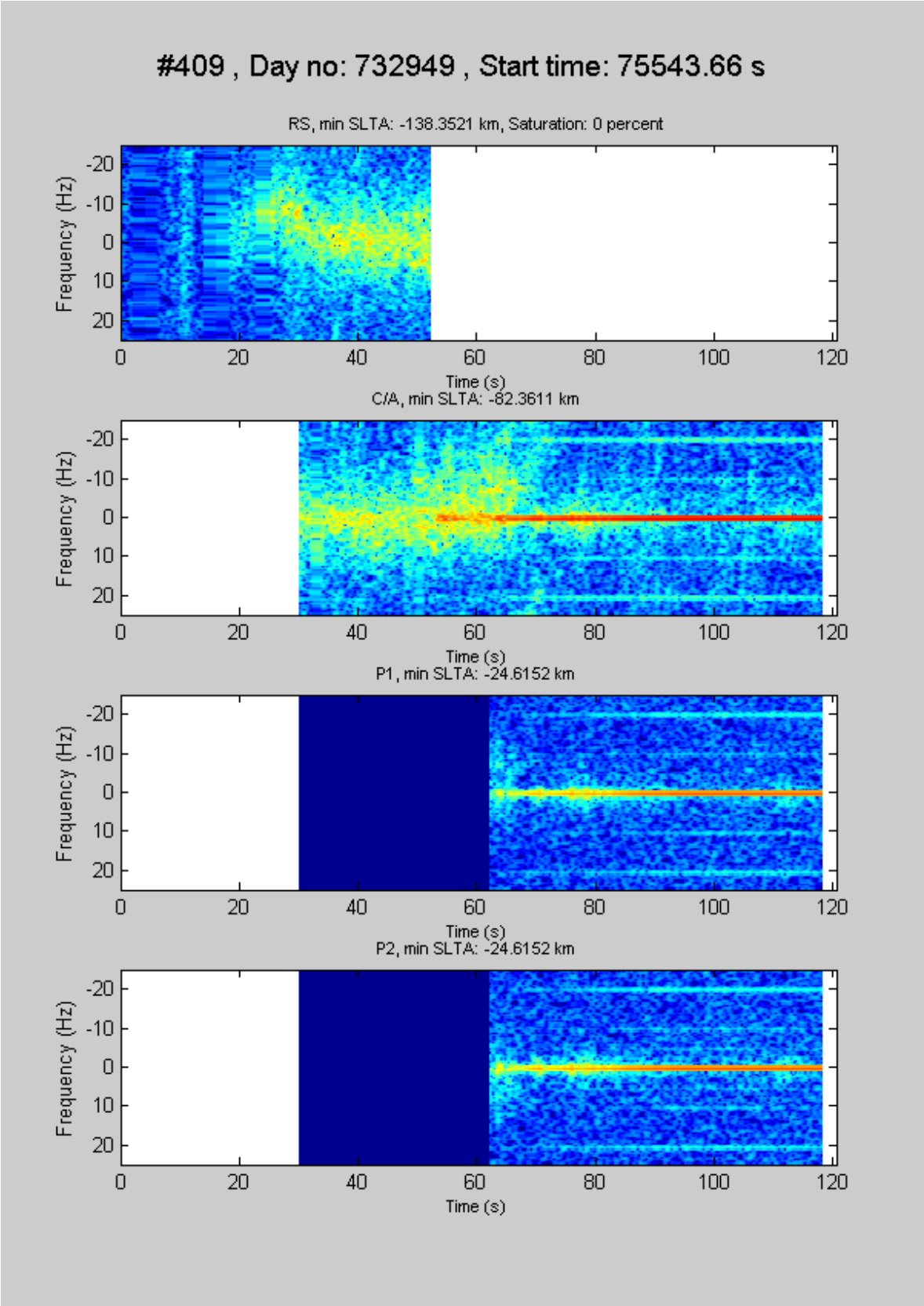

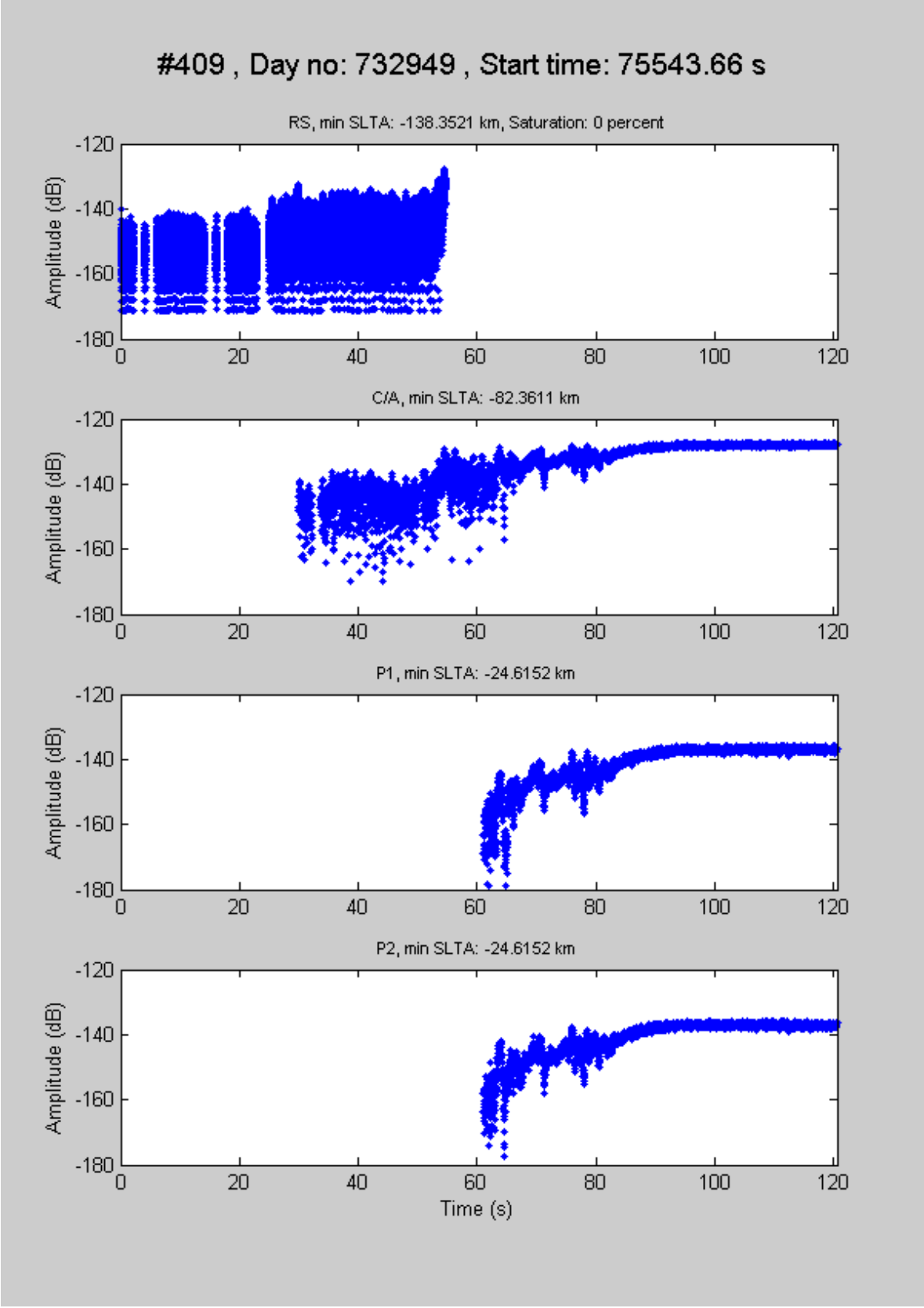
#409 , Day no: 732949 , Start time: 75543.66 s
RS, min SLTA: -138.3521 km, Saturation: 0 percent
C/A, min SLTA: -82.3611 km
P1, min SLTA: -24.6152 km
P2, min SLTA: -24.6152 km
Amplitude (dB)
-120
-140
-160
-180
0
20
40
60
80
100
120
Time (s)

Appendix A.7 Case 7: Raw sampling saturation

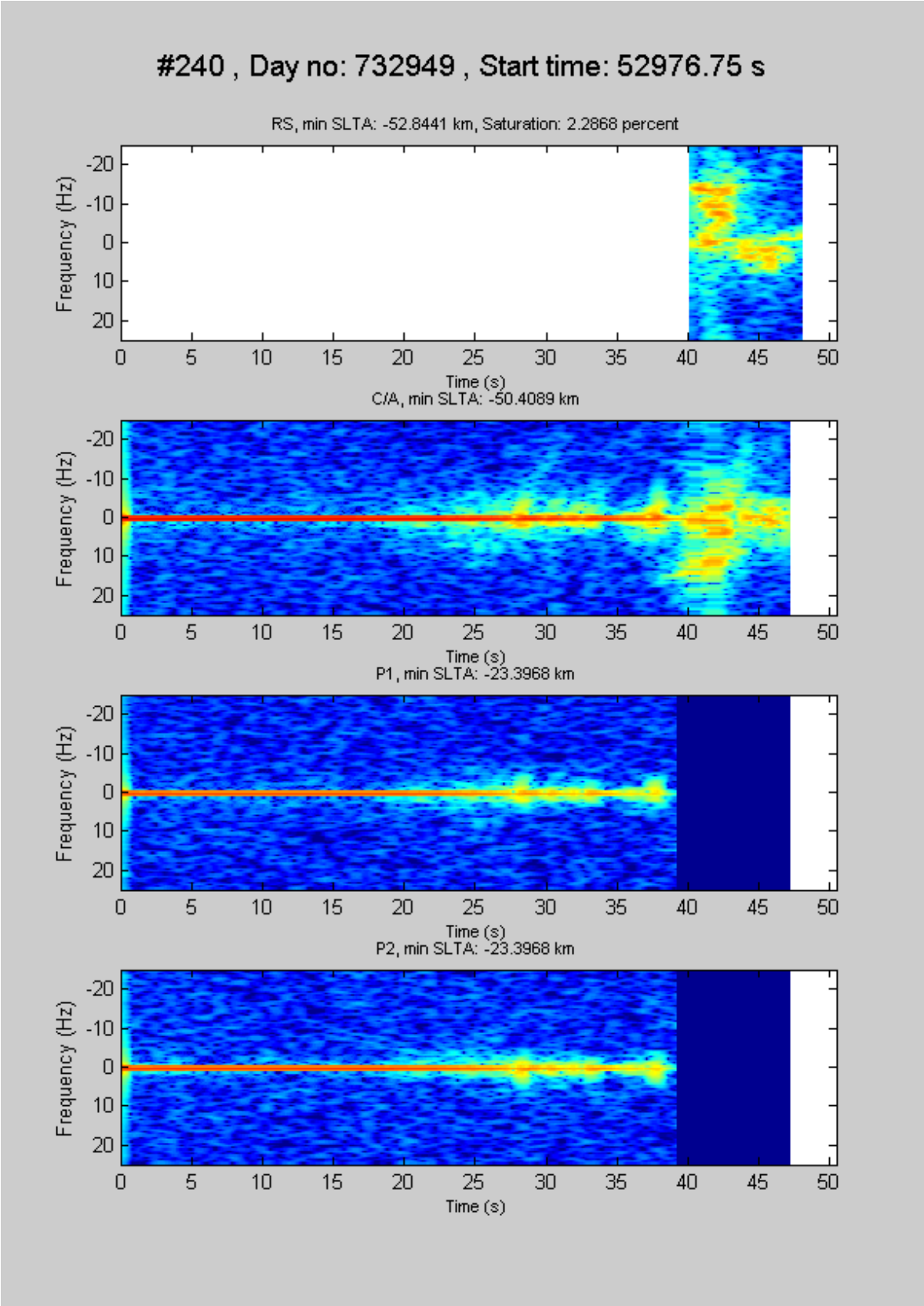

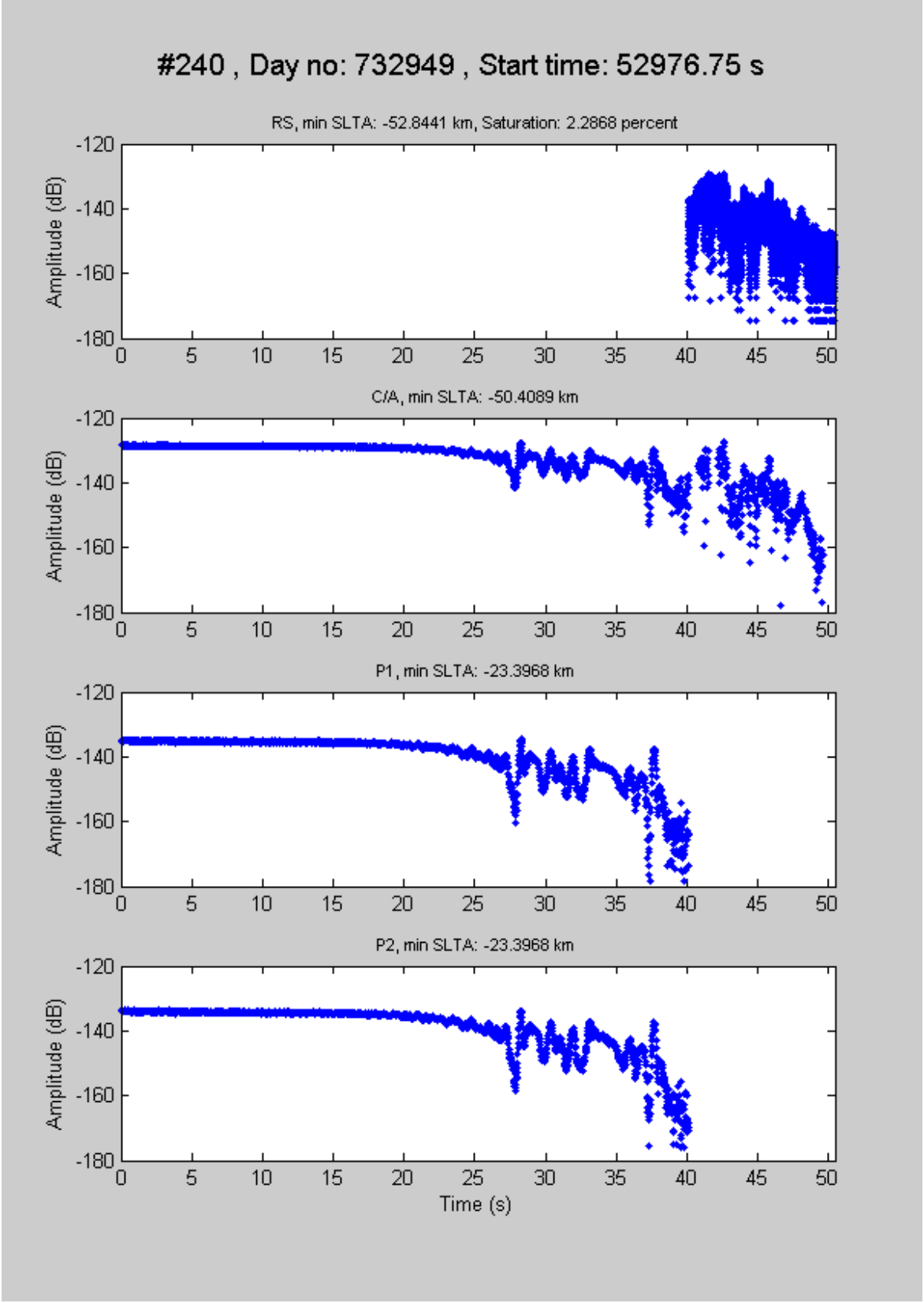
#240 , Day no: 732949 , Start time: 52976.75 s
RS, min SLTA: -52.8441 km, Saturation: 2.2868 percent
C/A, min SLTA: -50.4089 km
P1, min SLTA: -23.3968 km
P2, min SLTA: -23.3968 km
Amplitude (dB)
-120
-140
-160
-180
0
5
10
15
20
25
30
35
40
45
50
Time (s)

Appendix A.8 Case 8: Weak P(Y) code signal

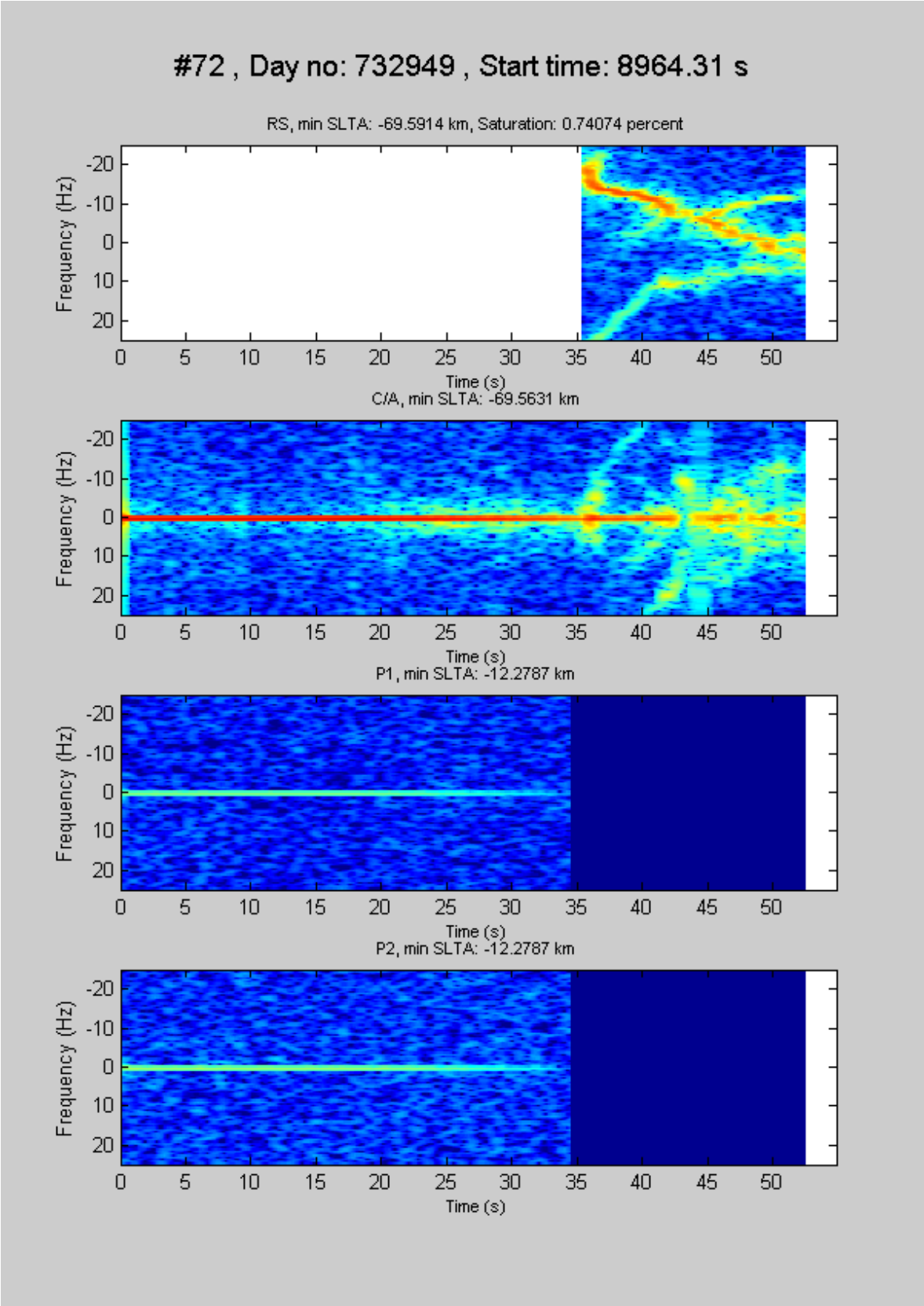

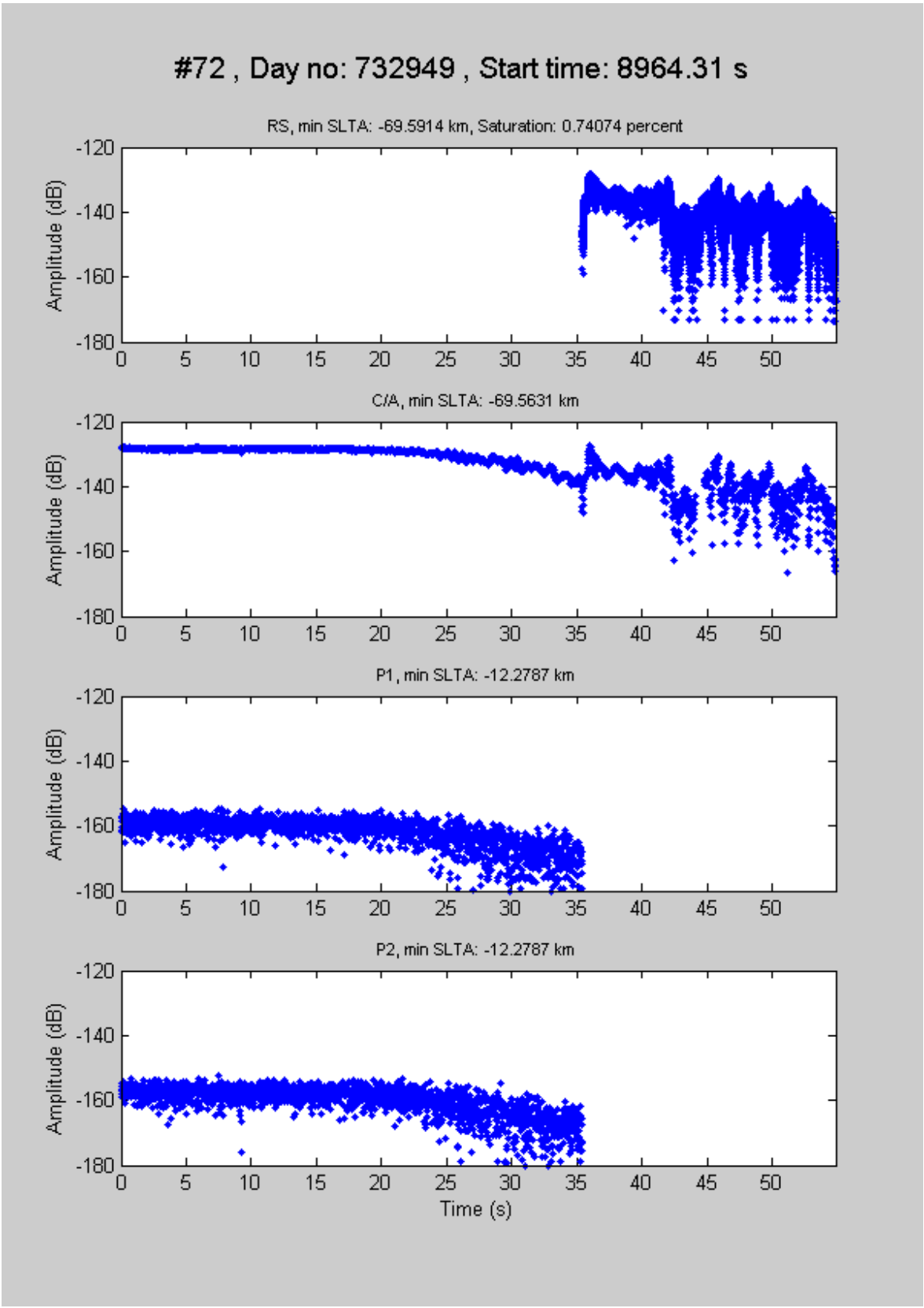
#72 , Day no: 732949 , Start time: 8964.31 s
RS, min SLTA: -69.5914 km, Saturation: 0.74074 percent
C/A, min SLTA: -69.5631 km
P1, min SLTA: -12.2787 km
P2, min SLTA: -12.2787 km
Amplitude (dB)
Time (s)

Appendix A.9 Case 9: False tracking

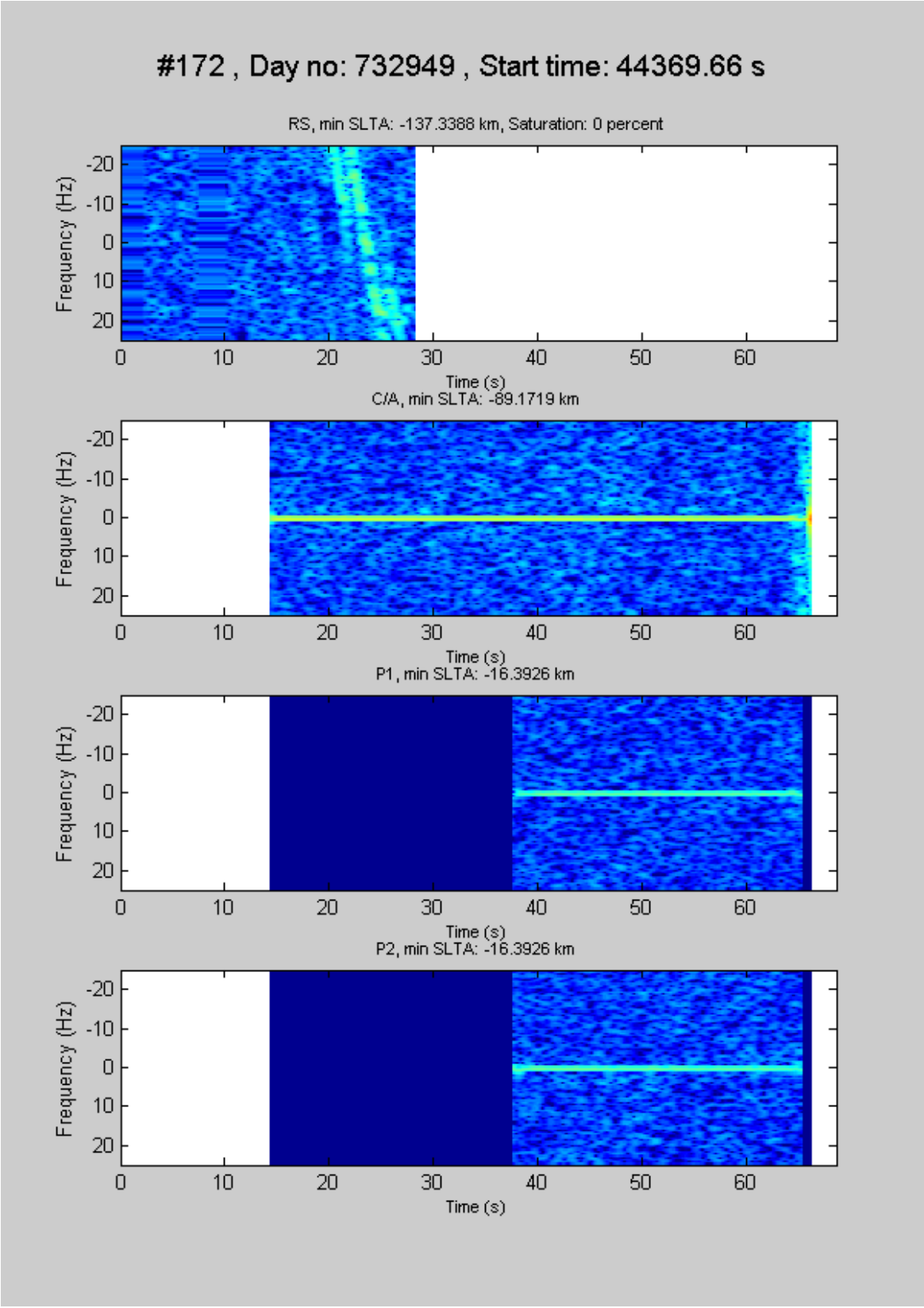

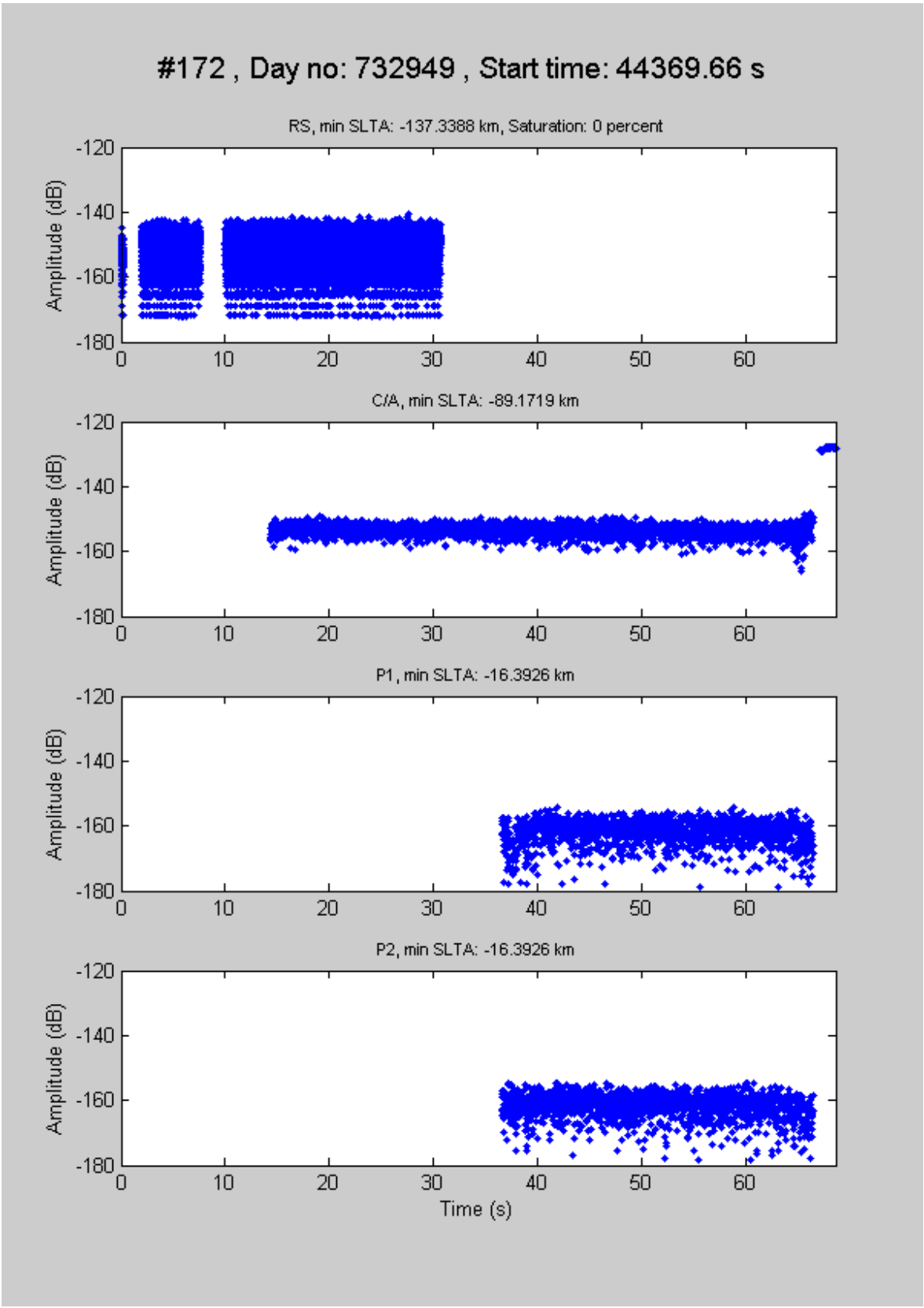
#172 , Day no: 732949 , Start time: 44369.66 s
RS, min SLTA: -137.3388 km, Saturation: 0 percent
C/A, min SLTA: -89.1719 km
P1, min SLTA: -16.3926 km
P2, min SLTA: -16.3926 km
Amplitude (dB)
-120
-140
-160
-180
0
10
20
30
40
50
60
Time (s)

Appendix A.10 Case 10: Wideband signature

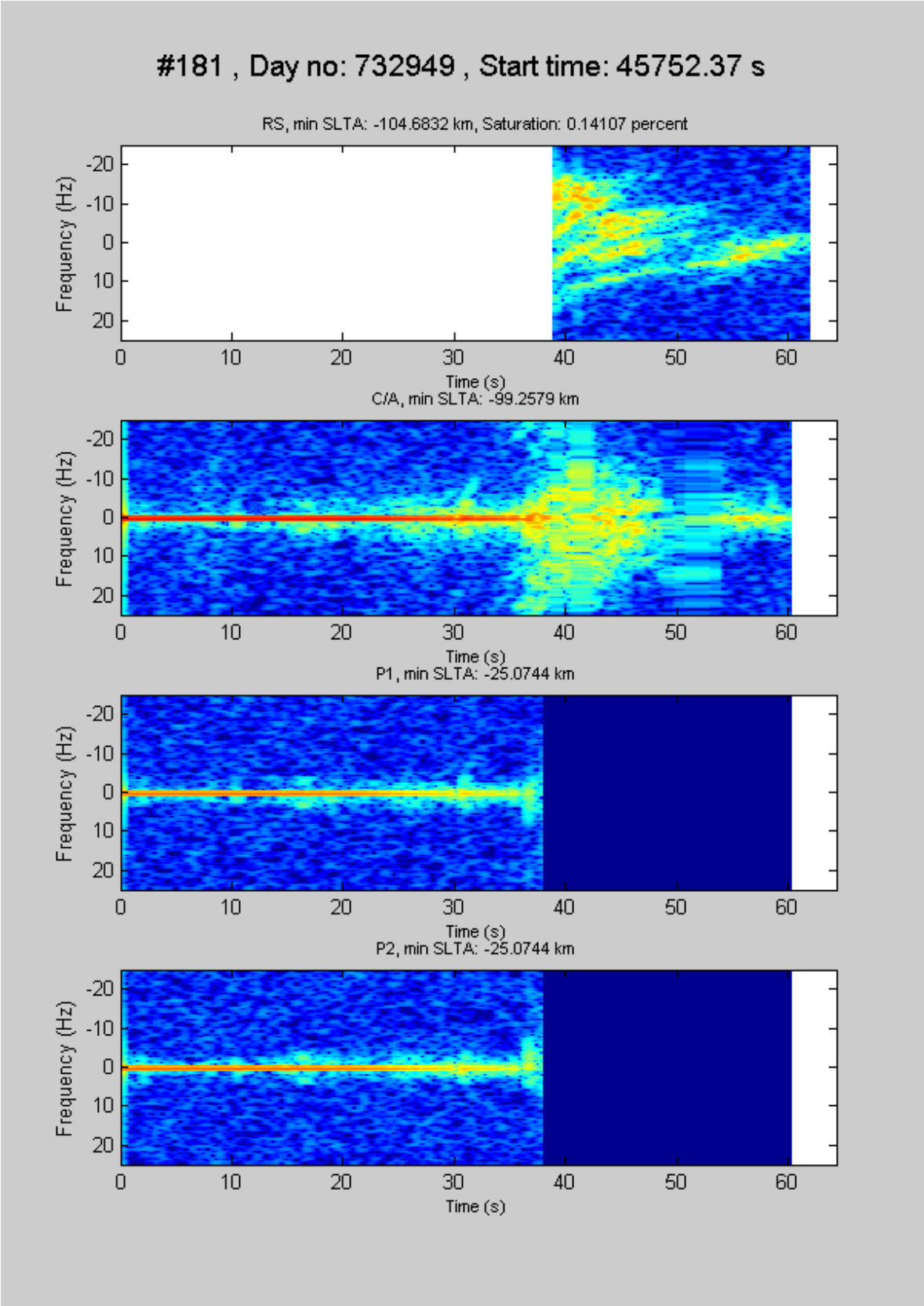

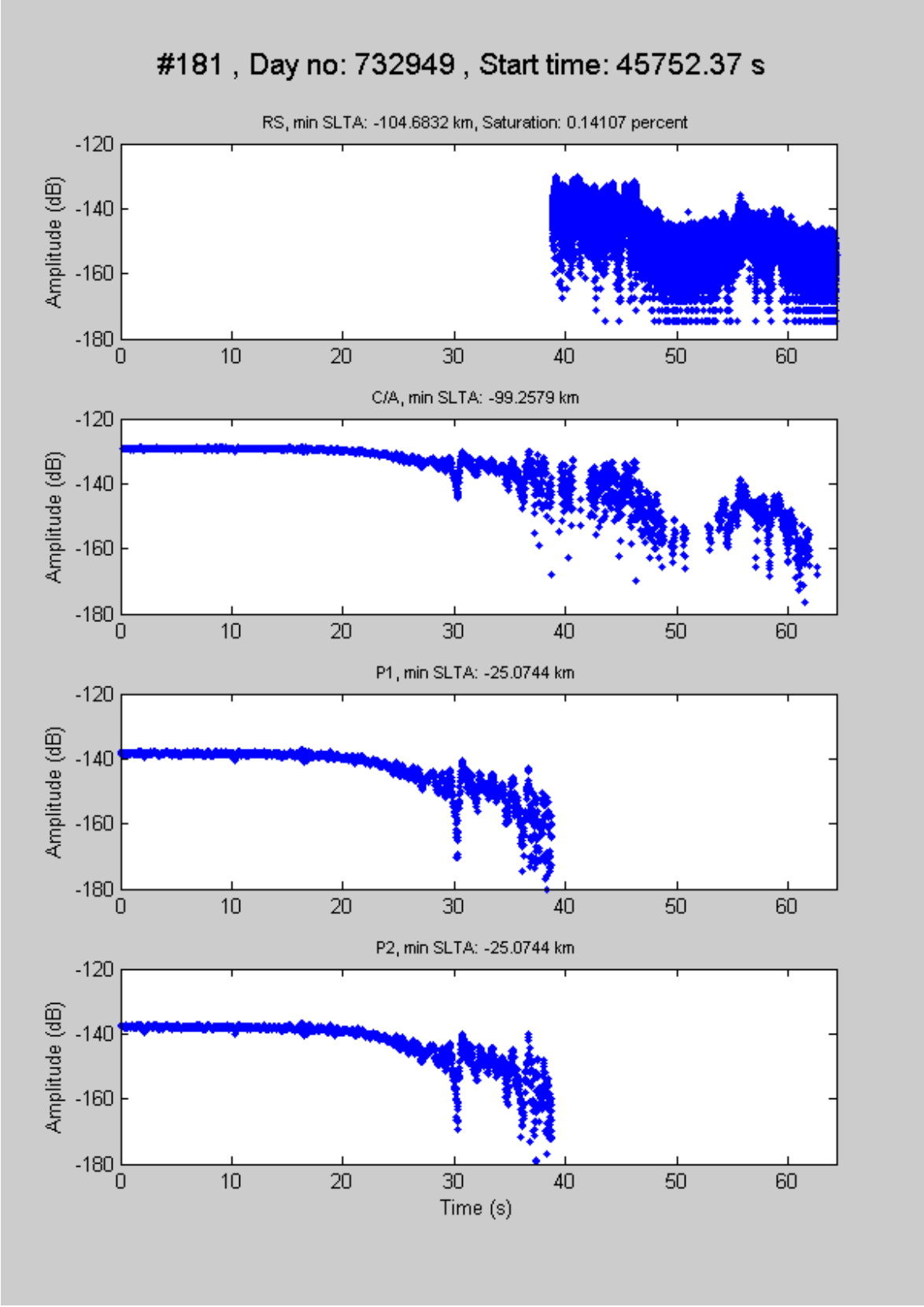
#181 , Day no: 732949 , Start time: 45752.37 s
RS, min SLTA: -104.6832 km, Saturation: 0.14107 percent
C/A, min SLTA: -99.2579 km
P1, min SLTA: -25.0744 km
P2, min SLTA: -25.0744 km
Amplitude (dB)
-120
-140
-160
-180
0
10
20
30
40
50
60
Time (s)

Appendix A.11 Case 11: Co-channel disturbance

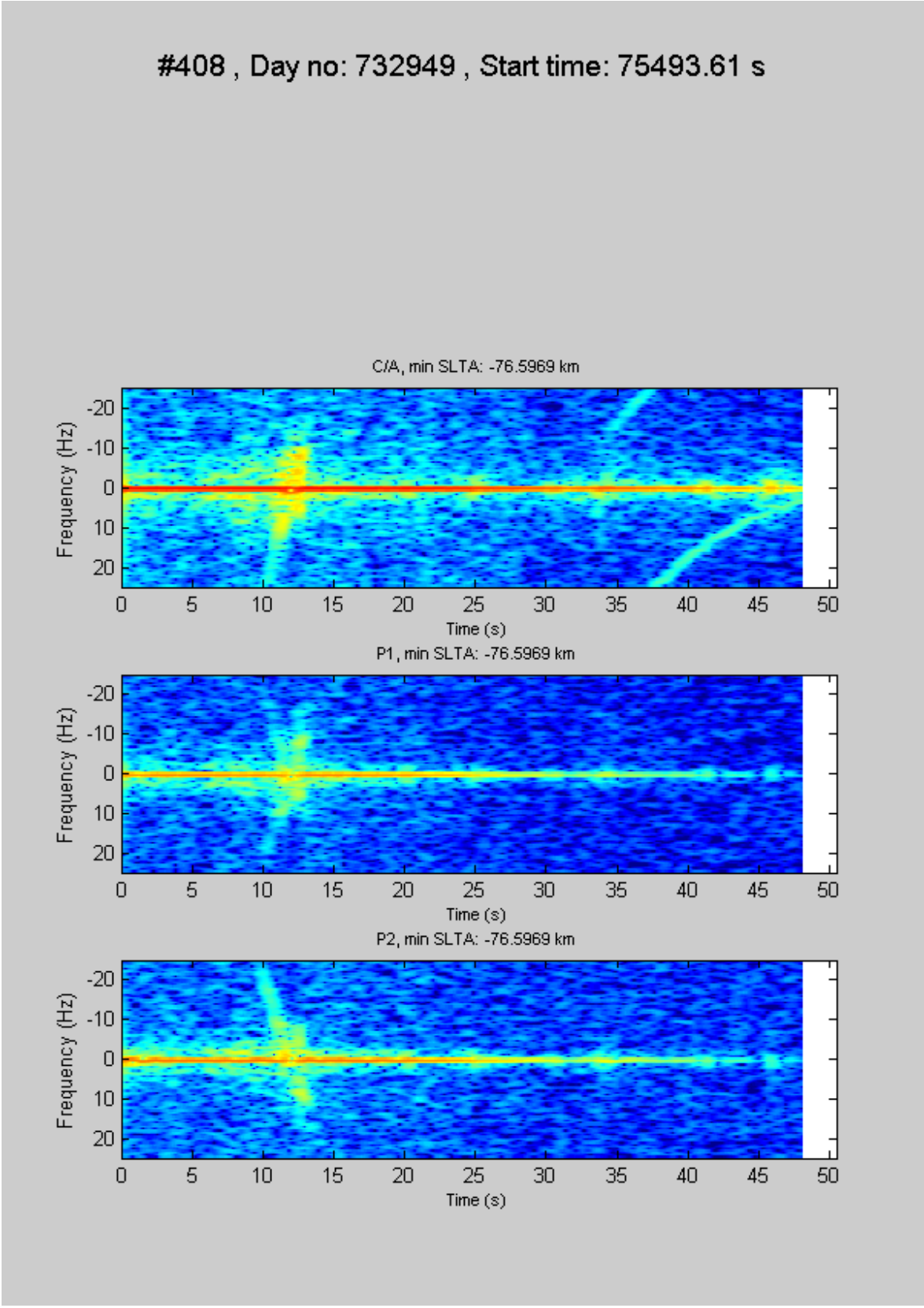

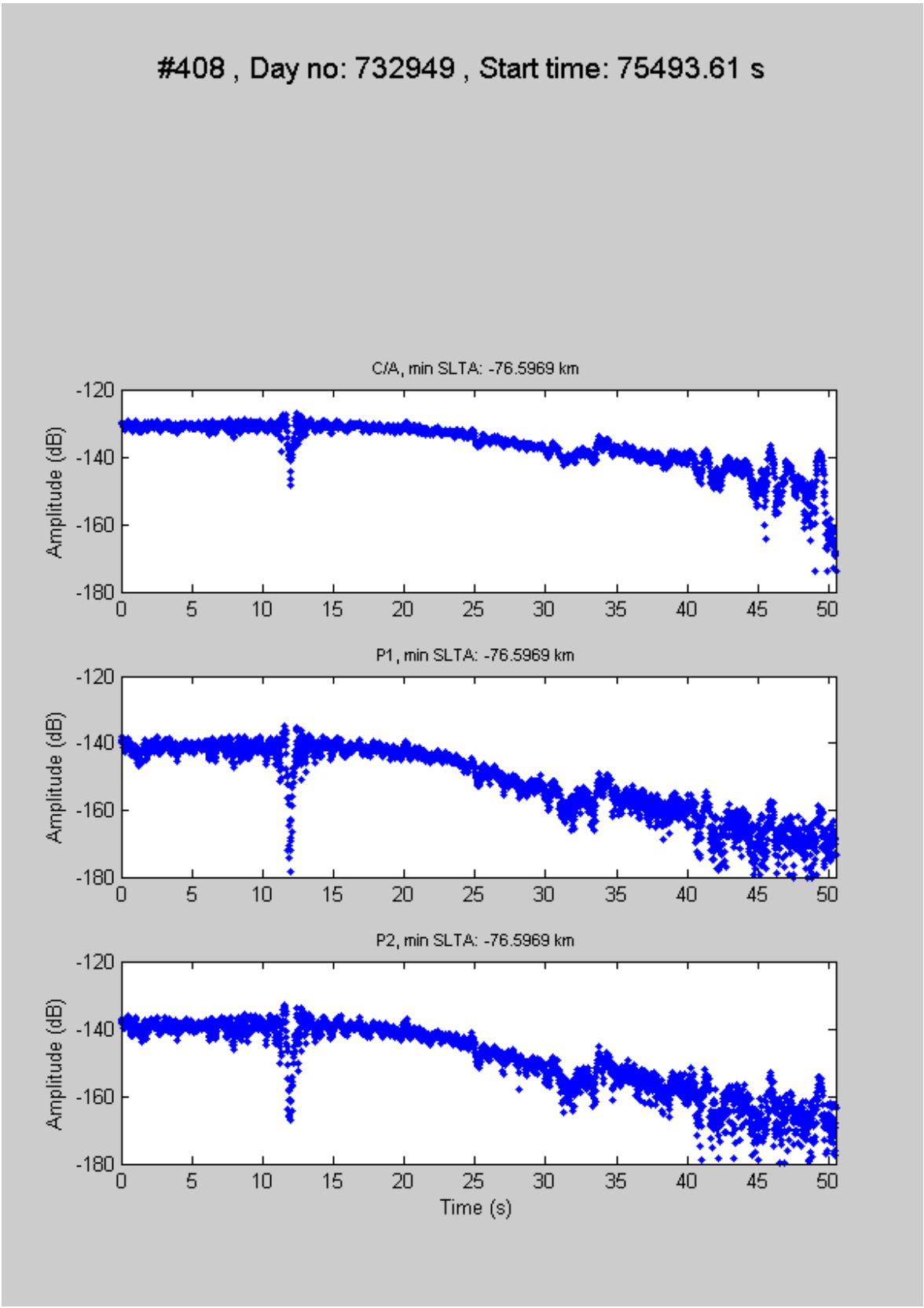
#408 , Day no: 732949 , Start time: 75493.61 s
C/A, min SLTA: -76.5969 km
P1, min SLTA: -76.5969 km
P2, min SLTA: -76.5969 km
Amplitude (dB)
-120
-140
-160
-180
0
5
10
15
20
25
30
35
40
45
50
Time (s)

Appendix A.12 Case 12: L1 data gap

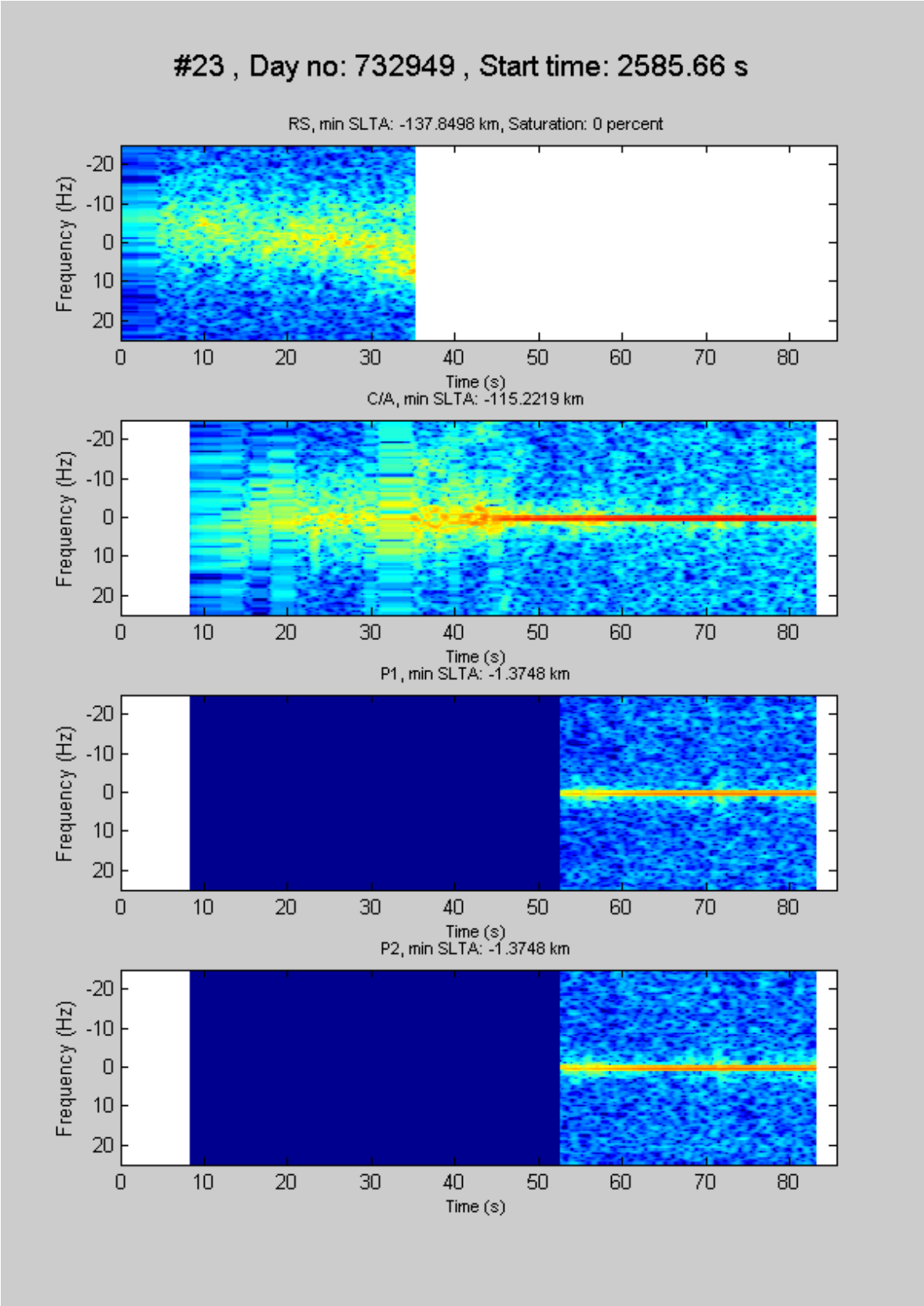

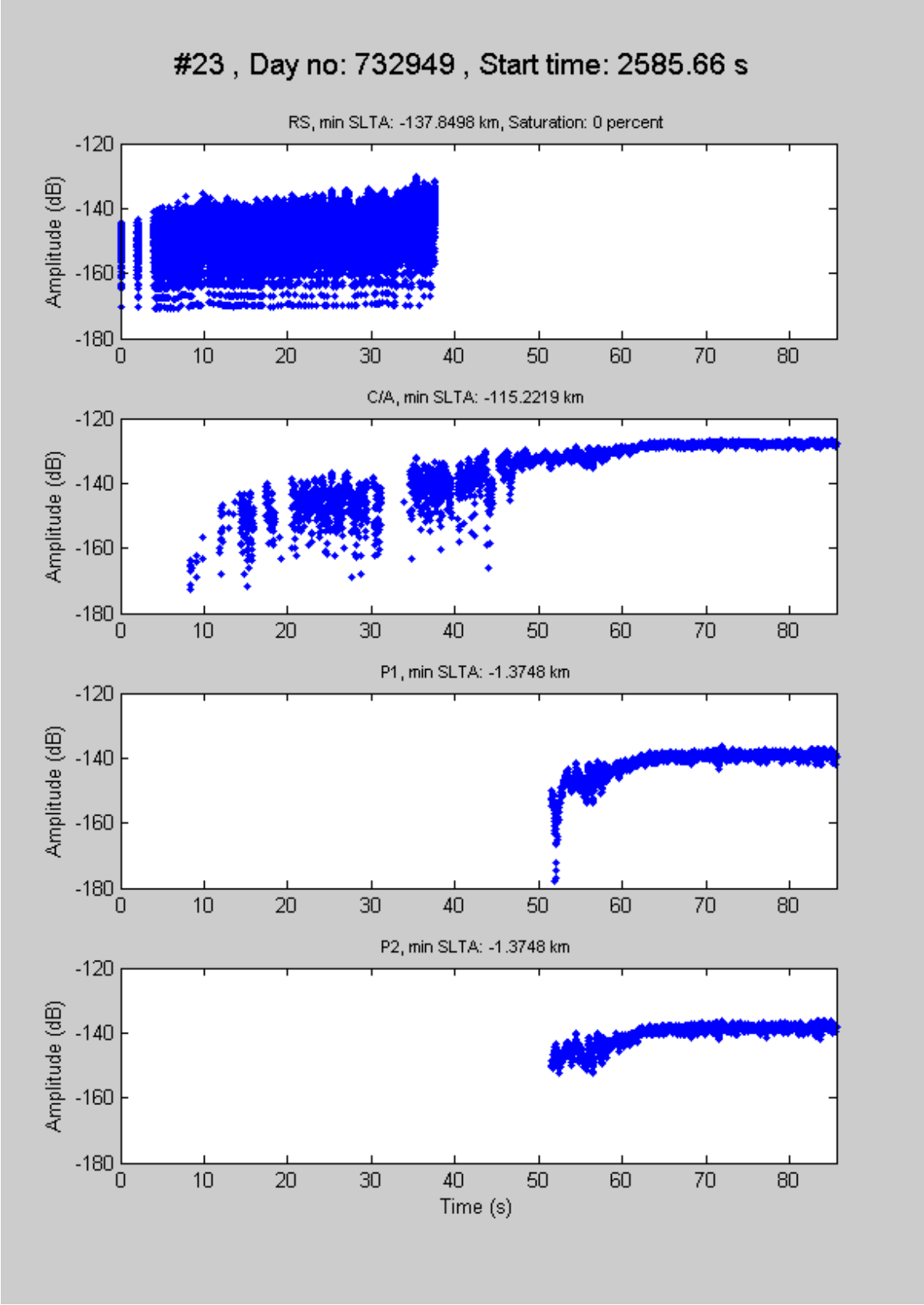
#23 , Day no: 732949 , Start time: 2585.66 s
RS, min SLTA: -137.8498 km, Saturation: 0 percent
C/A, min SLTA: -115.2219 km
P1, min SLTA: -1.3748 km
P2, min SLTA: -1.3748 km
Amplitude (dB)
-120
-140
-160
-180
0
10
20
30
40
50
60
70
80
Time (s)

APPENDIX B STUDY CASES RUN BY DMI

The results presented in section 7.1 include the processed data by the OCC code implementation. In the processing of GRAS data we observe all the typical features that we can also see in COSMIC data: multipath structures and reflected rays.

Below we present diagnostic plots for selected cases. The plots have 9 panels organized as table with 3 rows and 3 columns:

Upper row:

- The left panel in the upper row shows amplitudes (red line) and receiver mode (blue line, 0 for CL, 750 for OL).
- The middle panel in the upper row shows bending angles: L1 from GO processing (black line, GO L1), L2 from GO processing (red line, GO L2), and ionospherically-corrected neutral atmospheric bending angle from CT (green line, CT N).
- The right panel in the upper raw shows bending angles for large heights: ionospheric (blue line, IONO), linear combination of L1 and L2 (red line, LC), neutral bending angle from CT (green line, CT N).

Middle row:

- The left panel in the middle row shows tropospheric bending angles and receiver mode: GO L1 (black line), GO L2 (red line), CT L1 (green line), CT L2 (blue line), and the border between the CL and OL receiver modes in the bending angle – impact parameter space (violet line, CL/RS).
- The middle panel in the middle row shows the CT amplitude.
- The right panel in the middle raw shows the L1 radio-holographic spectra in the troposphere and CT L1 bending angles (red line). The RH spectra are useful for the visual inspection of data in order to detect multipath structure, as well signal tracking problems and noise properties.

Lower row:

- The left panel in the lower row indicates the L1 radio-holographic spectra up to a height of 30 km.
- The middle panel in the lower row indicates the L2 radio-holographic spectra up to a height of 30 km.
- The right panel in the lower row indicates the retrieved dry temperature profile.

Appendix B.1 Case 1: L2 tracking to low SLTA

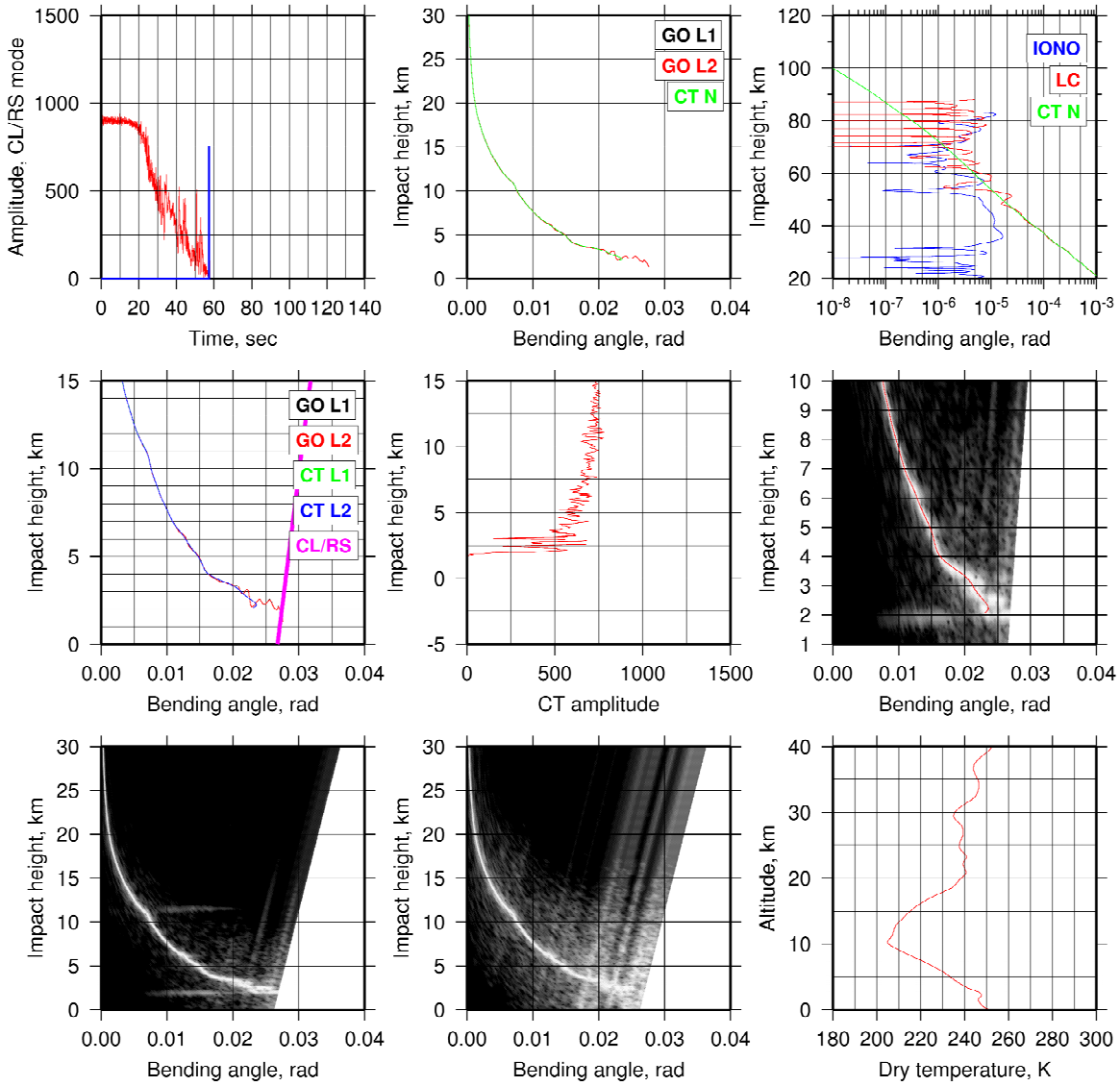

Figure 134. Occultation event observed on 2007/09/30 at UTC 21:47:03, 65.93°S 87.20°E, badness score 18.727.

The event shown in Figure 134 was correctly processed by our system. Almost the whole data set, except a small final fragment in the shadow zone, was recorded in CL mode. L2 was tracked down to the surface. L1 indicates a very distinct signature of a surface reflection.

Appendix B.2 Case 2: OL tracking to low SLTA

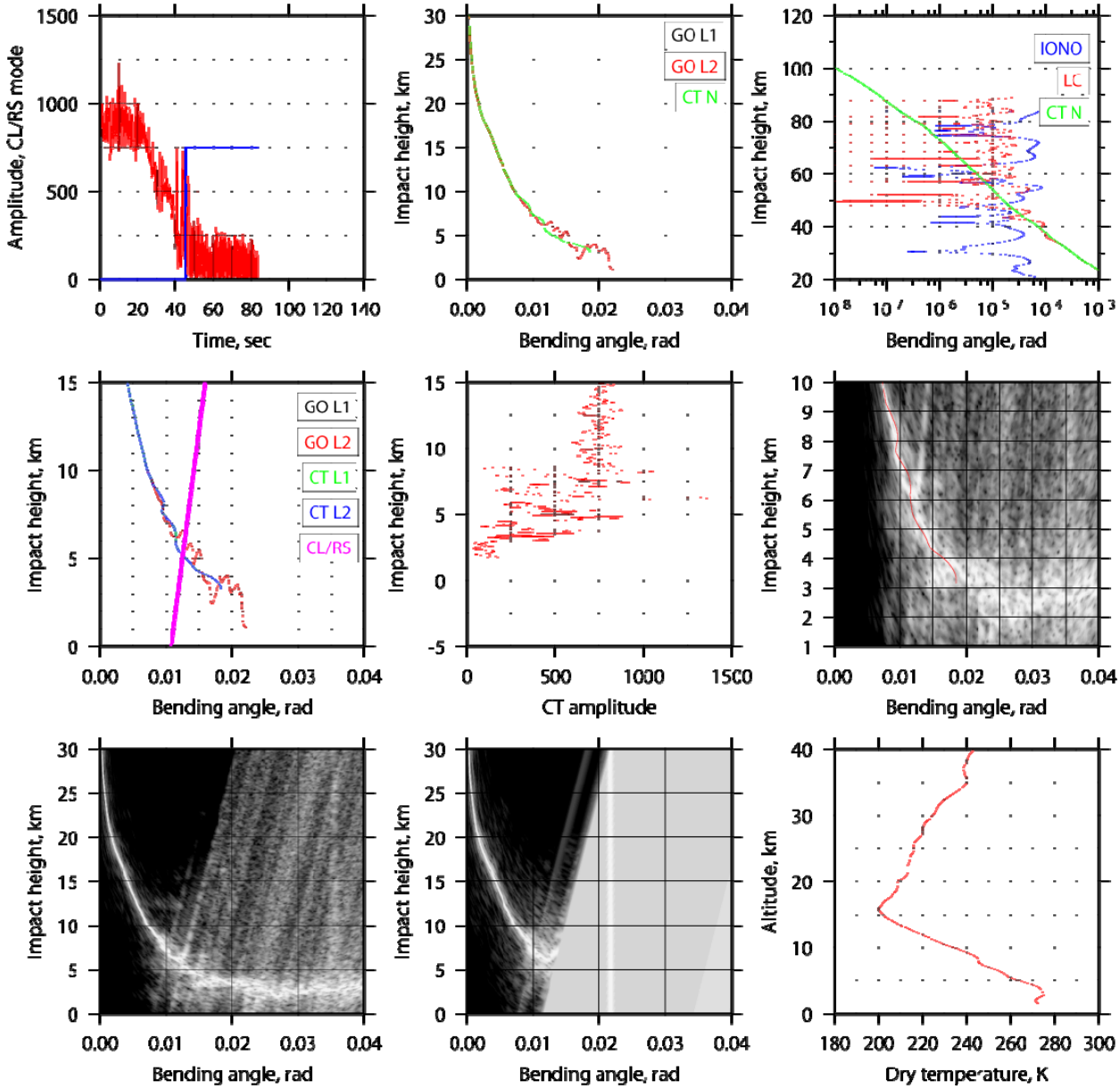

Figure 135. Occultation event observed on 2007/09/30 at UTC 00:20, 24.6°N 26.7°W, badness score 25.879.

The event shown in Figure 135 was correctly processed by our system. The amplitude plot indicates a level of noise higher than in most other events. Still, it does not create any significant problems.

Appendix B.3 Case 3: Ocean reflection

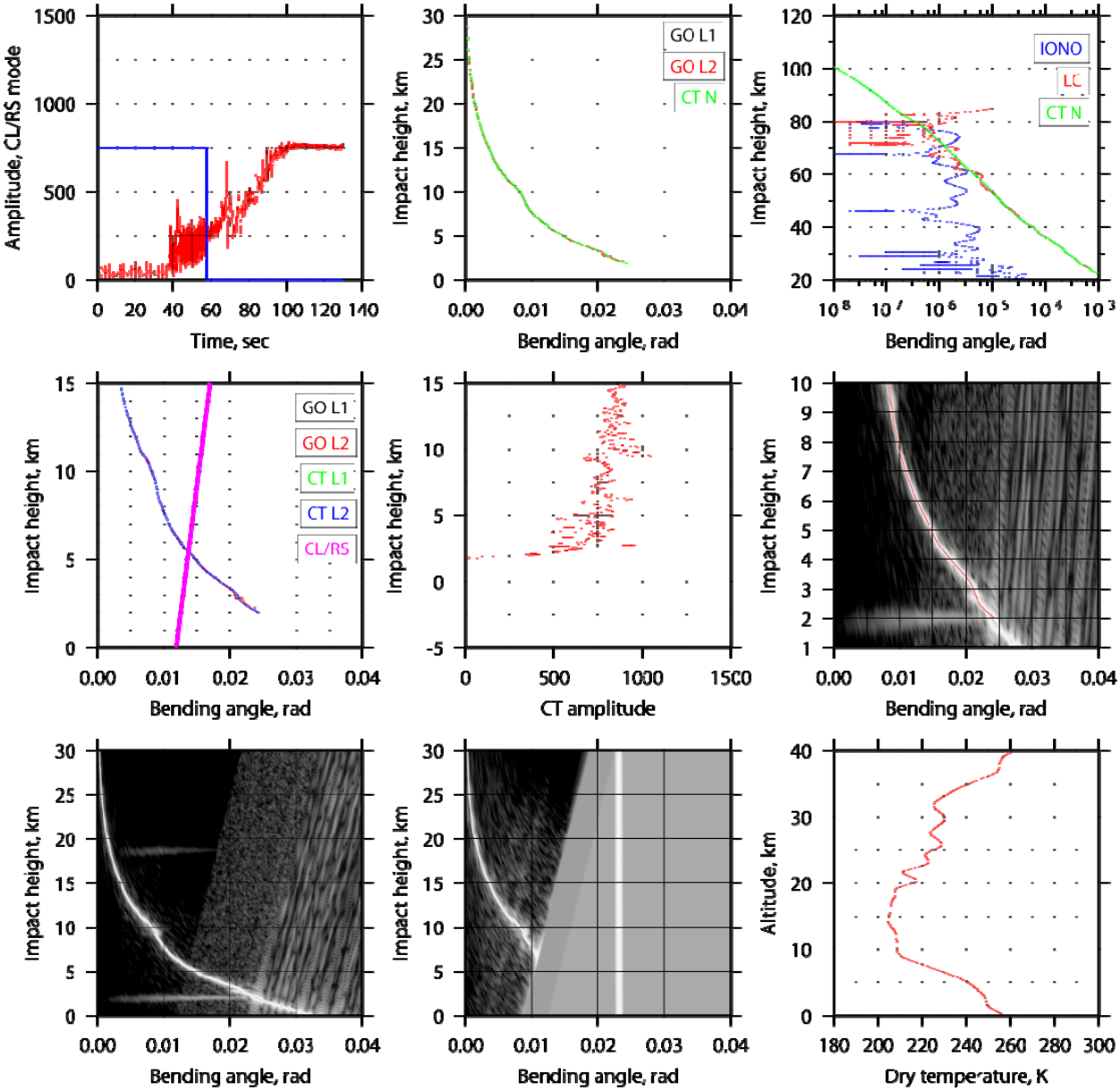

Figure 136. Occultation event observed on 2007/09/30 at UTC 01:22, 56.7°S 3.5°E, badness score 20.270.

The event shown in Figure 136 was correctly processed by our system. Such cases are normal and they do not create any processing problems for FIO-based algorithms, because direct and reflected rays are separated in the impact parameter space.

Appendix B.4 Case 4: L2 feature at high SLTA

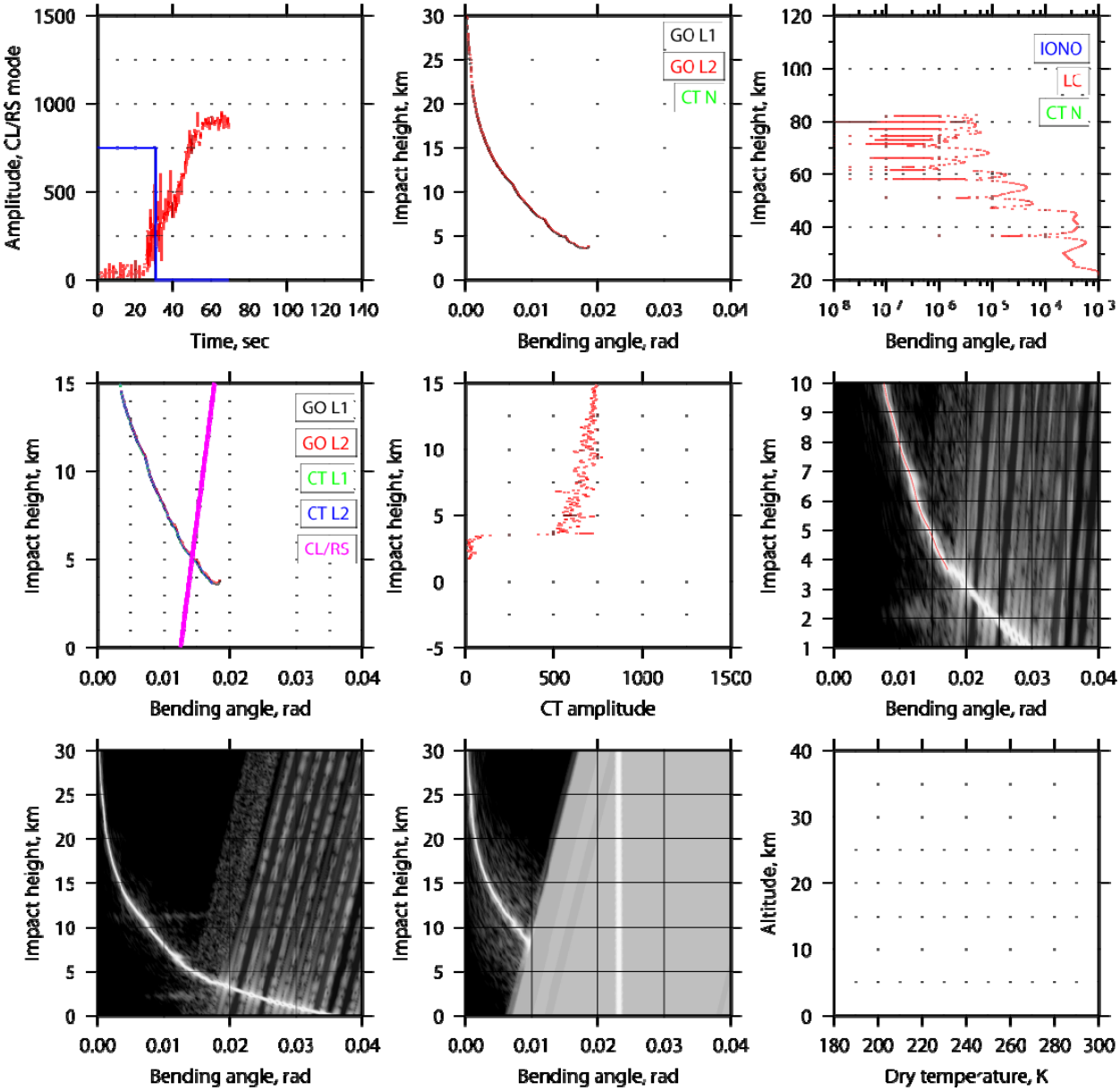

Figure 137. Occultation event observed on 2007/09/30 at UTC 04:40, 84.7°S 144.0°W, badness score 20215.970.

The event shown in Figure 137 did not pass our QC procedure. The L2 perturbation resulted in an abnormally high badness score (typical values for good profiles are less than 35), which would prevent this event from being included into further processing. The refractivity retrieval procedure returned an error code signifying occurrence of negative refractivity.

Appendix B.5 Case 5: Long fade

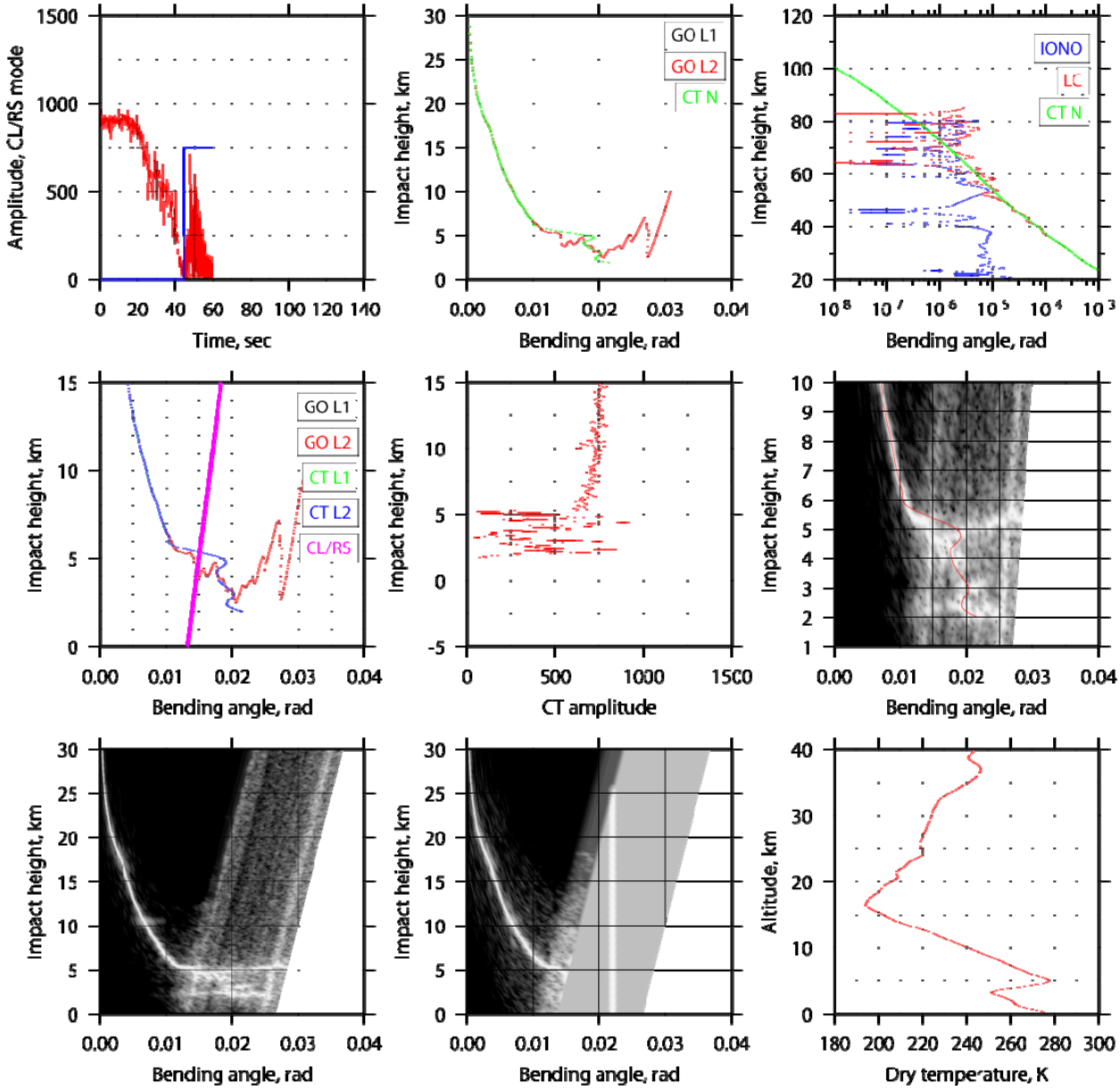

Figure 138. Occultation event observed on 2007/09/30 at UTC 15:35, 23.9°N 71.9°E, badness score 30.092.

The event shown in Figure 138 was correctly processed by our system. The event is interesting in that respect that it indicates a spike in the bending angle profile at an impact height of 5 km. This spike creates a fading signal in the vicinity of the shadow zone.

Appendix B.6 Case 6: 10 Hz disturbance

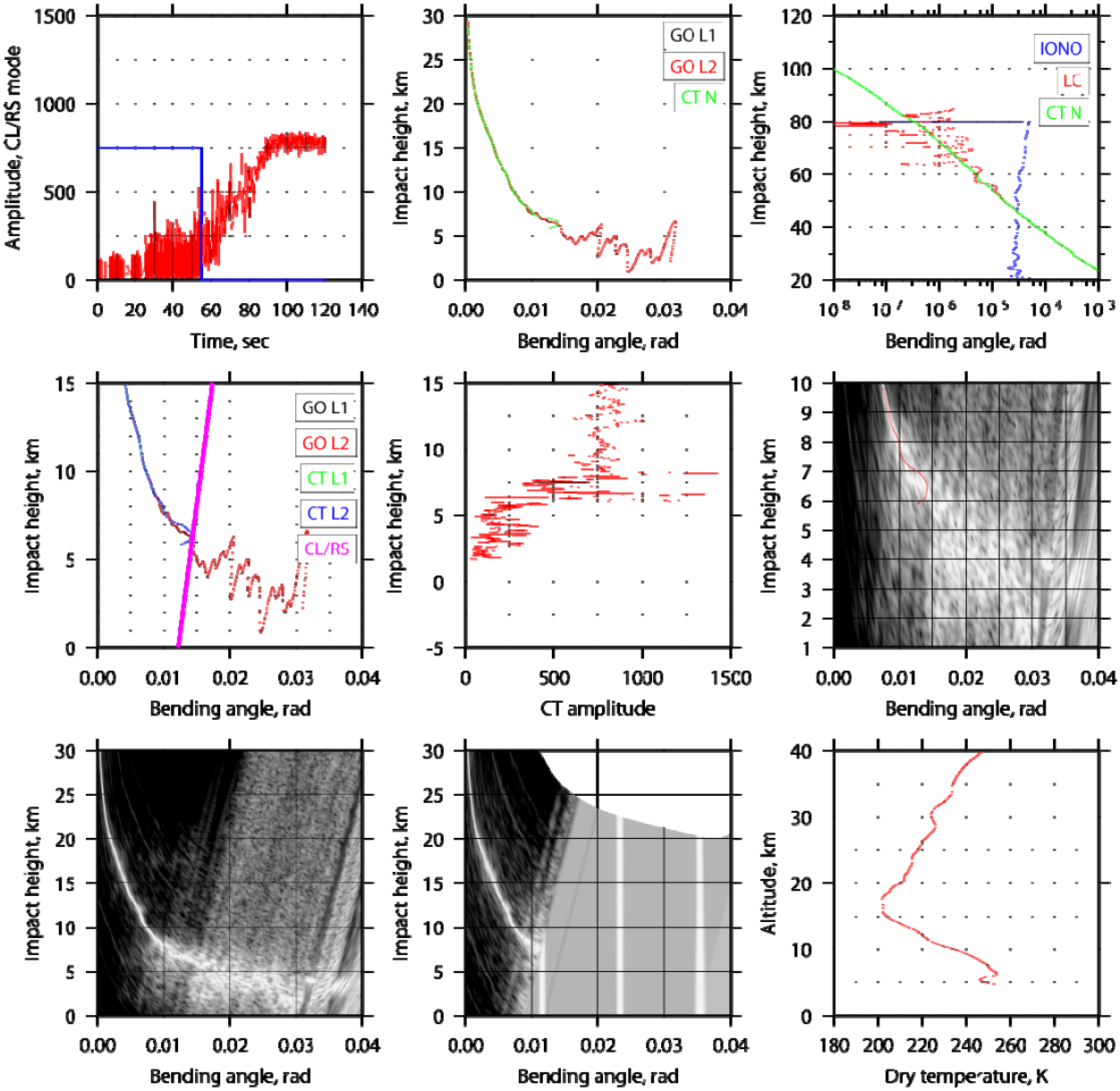

Figure 139. Occultation event observed on 2007/09/30 at UTC 20:59, 37.0°N 167.9°E, badness score 27.068.

The event shown in Figure 139 indicates a 10 Hz disturbance in CL part. This disturbance is visualized in the spectra as thin lines parallel to the main bending angle profile (these weak lines are more clearly visible in the original high resolution PostScript file). The perturbation is weak and it does not create problem for processing the CL data. Still, RS record indicates a high level of noise and all the RS data are identified as a 'shadow zone' because the CT amplitude drops below the height of 6 km.

Appendix B.7 Case 7: Raw sampling saturation

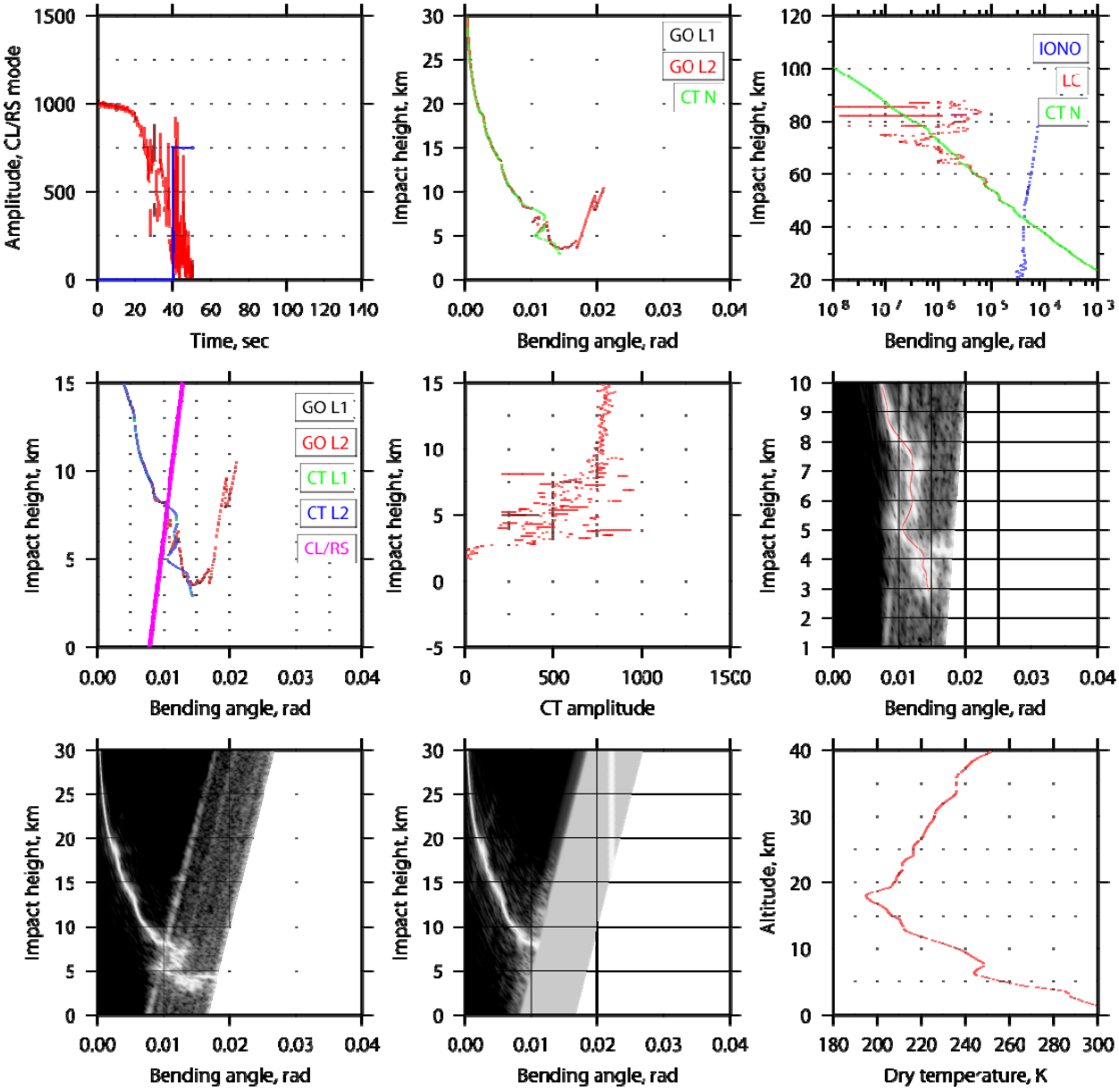

Figure 140. Occultation event observed on 2007/09/30 at UTC 14:42, 22.4°S 70.0°W, badness score 29.233.

Event shown in Figure 140 was processed by our system. The RS data indicate spectrum with an enlarged width, resulting in very low bending angles and corresponding high dry temperature. This anomaly is not identified by the badness score, mostly because it is not straightforward to formalize criteria for automatic recognition of such situation. However, this event is expected to not pass QC when being assimilated into numerical weather prediction model (since NWP models typically use a pre-screening based on the relative deviation of the measurement from the model state).

Appendix B.8 Case 8: Weak P(Y) code signal

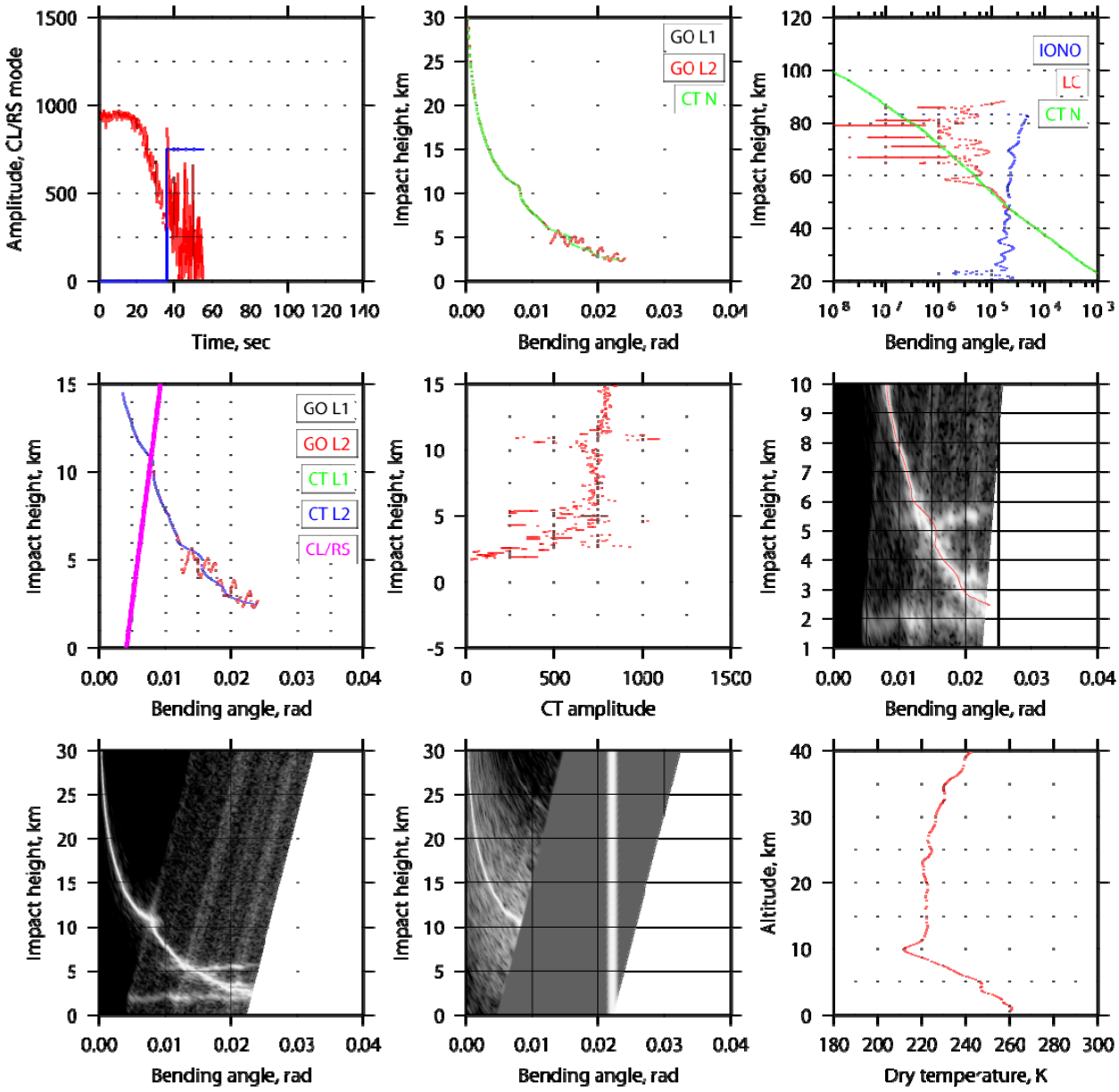

Figure 141. Occultation event observed on 2007/09/30 at UTC 02:29, 52.4°N 146.4°E, badness score 27.844.

Event shown in Figure 141 indicates a weak L2 signal, which results in noise L2 spectrum. Still, our L2 correction procedure has been able to correctly process L2 data without forming a high badness score.

Appendix B.9 Case 9: False tracking

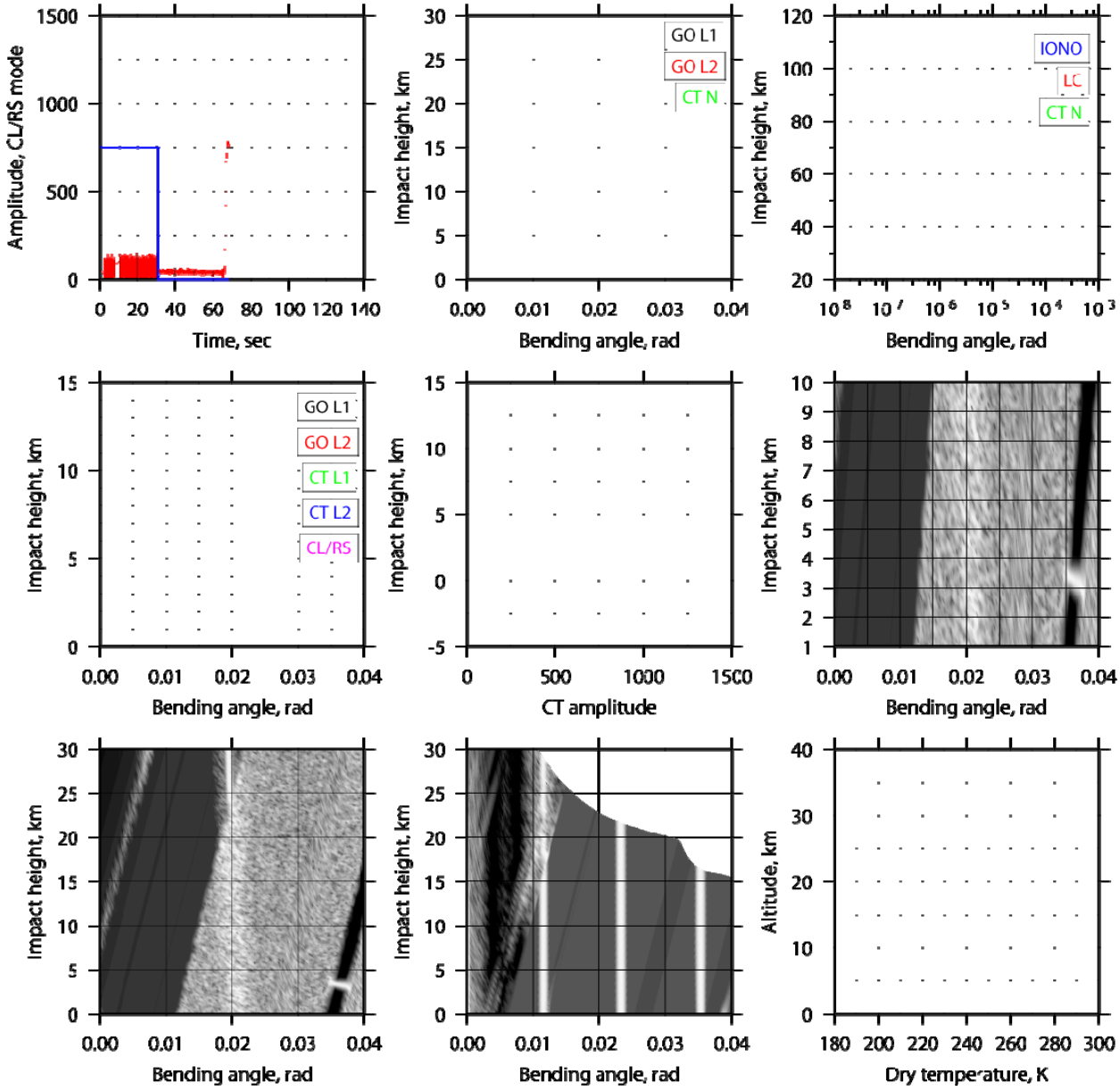

Figure 142. Occultation event observed on 2007/09/30 at UTC 12:19, 66.5°N 11.9°E.

The event shown in Figure 142 does not contain useful data. The processing of event finished early with an error code signifying that it was impossible to cut-off the data.

Appendix B.10 Case 10: Wideband signature

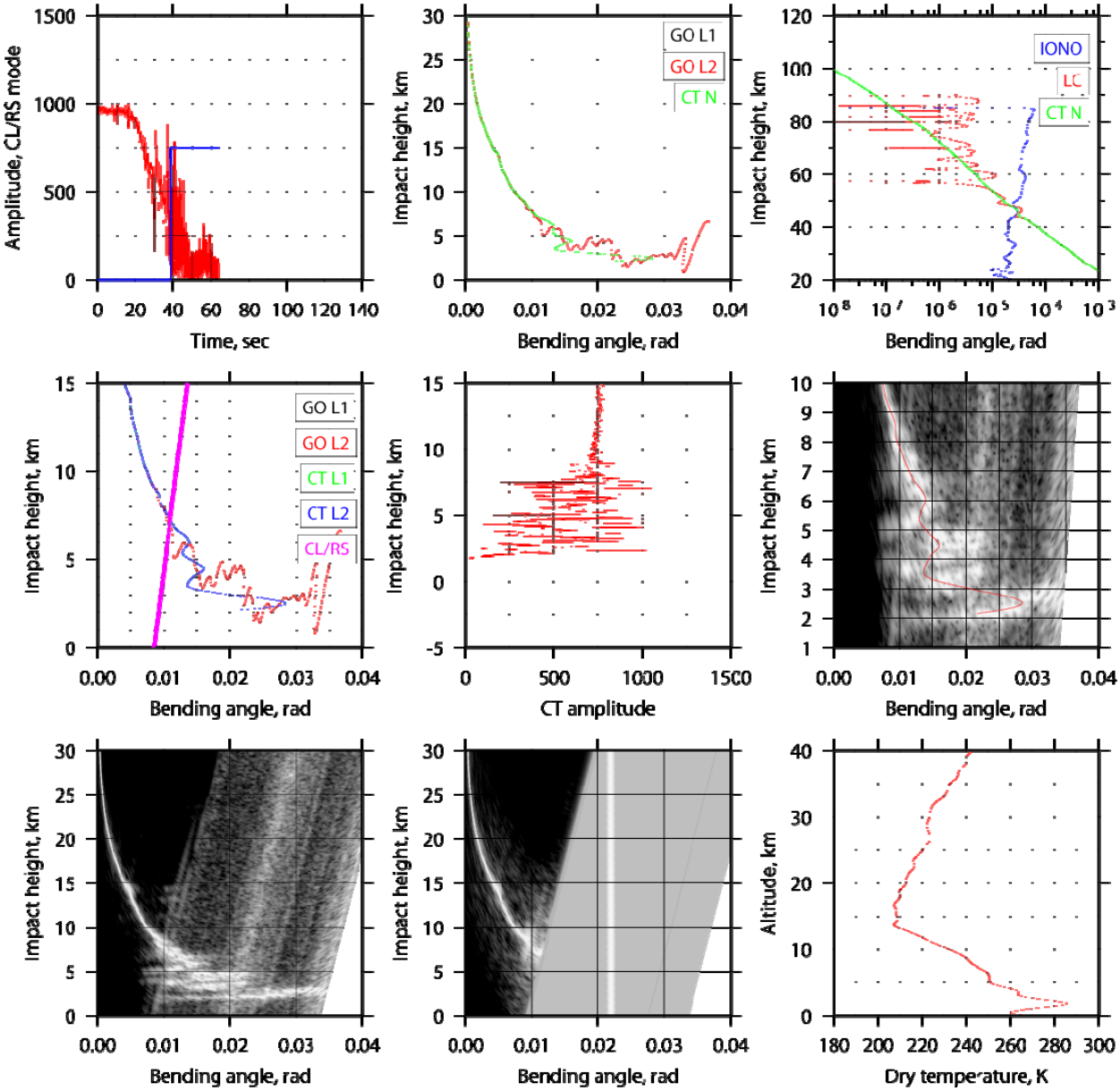

Figure 143. Occultation event observed on 2007/09/30 at UTC 12:42, 45.4°N 29.3°W, badness score 29.551.

The event shown in Figure 143 indicates a complicated tropospheric structure of bending angle, the fragments of the structure retrieved from CL and OL data fit each other very well. The event passed our processing with a moderate badness score.

Appendix B.11 Case 11: Co-channel disturbance

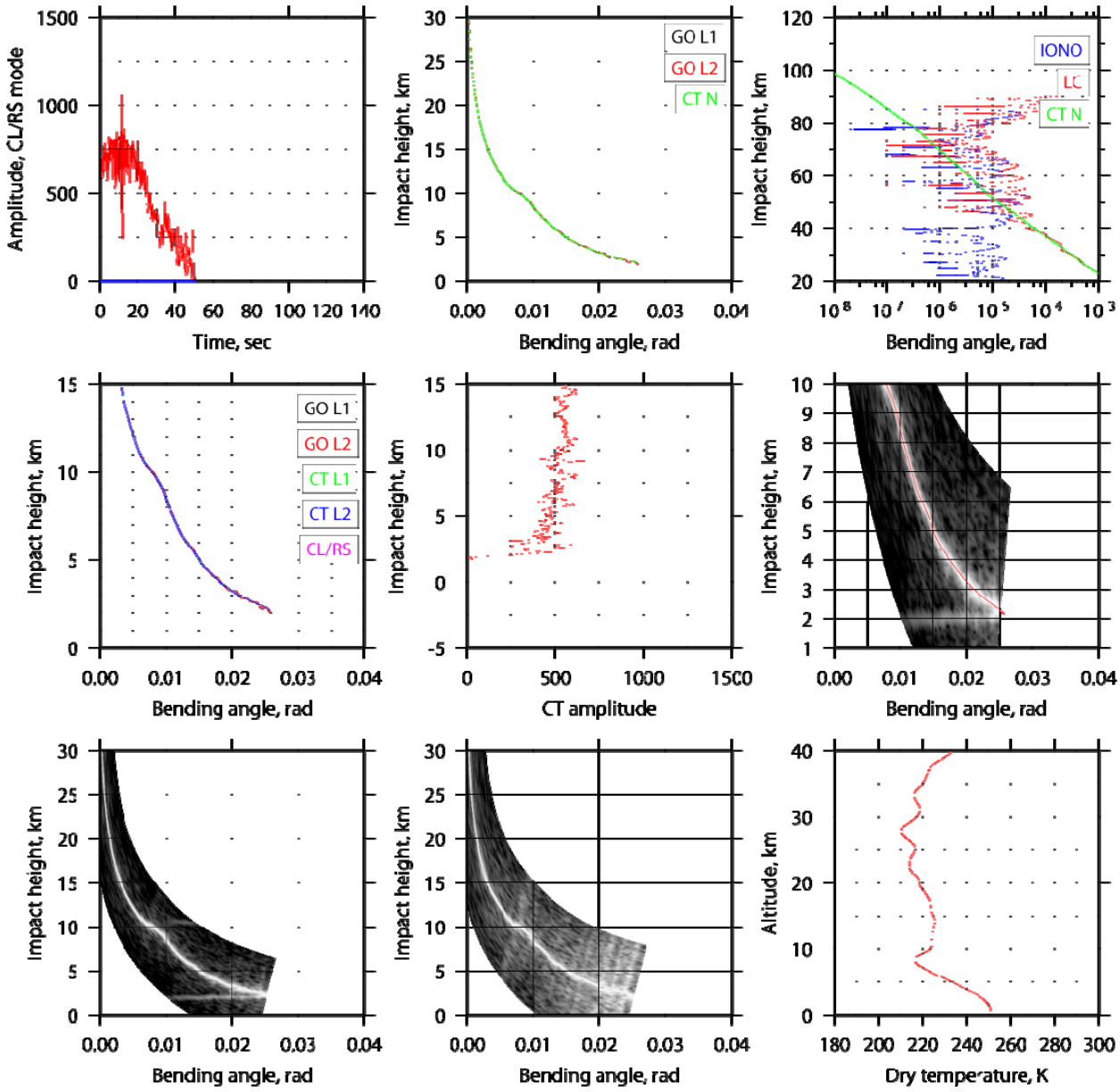

Figure 144. Occultation event observed on 2007/09/30 at UTC 20:58, 87.0°N 135.8°W, badness score 29.898.

This event (2007/09/30, UTC 20:58) was normally processed. The cross-channel disturbance is a weak parasitic signal.

Appendix B.12 Case 12: L1 data gap

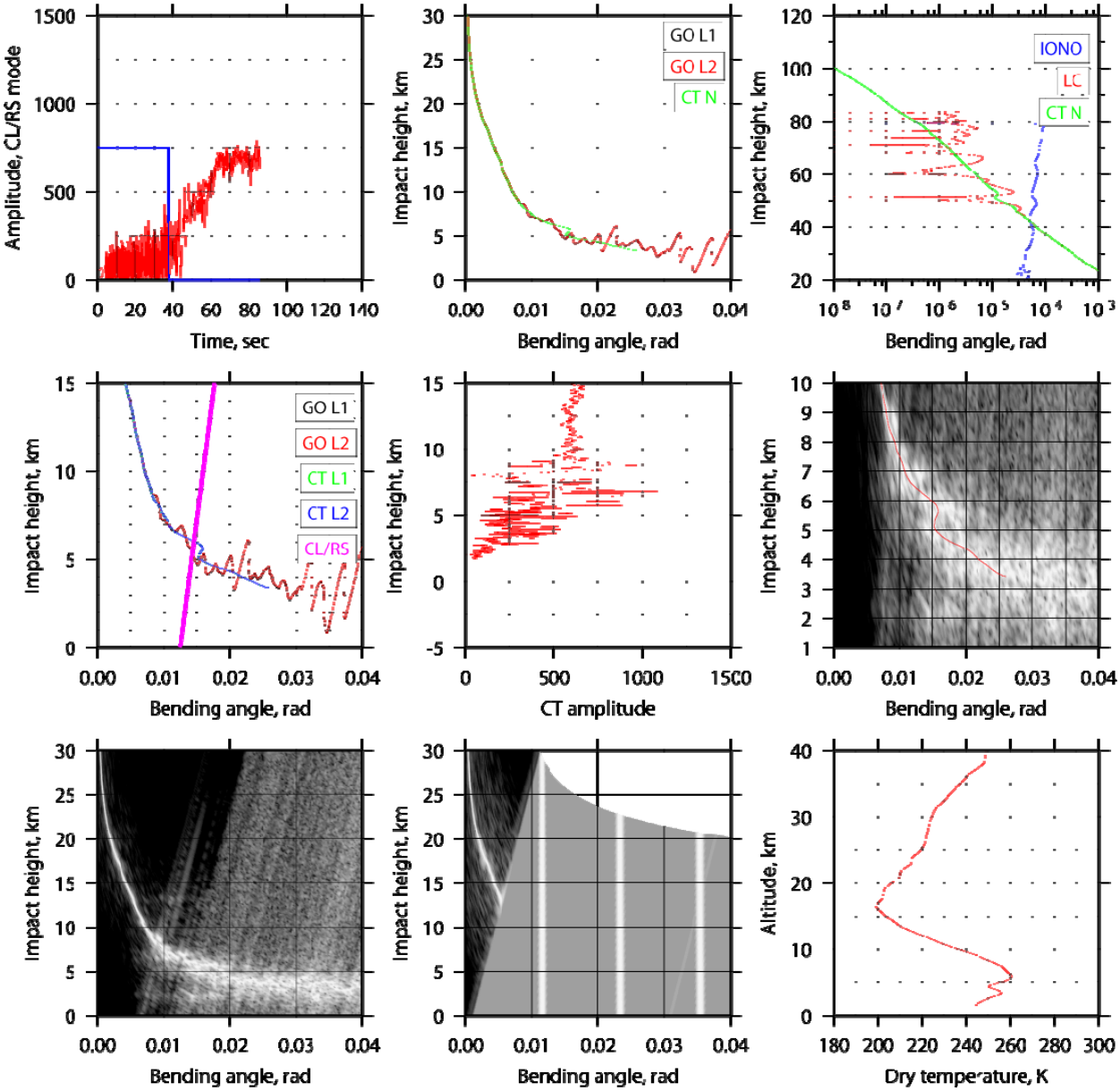

Figure 145. Occultation event observed on 2007/09/30 at UTC 00:43, 27.7°N 154.8°E, badness score 33.914.

The event shown in Figure 145 has a gap in the CL record that is not covered by the RS data. This results in a gap between CL and OL when merging them. The gap is shorter than 0.8 seconds, which was set as the acceptable gap length in this study. So our procedure filled-in the gap, which allowed using the RS data.

Appendix B.13 Additional Case: L1 data gap

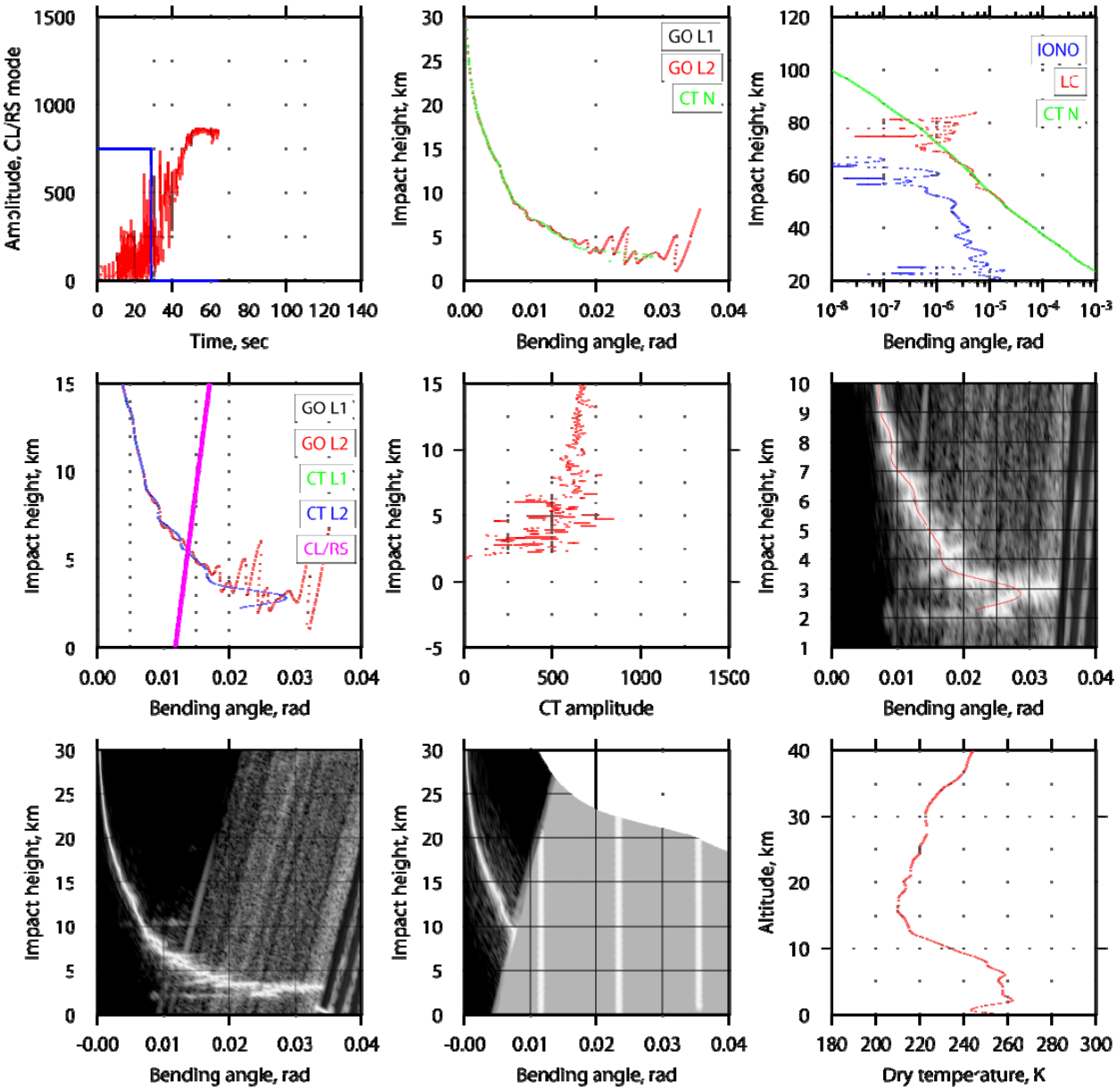

Figure 146. Occultation event observed on 2007/09/30 at UTC 00:13, 46.1°N 57.7°W, badness score 26.499. This is an example of a middle-latitude event with medium-strength multipath effects.

Figure 146 shows an example of a middle-latitude occultation. Here we observe multipath effects of medium strength. The CT amplitude also indicates scintillations, but they have lower spatial frequencies signifying a different type of structures as compared to the above tropical example. This is a rising event. In the deep shadow the RS record indicates multiple long gaps separated by short pieces of data. This is explained by the fact that receiver repeatedly attempted to lock the signal. The spectra also show the phase model, which was used to fill-in the gaps. This part of the record was cut-off in the inversion. The receiver left the RS mode and switched to CL at a height of 6 km.

APPENDIX C Radio Occultation Statistics for One Day

This appendix presents the results of the processing made for one day with the FSI processing chain. The day that has been selected is the 30th of September 2007. The total number of radio occultations for this day is 655. The closed loop and raw sampling sections of the measurements has been merged, this has been done for a total of 623 radio occultations. The position of the mean tangent points during the occultation event for the day 30th of September 2007 is shown in the figures below.

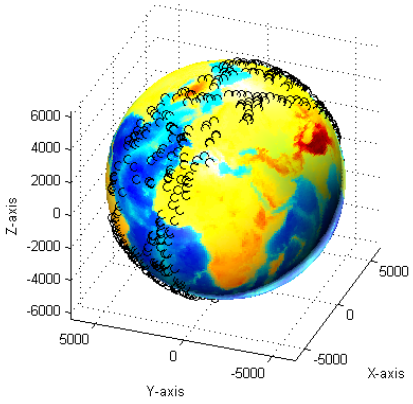

Figure 147 The positions of the mean tangent points for one day.

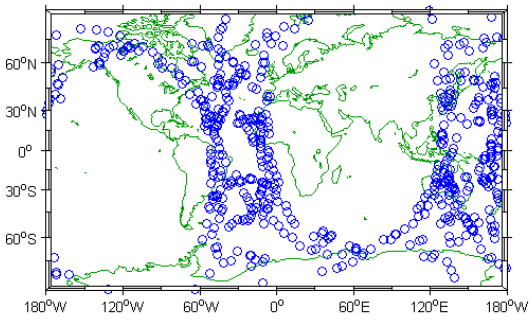

Figure 148 The map positions of the mean tangent points for one day.

The radio occultations during one day have been divided into 3 latitude bands. The size of the 3 latitude band is 60 degrees. The frequency function for each of these latitude bands is shown in the figure below. It is seen from the figure that the radio occultations for one day is not enough to make the occultations evenly distributed in latitude.

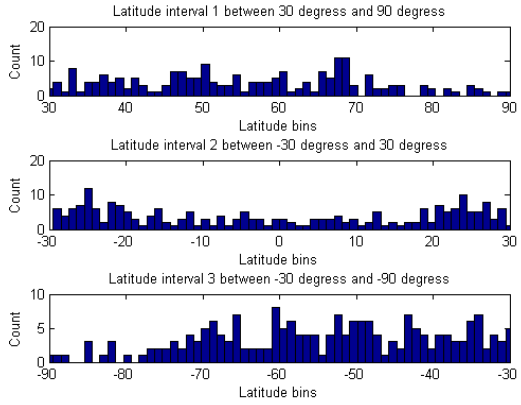

Figure 149The 3 plots show for the 3 latitude bands the number of radio occultations in each of the latitude bins.

Examples and statistics

This section presents the statistics for the day 30th of September 2007. The retrieved parameters are compared to the corresponding ECMWF values.

A statistical analysis will now be performed on the radio occultation data for the day 30 September 2007. Two statistical parameters are calculated. The two parameters are, normalized bias (BIAS), and normalized standard error of the difference (NSED).

The normalized bias (NBIAS) is defined as the mean value of the absolute error normalized with respect to the mean true value. This parameter can be estimated with the following equation

$$NBIAS = \frac{\frac{1}{N}\sum_{i=1}^{N}(x_{mi} - x_{vi})}{\frac{1}{N}\sum_{i=1}^{N} x_{vi}} \qquad \text{(D-1)}$$

where N is the number samples and x_{vi} and x_{mi} is the i'th sample of the true and measured value respectively.

The normalized standard error of the difference (NSED) is defined as the standard deviation of the absolute error normalized with respect to the mean value of the true value and is estimated by the following equation

$$NSED = \frac{\sqrt{\frac{1}{N}\sum_{i=1}^{N}(x_{mi} - x_{vi} - BIAS)^2}}{\frac{1}{N}\sum_{i=1}^{N} x_{vi}} \qquad \text{(D-2)}$$

These parameters have been calculated for the bending angle, refractivity and temperature profiles. The first batch of plots show the results when all of the data for the day is used while the following 3 batch of plots show the results when only the data in each of the 3 latitude band s are used. It seen from these figures that the error levels are as expected highest in the regions around the equator.

Statistics based on the radio occultation data for the day 30/9 2007

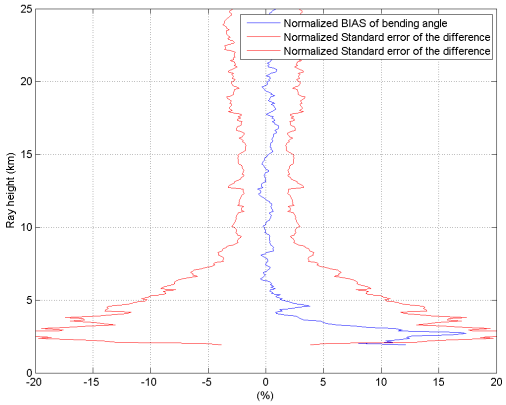

Figure 150 The bending angle bias (blue curve) and standard error of the difference for bending angle (red curve) as a function of height.

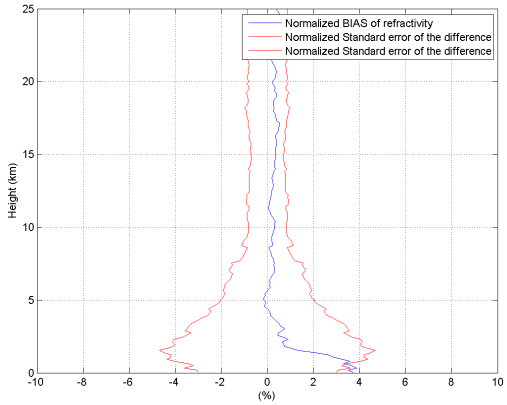

Figure 151 The refractivity bias (blue curve) and standard error of the difference for refractivity (red curve) as a function of height.

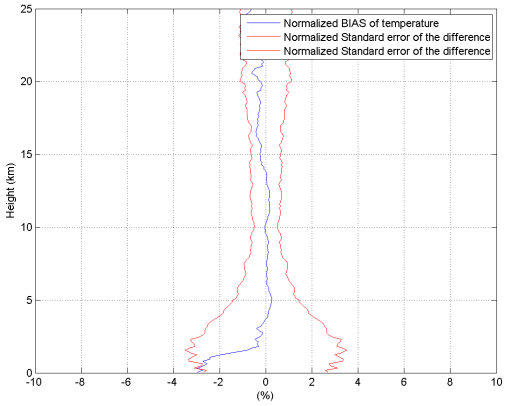

Figure 152 The temperature bias (blue curve) and standard error of the difference for temperature (red curve) as a function of height.

Statistics based on the radio occultation data in latitude interval 1 for the day 30/9 2007

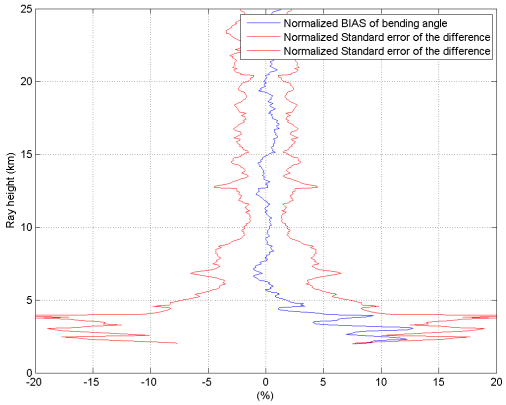

Figure 153 The bending angle bias (blue curve) and standard error of the difference for bending angle (red curve) as a function of height.

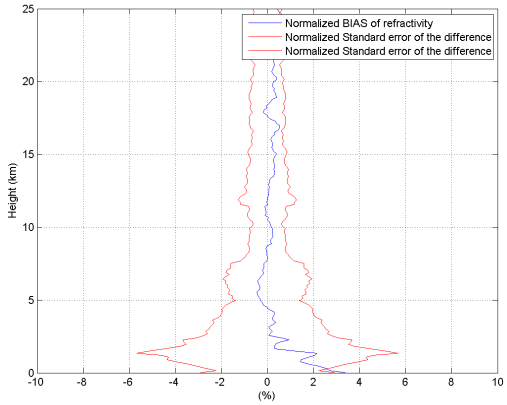

Figure 154 The refractivity bias (blue curve) and standard error of the difference for refractivity (red curve) as a function of height.

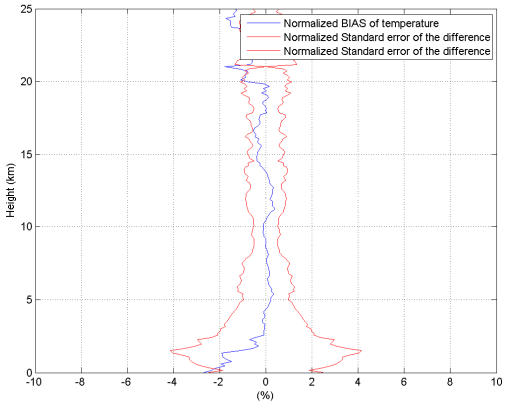

Figure 155 The temperature bias (blue curve) and standard error of the difference for temperature (red curve) as a function of height.

Statistics based on the radio occultation data in latitude interval 2 for the day 30/9 2007

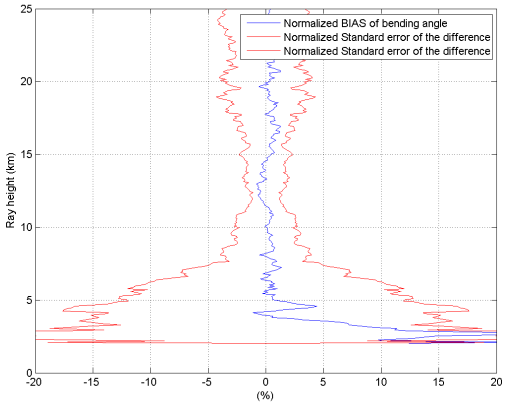

Figure 156 The bending angle bias (blue curve) and standard error of the difference for bending angle (red curve) as a function of height.

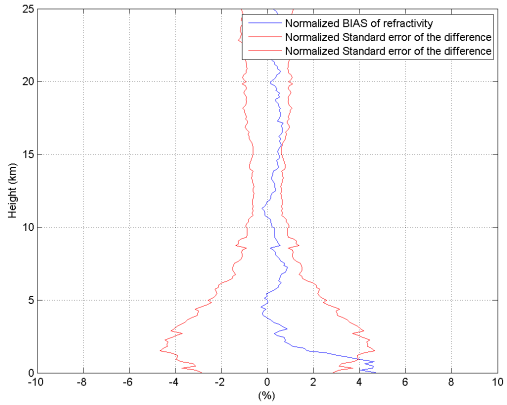

Figure 157 The refractivity bias (blue curve) and standard error of the difference for refractivity (red curve) as a function of height.

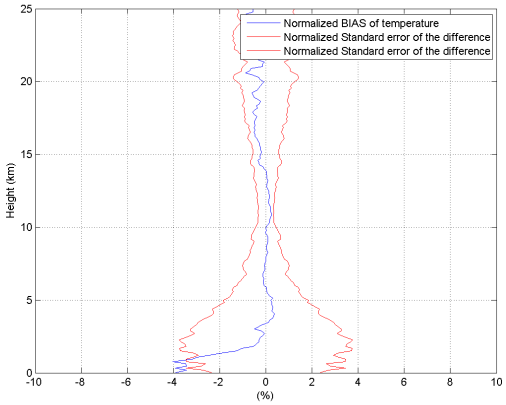

Figure 158 The temperature bias (blue curve) and standard error of the difference for temperature (red curve) as a function of height.

Statistics based on the radio occultation data in latitude interval 3 for the day 30/9 2007

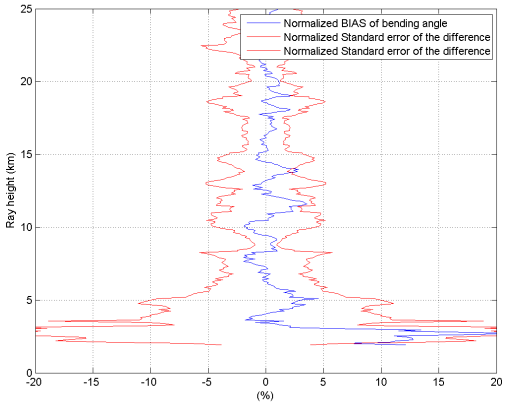

Figure 159 The bending angle bias (blue curve) and standard error of the difference for bending angle (red curve) as a function of height.

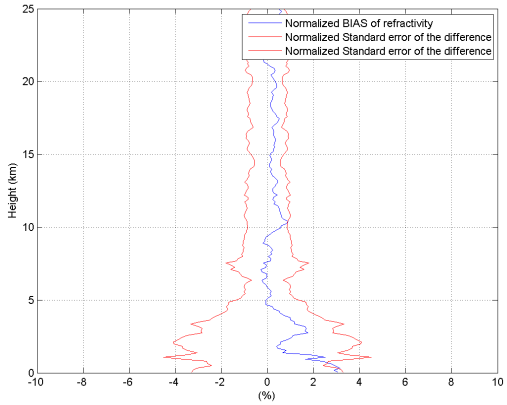

Figure 160 The refractivity bias (blue curve) and standard error of the difference for refractivity (red curve) as a function of height.

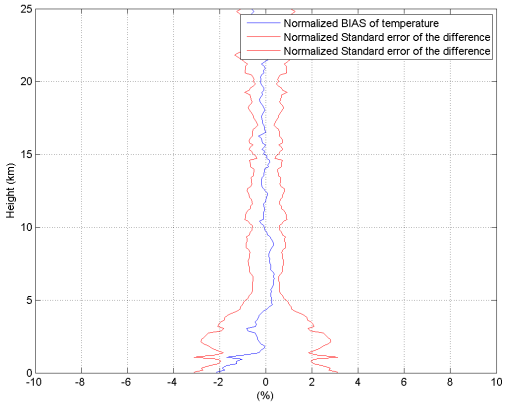

Figure 161 The temperature bias (blue curve) and standard error of the difference for temperature (red curve) as a function of height.

APPENDIX D WOP SIMULATION – AMPLITUDE PLOTS

The ten cases wave optics (WOP) propagation run with EGOPS (see section 6) are presented here as amplitude plots for the three centre frequencies in the bands L1, L2 and L5/E5. The amplitudes are given as function of time and the ray tangent height is also shown. The simulations geometry is chosen as a setting head on occultation with the occultation ended after 60 seconds.

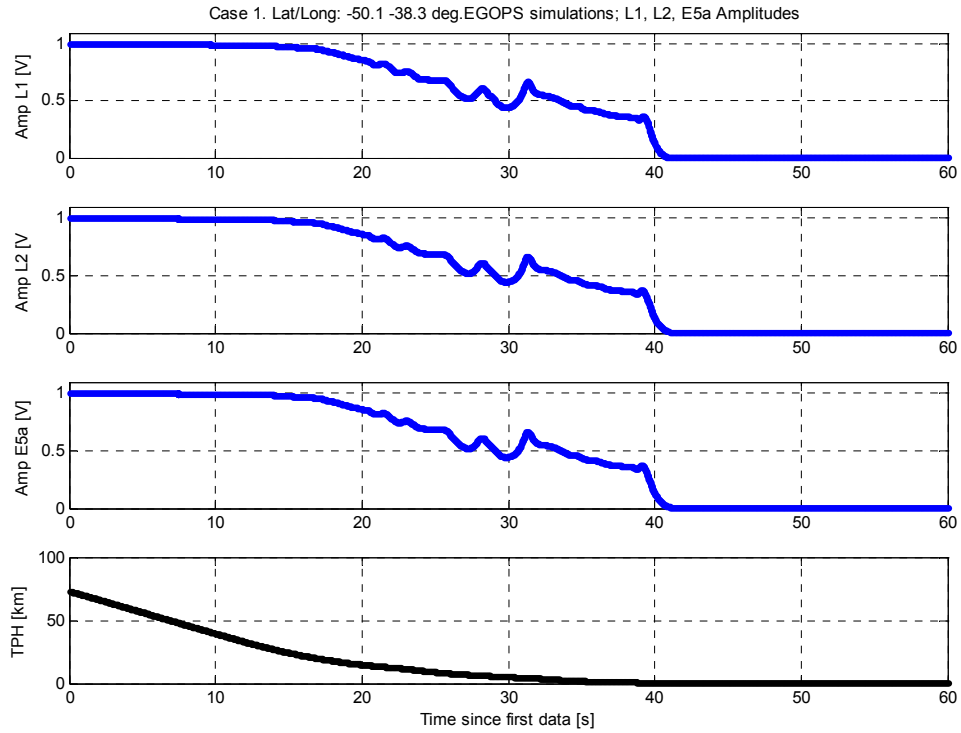

Figure 162 Case1: L1, L2 and L5 amplitudes and ray tangent height.

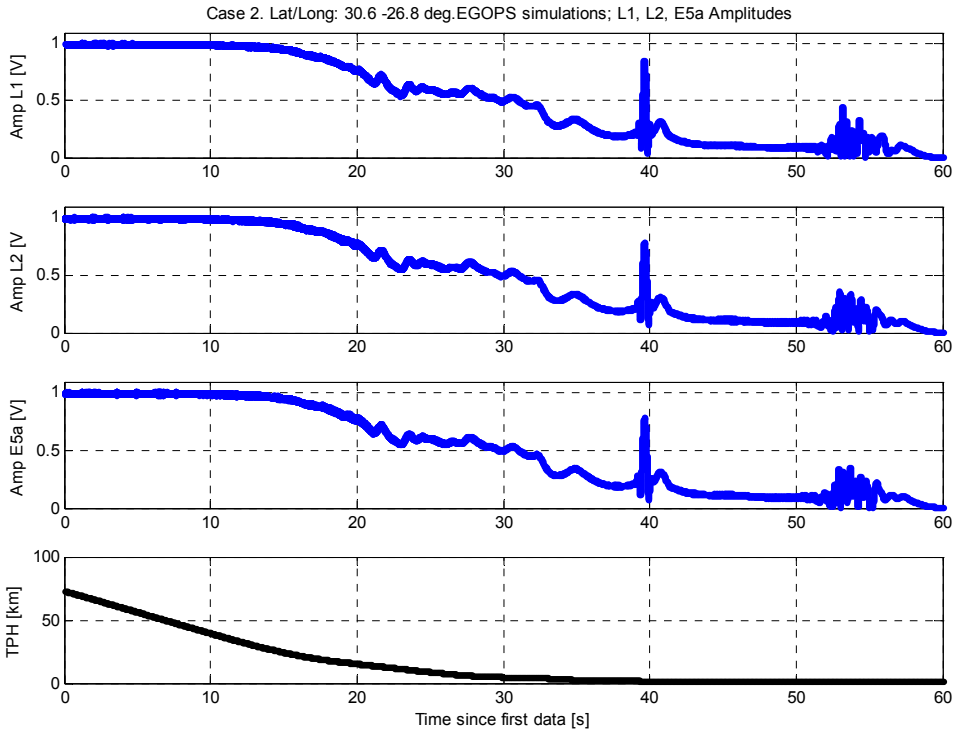

Figure 163 Case2: L1, L2 and L5 amplitudes and ray tangent height.

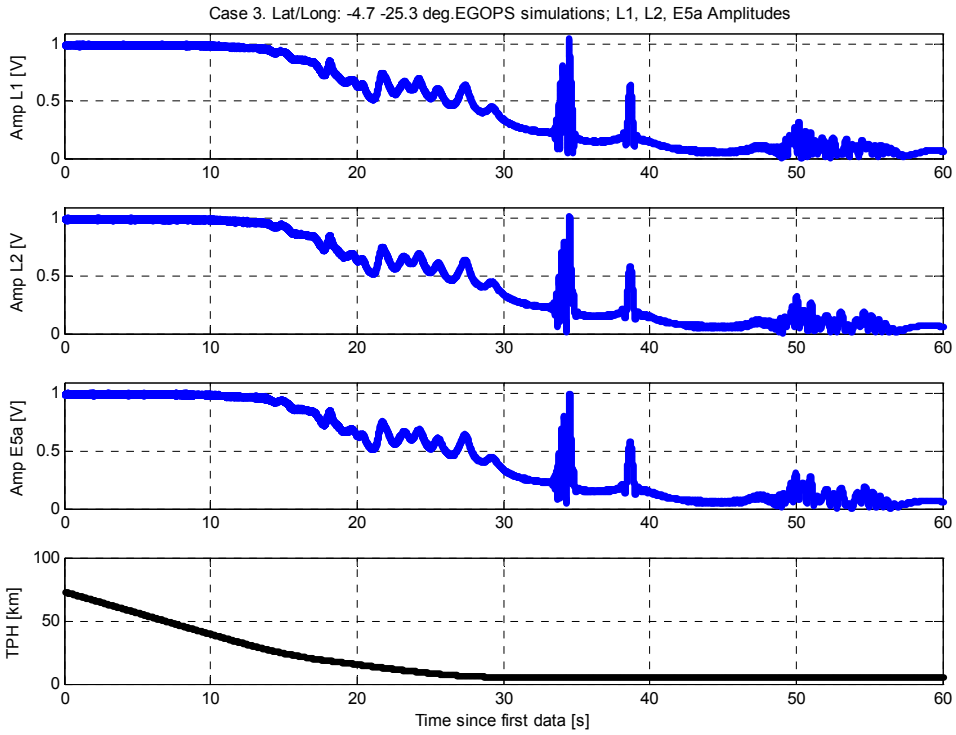

Figure 164 Case3: L1, L2 and L5 amplitudes and ray tangent height.

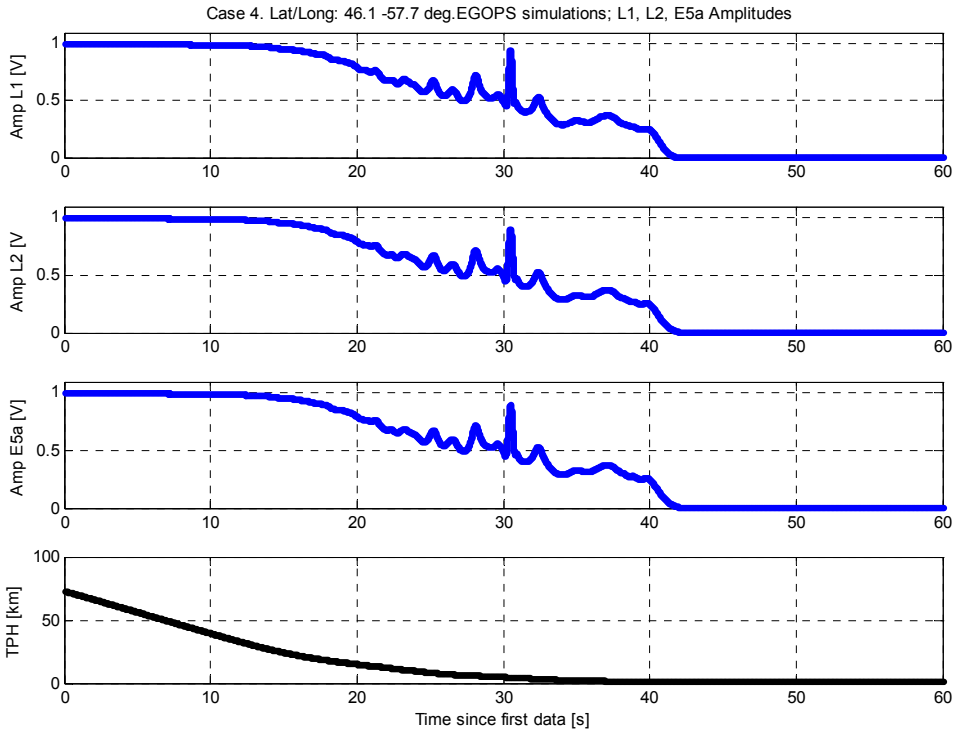

Figure 165 Case4: L1, L2 and L5 amplitudes and ray tangent height.

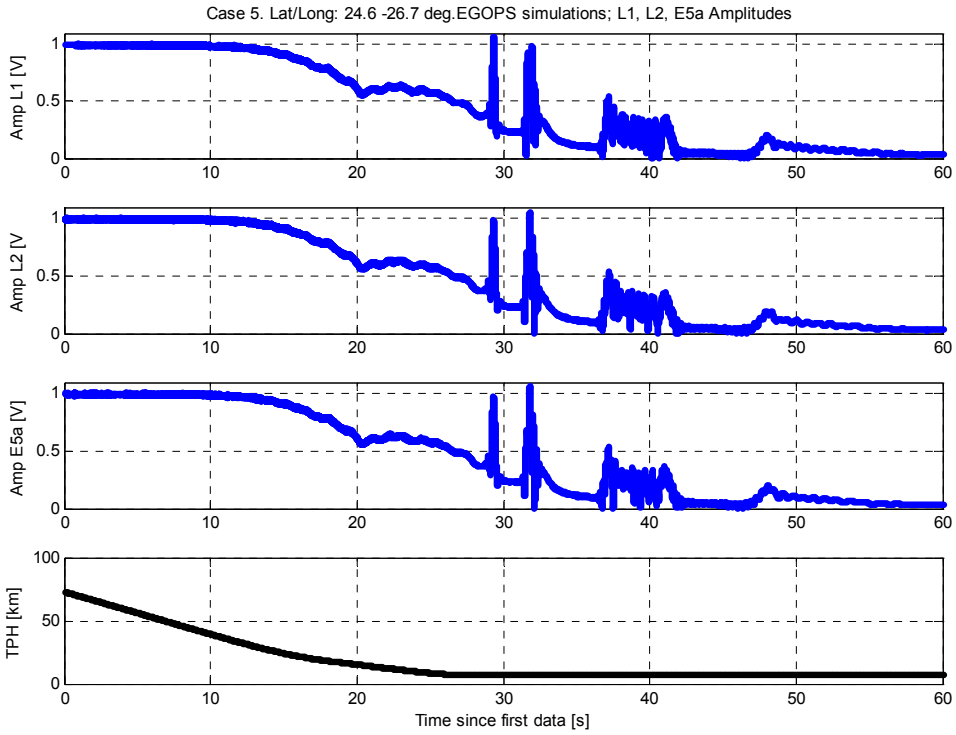

Figure 166 Case5: L1, L2 and L5 amplitudes and ray tangent height.

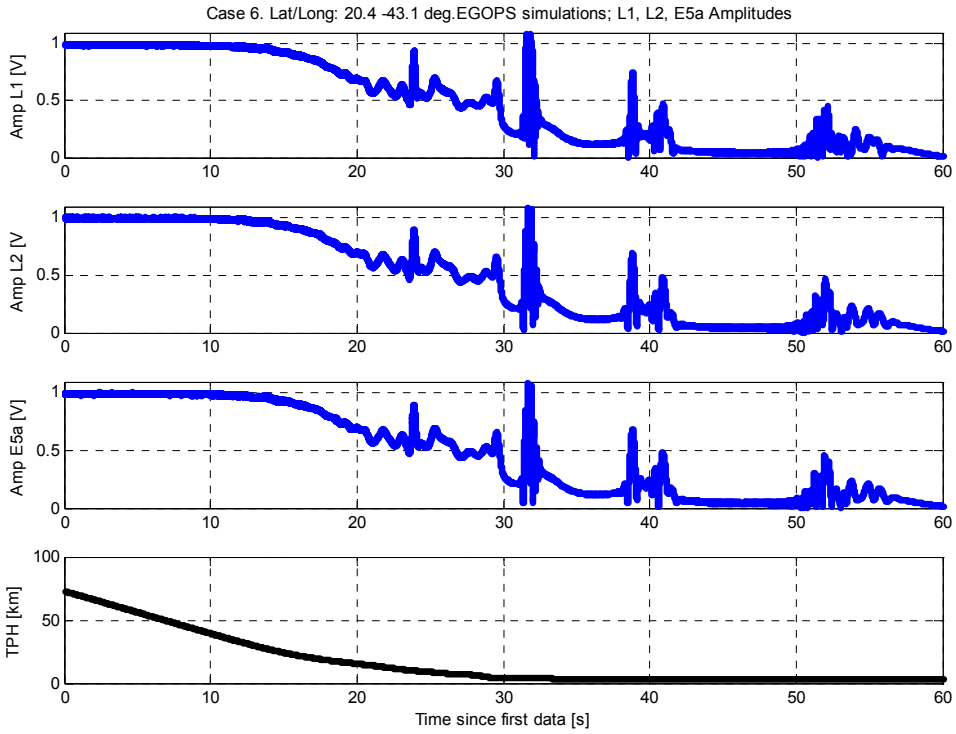

Figure 167 Case6: L1, L2 and L5 amplitudes and ray tangent height.

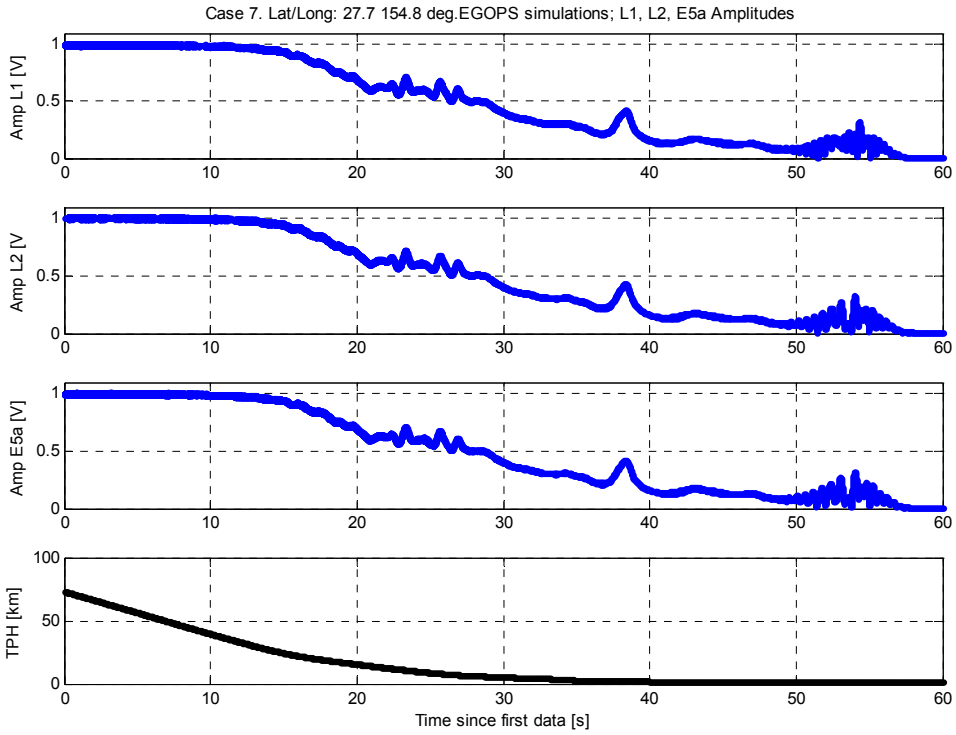

Figure 168 Case7: L1, L2 and L5 amplitudes and ray tangent height.

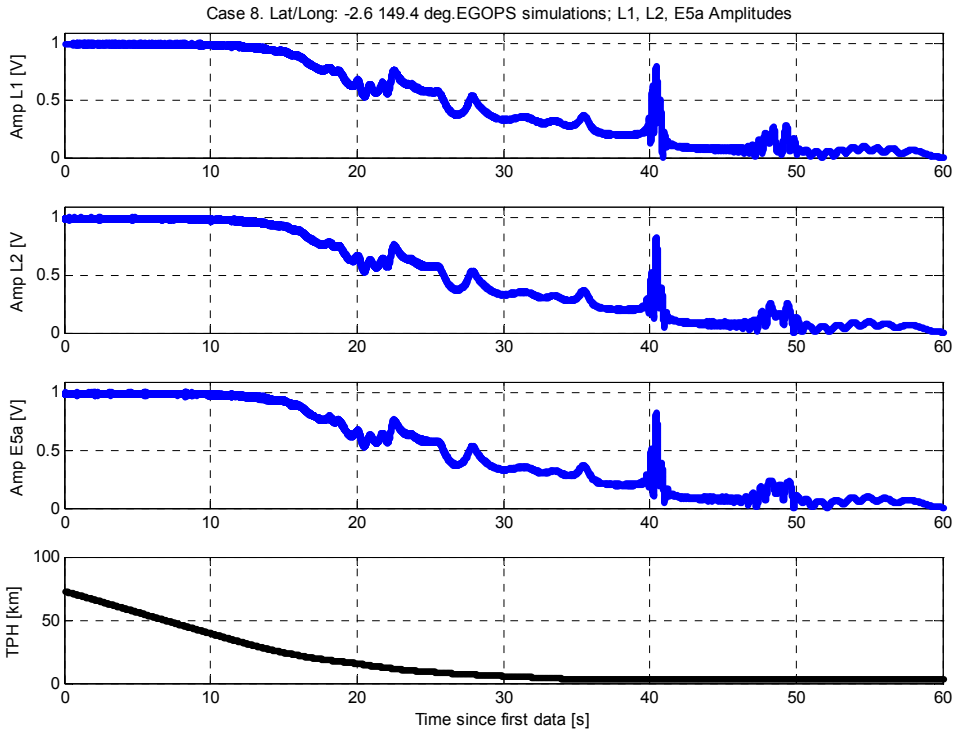

Figure 169 Case8: L1, L2 and L5 amplitudes and ray tangent height.

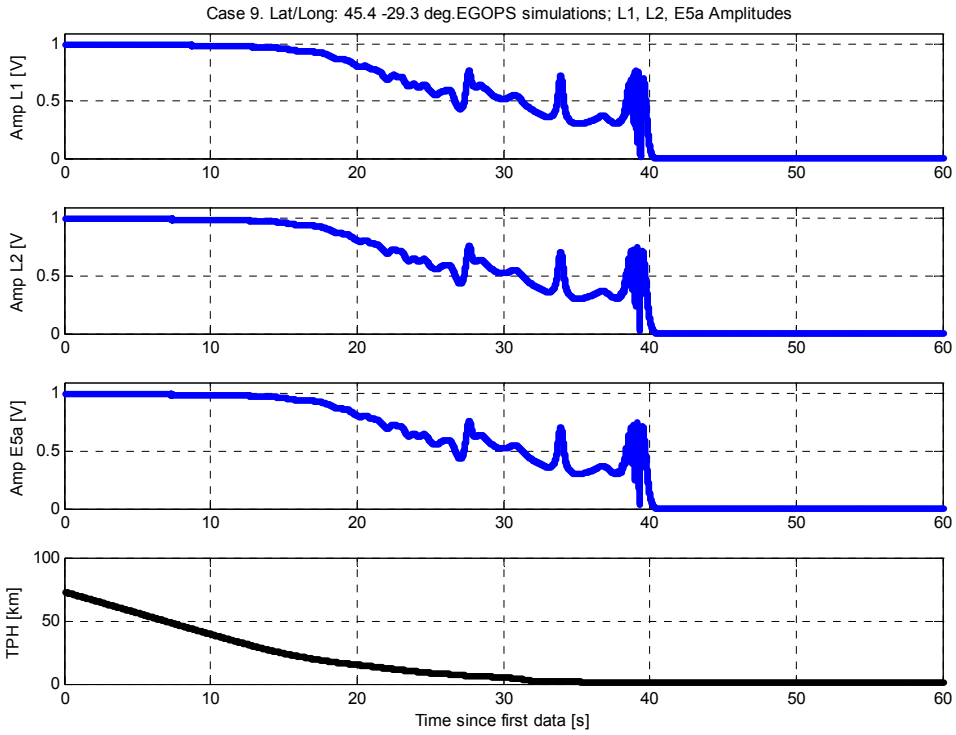

Figure 170 Case9: L1, L2 and L5 amplitudes and ray tangent height.

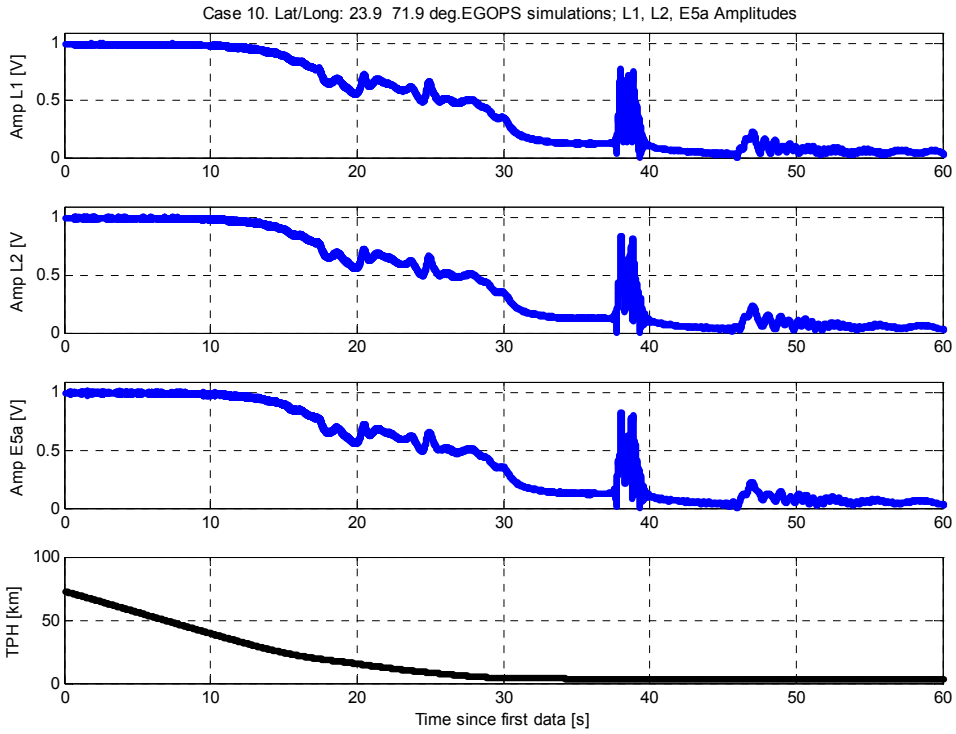

Figure 171 Case10: L1, L2 and L5 amplitudes and ray tangent height.